UNIVERSITY OF MILANO-BICOCCA
Department of Earth and Environmental Sciences
PhD Course in Earth Sciences (XXVII cycle)

RELATIONSHIPS BETWEEN LANDSLIDE SIZE DISTRIBUTION AND EARTHQUAKE SOURCE AREA IN A PERSPECTIVE OF SEISMIC HAZARD ZONINIG

Supervisor: Prof. Paolo FRATTINI
Co-supervisor: Prof. Giovanni B. CROSTA

PhD student:
Andrea VALAGUSSA
Number: 072715

Academic Year 2014

Index

1 Abstract

Earthquakes have been recognized as a major cause of landsliding (Keefer, 1984), and landslides triggered by earthquakes have been documented since the IV century (Seed, 1968).

The spatial distribution of earthquake-induced landslides around the seismogenetic source has been analysed to better understand the triggering of landslides in seismic areas and to forecast the maximum distance at which an earthquake, with a certain magnitude, can trigger landslides. However, when applying such approaches to old earthquakes one should be concerned about the undersampling of smaller landslides, which can be cancelled, by erosion and landscape evolution. For this reason, it is important to characterize carefully the size distribution of landslides as a function of distance from the earthquake source.

I analysed six earthquakes in the world that triggered significant amount of landslides (Finisterre 1993, Northridge 1994, Niigata 2004, Wenchuan 2008, Iwate 2008 and Tohoku 2011) to better understand the relation between the spatial distribution of the landslides, the peak ground acceleration (PGA), the distance from the sources, the relief and the lithologies of the area. I observed a strong relationship between landslides size and PGA, while the relationship between the distance from the source and the landslide size distribution is not clear, due to the interaction of different factors such as relief and lithology.

I also developed magnitude frequency curves (MFC) for different distances from the source area by using different methods, such as: the maximum likelihood estimator of cumulative power-law distribution (Clauset et al, 2009); the maximum likelihood estimator of non-cumulative power-law function; the least square regression of non-cumulative log power-law function and the maximum likelihood estimator of Double Pareto distribution. I observed a decrease of the spatial density of landslides with distance, with a small effect of the size of these landslides. I also identify the Double Pareto function as the best tool for the fitting of the data (Valagussa et al., 2014a).

In order to define the hazard due to earthquake-induced landslides, I developed a methodology for quantitative probabilistic hazard zonation for rockfalls (Valagussa et al., 2014b). I applied and demonstrated the method in the area of Friuli (Eastern Italian Alps) that was affected by the 1976 M_w 6.5 earthquake. Four rockfall datasets have been prepared from both historical data and field surveys. The methodology relies on a three-dimensional hazard vector (RHV_{mod}), whose components include the rockfall kinetic energy, the fly height, and the annual frequency. The values of the first two components are calculated for each location along the slope using the 3D rockfall runout simulator Hy-STONE. The rockfall annual frequency is assessed by multiplying the annual onset frequency by the simulated transit frequency. The annual onset frequency is calculated

through a procedure that combines the extent of unstable areas, calculated for 10 different seismic-hazard scenarios with different annual frequencies of occurrence, and the magnitude relative-frequency relationship of blocks as derived from the collected field data. For each annual frequency of occurrence, the unstable area is calculated as a function of morphometric and earthquake characteristics. A series of discriminant-analysis models, using the rockfall datasets and DEMs of different resolution (1 and 10 m), identified the controlling variables and verified the model robustness. In contrast with previously published research, I show that the slope curvature plays a relevant role in the computation of the unstable area. To ensure the validity of the peak ground acceleration used as seismic parameter in the discriminant function, I also try to define a map of PGA based on the precarious balanced rocks surveyed on the field.

2 Introduction

2.1 Earthquakes-induced landslides

Earthquakes have been recognized as a major cause of landslide (Keefer, 1984). Landslides triggered by earthquakes have been documented from at least as early as 373 or 372 B.C. (Seed, 1968). Keefer (1984) studied 40 historical earthquakes to analyse the relationship between landslides and earthquakes. He classified the landslide in three categories that are rockfall, rock slid and disrupted slide, and observed that the number of landslides triggered by earthquake generally increases with increasing magnitude. However, also the geological condition and the seismic parameters influence the landslide number. During his study, Keefer identified five measures:

- the smallest earthquakes that cause landslides; On the basis of the intensity reports for United State earthquakes and the 40 historical events, the smallest earthquakes for each type of landslide has been identified.
- the relation between magnitude and the area affected by landslide (Figure 1); For 30 of the historical earthquakes, the area affected by landslides has been found by drawing a boundary around all reported landslide localities and calculating the size of the region enclosed.

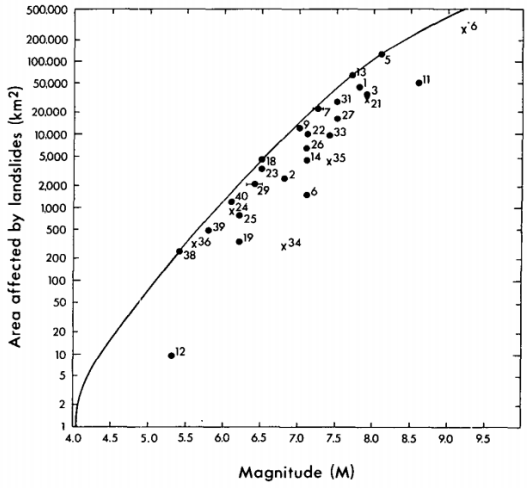

Figure 1. Area affected by landslides in earthquake of different magnitudes. The number refer to the earthquake reported in Keefer et al. (1984). Dots: onshore earthquake; x: offshore earthquake. Solid line is approximate upper bound enclosing all data.

- the relation between magnitude and maximum distance of landslide from the epicentre (Figure 2-a); In this case the relation was found for disrupted slide and falls, coherent slide and lateral spread and flows.
- the relation between magnitude and maximum distance from the fault rupture (Figure 2-b); The fault rupture zone were determined in different ways, and this kind of distance may be

more appropriate than the maximum epicentre distance. Also in this case, the three type of landslide of the previous relation were used.

- the minimum shaking intensity at which landslide are triggered. To define the lowest intensities, iso-seismal maps were compared with maps showing the landslide distribution for all the historical earthquakes.

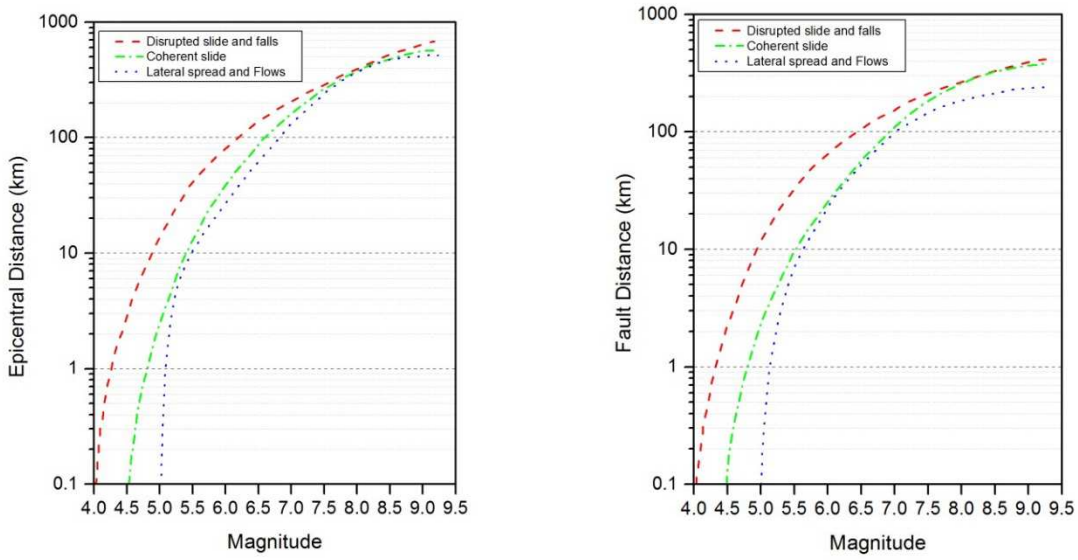

a b

Figure 2. Maximum distance from fault rupture zone to landslides for earthquakes of different magnitudes (a). Maximum distance from fault rupture zone to landslides for earthquakes of different magnitudes (b). Curves digitalized by Keefer et al. (1984)

Keefer and Wilson (1989) and Keefer (1994) identified a relation, as a linear regression, between the total landslide volumes of landslide and the magnitude of the earthquakes. The total landslide volume have been determined by field activity and interpretation of aerial photos. The earthquakes considered were shallow and onshore. Rodriguez et al. (1999) provides a significant extension of the database compiled by Keefer. The number of earthquakes was increased from 40 to 76 and updating to 1997. This work confirms the results of Keefer but show that the maximum area affected by landslides is greater than the upper bound proposed by Keefer for intermediate earthquakes, related also to the difference in the geographic location of the two datasets. Meunier et al. (2007) derived an equation to characterise the spatial variation of landslide density analogous with regional seismic attenuation laws, because, for the considered earthquakes (California, Taiwan and Papua New Guinea) landslide densities were higher in area with stronger ground motion and decay with the distance from the epicentre. More recently regional based curves has been proposed for Italy (Prestininzi and Romeo, 2000), Greece (Papadopoulos and Plessa 2000), and southern

Spain (Delgado et al., 2011). Prestininzi and Romeo (2000) found that landslides and fractures are more likely to be triggered by earthquake than topographic changes and liquefaction, because the first two categories require smaller site and epicentral intensities and occur at longer distances than the latter two types. On the basis of a set of 47 cases of earthquake-induced landslides in Greece, Papadopoulos and Plessa (2000) identified a range of magnitude (M_s) in which the landslide could be triggered in their country (between 5.3 and 7.9). Delgado et al. (2011a) analysed the seismically-induced landslide in the Betic Cordillera (Spain), and they found regression curves for the different type of landslides for the study area. Delgado et al. (2011b), on the basis of previously worldwide, country, and regional based datasets (Worldwide, Keefer, 1984; Costa Rica, Mora and Mora, 1994; Worldwide, Rodríguez et al., 1999; Greece, Papadopoulos and Plessa, 2000; Italy, Prestininzi and Romeo, 2000; Central America, Bommer and Rodríguez, 2002; New Zealand, Hancox et al., 2002; USA, Keefer, 2002; Colombia, Rodríguez, 2006; CEREIS, 2010; S Spain, Delgado et al., 2011a), found that most of the data were well contained by the upper bounds proposed by Keefer (1984), but there was a set of outliers for the disrupted and coherent landslide types (for low and moderate magnitude). These exceptions could be related to some local factors such as the susceptibility of slopes prior to earthquake occurrence, antecedent rain, site effect or the occurrence of seismic swarms/series. From the new compiled database, they concluded that, for earthquakes of equal magnitude, the disrupted landslides might occur further away than the coherent landslides.

2.2 Influence of seismic parameters on landslide size

With the increase of the distance from the seismic source, it is expected that the landslides size decrease. Keefer and Manson (1998) in the Loma Prieta earthquake (1989) found that beyond a certain distance only small rockfalls, rockslides, or soil slides with volume less than 100 m^3 occurred.

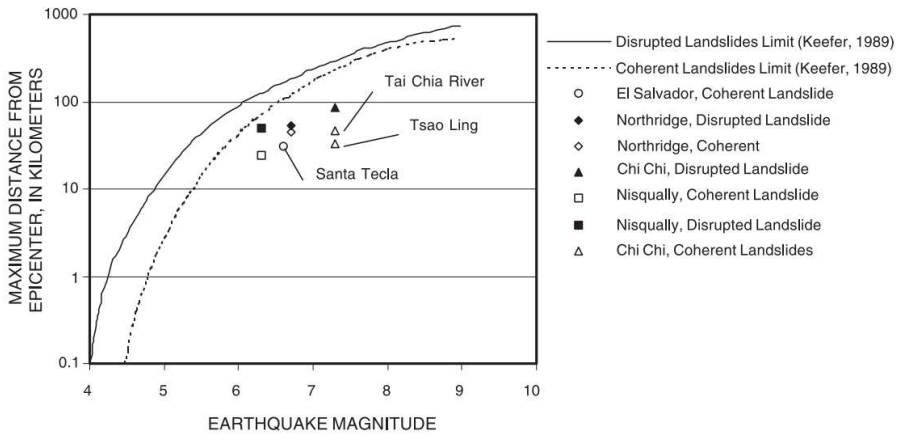

.

Figure 3. Maximum distance from epicenter for seismically induced landslides as a function of earthquake magnitude (limits from Keefer, 1989). Graph from Khazai and Sitar (2003).

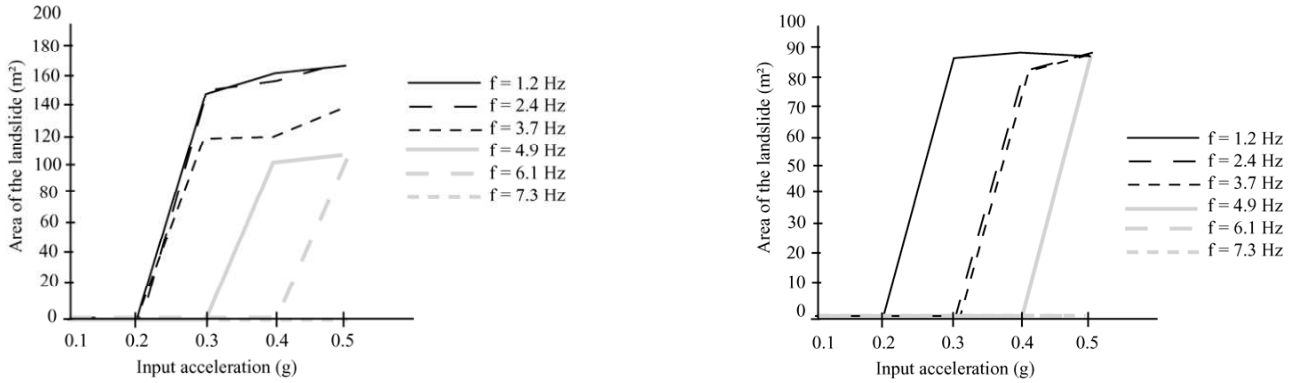

Figure 4. Calculated landslide areas for the whole ranges of frequencies and input accelerations for two models considered (see Bourdeau et al., 2004).

Khazai and Sitar (2004), observing the characteristics of the landslides triggered by the Chi Chi earthquake (1999), found that larger coherent landslides occurred at distance lower than shallow and disrupted landslides (Figure 3). From the graph, it possible to see that also for the Nisqually earthquake (2001) and Northridge earthquake (1994) is the same.

In order to better characterize the landslide potential under seismic condition, Bourdeau et al. (2004), through numerical modelling, defined how the size of a slope failure may be linked to the intensity of the seismic shaking and to the size of a seismic event, considering that large events producing strong ground accelerations in a lower frequency range.

Figure 4 shows that, the area of the sliding mass rapidly increases with the intensity of the seismic shaking. This increase is limited, in most of the cases, by an area value (plateau) corresponding to the area of the pseudo-static failure induced by large ground-motions. Figure 4 also shows that in addition to the amplitude the frequency content of the signal has an influence on the sliding area. The area is generally larger for lower frequencies, which may be a consequence of the distribution ground-motions in the slope.

For high frequency inputs, Bourdeau et al. (2004) found that the strong ground-motions are confined to the crest of the slope inducing a minor susceptibility to failure than for low-frequency shaking which produces relatively stronger ground-motions at depth. Combining a low-frequency input with a resonance phenomenon in the low-frequency range (1 to 3 Hz), the slope failure potential takes its highest values. Moreover, large magnitude earthquakes tend to trigger larger landslides because of the larger ground accelerations and the low-frequency content.

2.3 Implication for landslide hazard

The observation from Keefer and Manson (1998) and Khazai and Sitar (2003), and the results of numerical modelling by Bourdeau et al. (2004) have important implication for landslide hazard.

In fact, landslide hazard expresses the probability that a landslide with a certain intensity can occur in a certain location within a given period of time [ISSMGE Glossary of Risk Assessment Terms, http://140.112.12.21/issmge/2004Glossary_Draft1.pdf]. This definition underlines that hazard is a function of intensity. This function is usually known as hazard curve, in the literature generally related to seismic risk (Frankel et al., 1996), windstorms and floods (Grünthal et al., 2006) and tsunamis (PTHA, González et al., 2009; Annaka et al., 2007; Liu et al., 2007; Geist and Parsons, 2006). While the concepts of intensity and magnitude are well defined for these threats, the terms are not always really and easily formalised for landslides. A formalization was proposed by Hungr (1997), and some clarifying advices have been expressed in some recommendations for landslide risk assessment (e.g. OFAT-OFFE-OFEP, 1997; AGS, 2007; Fell et al., 2008; Corominas et al., 2014). In most cases, however, intensity is used as a general term, which can include different concepts, such as size, volume, velocity, energy. Magnitude is frequently used to describe the size of a landslide in terms of volume (e.g. Hungr et al. 1999; Marchi and D'Agostino, 2004; Jakob and Friele, 2010; Santana et al, 2012) or area (e.g.: Hovius et al, 1997; Stark and Hovius, 2001; Dussauge et al, 2003; Malamud et al., 2004b; Guthrie and Evans, 2004). A low consensus on the use of terms derives from the fact that landslides include different phenomena, which can be described by different parameters. Due to the objective difficulty to generate hazard curves for landslides, a reason why they are extremely rare in the landslide risk literature, the selection of an intensity parameter is still an important issue. Intensity should correspond to a measure of "damage potential". Hence, it should not express the size of a landslide, but its destructive power. On the other hand, the frequency of landslides is often related to their size and not necessarily to their destructive power, expressing the magnitude of the events, more than the intensity (e.g., Hungr et al, 1999; Dussauge et al, 2003). In this thesis hazard for seismically induced landslides is limited to rockfalls. Rockfalls are one of the most severe and recurrent dangerous events, and occurs where geological and weather conditions are particularly severe for slope stability. Moreover, rockfalls and in general landslide, represent one of the main secondary effect of large earthquakes (Keefer, 1984; Rodriguez, 1999; Hack et al., 2007). Rockfall hazard zoning is therefore fundamental for land planning, especially in seismic areas that are particularly prone to rockfalls. Hazard zoning is the division of land into homogeneous areas or domains and their ranking according to degrees of actual or potential landslide hazard (Fell et al, 2008). Different rockfalls hazard zoning methodologies have been proposed at different scales (Labiouse and Abbruzzese, 2011) through

multi-criteria rating approaches (e.g., Pierson, 1990) or approaches based on coupling energy and frequency (Raetzo, 2002; Corominas et al, 2003; Rouiller et al, 1998; Jaboyedoff et al, 2005). However, most of these approaches assess the rockfall frequency by heuristic approaches, expert judgement, or based on relatively small historical dataset. This makes them inapplicable in seismic areas, where the probability of rockfalls is mostly controlled by earthquake events. A rigorous rockfall hazard assessment for zoning purposes requires the definition of the probability of occurrence, and the level of energy associated to expected events. For rockfalls occurring along complex slope morphology, two aspects of probability should be analysed: the onset probability and the reach probability (Corominas et al. 2005; Jaboyedoff et al. 2005; Straub & Schubert 2008; Agliardi et al. 2009). The onset probability depends on several factors (e.g., geological, geomorphological, hydrological conditions) that locally control the stability of the cliffs, and on the probability of possible external triggering events (e.g., rainfall, earthquakes). For seismically triggered rockfalls, the onset probability is regulated by the probability of occurrence of earthquakes with different intensity. For other landslide typology the relationship between earthquake input and landslide occurrence has been extensively studied by means of empirical (Keefer 1984; Rodriguez et al, 1999; Lee et al., 2008; Miles et al., 2009) and physically based approaches (Jibson et al, 2000; Wasowski et al., 2000; Bommer and Rodriguez, 2002; Capolongo et al., 2002; Del Gaudio et al., 2003; Del Gaudio et al., 2004; Uchida et al., 2006; Peng et al., 2009; Rapolla et al., 2010; Motamedi et al., 2013). Indeed, only a few contributions focused explicitly on rockfalls. Based on Umbria and Marche 1977 earthquake (Mw 6.0), Marzorati et al. (2002) defined a multiple regression equation in which the density of landslide (D_r) is related to slope angle (S) and Peak Ground Acceleration (PGA) as follow: $\log D_r = - 4.565 + 0.056 \cdot S + 0.670 \cdot PGA$.

The reach probability depends on the path followed by rockfalls in their movement along the slope and it is controlled by several factors, such as the topographical surface at micro and macroscale, the rockfall volume, the shape and the size of blocks (Frattini et al, 2012a). For the assessment of the reach probability, a simulation of rockfall run out should be performed by using empirical methods (e.g. the “shadow cone” method, Evans and Hungr, 1993) or by simulating free-fall, impact, bouncing and rolling motions in a 2D or 3D space, through the use of kinematic (e.g., Stevens, 1998), hybrid (Pfeiffer & Bowen, 1990; Jones et al. 2000; Agliardi et al., 2003; Crosta et al. 2004) or dynamic mathematical models (Descouedres and Zimmermann, 1987; Azzoni et al. 1995; Leine et al , 2013).

2.4 Magnitude Frequency curves

As seen above, the size of the landslide is of paramount importance for landslide hazard because it controls the destructive power of landslides (i.e., the local intensity) and because it controls the frequency of landslides. It has been widely observed that larger landslides are less frequent than smaller landslides. The relationship between the size of the landslides and the frequency is called Magnitude frequency curves.

The magnitude-frequency curves has long been used in seismology, where the observed power-law relationship between earthquake magnitude and frequency is known as the Gutenberg-Richter Law (Gutenberg and Richter, 1954). The characterisation of landslide size distribution has recently deserved the attention of many researcher, with different scopes: the comprehension of landslide dynamics (Pelletier et al., 1997; Hergarten and Neugebauer, 1998; Dussauge et al., 2003; Katz and Aharonov, 2006; Guthrie et al., 2008; Stark and Guzzetti, 2009), the quantification of the erosion caused by landsliding (Hovius et al., 1997; Hovius et al., 2000; Stark and Hovius, 2001; Brardinoni and Church, 2004; Guthrie and Evans, 2004; Hungr et al., 2008; Chen, 2009), and the evaluation of landslide event magnitude in natural hazard studies (Hungr et al., 1999; Malamud and Turcotte, 1999; Guzzetti et al., 2002b; Malamud et al., 2004b; ten Brink et al., 2006; Van Den Eeckhaut et al., 2007; ten Brink et al., 2009). These studies carried out on landslide inventories from different locations allow to establish some points on which a general agreement exists: (1) the frequency distribution exhibits power-law scaling for landslides larger than a size threshold; (2) below this threshold, the distribution shows a deflection that deviate from power-law. In some cases the deflection occurs right below the modal peak of the distribution, known as roll-over (e.g., Malamud et al., 2004b). In other cases (Brardinoni and Church, 2004; Van Den Eeckhaut et al., 2007; historical inventories in Malamud et al., 2004b), the deviation from power law is progressive below a certain size, possibly due to incompleteness of the inventory (Guzzetti et al. 2002b).

Both the physical reasons for the power law scaling and the physical meaning of the deflection are not clearly understood.

The power law scaling for landslides has been variously interpreted in the literature as the result of: self-organized criticality (sandpile model, Bak et al, 1988; Hergarten and Neugebauer, 1998); heterogeneity of slopes and fracture systems (Katz and Aharonov, 2006), stochastic process of rupture propagation (Stark and Guzzetti, 2009).

The deflection from power-law below a size threshold has been interpreted as: (1) the result of undersampling (Hovius et al., 1997; Hovius et al., 2000; Stark and Hovius, 2001); (2) the effect of the distribution of soil moisture over the landscape (for shallow landslides, Pelletier et al., 1997); (3) the consequence of the transition from friction-controlled to cohesion-controlled strength when

decreasing the area (and the depth) of the landslide (Malamud et al., 2004b; Katz and Aharonov, 2006; Stark and Guzzetti, 2009); (4) the consequence of slope length constraint on the downslope propagation of long-runout landslides (Guthrie and Evans, 2004). A progressive deviation observed in some inventories has been explained as the effect of time-scale constraint on small-landslide detection in historical inventories (Malamud et al., 2004b) or the effect of man-made small landslides (Van Den Eeckhaut et al., 2007)

The origin of these differences is related to intrinsic problems in the characterisation of landslide inventories. The size distribution is controlled by both environmental factors (e.g., typology of landslides, geological setting, soil/rock properties) and man-made artefacts. Smaller landslides can be strongly underestimated because of censoring due to the scale of landslide survey or the obscuration over time leading to a systematic bias in historical inventories (Malamud et al., 2004b), or because of smaller landslides can be undetectable because reworked during the event by larger coalescent landslides. Another problem is related to the fact that the inventories seldom distinguish between the source areas and the depositional areas of landslides characterised by long-runout or large download displacement. Since physical, hydrological and mechanical processes controlling the initial slope failure and the run-out are very different, the scaling behaviour and the roll-over can be expected to be different.

2.5 On-field verification of PGA

The Peak Ground Acceleration (PGA) is the most commonly used parameter in seismic hazard analysis and in earthquake-induced landslide hazard. For this reason, the quality and reliability of PGA data is extremely important for hazard analysis.

For the validation of existing map or when data are not available, an useful tool for the understanding of the peak ground acceleration experienced by an area, come from the precarious balanced rocks.

The dynamics of the rocking response of fragile objects to earthquake-generated ground motions have been researched for over a century (Mallet, 1862; Milne, 1881; Milne and Omori, 1893; Kirkpatrick, 1927; Housner, 1963). Precariously balanced rocks are strong-motion seismoscopes that have been in place for years, and thus they can provide important information on ground motion and seismic hazard from large earthquakes over long periods of time (Brune, 1996; Bell et al., 1998; Anooshehpoor and Brune, 2002; Anooshehpoor et al., 2004; Brune et al., 2006). The rocks can be divided into two categories based on field observations: semiprecarious (quasi-static toppling accelerations 0.3–0.5 g) and precarious (quasi-static toppling accelerations 0.1–0.3 g)

(Brune, 1996). Further development of the methodology has allowed more accurate estimates with field tests and computer analysis (Anooshehpoor et al., 2004; Purvance, 2004).

Preliminary estimates of toppling accelerations can be made from visual inspection of the rocks in the field or from photographs. More accurate estimates may require field testing and computer modeling (Anooshehpoor et al., 2004; Purvance, 2004).

An important parameter that is used to model the rocking response of a precariously balanced rock (PBR) to ground motions is slenderness. A PBR's slenderness (αi in Figure 5) is defined as the angle made by the vertical (mg in Figure 5) passing through the PBR's center of mass and the lines that connect the PBR's rocking points to its center of mass (Ri in Figure 5). These values are typically estimated in the field using a plumb bob, measuring tape, and a trained eye.

Recently, photogrammetric and terrestrial laser scanning techniques (TLS) have been employed to capture the 3D geometry of a PBR at decimeter (photogrammetry) and millimeter (TLS) scales (e.g., Anooshehpoor et al., 2007; Haddad and Arrowsmith, 2009; Hudnut et al., 2009). These methods are especially useful to modeling the 3D rocking response of a PBR to ground motions (e.g., Hudnut et al., 2009). However, these techniques require a considerable amount of field preparation and data collection time and effort, making them impractical for studies that attempt to survey entire populations of PBRs at large scales. A semplifeid methodology is here adopted. The PBR’s dimensions are measured. Photographs of the PBR are taken perpendicular to the direction of toppling. The GPS coordinates of the PBR are recorded and noted.

Haddad (2009) developed a tool (PBR_slenderness_DH_v1_0) to estimate αi and Ri from unconstrained digital photographs of PBRs. Purvance (2005) first proposed this approach, where a photograph of a PBR is taken in the field and the outline of the PBR is digitized to compute its 2D center of mass, αi and Ri. Theoretically, a PBR can be sectioned along an infinite number of vertical planes that pass through its center of mass along an infinite number of azimuths. This results in an infinite number of local minimum slenderness values. Therefore, the azimuth at which the photograph is taken is critical to estimating the absolute minimum slenderness value of a PBR. The general workflow is as follows: the user digitizes the PBR's rocking points, plumb bob, scale, and the PBR's outline.

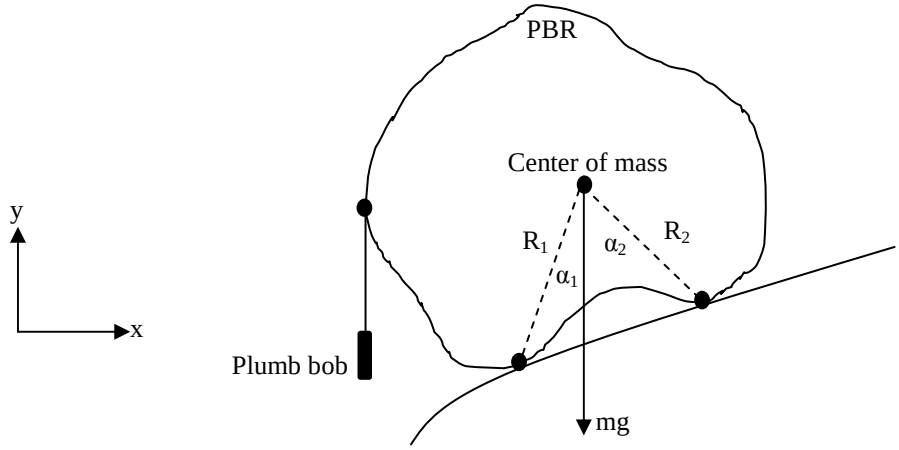

Figure 5. Geometric parameters of a precariously balanced rock (PBR). *αi* are the PBRs slenderness values, where the smallest *αi* value is assigned to the PBR as α_{min}.

2.6 PhD thesis outline

The first aim of this thesis is the spatial distribution of earthquake-induced landslides around the seismogenetic source to better understand the triggering of landslides in seismic areas and to forecast the maximum distance at which an earthquake, with a certain magnitude, can induce landslides of a certain size.

In the first chapter, six earthquakes (Papua New Guinea Earthquake, 1993; Northridge Earthquake, 1994; Niigata-Chuetsu Earthquake 2004; Iwate-Miyagi Nairiku Earthquake, 2008; Wenchuan Earthquake, 2008; Tohoku Earthquake, 2011) the geological setting of the affected area and the corresponding earthquake-induced landslides inventories were describe. The magnitude of these earthquakes ranging between 6.6 and 9.0 M_w. Another area that is subjective to high seismicity is considered in the first part: Northern Chile. Here a landslides inventory was mapped between Iquique and Arica. No dating is available for these landslides, as consequence, also the triggering factors.

In the second chapter, the spatial distribution of earthquake-induced landslides around the seismogenetic source has been analysed. The earthquake-induced landslides were divided in sub-set, based on the distance from the epicenter and from the fault rupture. The sub-set contain the same number of events. Through four different methodology, the magnitude-frequency curves of each sub-set were analysed to find the scaling parameter, α, of the landslide size distribution.

In the third chapter, the relationship between the landslides size and the lithology in the affected area has been analysed, because the geology is another important factor that control the occurrence

of landslides (Keefer, 1984). Through the analysis of the magnitude-frequency curves, developed for each lithology, the scaling parameter, α, of the landslide size distribution is found and analysed.
In the fourth chapter, by using the fitting curves of landslides from literature, from the inventories analysed in this thesis and the frequency density of Chile inventory for the selected areas, the magnitude required to generate such landslide distribution was derived, with different possible scenarios: a single earthquake, three-equal earthquakes and ten-equal earthquakes.

The second aim of this thesis is the development of a simple and readily applicable methodology for earthquake-induced hazard zoning in seismic areas.
In the fifth chapter, a hazard map for the area affected by the 1976 Friuli earthquake was developed, starting from the "Rockfall Hazard Vector" approach (RHV) proposed by Agliardi et al. (2003), and introducing the rockfall probability as a function of seismic hazard and rockfall dynamics. This allow also the definition of the most important variables controlling rockfall triggering, and in particular the role of PGA. In this thesis, the methodology for the definition of the quasi-static acceleration is applied in order to assess the reliability of the peak ground acceleration values of the ShakeMap model produced by the U.S. Geological Survey Earthquake Hazards Program (Wald et al, 2006) used in the analysis for the assessment of the rockfall hazard.

3 Methodology

In this thesis the magnitude-frequency curve are expressed as a function of the area. In particular, the MF curves have been developed by using either the frequency density (see chapter 7) or the probability density (see chapter 5 and 6).

The area-frequency distributions of landslides were examined by developing logarithmically binned, non-cumulative size frequency distributions that report either frequency density (f = dN/dA) or probability density (p = dN/dA/N) as a function of landslide planar area A (dN = number of landslides with an area between A and A+dA, N = total number of landslides).

The difference between probability density and frequency density lies in the fact that the probability density is normalized by the total number of landslides, and therefore it is independent from the size of the sample population: curves referring to samples with different number of object can be readily compared. On the other side, the frequency density depends on the landslide population, and therefore it is convenient when trying to analyse the magnitude of different inventories (in terms of number of landslides).

For the fitting of the MF curves, four methods have been applied:

1. Maximum likelihood estimator of cumulative power-law distribution (Clauset et al, 2009 Matlab tool);
2. Maximum likelihood estimator of non-cumulative power-law function;
3. Least square regression of non-cumulative log power-law function;
4. Maximum likelihood estimator of Double Pareto distribution.

The purpose of these methods is the definition of the parameter α, a constant value of the distribution known as the exponent or scaling parameter.

3.1 Maximum likelihood estimator of cumulative power-law distribution

The first methodology was performed in MATLAB were α is estimated in according to the goodness-of-fit based method of the maximum likelihood estimators (MLE, Clauset at al., 2007). To estimate α correctly, the lower bound (A_{min}) of the power law behaviour is required. The approach for estimating A_{min}, proposed by Clauset et al. (2009), can be applied to both discrete and continuous data. The value of A_{min} is chosen so as to make the probability distributions of the measured data and the best fit power law model as similar as possible above A_{min}. In general, if the chosen A_{min} is higher than the true value A_{min}, then the size of the data set is actually reduced,

which will make the probability distributions a poorer match because of statistical fluctuation. On the contrary, if the A_{min} value is smaller than the true A_{min}, the distributions will differ because of the fundamental difference between the data and model by which it is described. So the best estimate is between these two cases. There are a variety of measures for quantifying the distance between two probability distributions, but for non-normal data the most common is the Kolmogorov-Smirnov or KS statistic (Kolmogorov, 1933; Smirnov, 1933), which is a measure of the largest vertical distance between the empirical and the modelled distribution. The A_{min} value that minimizes the KS statistic is the chosen A_{min}. After the identification of A_{min}, it is possible to define α. Given a dataset containing n observations $A_i \geq A_{min}$, the value that maximizes the likelihood function, the probability that the data were drawn from the model, is chosen as scaling parameter. The methodology gives (table 1):

- α, the maximum likelihood estimate of the scaling exponent,
- A_{min}, the estimate of the lower bound of the power-law behaviour,
- L, the log-likelihood of the data $A \geq A_{min}$ under the fitted power law.

The method is based on the follow equation:

$$P(A) = \int_A^{\infty} p(A')dA' = \left(\frac{A}{A_{min}}\right)^{-\alpha+1}$$

3.2 Maximum likelihood estimator of non-cumulative power-law function

The second methodology is based on the maximum likelihood estimator of non-cumulative power-law function. Mathematically, a quantity A obeys a power law if it is drawn from a probability distribution

$$p(A) \propto A^{-\alpha}$$

where A is the landslide area, and α is the scaling parameter. The scaling parameter typically lies in the range $2 < \alpha < 3$, although there are occasional exceptions. Plots of data are typically shown after log-log transforming both axes, so that the power-law function a provides a linear fit to the data. In practice, few empirical phenomena obey power laws for all values of A. More often the power law applies only for values greater than some minimum, A_{min}, this occurs when the tail of the distribution follows a power law. The position of A_{min} (the minimum area) could be estimate visually from the data. It is the point beyond which the probability density function (PDF) of the distribution becomes straight on a log-log plot. This kind of approach is clearly subjective and can be sensitive to noise in the tail of the distribution. The method is performed in Origin Lab where the

area for the fit is chosen by the user through a moving window. In general Amin is selected so that the $\varkappa^2$ and R^2 of the fitting function is maximized.

3.3 Least square regression of non-cumulative log power-law function

The third methodology is based on a least square regression of non-cumulative log power-law function. This method calculates the best-fitting line for the data by minimizing the sum of the squares of the vertical deviations from each data point to the line, e.g. if a point is placed on the fitted line its vertical deviation is 0. To apply this method it is necessary to plot the logarithmic values of the probability density with the logarithmic values of the area.

The equation is:

$$log(N) = log(c) - \alpha \cdot log\ (A)$$

Also in this method A_{min}, the minimum area, is chosen by the user through a moving window. The analysis is performed in Origin Lab.

3.4 Maximum likelihood estimator of Double Pareto distribution

The last methodology utilized is the Double Pareto distribution (Stark & Hovius, 2001). This method was applied because the observed size distribution exhibit two scaling regimes: for large landslides it can be observe power law scaling with a negative scaling exponent, whereas for small landslides there is an apparent positive power law scaling. A peak (t) in the distribution divides this two regimes and reflects a crossover length scale. For this reason it is necessary to consider all the distribution in order to estimate the asymptotic negative power law tail.

The probability density equation takes the following form:

$$P(A) = \eta \left[\frac{[1 + (m/t)^{-\alpha}]^{\beta/\alpha}}{[1 + (A/t)^{-\alpha}]^{1+\beta/\alpha}} \right] \cdot (A/t)^{-\alpha-1}$$

$$\eta = \frac{\beta}{t(1-\delta)} \qquad \delta = \left[\frac{1+(m/t)^{-\alpha}}{1+(c/t)^{-\alpha}} \right]^{\beta/\alpha}$$

In the equation the five parameters (α, β, c, m and t) are: α, the slope of the power law tail for large landslide areas; β, the slope of the power law decay of the distribution for small landslide areas; c and m, the cut off values for small and large landslides, respectively; and t, the maximum value of the probability distribution, i.e. the area for which landslides are most abundant and below which a rollover occurs in the distribution.

4 Case Studies

4.1 Papua New Guinea Earthquake, 1993

On 13 October 1993, a shallow earthquake with magnitude 7.0 occurred near Tauta in the Finisterre Range of Papua New Guinea (PNG). The hypocenter is located at a depth of 25 km (5.84S, 146.13E). The earthquake altered the form of many of the valleys and rivers draining into the Markham and Ramu valleys. Oblique convergence of the Australian and Pacific plates drives uplift and deformation of the Finisterre Mountains. Bounded to the south by the Ramu-Markham thrust fault, at the origin of the earthquake, the mountain range has attained an elevation of 4 km since onset of deformation around 3.7 Ma (Abbott et al., 1997). Its orographic effect and near-equatorial location force intense, seasonal rainfall, with mean annual precipitation rates of about 4 m at intermediate elevations. Bedrock landsliding appears to be the dominant mode of hillslope mass wasting in the range (Hovius et al., 1998; Densmore and Hovius, 2000), driven by frequent, heavy rainfall and periodic, large earthquakes along the Ramu-Markham fault. Equally destructive seismic episodes occurred on the central section of the Ramu-Markham fault in 1922 (Ripper and Letz, 1991) and October 1993 (Tutton and Browne, 1994). The earthquake hypocenter were located at 19 and 20 km depth, less than 5 km apart.

The peak ground acceleration (PGA) experienced in the area, as result of 1993 earthquake, ranging from 0.02 g to 0.34 g (USGS, ShakeMap, Figure 6).

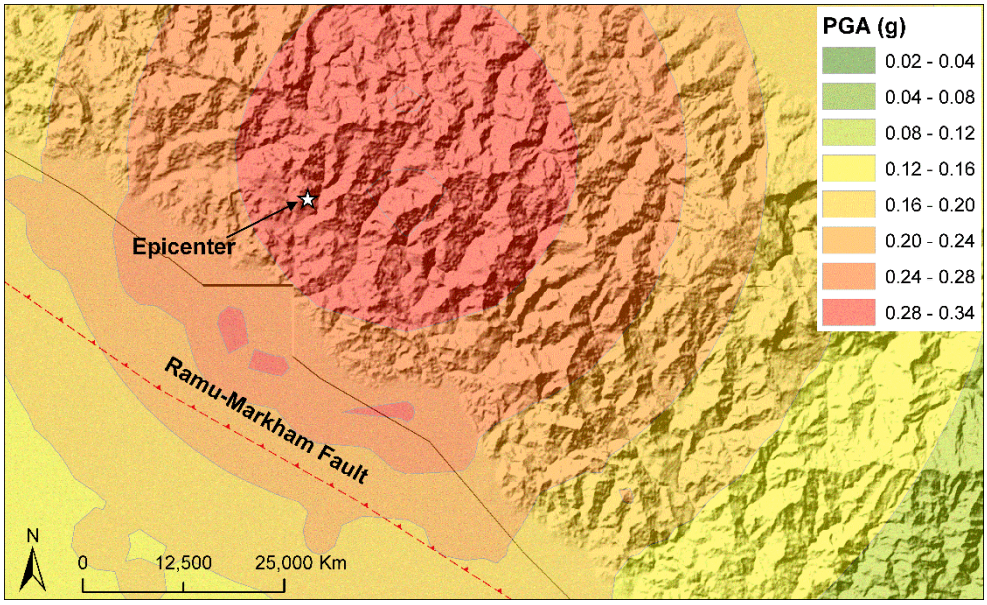

Figure 6. Pack ground acceleration (g) related to the 1993 Papua New Guinea Earthquake. ShakeMap model produced by the U.S. Geological Survey Earthquake Hazards Program (Wald et al, 2006).

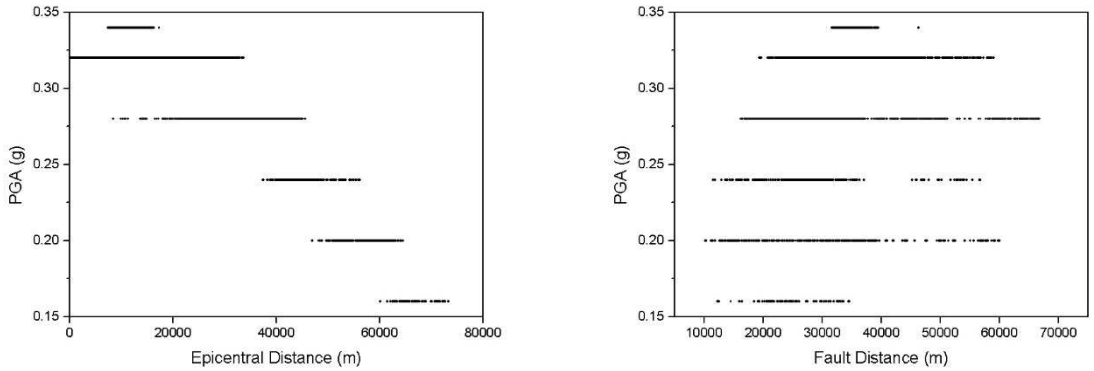

Figure 7. Graphs showing the distribution of the PGA (g) in relation to the epicentral and the fault distance (m).

Considering the distribution of the PGA (g) in relation to the epicentral distance it is possible to observe a clear trend; with the increase of the distance there is a decrease of the PGA, while the same trend it is not present for the fault distance (Figure 7).

4.1.1 Digital Elevation Model

For the analysis in Papua New Guinea, a good quality 50 m gridded DEM based on photogrammetry is used for the analysis. Two maps were realized from this DEM: the slope gradient map (Figure 8) and the relief map (Figure 9). The slope gradient is the spatial variability of elevation and controls the local stability of landscapes and therefore, sediment transport, and it is measured in degree. The relief shows the difference between the highest and lowest elevations in an area, so the topography of the area. The higher the relief, the higher the probability for a instability to interest a larger area in the same conditions. This map is realized though a moving-window with a radius 1km and 5km, the last was used for the world analysis of the relief by Korup et al. (2007).

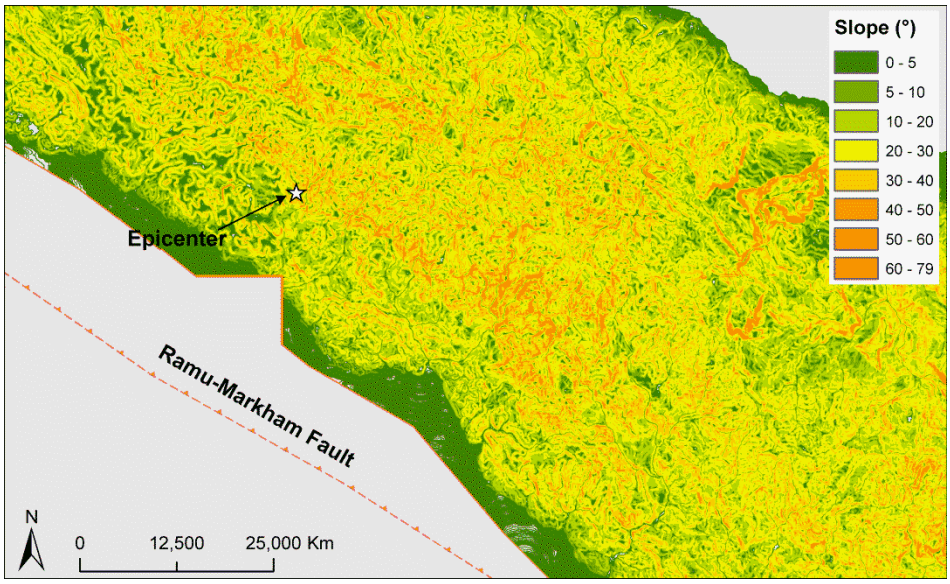

Figure 8. Slope gradient Map of the Finisterre Range

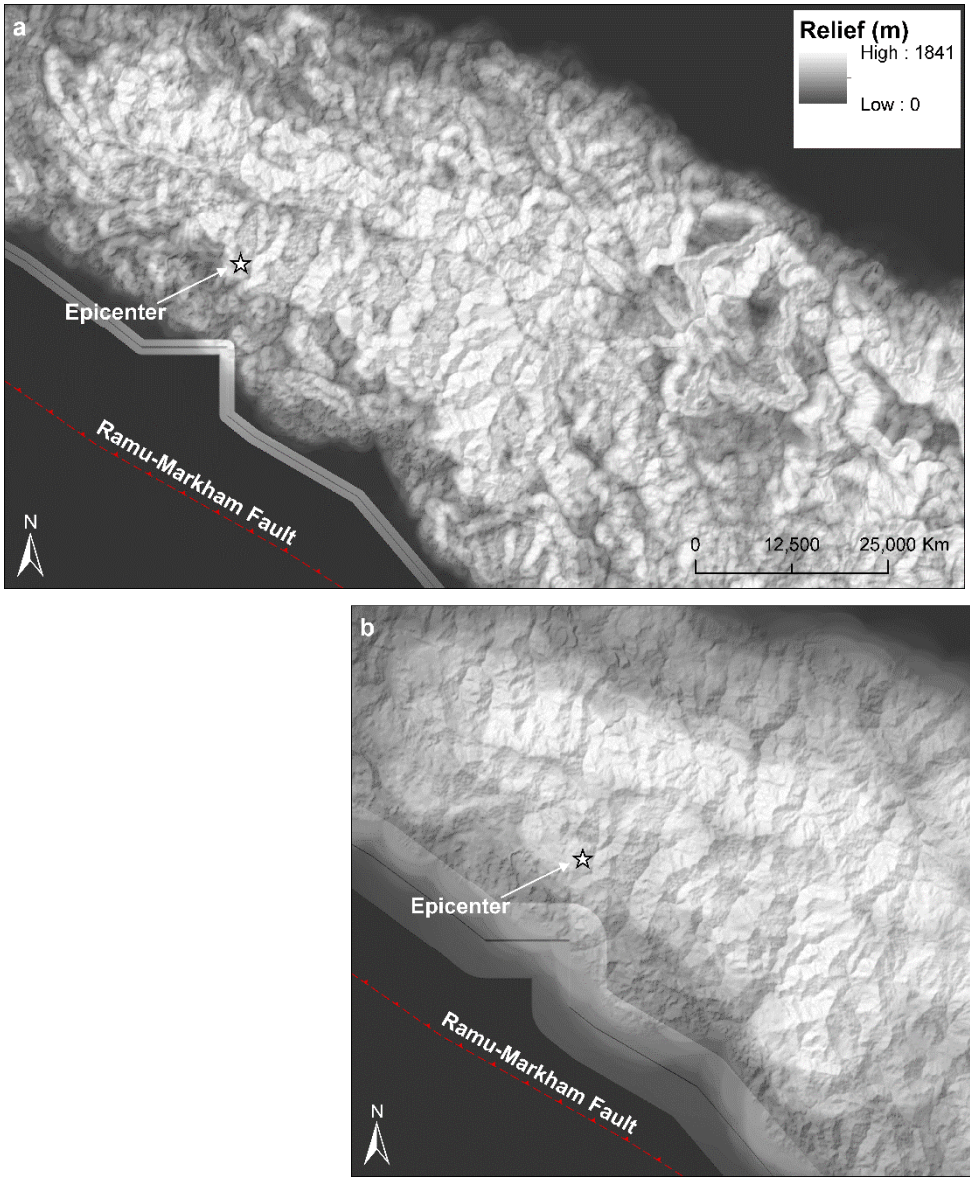

Figure 9. Relief Map at 1Km (a) and at 5Km (b) for the Finisterre Range.

4.1.2 Geological setting

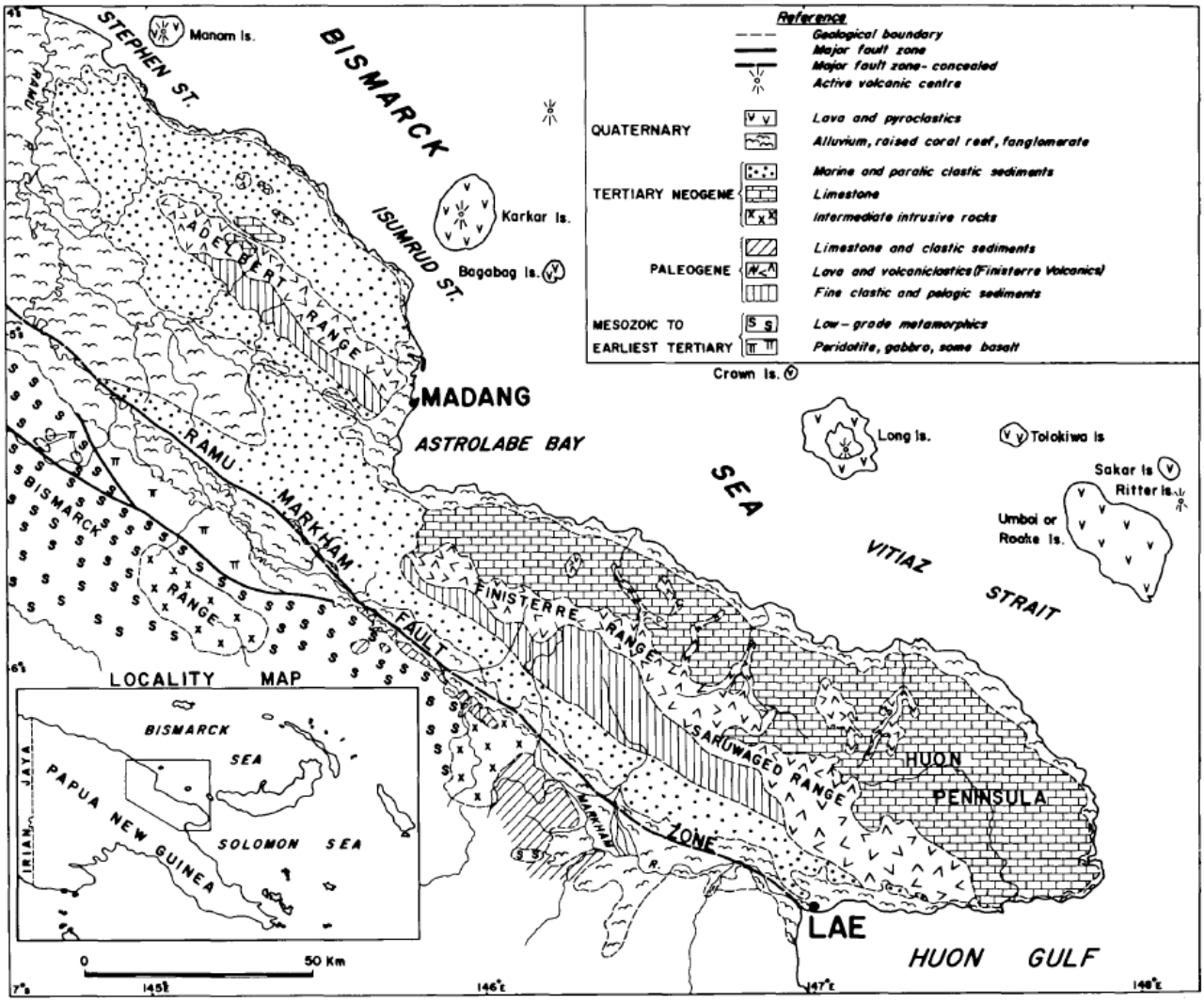

Figure 10. Simplified geology of the Adelbert-Finisterre Range-Huon Peninsula region, northern New Guinea,, by Jaques, 1976.

The Adelbert, Finisterre and Saruwaged ranges comprise Oligocene–early Miocene arc volcanic rocks overlain by Miocene and younger limestone (Jaques 1976, Jaques and Robinson, 1977; Davies et al., 1987; Abbott, 1995) (Figure 10). Fault deformation of the volcanic rocks preceded deposition of limestone. The volcanic rocks and limestone form a great S-facing thrust based antiform marked by limestone dip-slopes on the N side and by faulted and rapidly eroding volcanic rocks on the S side. The Finisterre range consists of three southeast trending lithologic belts. The core of the range is the Oligocene through Early Miocene Finisterre Volcanic rocks. These basic volcanic and volcanoclastic rocks were generated by activity along the intraoceanic Finisterre volcanic arc (Jaques and Robinson, 1977). The northern lithologic belt consists of Neogene carbonate rocks of the Gowop Limestone and associated units (Robinson, 1974; Robinson et al., 1976). The limestone is well-exposed in the Finisterre block. The southern lithologic belt is a

sequence of clastic sediments that was deposited both prior to and during arc-continent collision. The stratigraphy of the Finisterre range is very similar to that of the islands of New Britain, New Ireland, the Solomon Islands and Vanuatu (e.g. Jaques and Robinson, 1977). This similarity suggests that all of these islands were once part of a continuous Oligocene-Early Miocene arc that Robinson (1974) named the Outer Melanesian Arc. Falvey and Pritchard (1984) provided paleomagnetic data that support this argument. Many workers have suggested that Miocene collision with the Ontong Java Plateau caused the demise of the Outer Melanesian Arc and led to an eventual reversal of subduction polarity (Kroenke, 1984; Musgrave, 1990) to form the Bismarck Arc, a 1000 km long chain of active volcanoes that run north of the Papua New Guinea mainland and along the north side of New Britain. Subduction was occurring along the New Britain Trench and its extension along the present day Ramu and Markham valleys by the late Miocene (~ 10 Ma; Musgrave, 1990; Berger et al., 1992) or Pliocene (Johnson and Jaques, 1980). Subduction polarity reversal caused the Bismarck Arc to form just north of the Finisterre range, placing the range in the Bismarck forearc. Continued subduction along the New Britain Trench caused eventual collision between the Finisterre range and the continent, uplifting the Adelbert and Finisterre mountain ranges.

4.1.3 Analysis

The relationships between lithology, relief, peak ground acceleration, epicentral distance and the fault distance are analysed.

The lithologies recognized in the area were grouped in to four classes, following the simplified geological map proposed by Jaques (1976). (see Table 1).

Table 1. Simplified geology of Finisterre Mountains (Jaques, 1976).

#	Lithology
1	Fine clastic and pelagic sediments
2	Lava and Pyroclastics
3	Limestone
4	Marine and clastic sediments

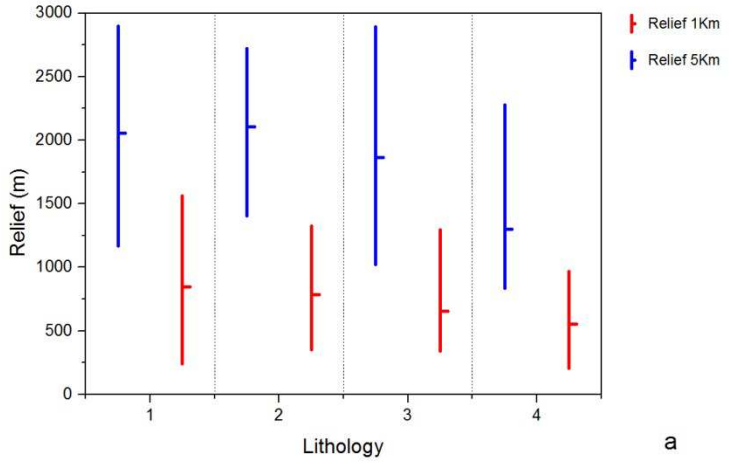
Relief 1Km
Relief 5Km
Relief (m)
3000
2500
2000
1500
1000
500
0
1
2
3
4
Lithology

a

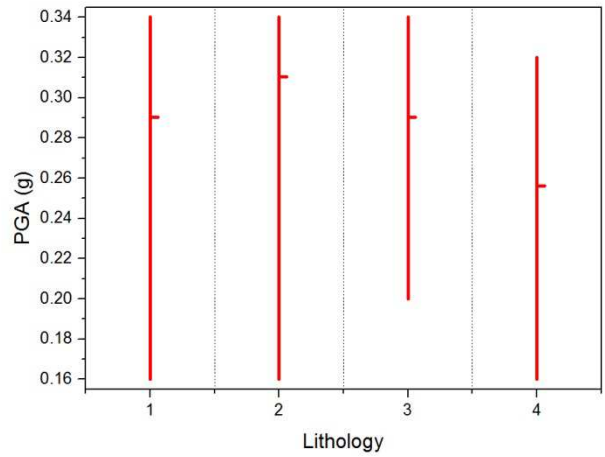
PGA (g)
0.34
0.32
0.30
0.28
0.26
0.24
0.22
0.20
0.18
0.16
1
2
3
4
Lithology

b

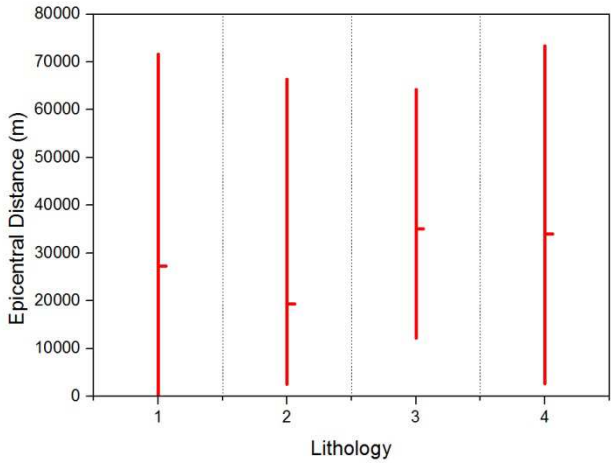
Epicentral Distance (m)
80000
70000
60000
50000
40000
30000
20000
10000
0
1
2
3
4
Lithology

c

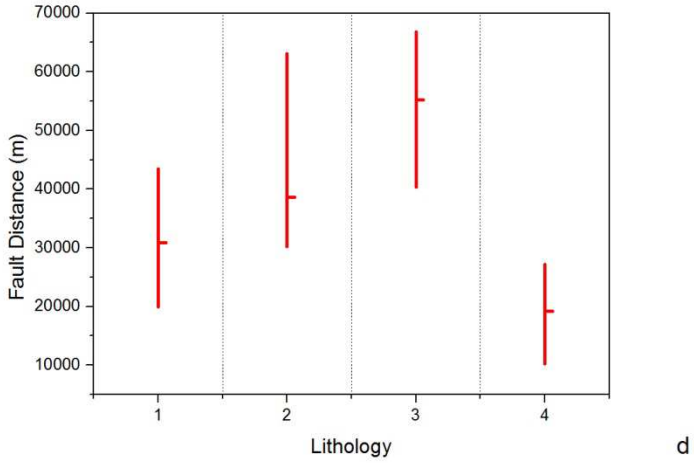

Figure 11. Graphs showing the relationships of the lithology with: a) Relief (m); b) PGA (g); c) Epicentral Distance (m); d) Fault Distance (m).

As expected the relief increases with increasing of the range from 1 to 5km the different lithologies show similar relief with the exception of the Marine and clastic sediments (#4, Figure 11) with ales relief. The PGA (g) experienced by the different lithologies cover all the range, this is probably related to the position of each lithology respect the epicenter. In fact the maximum values of PGA (g) are closed to the epicenter (Figure 11).

4.1.4 Landslide Dataset

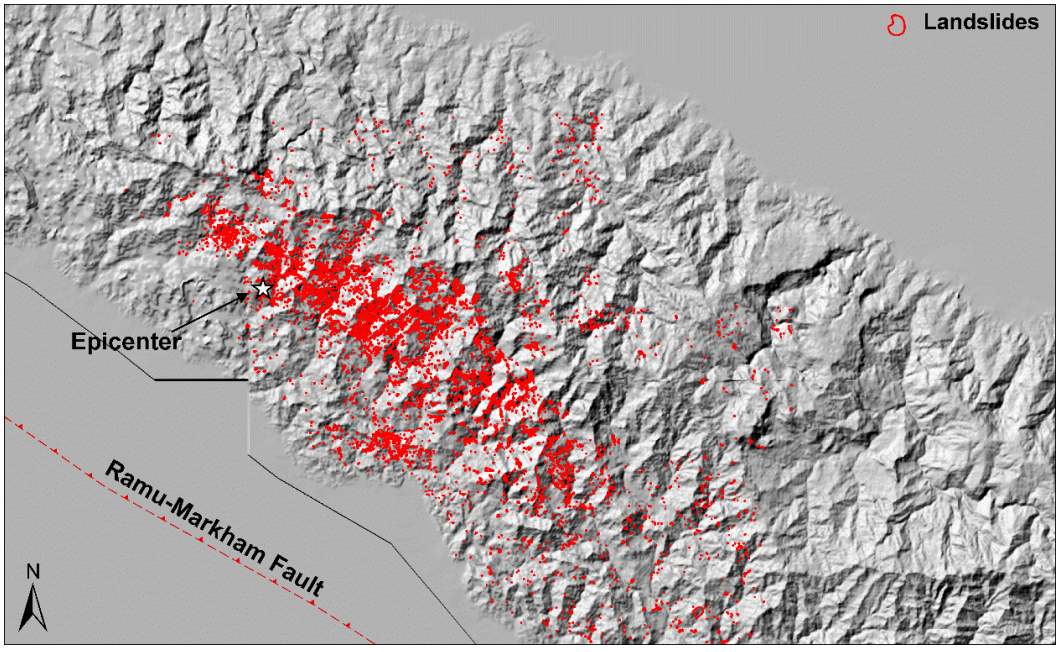

Figure 12. Landslides dataset related to the 1993 New Papua Guinea Earthquake; Meunier et al. (2008)

The landslide dataset was realized by Meunier et al. (2008) from 30 m resolution SPOT images (Figure 12). It include 4790 landslides, and most of them are disrupted landslides.

The spatial distribution of the landslides area was analysed in relation to the different lithologies present in the area (Figure 13), the relief reclassified (threshold of 500 m) (Figure 14), the mean slope at which each landslide occurred (Figure 13), both for epicentral and fault distance.

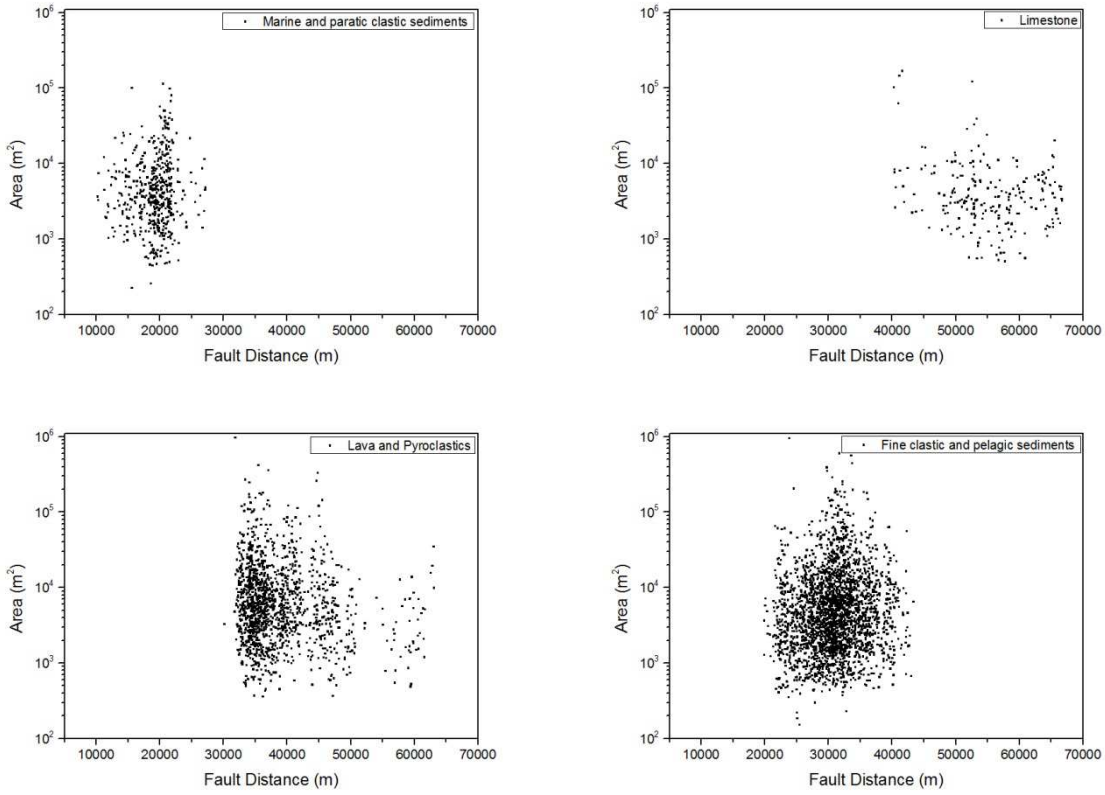

Figure 13. Landslide size as function of the fault distance, for each lithology, see appendix 1 for the epicentral distance.

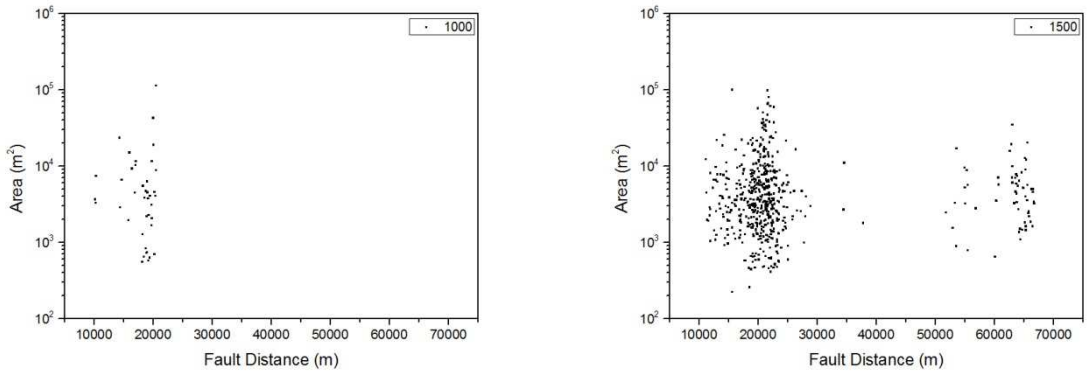

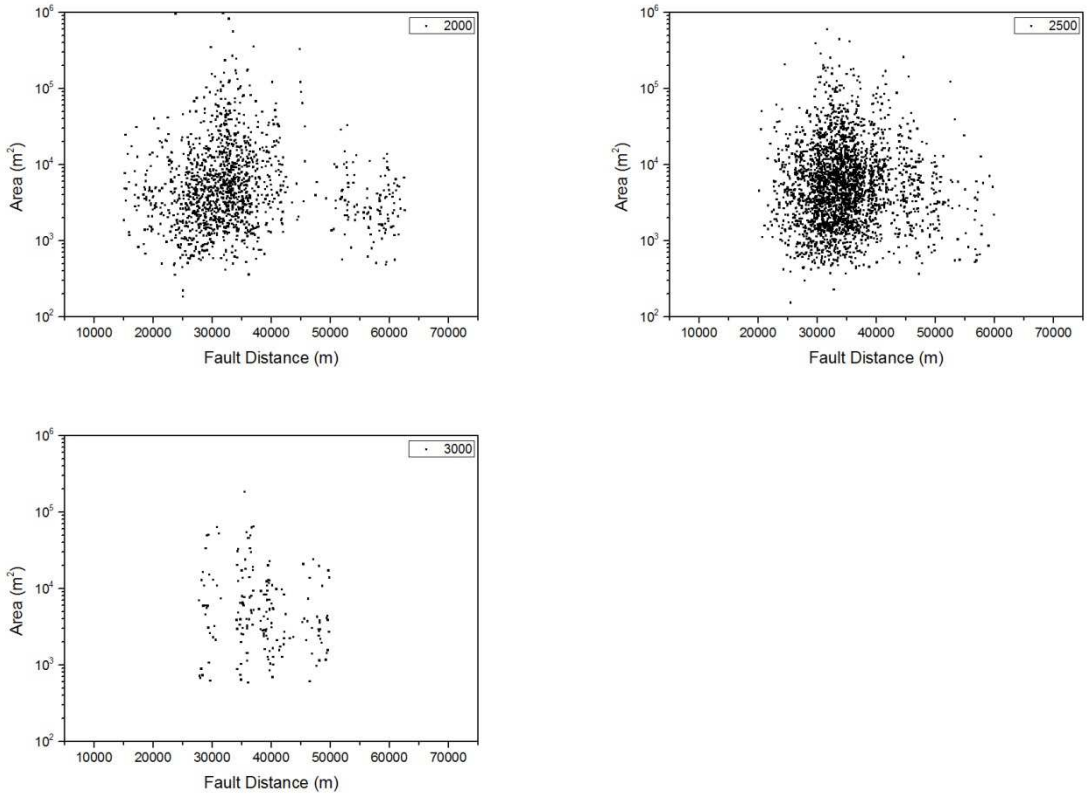

Figure 14. Landslide size as function of the fault distance, for each relief class, see appendix 1 for the epicentral distance.

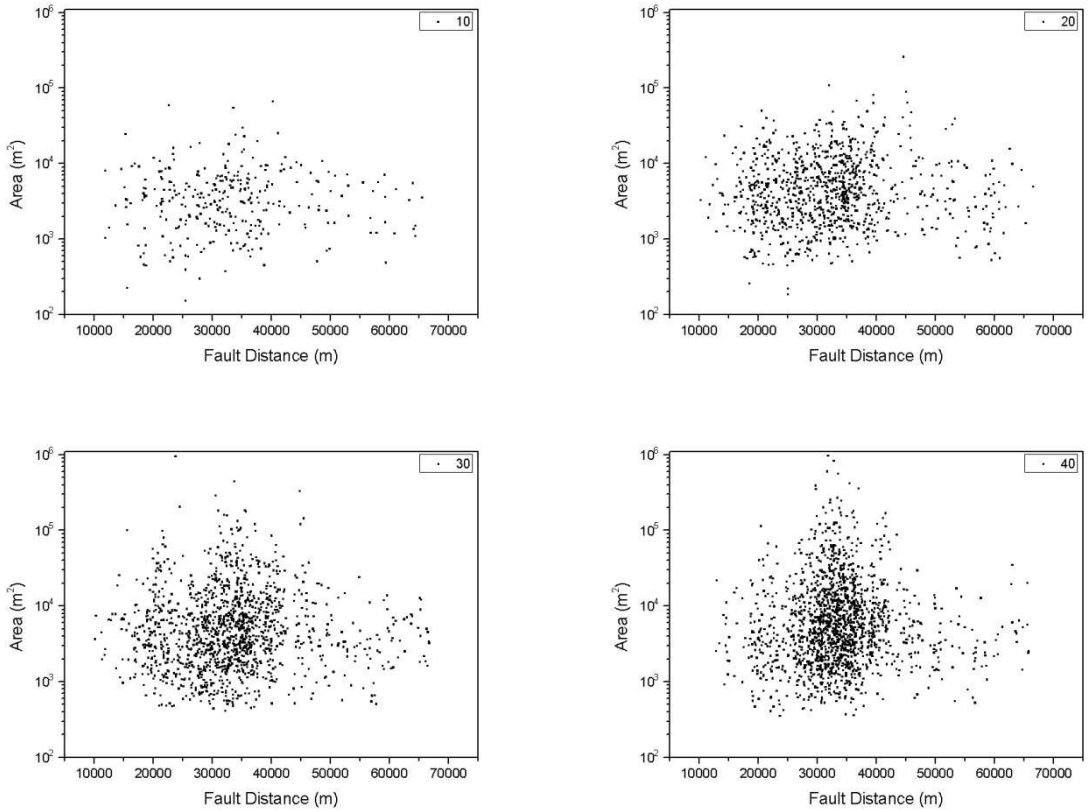

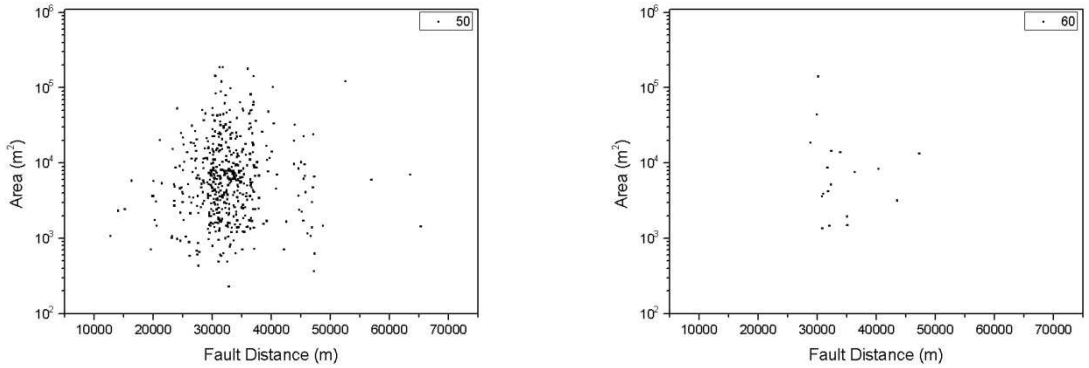

Figure 15. Landslide size as function of the fault distance, for each slope class, see appendix 1 for the epicentral distance.

Most of the landslides are in fine clastic and pelagic sediments in a relief between 1500 and 2000 m, and with a slope gradient ranging between 20 and 40°. both for the relief and for the slope gradient, there is a maximum increase of number of landslides and size for the intermediate classes. In terms of landslide size, it seems that Limestone is characterized by smaller bounds with respect the others, and in particular with respect to Lava and Pyroclastic. This could be also due to the relative small number of landslides, thus making the statistic not representative. Regarding the relief, it is possible to see a slight increase of the size with class 2500 m, although the larger landslides are in class 2000 m.

4.2 Northridge Earthquake, 1994

On 17 January 1994 an earthquake occurred in the San Fernando Valley in southern California with a magnitude of 6.7 (http://earthquake.usgs.gov/). The epicenter was located in urban area of Northridge. The depth was estimated around 18 Km.

The shaking heavily damaged communities throughout the San Fernando Valley and Simi Valley, and their surrounding mountains north and west of Los Angeles, causing estimated losses of 20 billion dollars. Sixty people died, more than 9,000 were injured, and more than 20,000 were displaced from their homes by the effects of the quake. Although moderate in size, the earthquake had immense impact on people and structures because it was centered directly beneath a heavily populated and built-up urban region. Thousands of buildings were significantly damaged, and more than 1,600 were later "red-tagged" as unsafe to enter. Other 7,300 buildings were restricted to limited entry ("yellow-tagged"), and many thousands of other structures incurred at least minor damage. The 10-20 seconds of strong shaking collapsed buildings, brought down freeway interchanges, and ruptured gas lines that exploded into fires. Yeats et al (1995) proposed that the earthquake happened on a continuation of the Oak Ridge fault system, which reaches the surface in the Ventura basin to the west. This blind thrust fault is known either as the Pico Thrust, named often the Pico Anticline or as the Northridge Thrust. During the event a peak ground acceleration ranging between 0.02 and 0.74 g was registered (Figure 16). By analysing the distribution of the PGA in relation to the distance from the source area (Figure 17), there is a trend between the PGA and the epicentral distance, however this trend is less clear in the case of the fault distance.

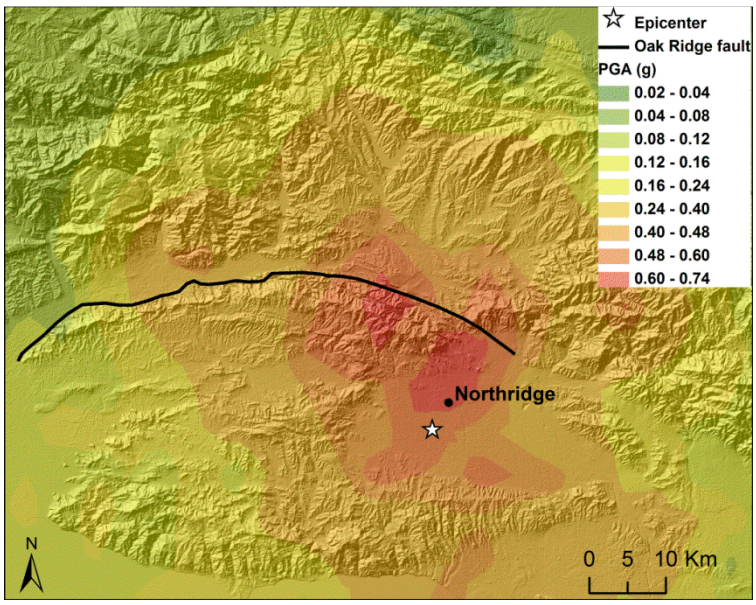

Figure 16. Peak Ground Acceleration (g) of the 1994 Northridge Earthquake. ShakeMap model produced by the U.S. Geological Survey Earthquake Hazards Program (Wald et al, 2006).

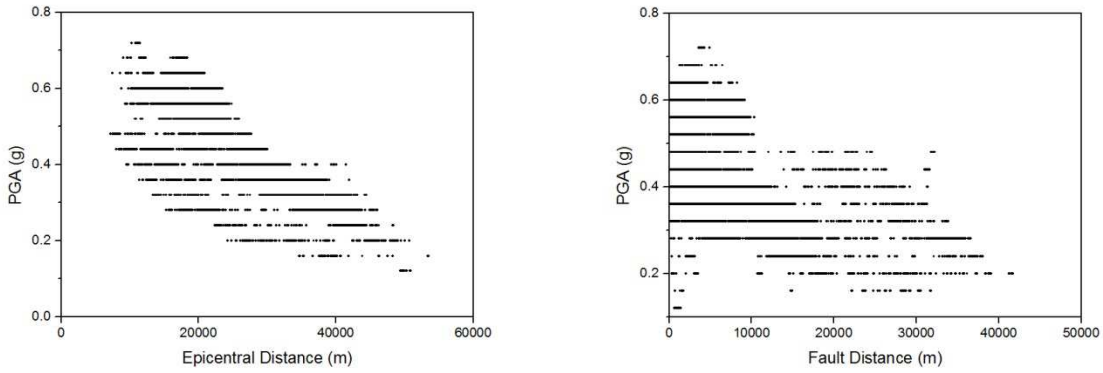

Figure 17. Graphs showing the distribution of the PGA (g) in relation to the epicentral and the fault distance (m).

4.2.1 Digital Elevation Model

The ASTER Global Digital Elevation Model (ASTER GDEM) is a joint product developed and made available to the public by the Ministry of Economy, Trade, and Industry (METI) of Japan and the United States National Aeronautics and Space Administration (NASA). It is generated from data collected from the Advanced Spaceborne Thermal Emission and Reflection Radiometer (ASTER), a spaceborne earth observing optical instrument. The ASTER GDEM is the only DEM that covers the entire land surface of the Earth at high resolution. The ASTER GDEM covers land surfaces between 83°N and 83°S and is composed of 22,600 1°-by-1° tiles. The ASTER GDEM is in GeoTIFF format with wgs84 geographic lat/long coordinates and a 1 arc-second (30 m) grid of elevation postings. Two maps were realized from this DEM: the slope gradient map (Figure 18) and the relief map (Figure 19), with a radius 1km and 5km (*see 1993 Papua New Guinea earthquake for more details*).

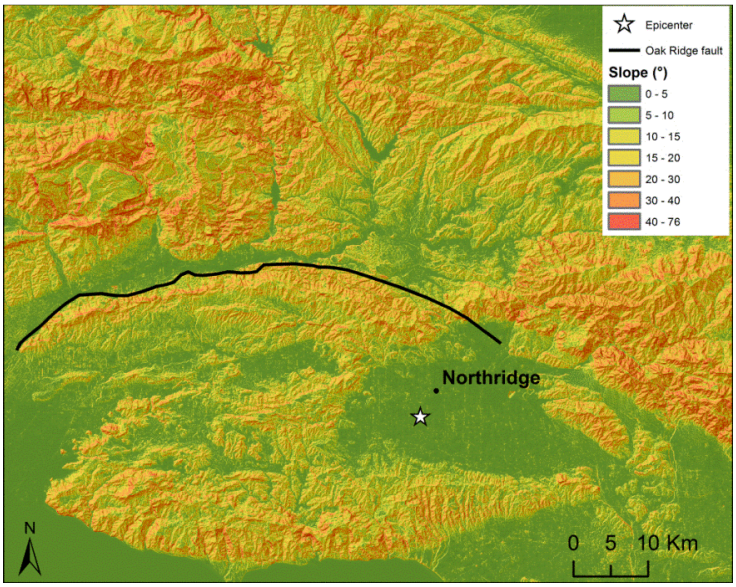

Figure 18. Slope gradient map of the ASTER GDEM.

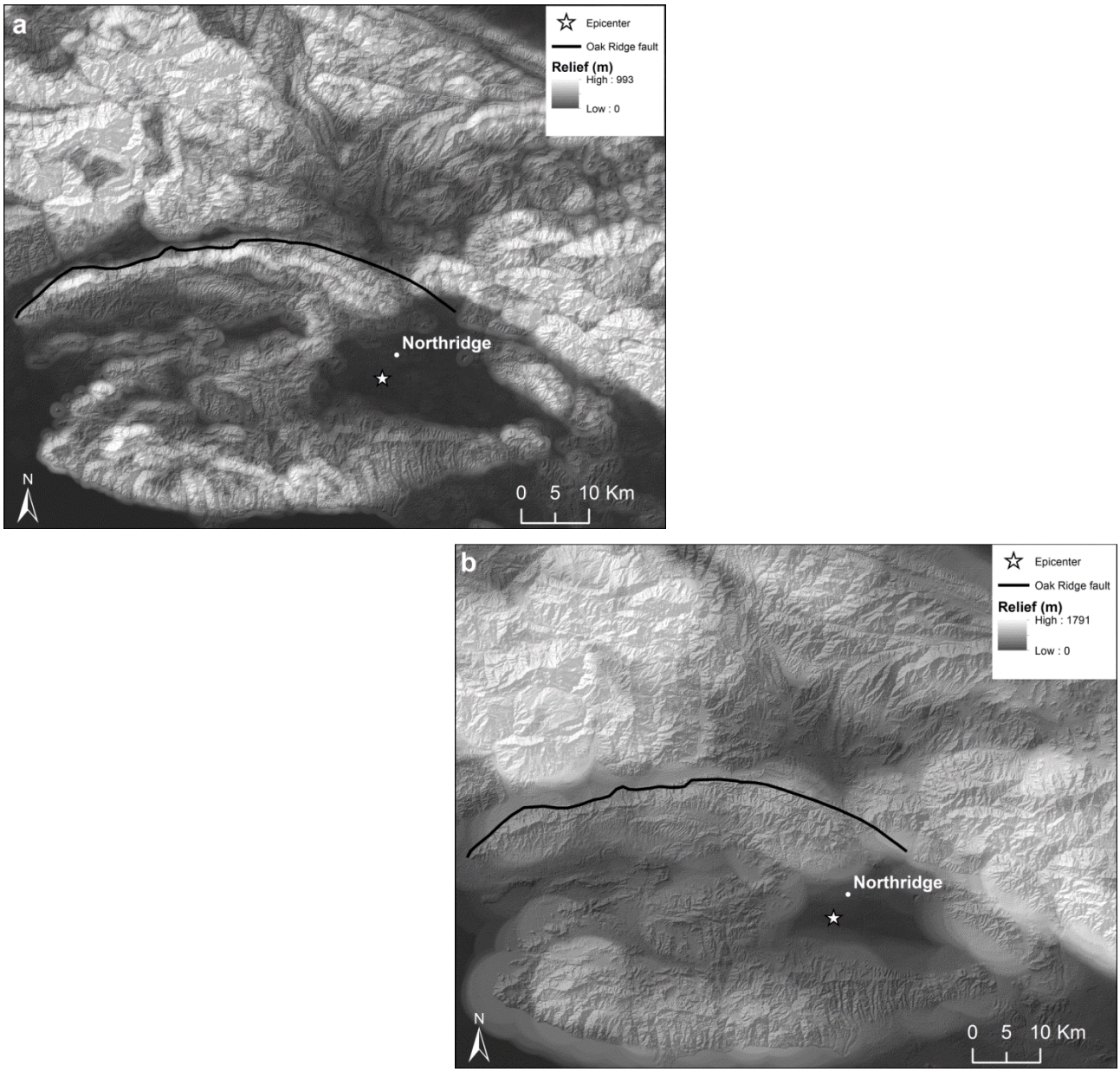

Figure 19. Relief map of the ASTER GDEM with a radius of 1 Km (a) and 5 Km (b).

4.2.2 Geological Setting

The Simi Valley, San Fernando Valley and adjacent mountains are part of the Transverse Ranges physiographic province that is composed of parallel, east-west trending mountain ranges and sediment-filled valleys. The Simi Valley contain a thick section of clastic sedimentary rocks and volcanic rocks (Squires, 1998). To the north it is flanked by the Big Mountain area and to the southwestern by the Santa Susana Mountains (Figure 20). The San Fernando Valley is broadly elliptical, about 30 km long on its east-west axis and 16 km wide. It is bounded to the northeast by the Verdugo Mountains and to the west by San Gabriel Mountains, to the northwest by the Simi Hills and the Santa Susana Mountains, and to the south by the Santa Monica Mountains (Figure 20).

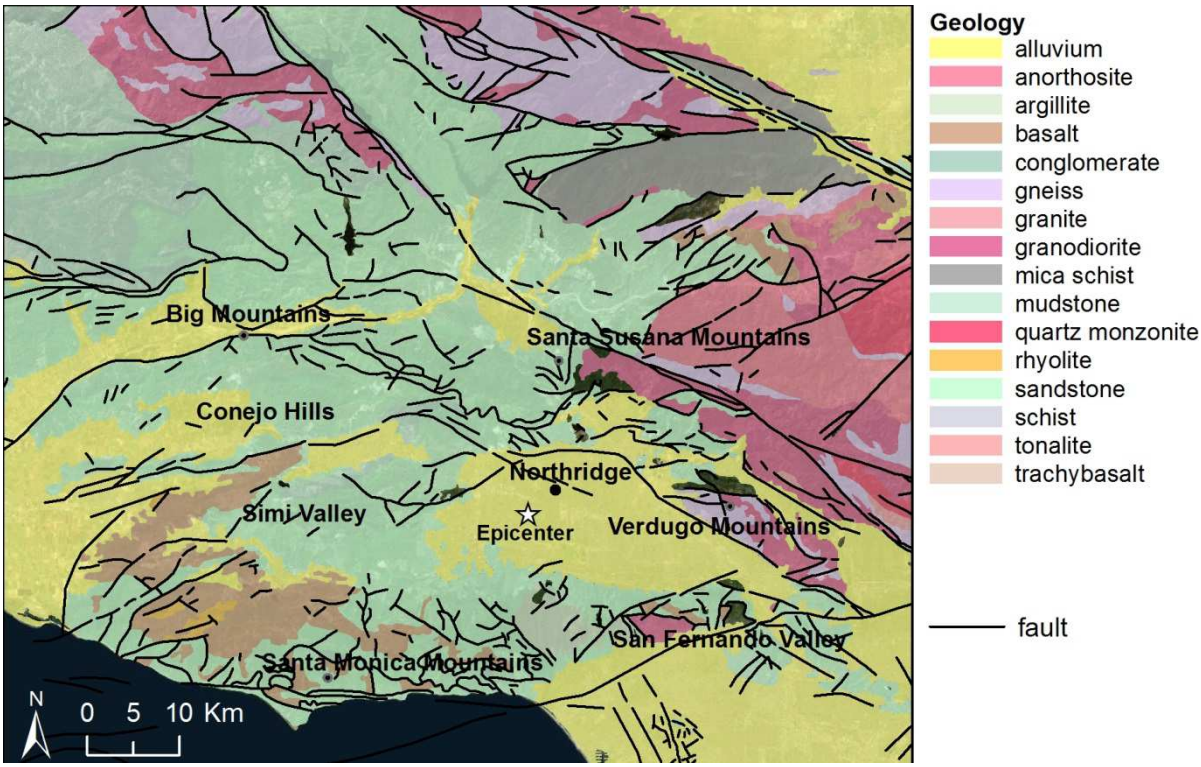

Figure 20. Geological Map of the area affected by the 1994 Northridge Earthquake. (Jennings et al., 1977).

The mountains have an east-west trend, which is consistent with being part of the Transverse Ranges. The ranges are actively deforming by folding and thrust-faulting in response to the north-south-directed compression that is occurring across the "big bend" region of the San Andreas Fault. The San Fernando Valley is underlain by a thick fill of alluvium.

This alluvium is underlain by thousands of meters of sediments, mostly of marine origin, which were deposited upon granitic and metamorphic basement rocks. The Transverse Ranges result from Pliocene-Pleistocene compression associated with the opening of the Gulf of California (Crowell, 1975; Anderson, 1971). Hadley and Kanamori (1977) discovered that the Transverse Ranges lack a crustal root and are underlain by an anomalous high seismic velocity structure in the mantle. The Conejo Volcanics (Taliaferro and others, 1924) occur in the Santa Monica Mountains, Conejo Hills (Shelton, 1954), and on Anacapa Island (Scholl, 1960). These rocks consist of a sequence of volcanic breccia, tuff breccia, pillow lavas, and massive flows, which are intruded by dikes, and sills. Andesitic and basaltic rocks predominate, although dacitic to rhyolitic compositions occur, generally toward the top of the section. Submarine to subaerial origin for the volcanics suggests an emerging submarine volcanic structure in the Conejo Hills area (Williams, 1977).

4.2.3 Analysis

The relationships between the lithology relief, peak ground acceleration, epicentral distance and the fault distance are analysed.

The lithologies identified in the area were grouped into eight classes, based on the Geologic map of California at a scale 1:750,000 (Jennings et al., 1977). (see Table 1).

Table 2. Lithologies reclassified for the analysis.

#	**Lithologies**
1	Alluvium
2	Argilliti and Mudstone
3	Conglomerate
4	Gneiss
5	Mica schist
6	Plutonic Rock
7	Sandstone
8	Volcanic Rock

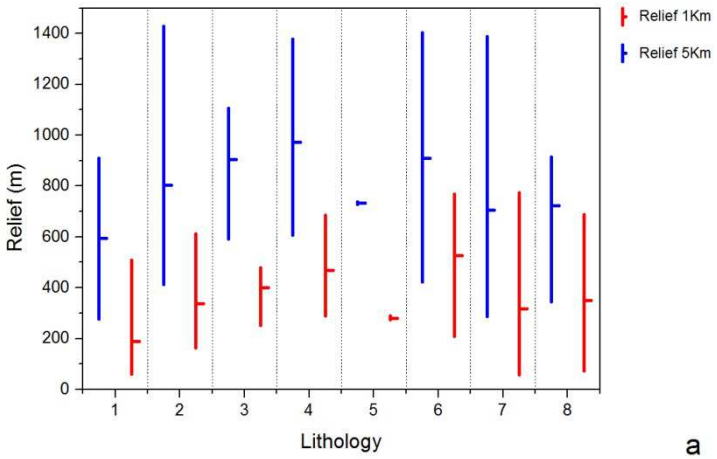

a

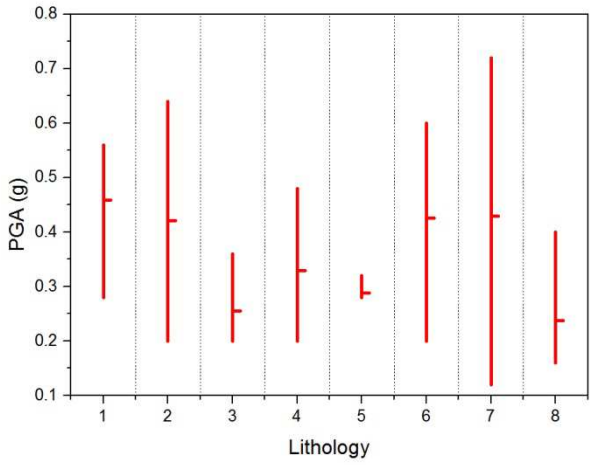

b

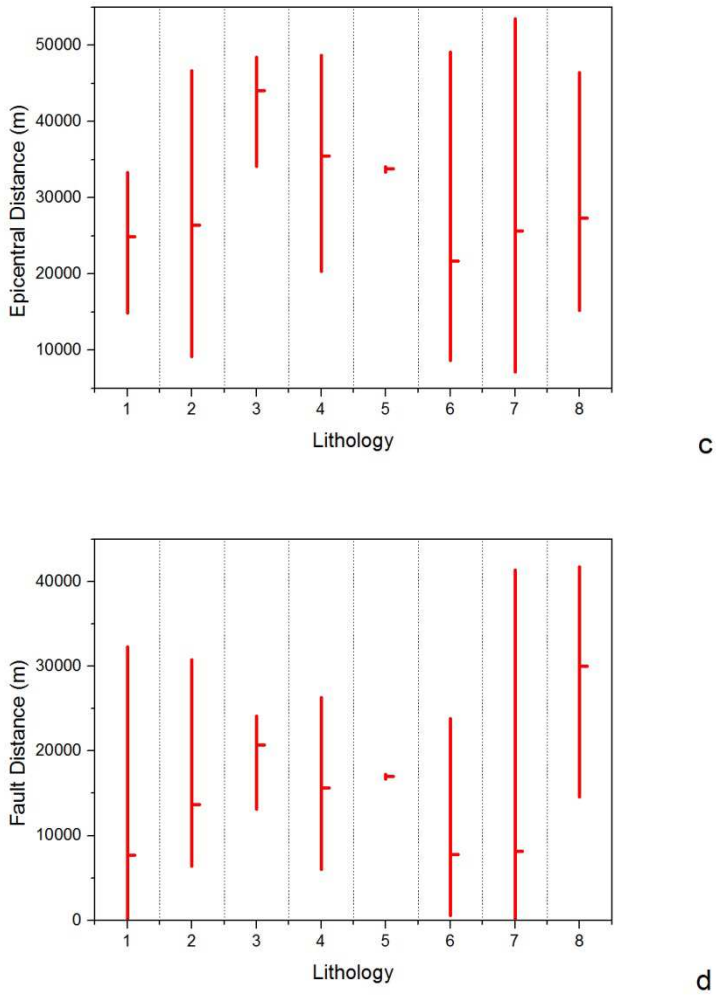

Figure 21. Graphs showing the relationships of the lithology with: a) Relief (m); b) PGA (g); c) Epicentral Distance (m); d) Fault Distance (m).

About the value of PGA registered in each lithologies: the Sandstone (#7, Table 1, Figure 21b) covers all the range of values, but this is related also to the fact that this lithology is present at all distances from the epicenter and fault (Figure 21c,d). The Volcanic Rocks (#8, Table 1, Figure 21b) experienced the lower values, in mean, of PGA also related to the position with respect to the fault (Figure 21,d). The same explanation can be made for the Conglomerates and Mica Schist (#3 and 5, Table 1, Figure 21b,c,d).

4.2.4 Landslide Dataset

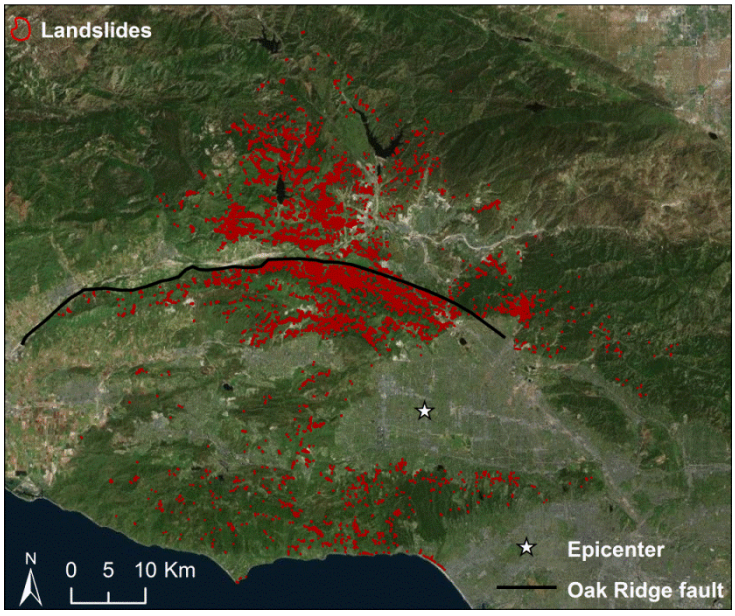

Figure 22. Landslide dataset for the 1994 Northridge Earthquake (Harp et al, 1995)

The 17 January 1994 Northridge earthquake triggered more than 11,000 landslides over an area of about 10,000 km² (Harp et al, 1995) (Figure 22). Most of the landslides were concentrated in a 1,000 km² area that includes the Santa Susana Mountains and the mountains north of the Santa Clara River valley. The landslides were mapped in the field and from aerial photography (scale 1:60,000) provided by the U.S. Air Force and taken the morning of the earthquake. Most of the triggered landslides were shallow (1-5 m), highly disrupted falls and slides in weakly cemented Tertiary to Pleistocene clastic sediment. Average volumes of these types of landslides were less than 1,000 m³, but many had volumes exceeding 100,000 m³. Many of the larger disrupted slides traveled more than 50 m, and a few moved as far as 200 m from the bases of steep parent slopes. Deeper (>5 m) rotational slumps and block slides numbered in the hundreds, a few of which exceeded 100,000 m³ in volume. The largest triggered landslide was a block slide having a volume of $8 \cdot 10^6$ m³.

The realization of the dataset showed some problems for the authors, Where the slopes were sunlit landslides as small as 1-2 m across were visible, while where the slopes were shaded, slides about 5-10 m across are the smallest that could be mapped. This means that the inventory is not complete. However, the field activity indicate that south-facing slopes in most of the landslide area generally are steeper and produced far more landslides than north-facing slopes. Therefore, landslides on north-facing slopes that are not visible on the photos because of shadows probably account for only a small proportion of the total landslides. The authors estimate that no more than about 20% of the

landslides that exceeded 5 m in maximum dimension were missed, and no more than 50% of those smaller than 5 m. However, they estimate that more than 90% of the area covered by triggered landslides were mapped, because most of the landslides that are not visible on the photos are small. The spatial distribution of the landslides size was analysed in relation to the different lithologies present in the area (Figure 23), the relief reclassified (classes of 500 m) (Figure 24), the mean slope at which each landslide occurred (Figure 25), for the epicentral distance. Most of the landslide were triggered in Sandstone, In this lithology is possible to see a decrease of the landslide size with the fault distance. Over the Sandstone only two lithology groups (Plutonic rocks, and Argillite and mudstone group) show landslide with a size above 10,000 m^2. Most of the landslides were triggered in a relief class of 1000 m, and also here a decrease of the landslide size with the sizes is visible (both for large and small events), The slope gradient do not show significant variation in landslide size, under 40° class. For the 20° and 30° l slight decrease in landslide size is visible.

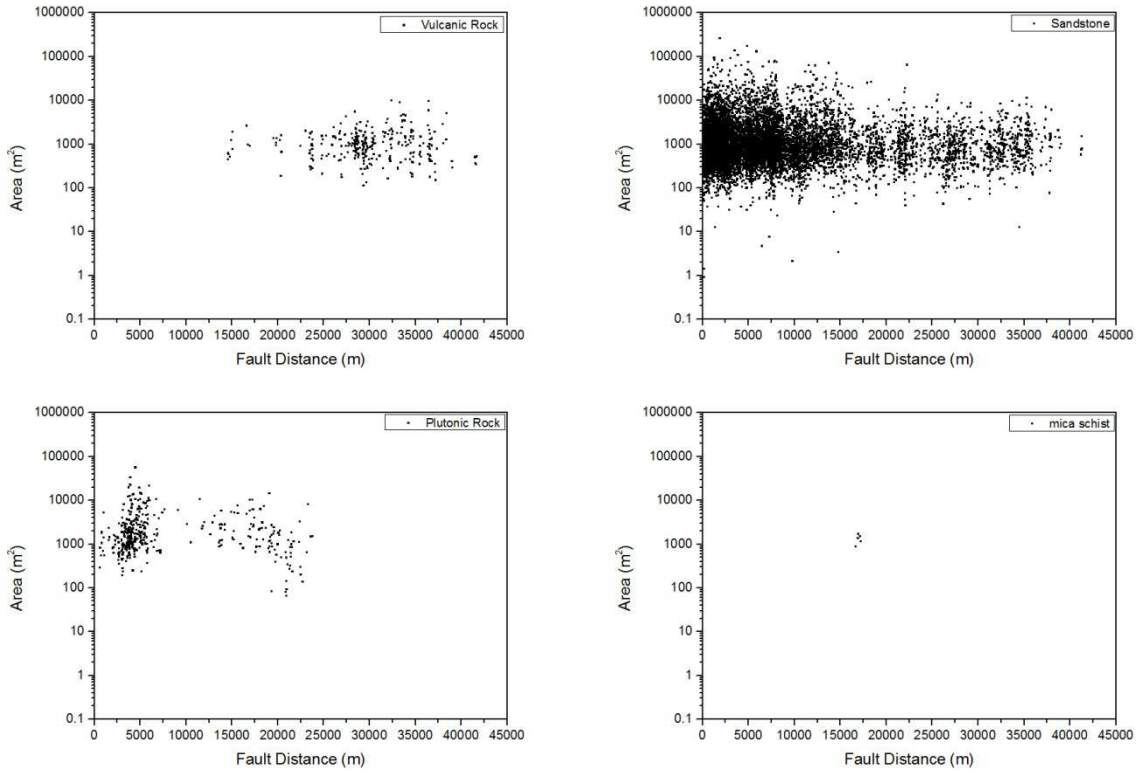

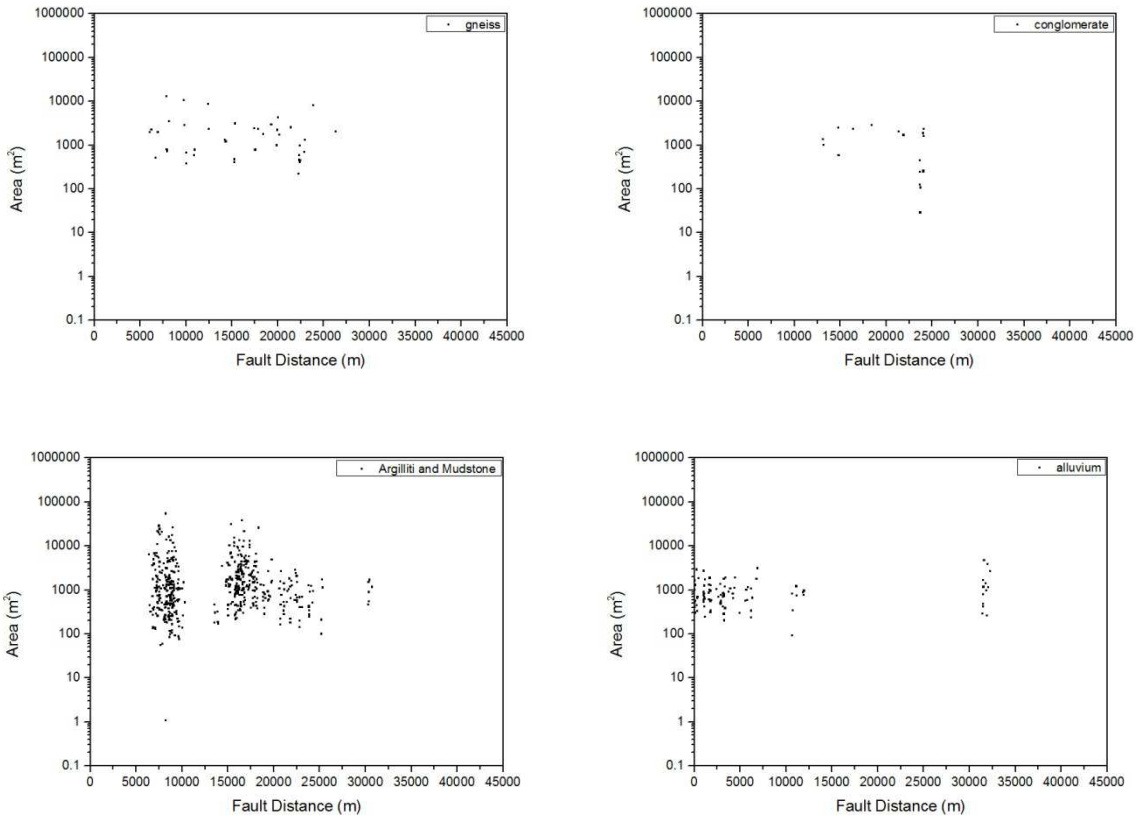

Figure 23. Landslide size as function of the fault distance, for each lithology, see appendix 1 for the epicentral distance.

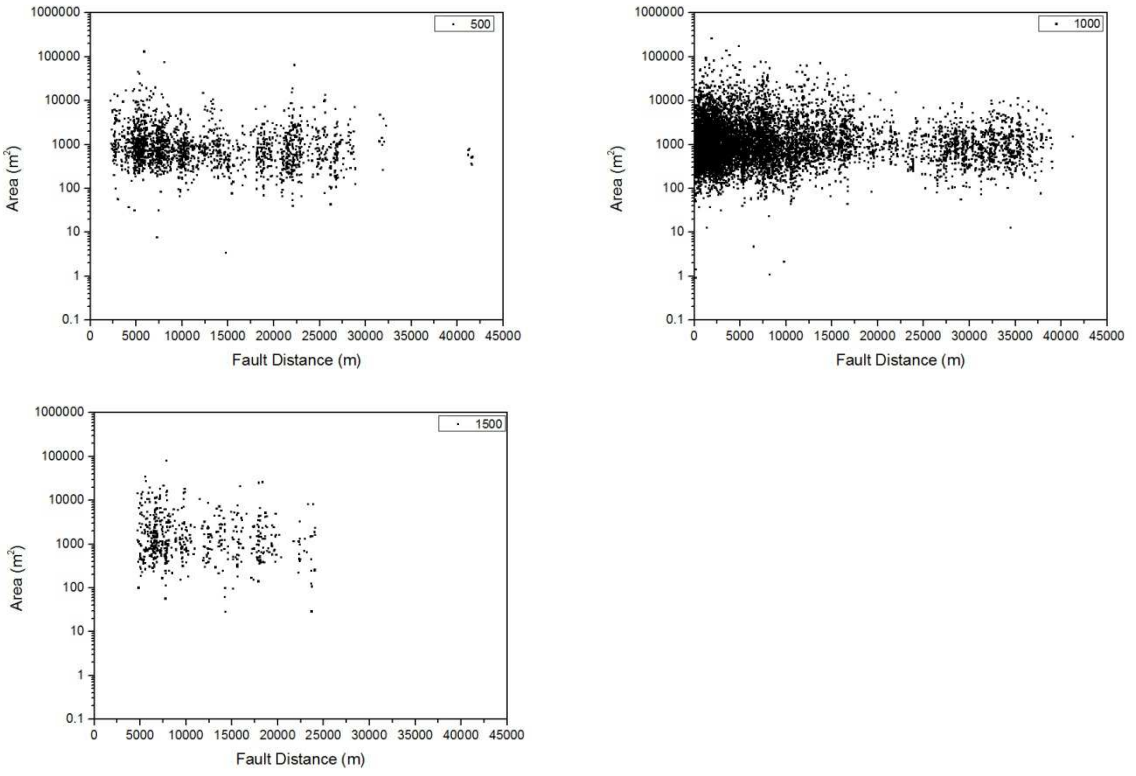

Figure 24. Landslide size as function of the fault distance, for each relief class, see appendix 1 for the epicentral distance.

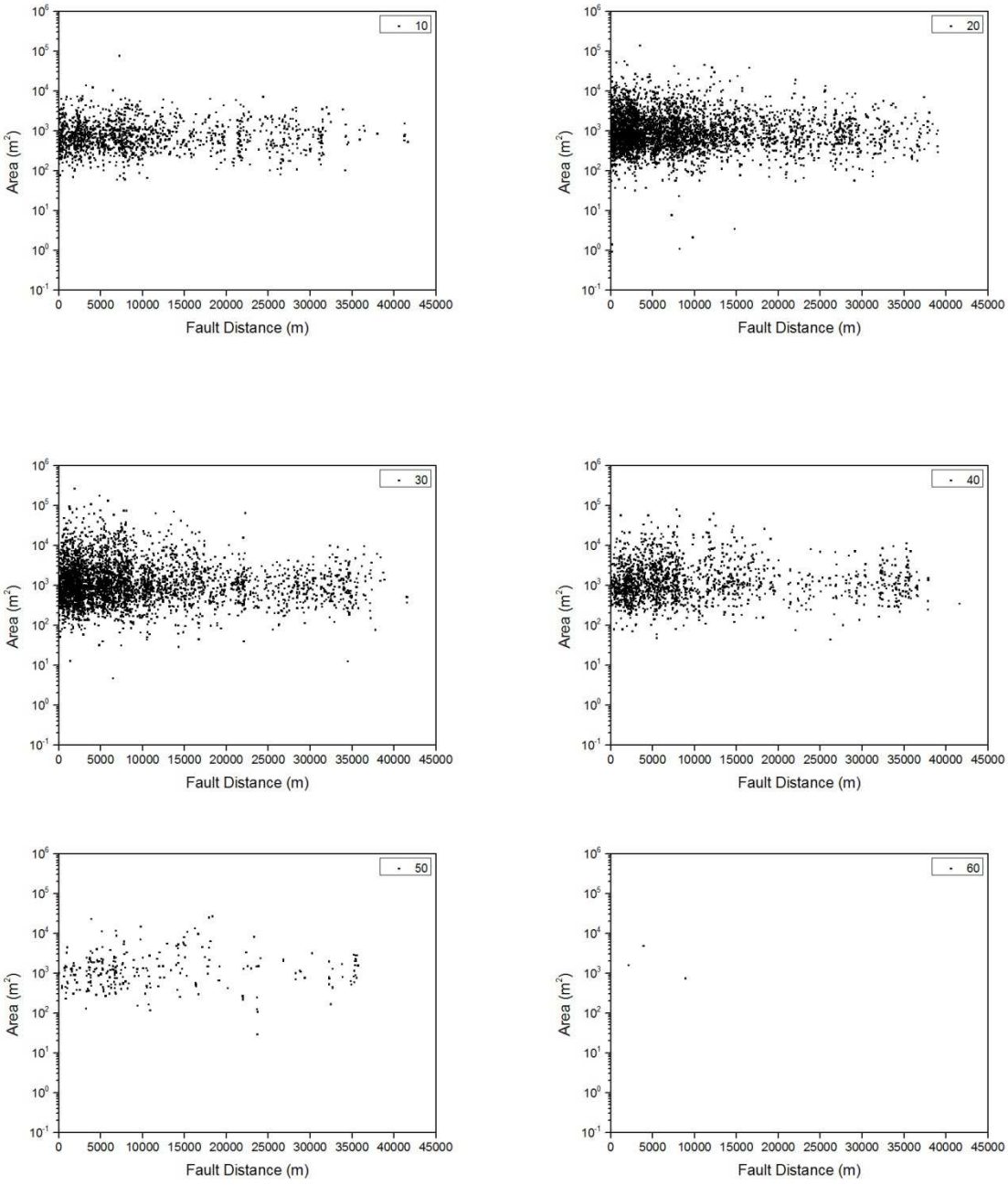

Figure 25. Landslide size as function of the fault distance, for each slope class, see appendix 1 for the epicentral distance.

4.3 Niigata-Chuetsu Earthquake, 2004

On October 23, 2004, an earthquakes (Mw 6.6) located near the western coast of northern Honshu Island struck parts of northern Japan, especially Niigata Prefecture, about 250 km north of Tokyo. The epicenter of the main shock was located at 37.231°N, 138.753°E at a depth of 16 km, and many aftershocks occurred (http://earthquake.usgs.gov/). Most active faults in the area affected by the earthquakes are reverse faults that dip to NW (Research Group for Active Faults, 1980). Despite the shallow activity of the present earthquakes, no active fault has been recognized in the aftershock area. Analysis of the aftershock distribution and geodetic modeling by several investigators resulted in slightly different explanations for the fault rupture location (Geographical Survey Institute of Japan (GSI) 2004; National Research Institute of Earth Science and Disaster Prevention (NIED) 2004a; Earthquake Research Institute, The University of Tokyo 2004). The earthquake occurred on a blind-thrust fault. The area on the hanging-wall block directly above the fault rupture is steep terrain that produced most of the landslides. Basically, it can be interpreted that the focal mechanism of those major earthquakes shows almost pure reverse faulting dipping NW/SE. This area is tectonically very active with many folds and active faults trending NNE/SSW. The Islands of Japan lie on a ring of seismically active plate boundaries that surround the Pacific Ocean known as the Ring of Fire. Earthquakes throughout Japan are caused by the relative motion of several major and minor tectonic plates including the Pacific plate, the Philippine Sea plate, the Okhotsk plate, and the Amur plate. Annual precipitation ranges from about 136 mm to 255 mm. However, seasonal antecedent rainfall from July 1, 2004, through October 23, 2004, totaled 1055 mm in Nagaoka City, as compared to a mean value of 1106 mm for the vicinity of the earthquake-impacted areas. Thus, the total rainfall for the four months prior to the earthquakes was four to five times the annual average for the area. Three months before the earthquake event in the Chuetsu area, heavy rainfall of as much as 400 mm in 24 h triggered more than 1000 landslides in the study area (Yamagishi et al. 2005); some of these landslides were reactivated by the earthquakes. The earthquakes occurred only a few days after Typhoon Tokage; the strong shaking of rain-soaked hillsides triggered numerous mudslides and debris flows. The earthquake produced very high levels of ground motion in the epicentral area, including two sites that recorded peak horizontal ground accelerations of 1.3–1.8 g and several other sites that recorded accelerations greater than 0.3 g. A Japan Meteorological Agency (JMA) strong-motion station was in Yamakoshi, which is in the center of the landslide region. This station recorded peak horizontal ground accelerations of 0.55 g (NS) and 0.74 g (EW) and a peak vertical acceleration of 1.08 g. The ShakeMap model produced by the U.S. Geological Survey Earthquake Hazards Program (Wald et al, 2006). for this earthquake shows a peak ground acceleration ranging from 0.02 to 0.62 g (Figure 16).

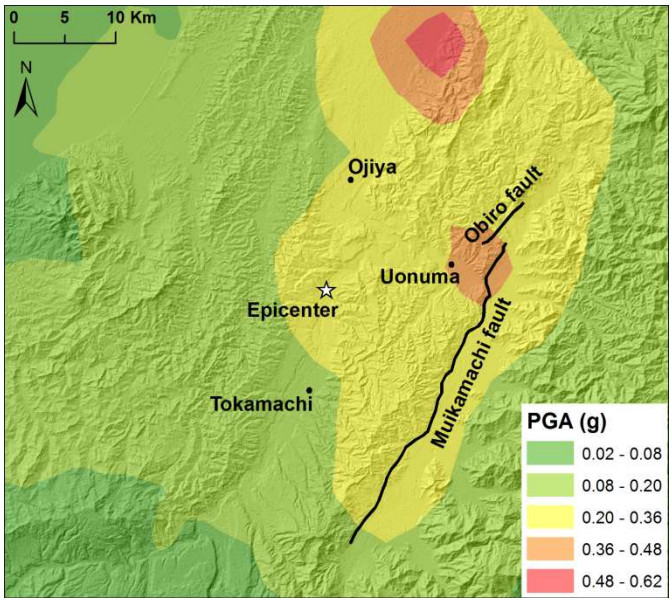

Figure 26. Peak ground acceleration (g) related to the 2004 Niigata Earthquake. ShakeMap model produced by the U.S. Geological Survey Earthquake Hazards Program (Wald et al, 2006).

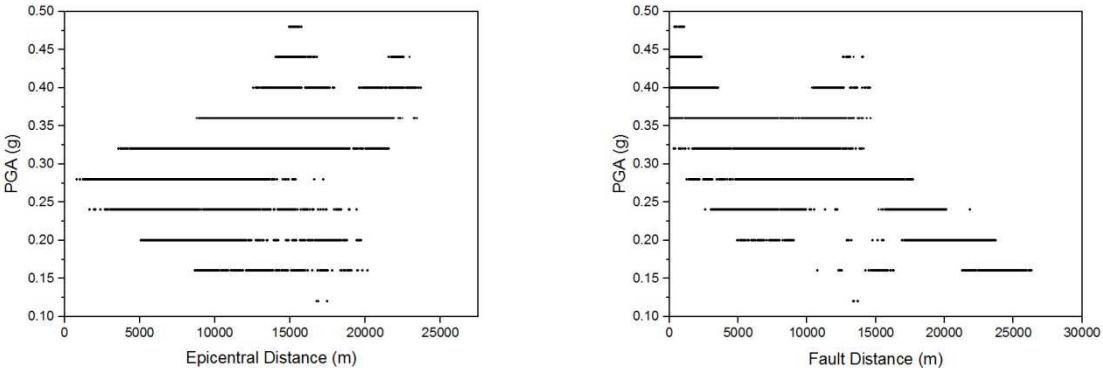

Figure 27. Graphs showing the distribution of the PGA (g) in relation to the epicentral and the fault distance (m).

The spatial distribution of the peak ground acceleration in the area do not show a clear trend with the distance from the epiceter. While the PGA values decrease with the fault distance (Figure 27).

4.3.1 Digital Elevation Model

The ASTER GDEM is used as a GeoTIFF format with wgs84 geographic lat/long coordinates and a 1 arc-second (30 m) grid of elevation postings. Two maps were realized from this DEM: the slope gradient map (Figure 28) and the relief map (Figure 29). (*See 1993 Papua New Guinea and 1994 Northridge Earthquakes for more details*).

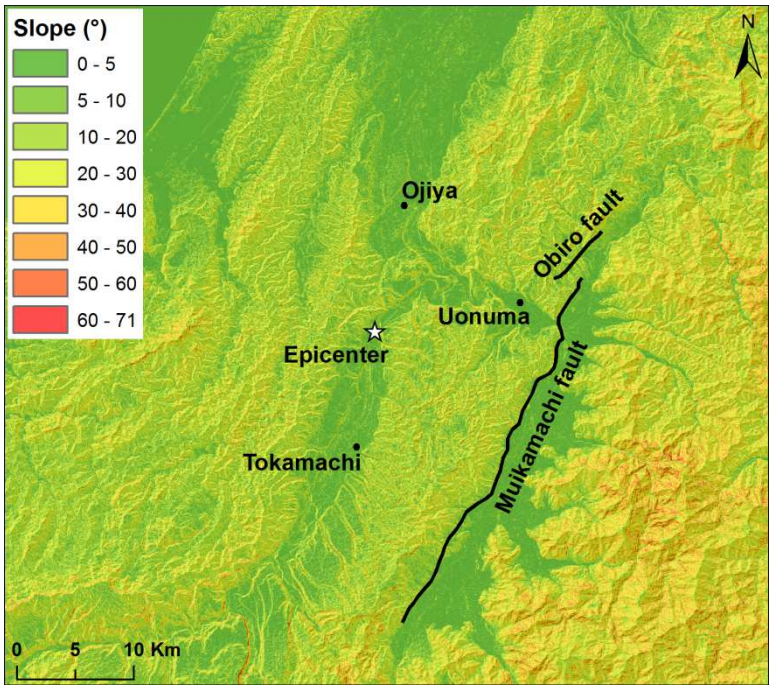

Figure 28. Slope gradient map of the ASTER GDEM.

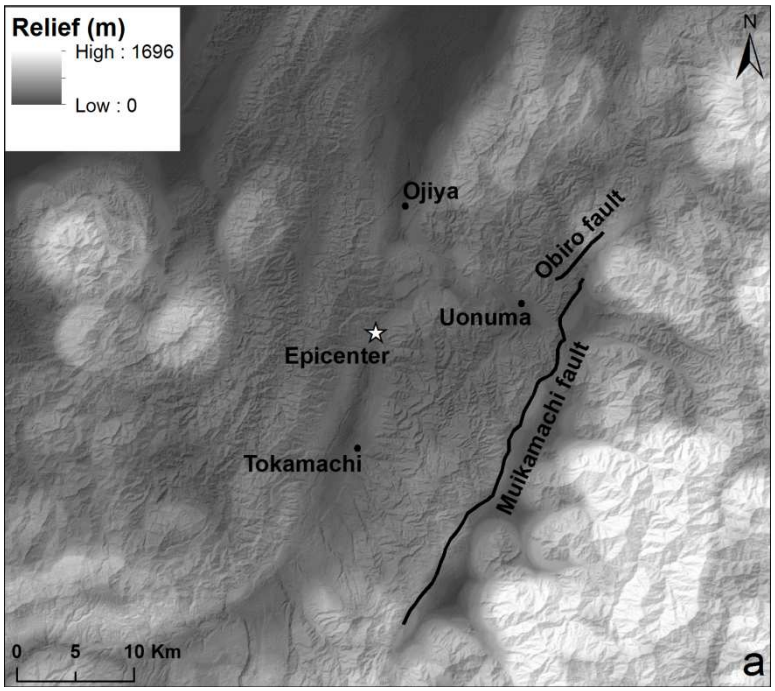

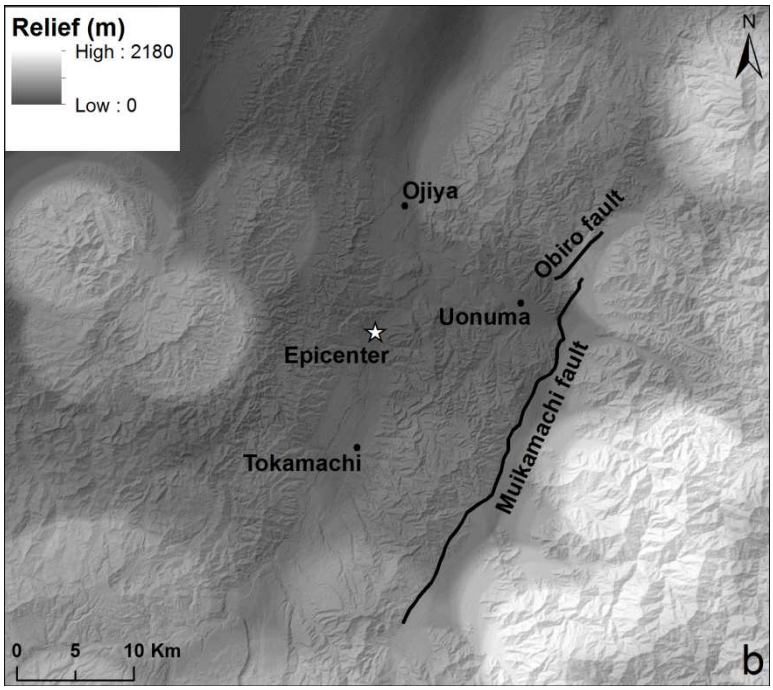

Figure 29. Relief map of the ASTER GDEM with a radius of 1 Km (a) and 5 Km (b).

4.3.2 Geological Setting

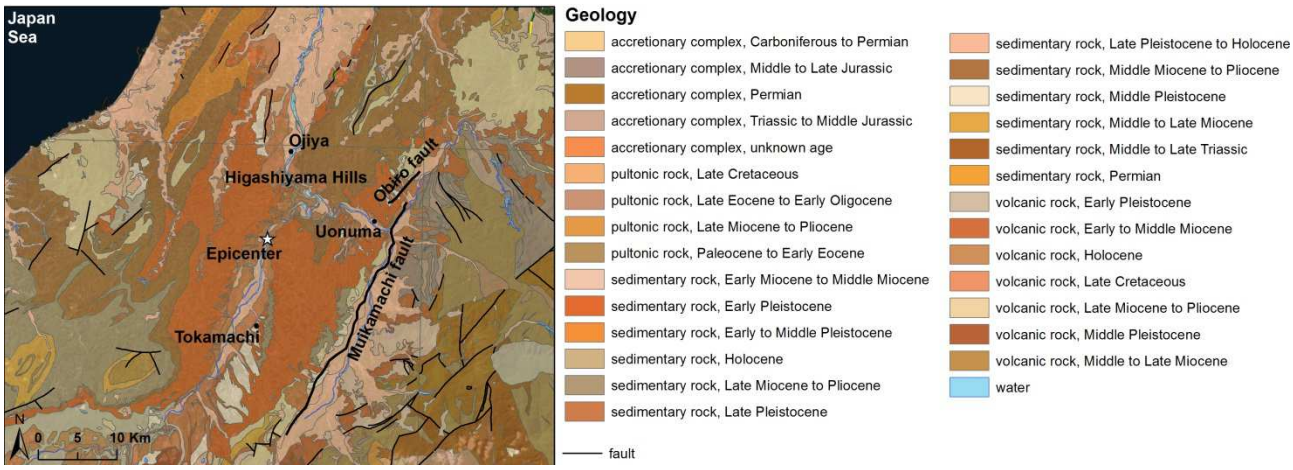

Figure 30. Digital geological map of Japan at a scale 1:200,000 realized by the Geological Survey of Japan (2012). Black line indicate the fault at the origin of the 2004 earthquake.

Most of the areas affected by the earthquakes are underlain by Neogene-Quaternary sedimentary units (Figure 30), which consist of a sequence of claystone and siltstone that is relatively nondurable, with interbeded sandstone and minor conglomerate, partly associated with a minor amount of volcanic rocks (Geological Survey of Japan 1982). These rocks are typically poorly or moderately indurated, and are structurally deformed by pervasive folding and local faulting. Prehistoric landslide deposits are widespread, and thousands of landslides have occurred historically in and around this area (NIED 2004b), characterizing the geomorphic features. A terrace is well

developed, and its deposits of gravel, sand and mud covered with a weathered volcanic ash layer, are located at three levels, some of which are interbeded with slope deposits (Yanagisawa et al. 1986). In addition, the geomorphological setting of the area has resulted from a general conformity between structural and lithological elements and morphology. To some extent, step cultivation of paddy fields and fish ponds for carp feeding, have also formed the landscape of this area, and increased the risk of slope failures due to the infiltration of surface water into soil or rock. Topography in the study area ranges from hilly to mountainous in the Higashiyama Hills (Figure 30), located in the southwestern part of the Niigata coastal plain along the Japan Sea. Elevations range from 25 m asl to 780 m asl.

4.3.3 Analysis

The relationships of the lithology with the relief, the PGA (g), the epicentral distance and the fault distance have been analyzed. The lithologies identified in the area were grouped in five groups, starting from the digital geological map of Japan at a scale 1:200,000 realized by the Geological Survey of Japan (2012). (see Table 1). The definition of the lithological classes were already available in the 1:200,000 Digital geological map of Japan (Figure 30), some sedimentary rocks have been classified on the basis of the age.

Table 3. Simplified geology of Iwate–Miyagi Nairiku Earthquake.

#	Lithology	Group Name
1	Limestone	Limestone
2	Sedimentary deposits and rocks	Quaternary
3	Sandstone	Sandstone
4	Sedimentary rocks	Tertiary
5	Volcanic Rock	Volcanic Rock

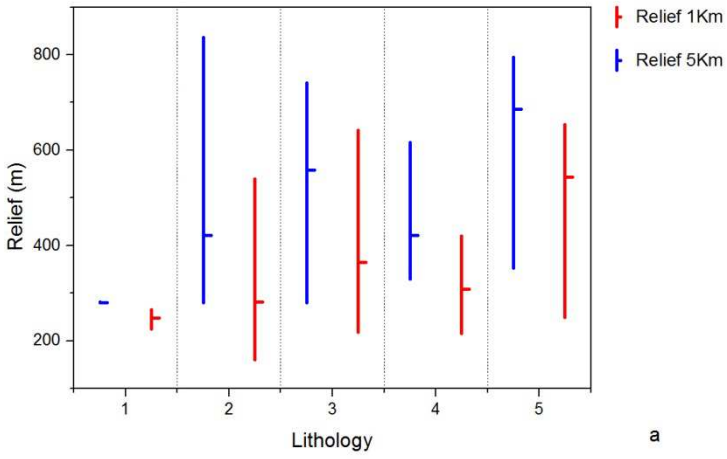

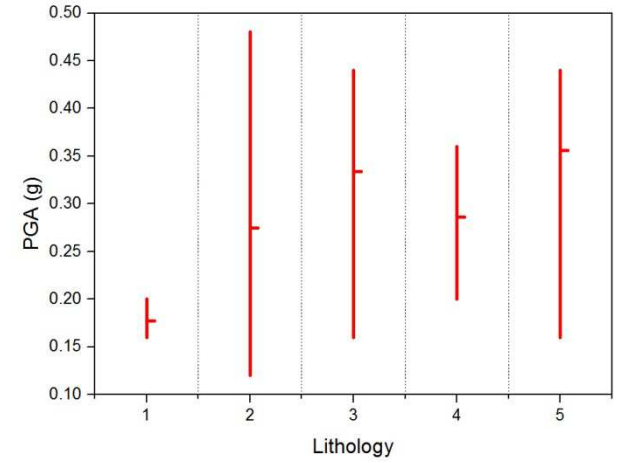

b

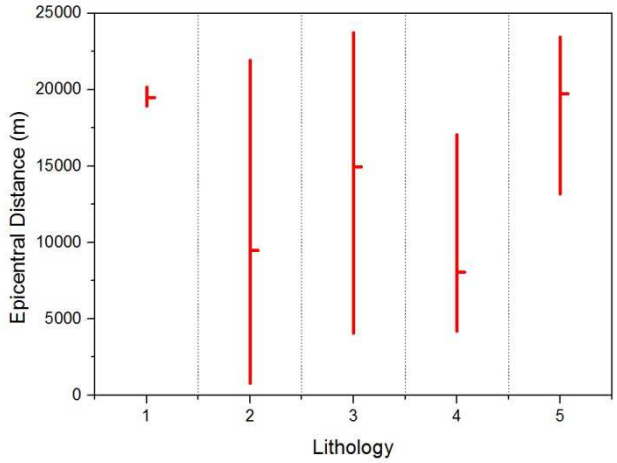

c

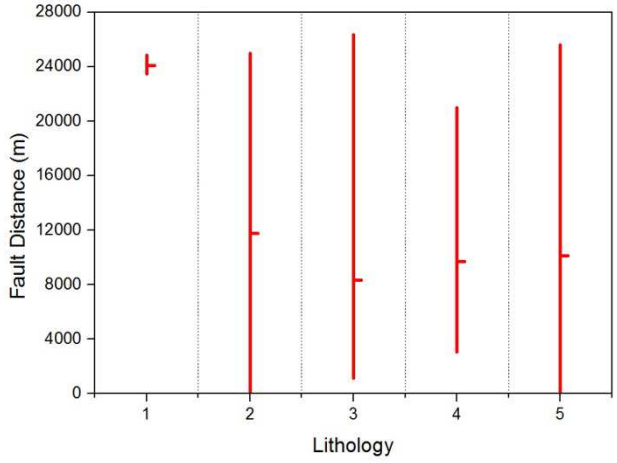

d

Figure 31. Graphs showing the relationships of the lithology with: a) Relief (m); b) PGA (g); c) Epicentral Distance (m).

The relief increase with the range from 1 to 5 km, and change between the different lithologies (Figure 31a). In particular the Volcanic rocks show, in mean, the higher values, while the

Limestone the lower. Limestone (#1, Figure 31b) experienced the lower values of PGA, probably related to the position (far) from the seismic source, and to the little distance at which this lithology is present. The others lithologies covered the more or less all the distances and registered both low and high values of PGA (Figure 31b).

4.3.4 Landslide Dataset

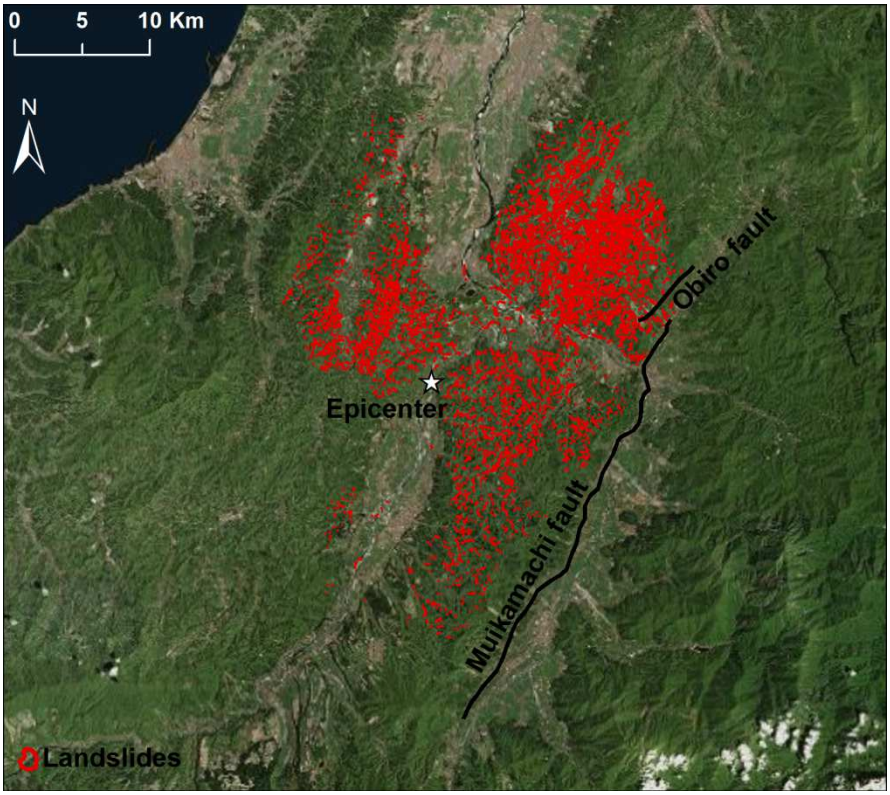

Figure 32. Landslide dataset developed by Yagi et al. (2007).

The Chuetsu earthquake triggered 10525 landslides (Yagi et al., 2007, Figure 32). Aerial photographs and satellite photos taken after the earthquake were interpreted to provide extensive information on landslide locations, geometries, types, and characteristics. The landslides triggered by the earthquake can be classified into six categories: (1) rock falls; (2) rock slides; (3) disrupted soil slides; (4) debris flows; (5) soil block slides; and (6) complex landslide (Cruden and Varnes 1996; Keefer 2000). The most widespread types of landslides induced by the earthquake were highly disrupted, relatively shallow slides and soil (debris) flows. The disrupted shallow slides consisted of regolith and highly weathered bedrock materials on very steep slopes flanking floodplains and along incised valleys and creek channels. In several cases, debris flows traveled long distances and blocked natural drainage courses, generating landslide dams. In some cases, slope failures were obviously controlled by pre-existing planes of weakness. Several of these large

landslides blocked streams, forming landslide dams. Transitional soil slide are triggered by slope-parallel failures involving colluvium, residual soil, and highly weathered bedrock on steep slopes 55°, and represent most of the observed landslides. Although these failures were typically only a few meters deep, they covered extensive slope areas and produced great volumes of landslide debris that filled valley bottoms and locally blocked floodplains. The failure surfaces commonly developed along the boundary with more intact and less weathered bedrock. Typically, all vegetation was stripped off the surface, along with the soil cover.

Deep rotational failures slumps, with backward rotation resulting from shear along a curved failure surface, are typically associated with clay-rich soils. This failure mode is generally found only in rock masses that are relatively soft and free of weak seams or joints, or in rocks so highly fissured as to be effectively homogeneous. Rock types that can generate slumps are typically clay-rich rocks that have been softened by loosening and wetting, rock masses in and adjacent to major fault zones, and Tertiary sediments. Block slides occurred in competent bedrock where adversely oriented discontinuities in the rock mass existed. Slump-flow complexes within colluvium-filled swales and in areas of deep regolith and highly weathered bedrock represent another commonly observed mode of failure. The largest block slide, which was located in the Dainichisan Mountain 5 km far from the epicenter, was reactivated from a pre-existing slide mass. As observed in the field investigation, this landslide was a typical rotational soil slide on a dip slope, which failed along a bedding plane. The maximum depth of the sliding surface was estimated at 75 m. The slump-flow complexes generally occurred on moderately steep slopes and typically had very long runout distances. The earthquake triggered many debris flows that had significant runout distances. Landslide dams were also remarkable phenomena triggered by the ground motion in the Chuetsu earthquake (Wang et al., 2007). The spatial distribution of the landslides area was analysed in relation to the different lithologies present in the area (Figure 33), the relief reclassified (threshold of 500 m,

Figure **34**), the mean slope at which each landslide occurred (Figure 35), for the epicentral distance. The high number of landslides occurred in Sandstone and Quaternary deposits. In particular, Sandstone show a decrease of the landslides with the distance from the source, while the Quaternary deposit seem to have the same size of landslides at all the distances. The relief in the affected area is lower than 1000 m, with the high values near the seismic source. Regarding the slope gradient, it possible to see that for most of the classes there is a decrease of the landslide size with the distance, especially for large events. The high number of landslides occurred in the 20° and 30° classes.

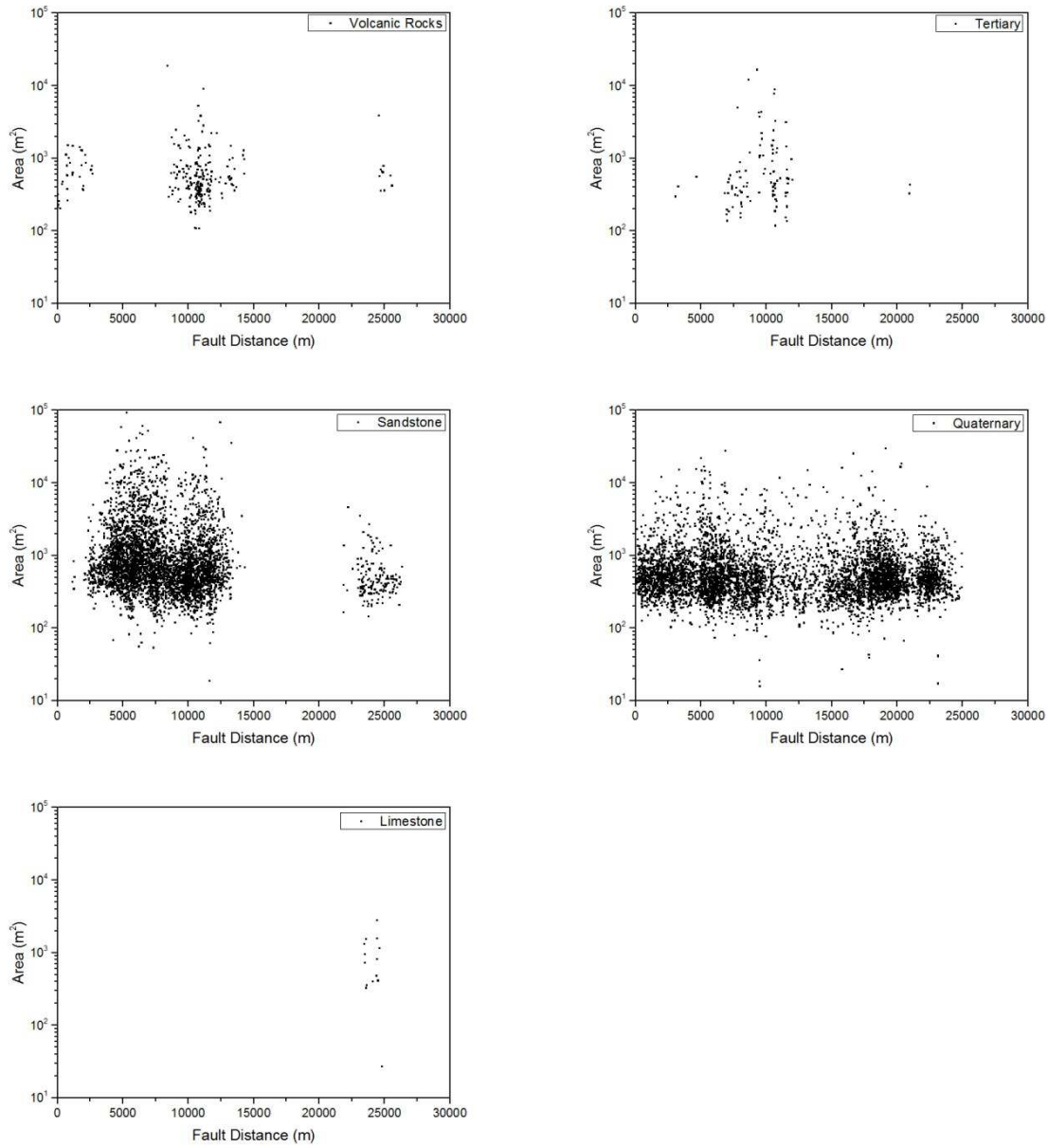

Figure 33. Landslide size as function of the fault distance, for each lithology, see appendix 1 for the epicentral distance.

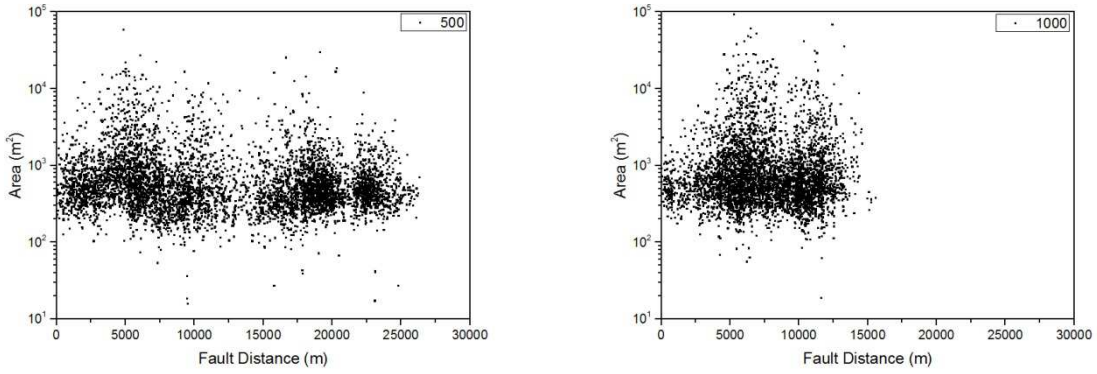

Figure 34. Landslide size as function of the fault distance, for each relief class, for the fault distance, see appendix 1 for the epicentral distance.

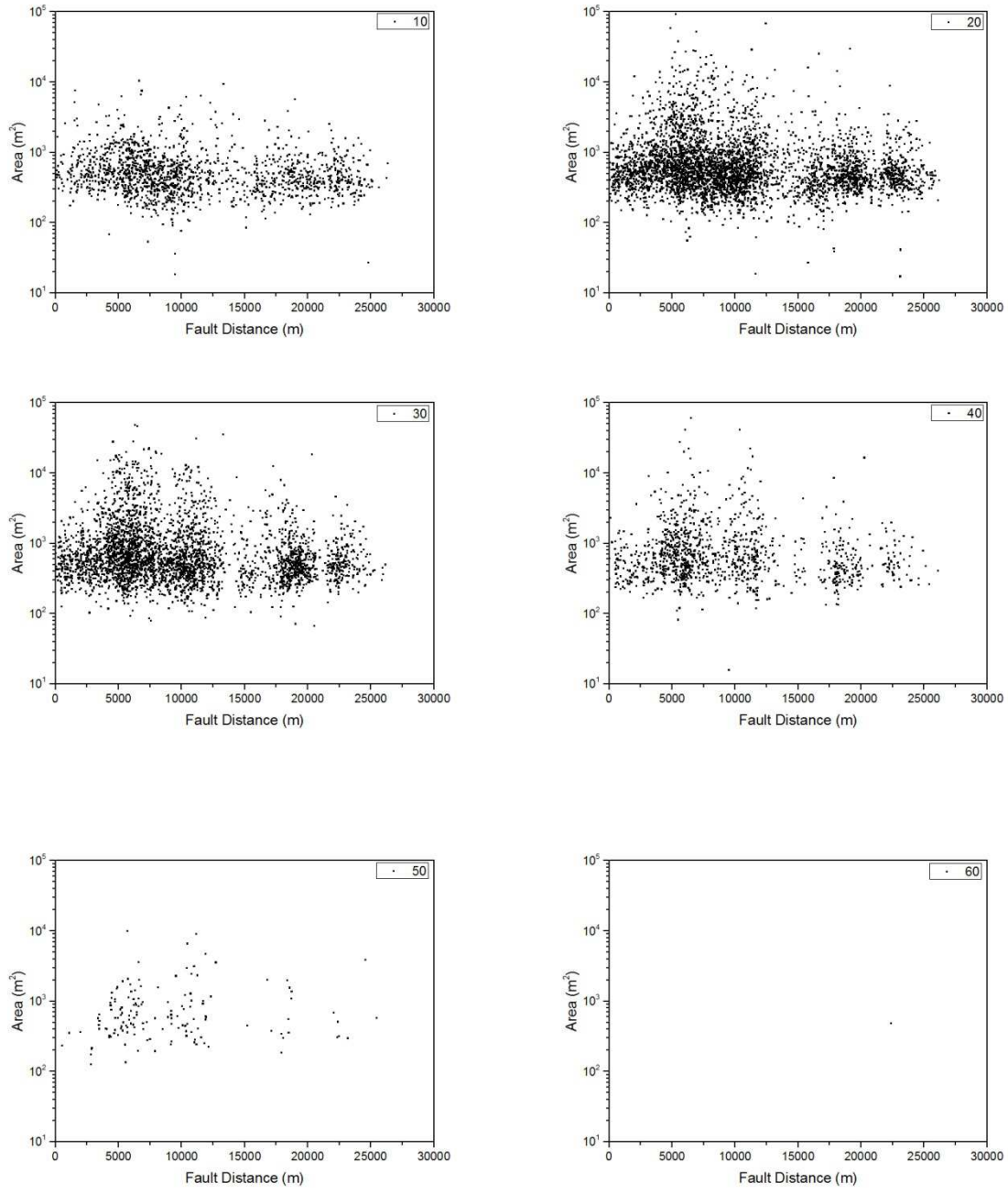

Figure 35. Landslide size as function of the fault distance, for each slope class, see appendix 1 for the epicentral distance.

4.4 Wenchuan Earthquake, 2008

The May 12, 2008 Wenchuan earthquake (Mw 7.9) triggered hundreds of thousands of landslides. Its epicentre was located in the administrative region of Wenchuan County. The hypocenter is located at 31.021°N and 103.367°E at a depth of 19 km. The event occurred at a distance of 80 km WNW of Chengdu, 145 km WSW of Mianyang, 50 km WNW of Chongqing, 1545 km SW of Beijing (http://earthquake.usgs.gov/).

The landslides triggered by the 2008 Wenchuan earthquake have received much attention due to the size of the event and the resulting tragic loss of life and economic devastation. More than 45.5 million people were affected by the event. 69,195 people killed, 374,177 injured and 18,392 missing and presumed dead in the Chengdu-Lixian-Guangyuan area. An estimated 5.36 million buildings collapsed and more than 21 million buildings were damaged in Sichuan and in parts of Chongqing, Gansu, Hubei, Shaanxi and Yunnan. The total economic loss was estimated at 86 billion US dollars. Beichuan, Dujiangyan, Wuolong and Yingxiu were almost completely destroyed. Landslides and rockfalls damaged or destroyed several mountain roads and railways and buried buildings in the Beichuan-Wenchuan area, cutting off access to the region for several days. Landslides also dammed several rivers, creating 34 barrier lakes which threatened about 700,000 people downstream. A train was buried by a landslide near Longnan, Gansu. At least 2,473 dams sustained some damage and more than 53,000 km of roads and 48,000 km of tap water pipelines were damaged. About 1.5 km of surface faulting was observed near Qingchuan, surface cracks and fractures occurred on three mountains in the area, and subsidence and street cracks were observed in the city itself (http://earthquake.usgs.gov/).

The earthquake, occurred in the Longmenshan mountain range, is the result of motion on a thrust fault on the northwestern margin of the Sichuan Basin. The earthquake reflects tectonic stresses resulting from the convergence of crustal material moving from the high Tibetan Plateau against the crust below the southeastern China.

On a continental scale, the seismicity of central and eastern Asia is a result of northward convergence of the India plate against the Eurasia plate. The moving has a velocity of about 50 mm/y. The convergence of the two plates is broadly accommodated by the uplift of the Asian highlands and by the motion of crustal material to the east away from the uplifted Tibetan Plateau. Eleven earthquakes with a magnitude higher than 7 Mw occurred in the Sichuan area in the last 200 years.

During the event a peak ground acceleration ranging between 59 and 1275 cm/s^2 (0.06 and 1.3 g), was registered (Figure 16). Analysing the distribution of the PGA in relation to the distance from

the source area (Figure 37), there is a clear trend between the PGA and the fault distance, however this trend is not so clear in the case of the epicentral distance.

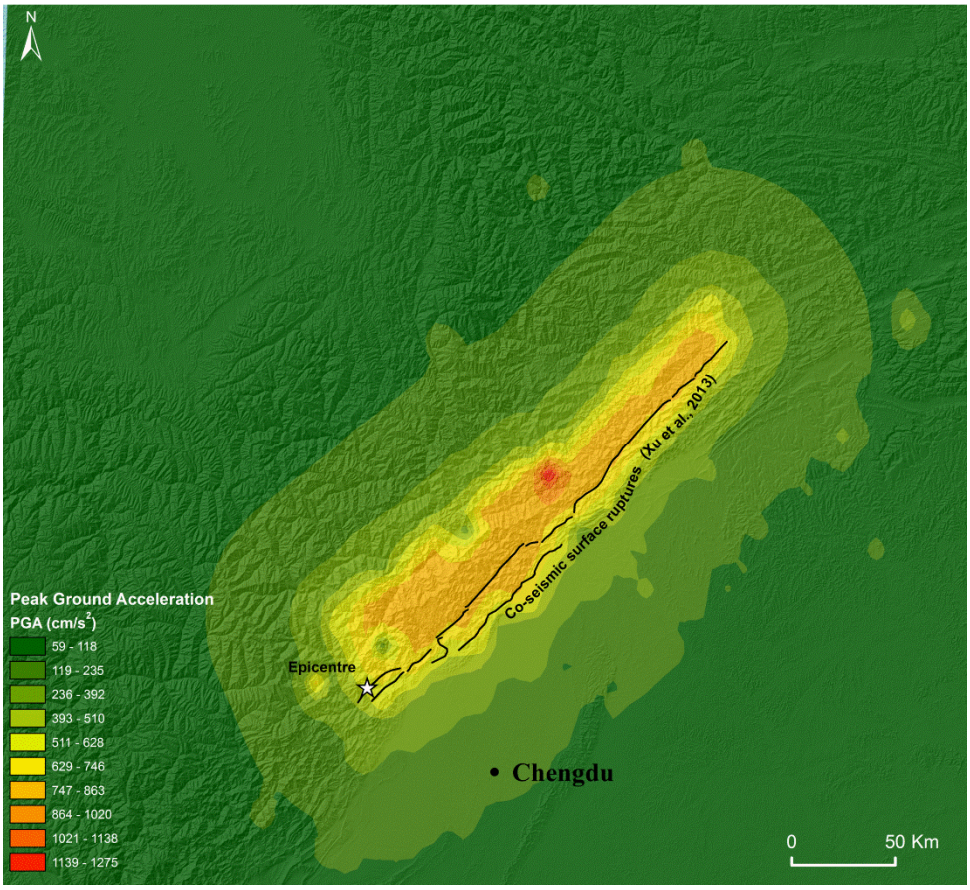

Figure 36. Peak ground acceleration (cm/s^2) related to the 2008 Wenchuan Earthquake. ShakeMap model produced by the U.S. Geological Survey Earthquake Hazards Program (Wald et al, 2006).

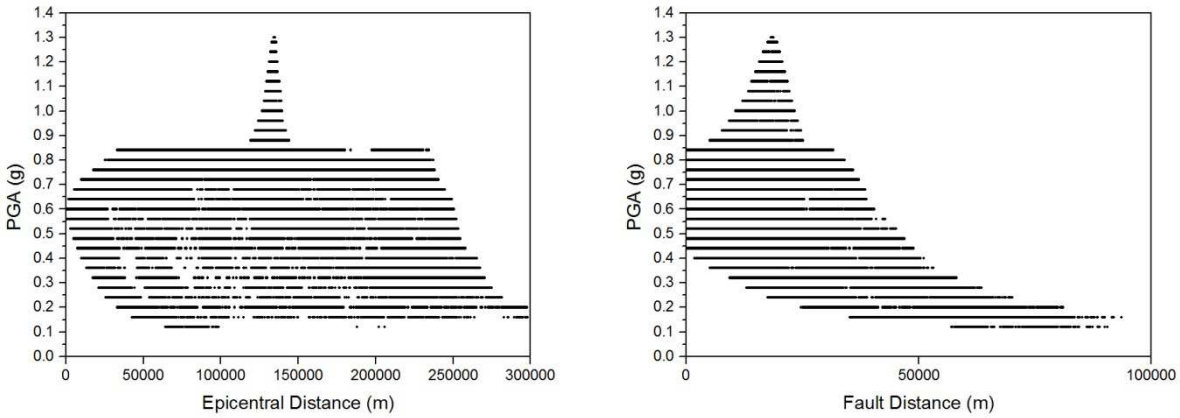

Figure 37. Graphs showing the distribution of the PGA (g) in relation to the epicentral and the fault distance (m).

4.4.1 Digital Elevation Model

The ASTER Global Digital Elevation Model (ASTER GDEM) is used for this earthquake as a GeoTIFF format with wgs84 geographic lat/long coordinates and a 1 arc-second (30 m) grid of elevation postings. Two maps were realized from this DEM: the slope gradient map (Figure 38) and the relief map (Figure 39). (*See 1993 Papua New Guinea and 1994 Northridge Earthquakes for more details*).

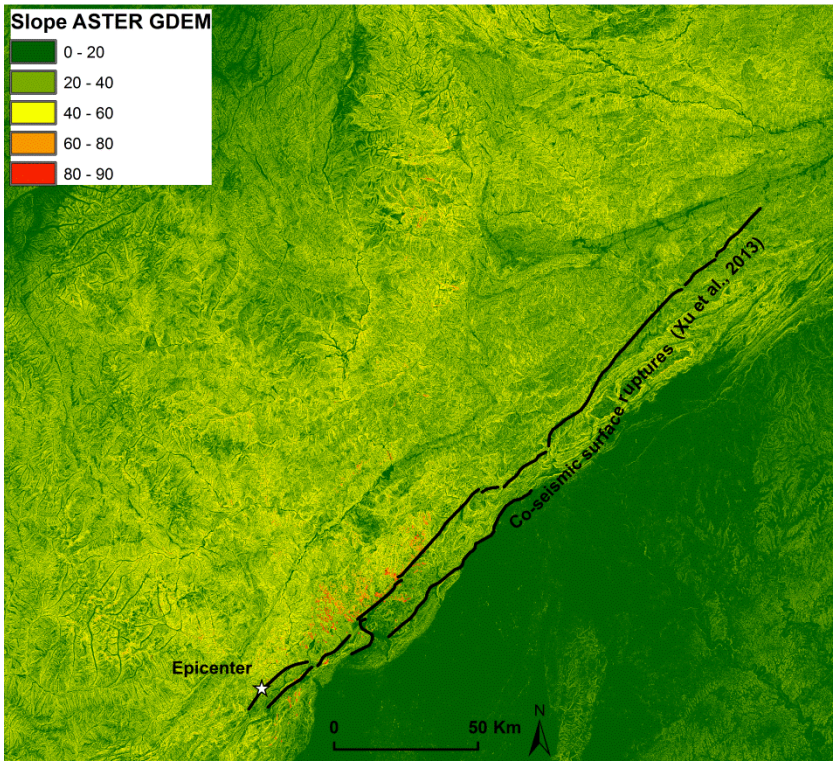

Figure 38. Slope gradient map of the ASTER GDEM.

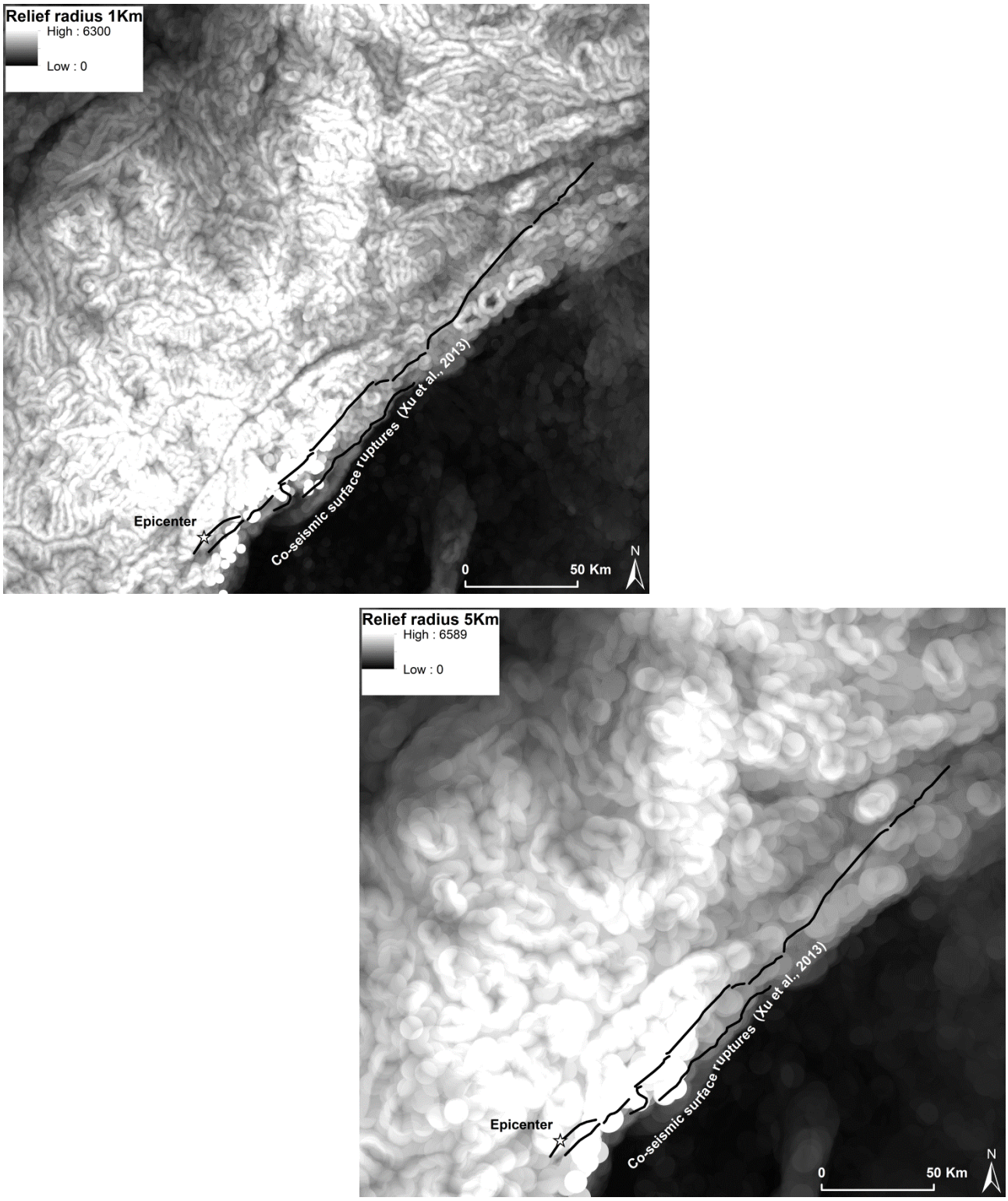

Figure 39. Relief map of the ASTER GDEM with a radius of 1 Km and 5 Km.

4.4.2 Geological setting

The Cenozoic deformation of the Longmen Shan, including the active faulting related to the Wenchuan earthquake, is superimposed on a preexisting Mesozoic orogen. This older deformation provides the starting geometry for later Cenozoic deformation (see Burchfiel et al., 1995). Mesozoic deformation in the Longmen Shan took place in Late Triassic and Jurassic time, when two distinct structural sequences were deformed and juxtaposed by thrust faulting. The autochthonous lower sequence consists mainly of late Precambrian basement rocks overlain by an incomplete section of latest Proterozoic to Middle Triassic shallow-water sedimentary rocks and Upper Triassic–Jurassic clastic rocks that appear to be foredeep basin deposits and grade eastward into finer-grained strata in the Sichuan Basin. The eastern part of the upper structural sequence has a Precambrian crystalline basement overlain by a thick succession of latest Proterozoic to Lower Triassic shallow-water, highly metamorphosed sedimentary rocks. The western part of the upper sequence consists of up to 10 km of Middle to Upper Triassic flysch, which extends across a broad area of eastern Tibet as the Songpan Garze flysch. This upper structural sequence was imbricated and emplaced eastward over the lower structural sequence in Late Triassic to Middle Jurassic time. Transitional units between the two structural sequences are generally not found. Thrust sheets override the older foredeep deposits, and thrust contacts are sealed in places by Middle Jurassic strata, constraining the end of thrusting to the pre–Middle Jurassic. The foredeep deposits continue into the Late Cretaceous, but large post–Middle Jurassic, pre-Oligocene structures have not been identified. The Mesozoic thrust complex and its underlying autochthon were refolded and thrust eastward in Cenozoic time. Cenozoic folding of the Precambrian basement is well expressed in the Baoshan and Pengguan massifs (Figure 40; Figure 41). Along the southwestern margin of the Sichuan Basin, Eocene and probable Oligocene red beds are deformed by northeast-trending folds and thrust faults that merge northward into the Longmen Shan. These rocks constrain the Cenozoic deformation in this area to have been initiated in the late or post- Oligocene. Uncommon, presumed Neogene, conglomerates in the Longmen Shan are less folded than the underlying Early Cenozoic rocks. Cenozoic thrust faults in the Longmen Shan do not have large displacements; folded strata can be matched across the faults. At the north end of the Pengguan massif, the plunging fold that involves basement also folds the overlying Mesozoic thrust complex, and at the north end of both basement massifs, sedimentary rocks on the west side of the massifs have a gentle west dip where the basement plunges beneath them. The large scale Cenozoic structure of the Longmen Shan appears to be similar to that of a fault propagation fold that has been strongly modified by faults. External structures of the Longmen Shan merge with those of the western Sichuan Basin. Folds in the Sichuan Basin are underlain by a décollement that continues to the west beneath the folds of the

eastern Longmen Shan. This décollement must ramp down into the basement east of the Pengguan and Baoshan massifs. Some thrust faults along the eastern front of the Longmen Shan may also root into the basement, but correlation of sedimentary strata across these thrust faults suggests small displacements. Northwest of Chengdu, most of the Cenozoic shortening appears to be concentrated in the folded structure of the Pengguan massif. At this latitude, only one fold (the Longchuan anticline) is present in the Sichuan Basin, indicating only a few kilometers of displacement on the décollement beneath the basin. Here, Cenozoic folding along the eastern front of the Longmen Shan also does not require much shortening. North of the Longchuan anticline, the Mesozoic foredeep deposits are more uniformly inclined, dipping 15°–20°E and flattening eastward to merge with strata in the Sichuan Basin. This suggests that a triangle zone (a type of blind thrust fault) may be present at depth beneath the range front. South of the Pengguan massif, folding in the basin becomes more widely distributed; thrust faults also appear to the west within the Sichuan Basin and along the eastern flank of the Longmen Shan (Figure 40), indicating increased displacement on the décollement. South of the Sichuan Basin, the structures are more complex and involve crystalline basement. A series of steeply dipping faults, some of which are active, parallel the Longmen Shan margin and cut or otherwise interact with the Cenozoic fold-and-thrust structure. The contact of Paleozoic and Mesozoic rocks with the Precambrian basement along the east side of the Pengguan massif is a steep-to-vertical fault or faults. The same contact is depositional on the east side of the Baoshan massif and the northeast side of the Pengguan massif. To the north, these faults offset the thrusts of the Mesozoic thrust complex by <1 km, indicating little displacement on this steep fault system. The fault system continues northeast for >100 km as the Beichuan fault, a likely candidate for rupture during the 12 May Wenchuan earthquake. The west sides of the Baoshan and Pengguan massifs are truncated by steep, west-dipping normal faults that have a right-slip component and merge with the eastern boundary faults at the southern end of the Pengguan massif. The fault system is exposed almost directly above the epicenter of the Wenchuan earthquake as the Wenchuan-Maowen fault; however, this fault's location, sense of shear, and surface dip are not compatible with the focal mechanism for the initial rupture. The magnitude of Cenozoic shortening across the Longmen Shan is variable but small, probably on the order of tens of kilometers. In eastern Tibet, few Cenozoic shortening structures are observed in the field, except in the Min Shan range to the north. The geometry of the Cenozoic shortening structures in the Longmen Shan is such that only some of the dip-slip displacement on deep faults may reach the surface, while the rest may be absorbed by folding within the overlying layers and in the Sichuan Basin.

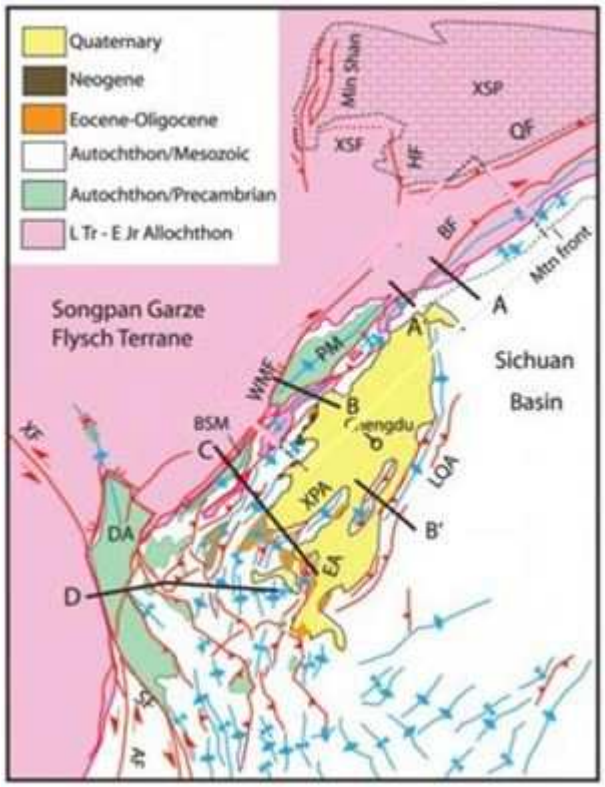

Figure 40. General tectonic map of the Longmen Shan region. AF-Anninghe fault; BF-Beichuan fault; HF-Huya fault; QF-Qingchuan fault; SF-Shimian fault; WMF-Wenchuan-Maowen fault; XF-Xianshuihe fault; XSF-Xue Shan Fault; BSM-Baoshan massif; PM-Pengguan massif; XSP-Xue Shan plateau (pattern/dashed outline); DA-Danba antiform; EA-Emei anticline; LQA-Longquan anticline; XPA-Xiong Po anticline. Red-major Cenozoic faults; purple-Upper Triassic–Lower Jurassic thrusts; blue-Cenozoic folds. On Cenozoic faults: barbs-thrust faults; ticked lines-normal faults; arrows-strike-slip. Cross sections and location of map in Figure 41 also indicated. (der Hilst, 2008).

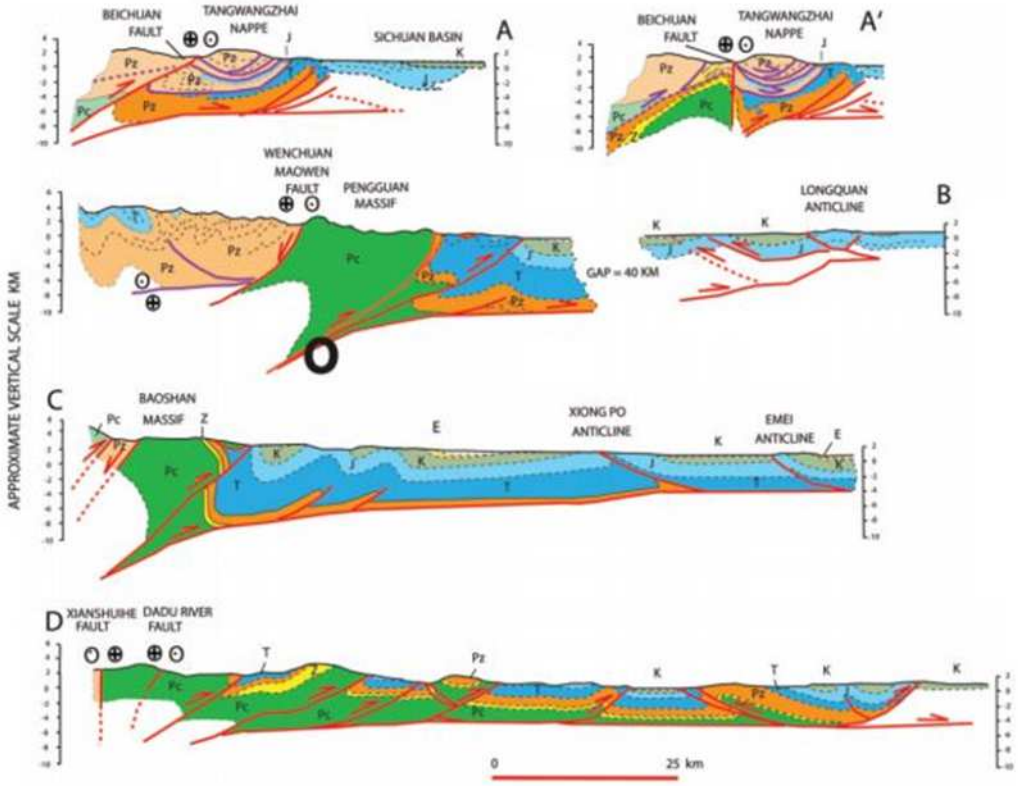

Figure 41. Cross sections of the Longmen Shan and adjacent area; locations in Figure 40. Pc-Precambrian; Z-latest Proterozoic (Sinian); Pz-Paleozoic; T-Triassic; J-Jurassic; K-Cretaceous; E-Eocene; red lines are Cenozoic faults; purple lines are Mesozoic faults. Large, bold O on section B is approximate hypocenter location of the 12 May 2008 earthquake, with an uncertainty in depth of ± 5 km. (der Hilst, 2008).

4.4.3 Analysis

The relationships between the lithology relief, peak ground acceleration, epicentral distance and the fault distance were analysed. For reasons related to the complexity of the geology in the area and to allow the analysis, the lithologies identified in the area were grouped in ten classes (see Table 4).

Table 4. Lithologies reclassified for the analysis. The group name derived from the geological map on a scale of 1:200,000 from China Geological Survey.

#	Lithology	Group Name
1	Sandstone and Siltstone	16; Z
2	Granitic Rocks	20
3	Limestone and Phyllite	C-P; C2; O
4	Limestone and Sandstone	D1
5	Phyllite and Limestone	D2; S1; S2
6	Conglomerates and Sandstone	K-N; J; T2
7	Quartz and Feldspathic Sandstone	PZ1
8	Schist and Andesite	PZ2
9	Quaternary Deposits	Q
10	Limestone	T1; P1; P2; C1

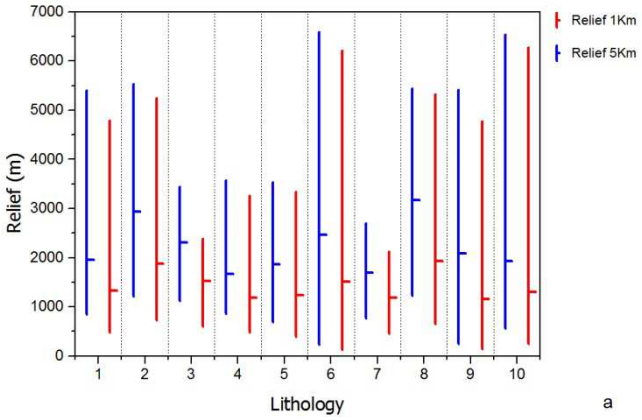

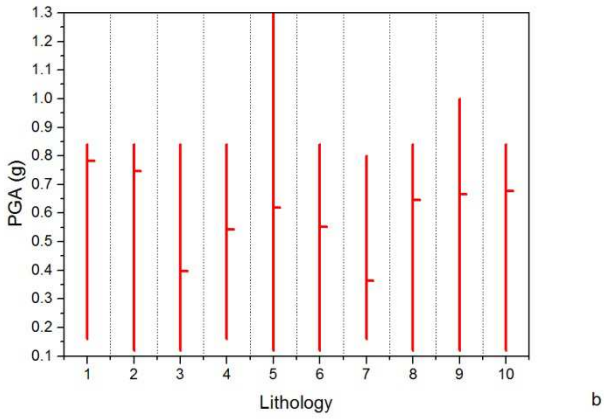

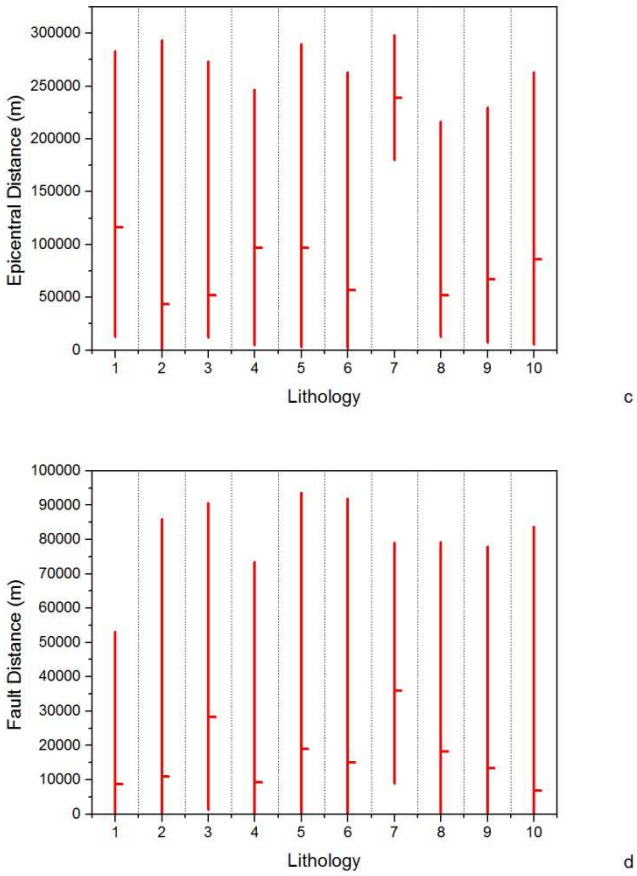

Figure 42. Graphs showing the relationships of the lithology with: a) Relief (m); b) PGA (g); c) Epicentral Distance (m); d) Fault Distance (m).

It is possible to see that in the case of the Wenchuan area there is not a different variation of the trend between the two range analysed for the different lithologies (Fig. 6a).

Regarding the value of PGA registered in each lithologies, the Phyllite and Limestone (#5, Table 4, Figure 42b) cover all the range of values, but this is related also to the fact that this lithology is present at all distance from the epicentre and fault (Fig. 6c,d). The Quartz and Feldspathic Sandstone (#7, Table 4, Figure 42b) experienced the low value, in mean, of PGA and also in this case it is related to the position with respect to the epicenter and the fault (Fig. 6c,d). These lithologies are far from the seismic source. The same reasoning can be made for the Limestone and Phyllite (#3, Table 4, Figure 42b,c,d).

4.4.4 Landslide Dataset

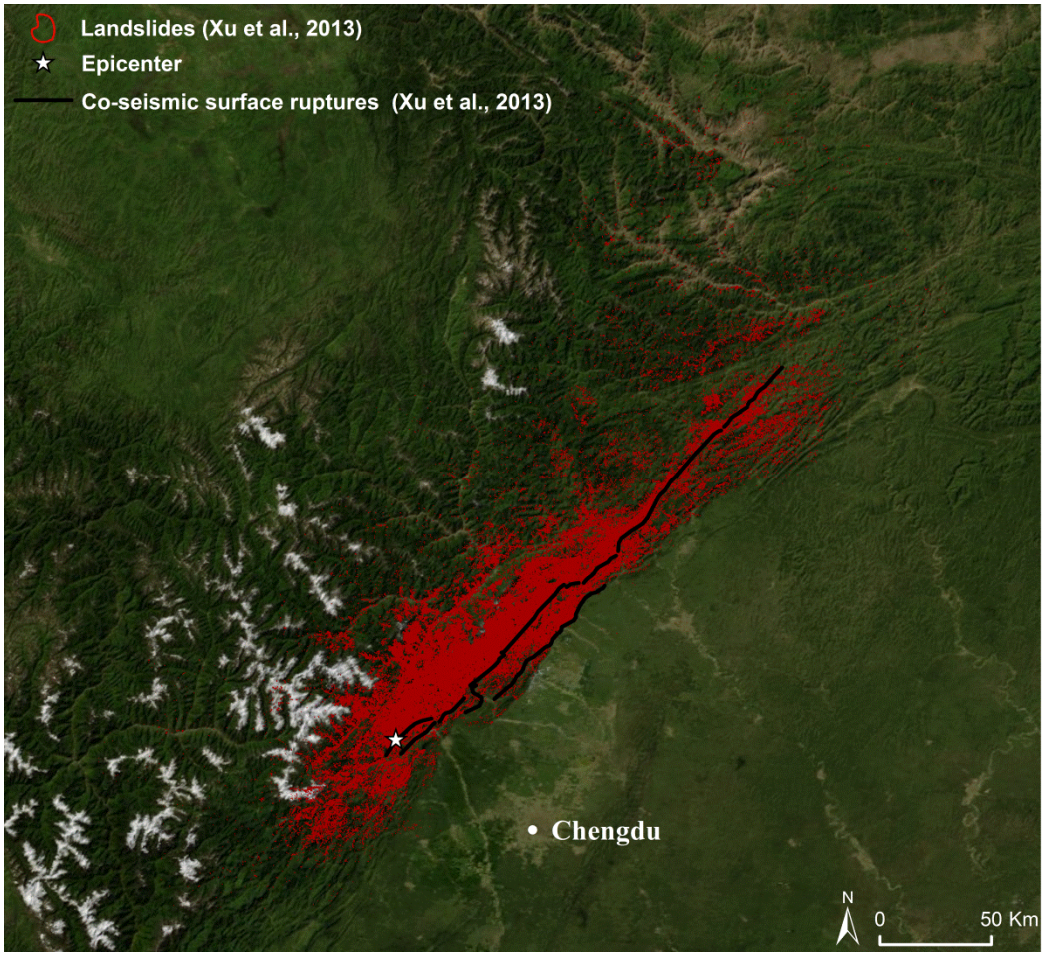

Figure 43. Landslides Dataset from Xu et al., 2014.

The analysis was performed in the Sichuan area, near Chengdu, on a dataset of 19,7481 landslides with a total area of 1,160 km^2 (Xu et al. 2014, Figure 43). The study area covers approximately 88,346 km^2. Because of the large area throughout which the Wenchuan earthquake triggered landslides, in the dataset realized by Xu et al. (2014), the location and boundary of each landslide was delineated by computer screen-based visual interpretation of high-resolution color aerial photographs and satellite remote sensing images, and some landslides were verified by field checking. Due to the high resolution of the true color aerial photographs and satellite remote sensing images, almost all the Wenchuan earthquake-triggered landslides, including the small slope failures, were detected. A spatial distribution map of the earthquake-triggered landslides was prepared in a GIS platform by the authors. They constructed also two types of landslide point inventories, including landslide centroid points similar to Dai et al. (2011) and landslide top points similar to Qi et al. (2010) and Gorum et al. (2011).

The inventory contains rock avalanches, rockfalls, translational and rotational slides, lateral spreads and debris flows.

The size of the landslides was analysed in relation to the different lithologies of the area (Figure 44), the mean slope at which each landslide occurred (Figure 45), the relief reclassified (threshold of 500 m, Figure 46), epicentral distance and fault distance.

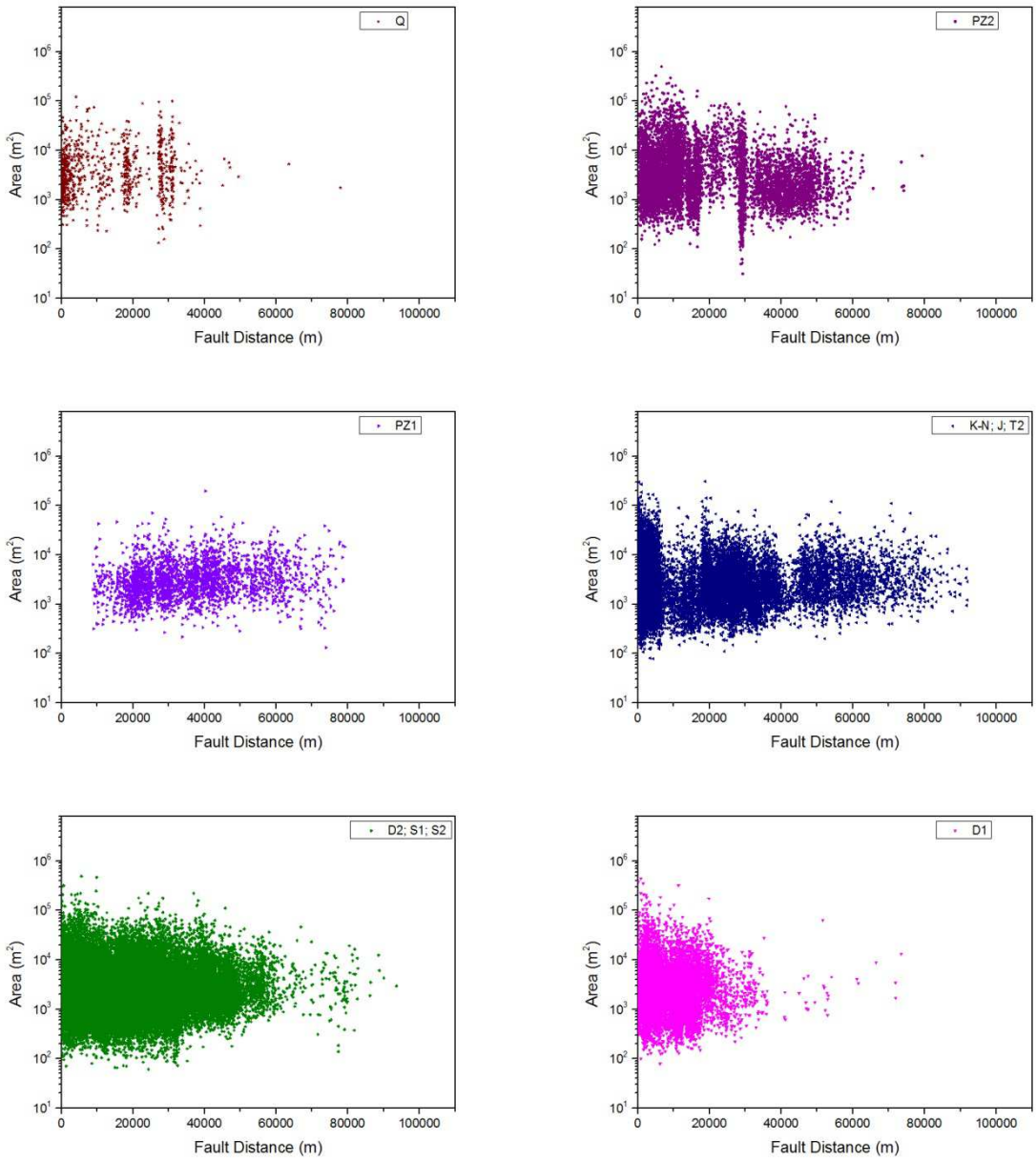

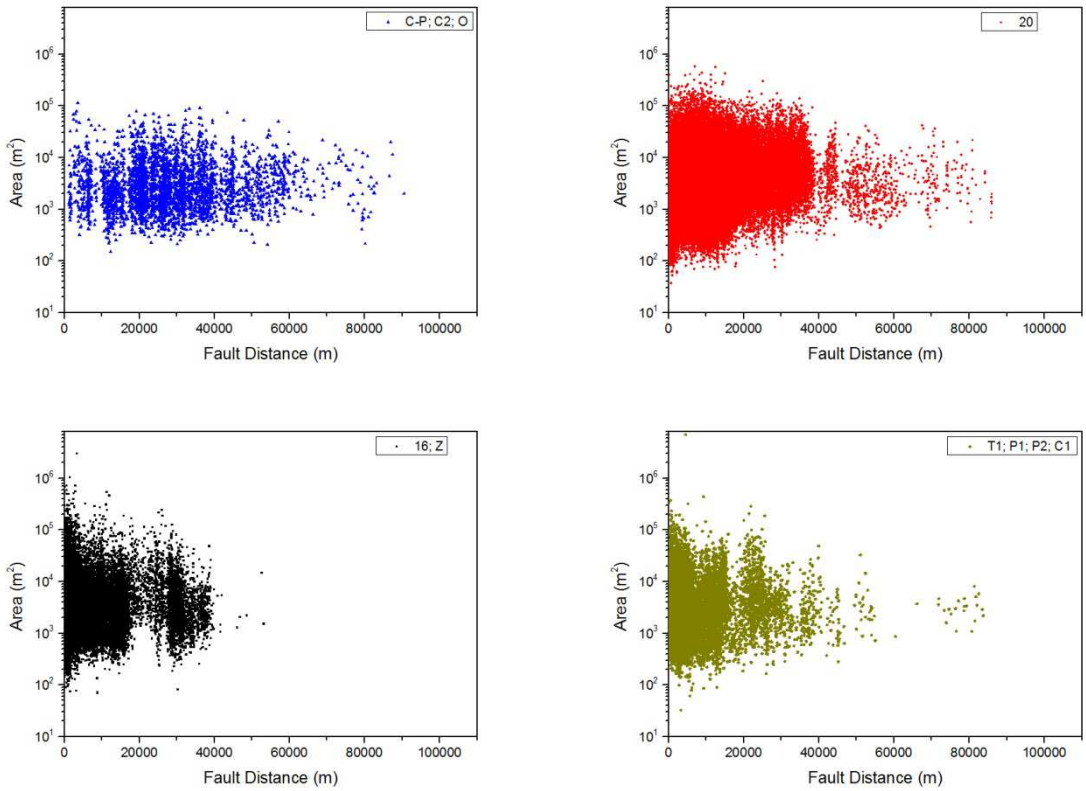

Figure 44. Landslides area distribution for each lithologies, for the fault distance, see appendix 1 for the epicentral distance.

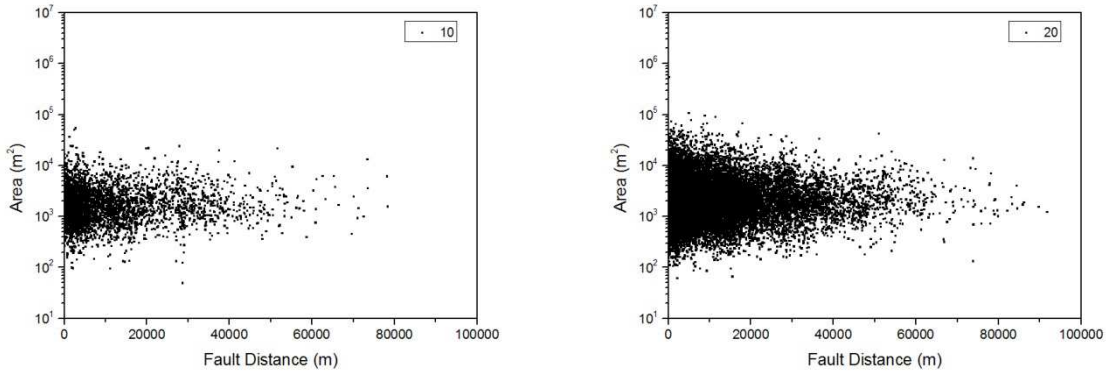

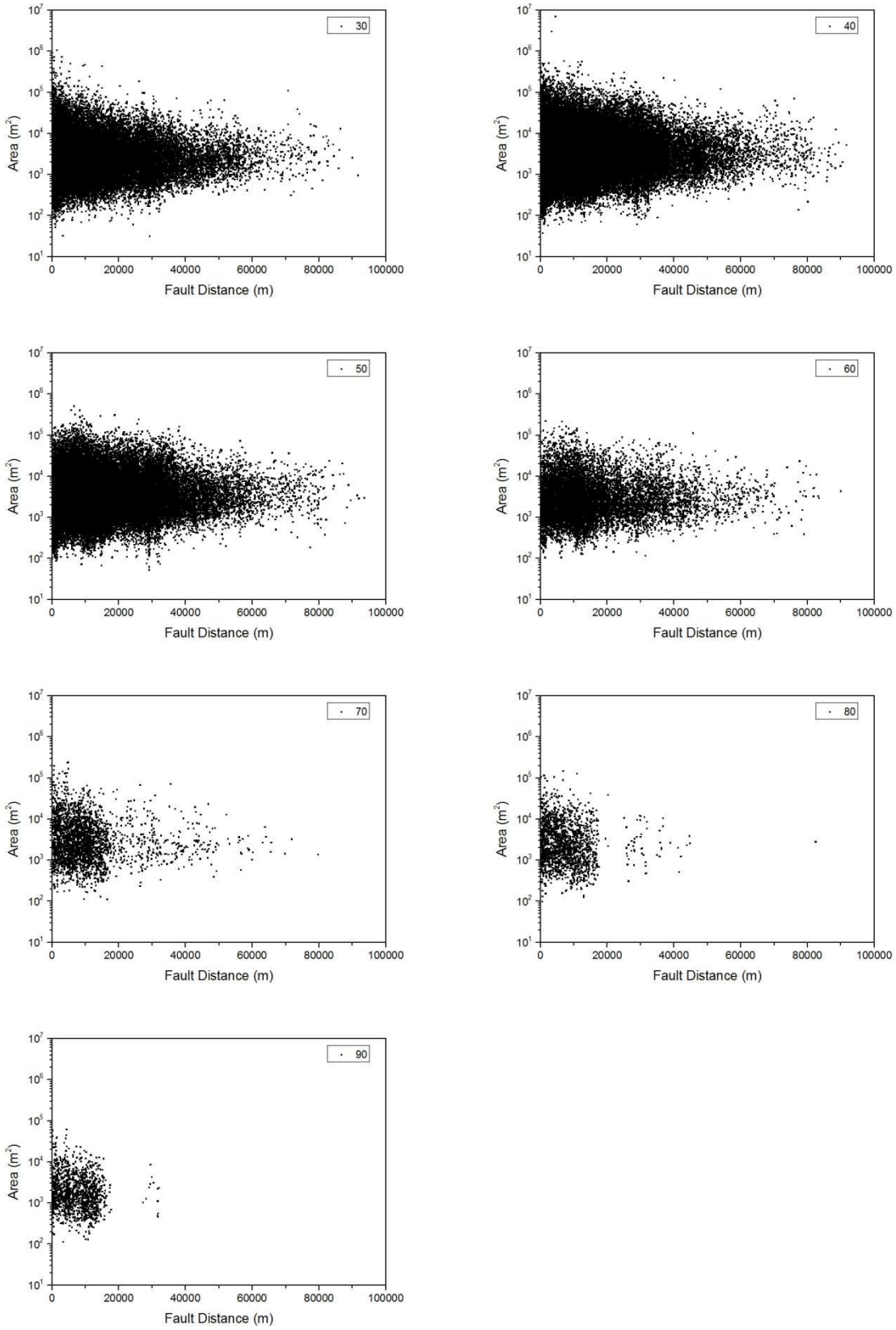

Figure 45. Landslides area distribution for each slope class, for the fault distance, see appendix 1 for the epicentral distance.

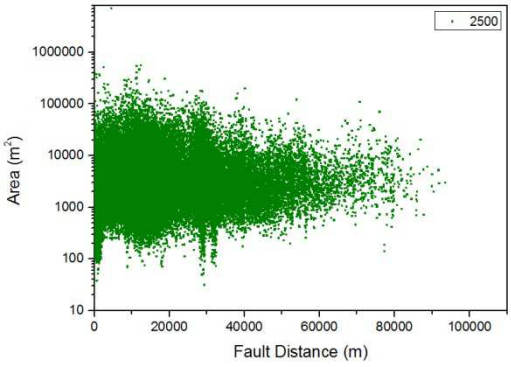
2500
Area (m²)
Fault Distance (m)

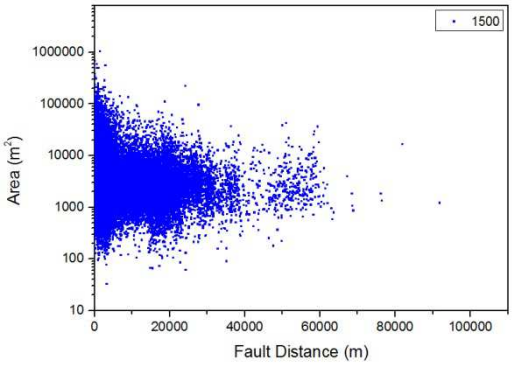
1500
Area (m²)
Fault Distance (m)

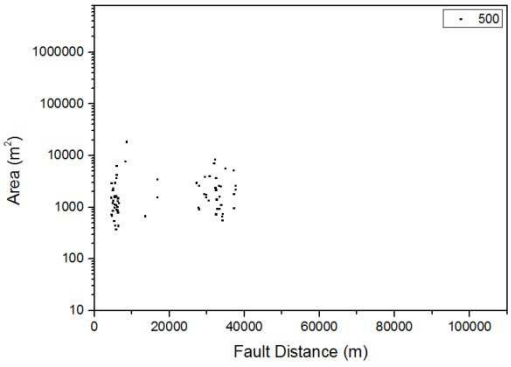
500
Area (m²)
Fault Distance (m)

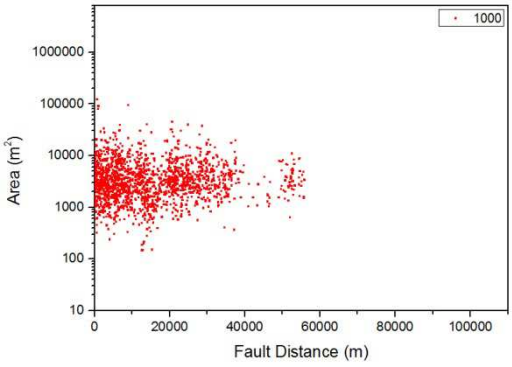
1000
Area (m²)
Fault Distance (m)

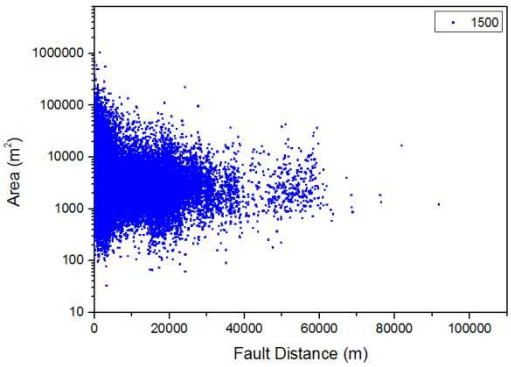
1500
Area (m²)
Fault Distance (m)

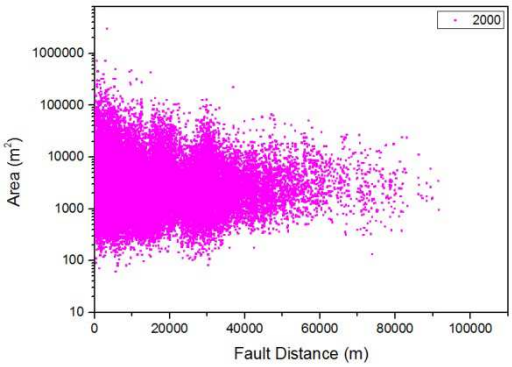
2000
Area (m²)
Fault Distance (m)

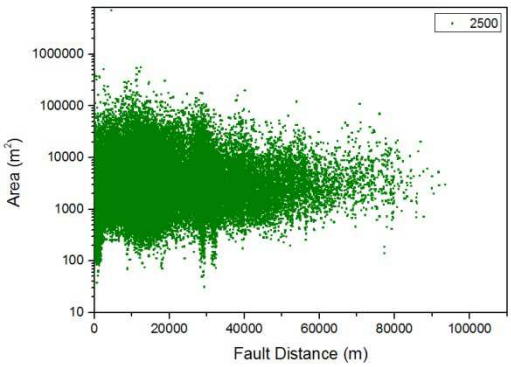
2500
Area (m²)
Fault Distance (m)

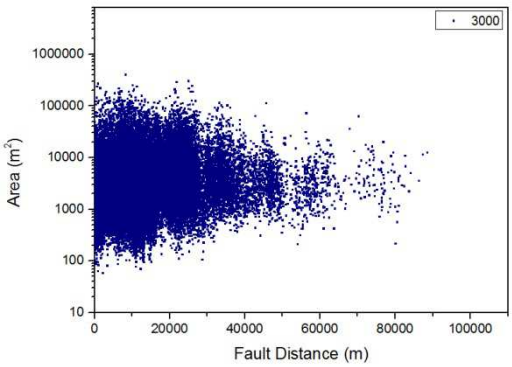
3000
Area (m²)
Fault Distance (m)

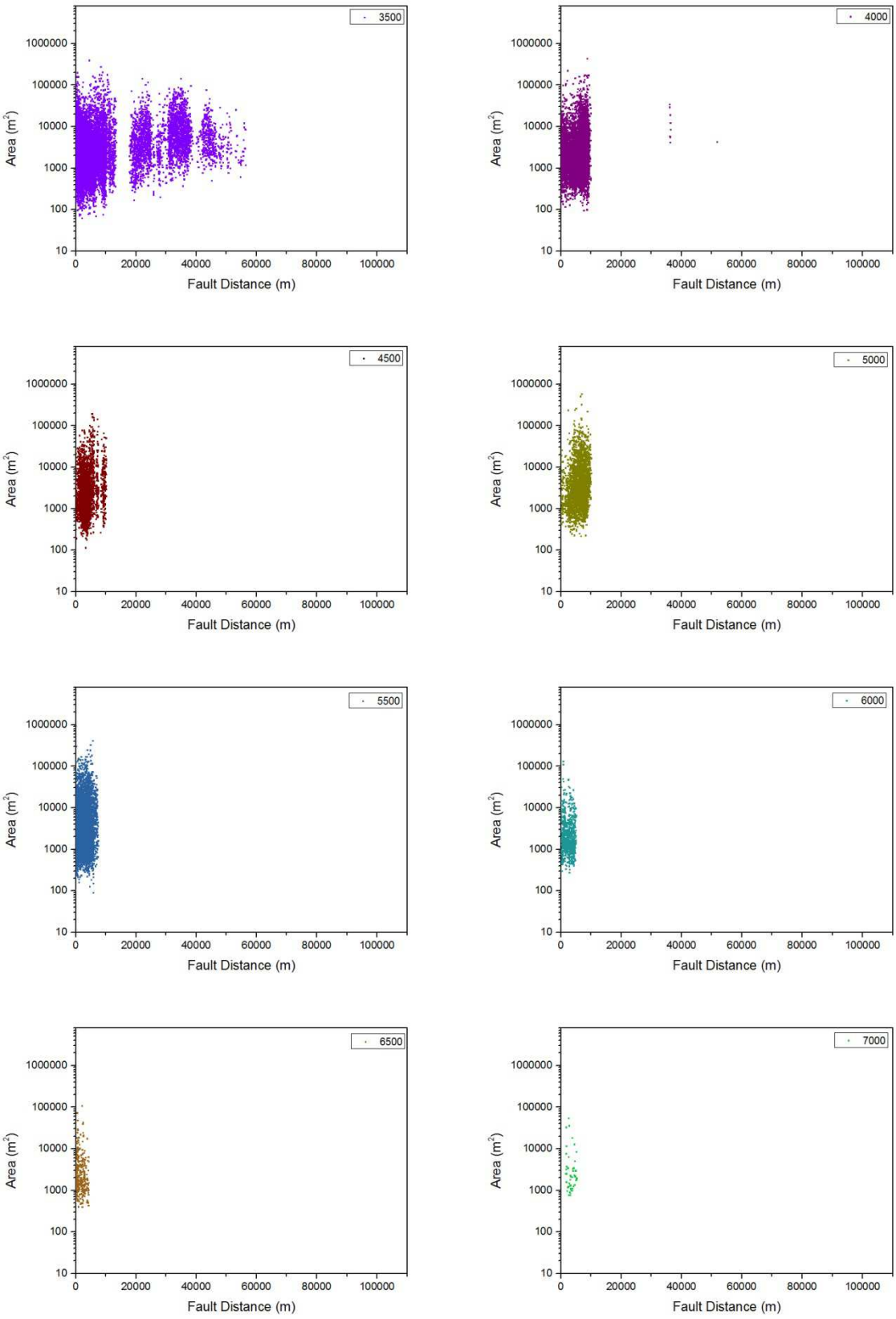

Figure 46. Landslides area distribution for each threshold of relief, for the fault distance, see appendix 1 for the epicentral distance.

The Wenchuan earthquake is characterized by a very high number of triggered landslides, as it is possible to see by the different figures. The different lithologies show a decrease of the large size and an increase of the small size with the distance, with a settling around 30,000 m^2. An exception is the Quartz and Feldspathic Sandstone group that have the same size distribution at all distances (PZ1, Figure 44). Also the Quaternary deposits show a slight decrease, but in this case a possible relation could be found with the low number of landslides respect the others lithologies (Q, Figure 44). Regarding the slope gradient, the landslides occurred in prevalence in the 30°, 40°, and 50° classes. All the slope classes show a decrease of the landslide size with the distance, but also a decrease in the number of small landslides. Also the relief have a decrease of the landslides size with the distance, and an increase of the smaller size. As it is possible to see, the landslides occurred at a high relief classis (above 4,000 m) are close to the seismic source.

4.5 Iwate-Miyagi Nairiku Earthquake, 2008

The Iwate-Miyagi Nairiku Earthquake (Mw 6.9) occurred on 14th June 2008. The hypocenter was located at 39.122°N, 140.678°E and 10 km in depth by U.S. Geological Survey (http://earthquake.usgs.gov/). The reverse fault at the origin of the earthquake is unknown, Suzuki et al. (2010) defined the rupture process of the 2008 Iwate-Miyagi Nairiku earthquake by using strong-motion data recorded at 14 near-source stations based on the multi-time-window linear waveform inversion method. The earthquake affected an area greater than 600 km^2 along the lower flank of Mt. Kurikoma, one of the Quaternary volcanoes allocated along the range. Many tourism facilities located on mountainous terrain were destroyed. Moreover, casualties due to the earthquake amount 23 fatalities and missing and more than 450 injured (Yagi et al., 2009). These losses were mostly induced by landsliding throughout the region. The most tragic disaster resulted in the destruction of a hotel and seven victims was caused by the shallow debris slide that occurred just below Mt. Higashi-Kurikoma (Eastern Kurikoma Volcano) and the subsequent debris flow that flushed down along the Dozosawa River, the uppermost course of Sanhazama River. According to he ShakeMap model produced by the U.S. Geological Survey Earthquake Hazards Program (Wald et al, 2006), peak ground acceleration in the study area was in a range between 0.02 and 0.38 g (Figure 16). Considering the distribution of the PGA (g) values in relation to the epicentral distance, it is possible to observe a decrease of the PGA with the distance (Figure 48).

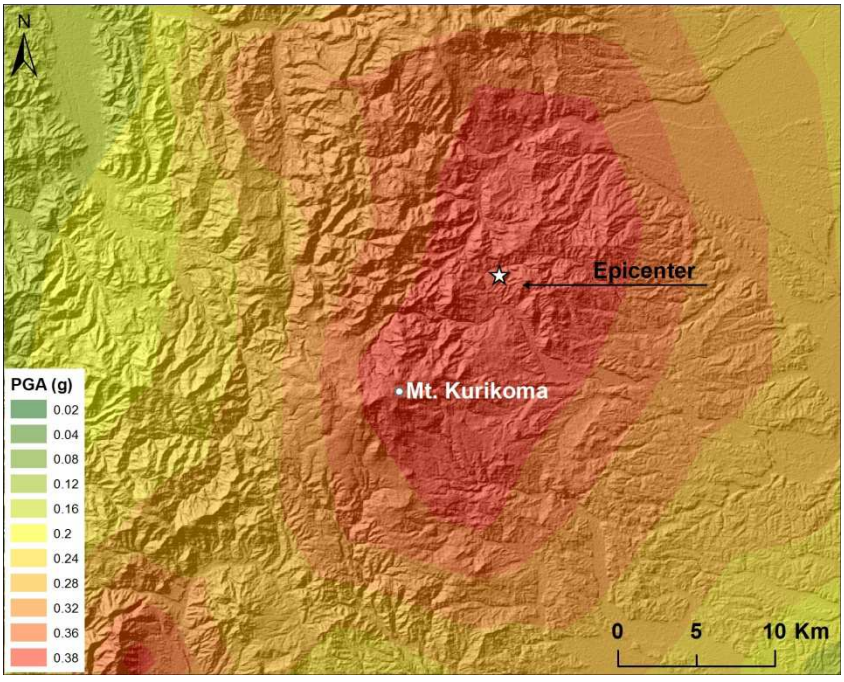

Figure 47. Peak ground acceleration (g) related to the 2008 Iwate-Miyagi Nairiku Earthquake. ShakeMap model produced by the U.S. Geological Survey Earthquake Hazards Program (Wald et al, 2006).

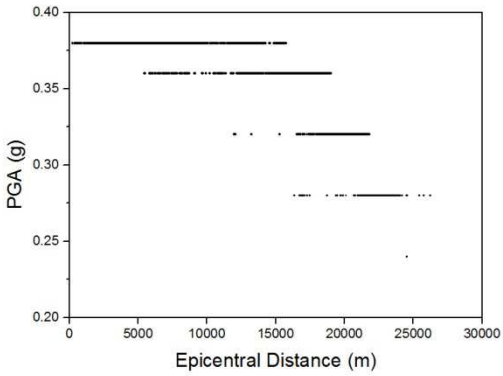

Figure 48. Graphs showing the distribution of the PGA (g) in relation to the epicentral distance (m).

4.5.1 Digital Elevation Model

For this case study two Digital Elevation Model were available: One with a cell size of 10X10 m and the ASTER GDEM with a cell size of 30X30 m (*See 1994 Northridge Earthquake for more details*). For the DEM with a 10 m resolution the slope gradient map (Figure 49) and the relief map (Figure 50) were generated (*See 1993 Papua New Guinea Earthquake for more details*). The choice of this DEM for the analysis is related to the higher resolution with respect to the ASTER GDEM.

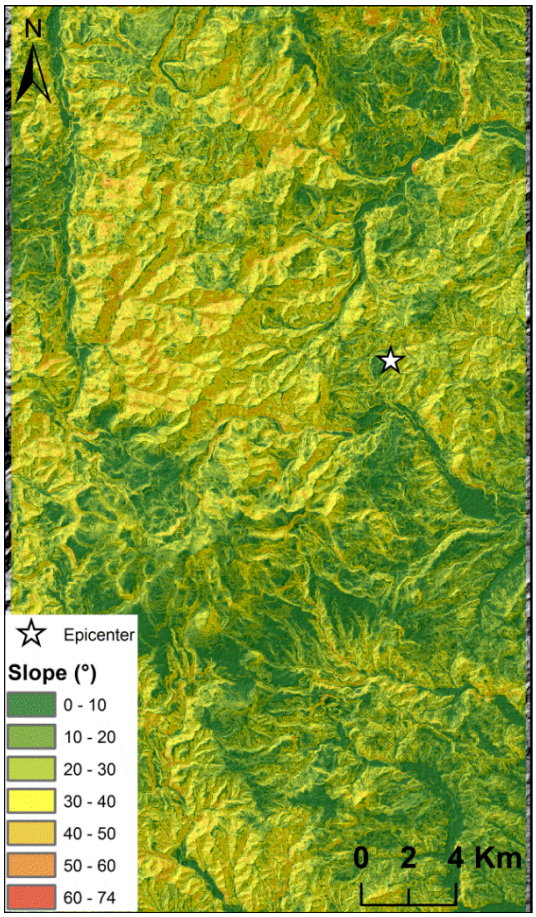

Figure 49. Slope gradient map of the area affected by the earthquake.

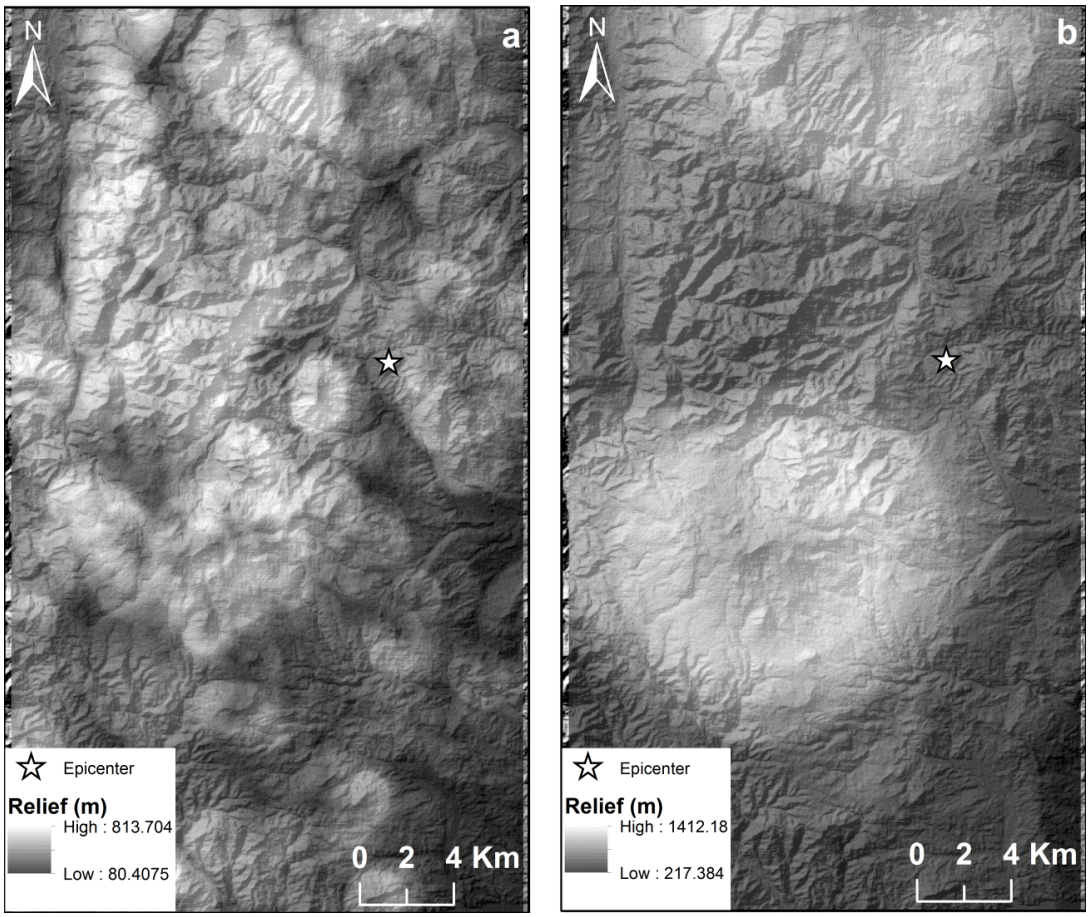

Figure 50. Relief map at 1Km (a) and at 5Km (b).

4.5.2 Geological setting

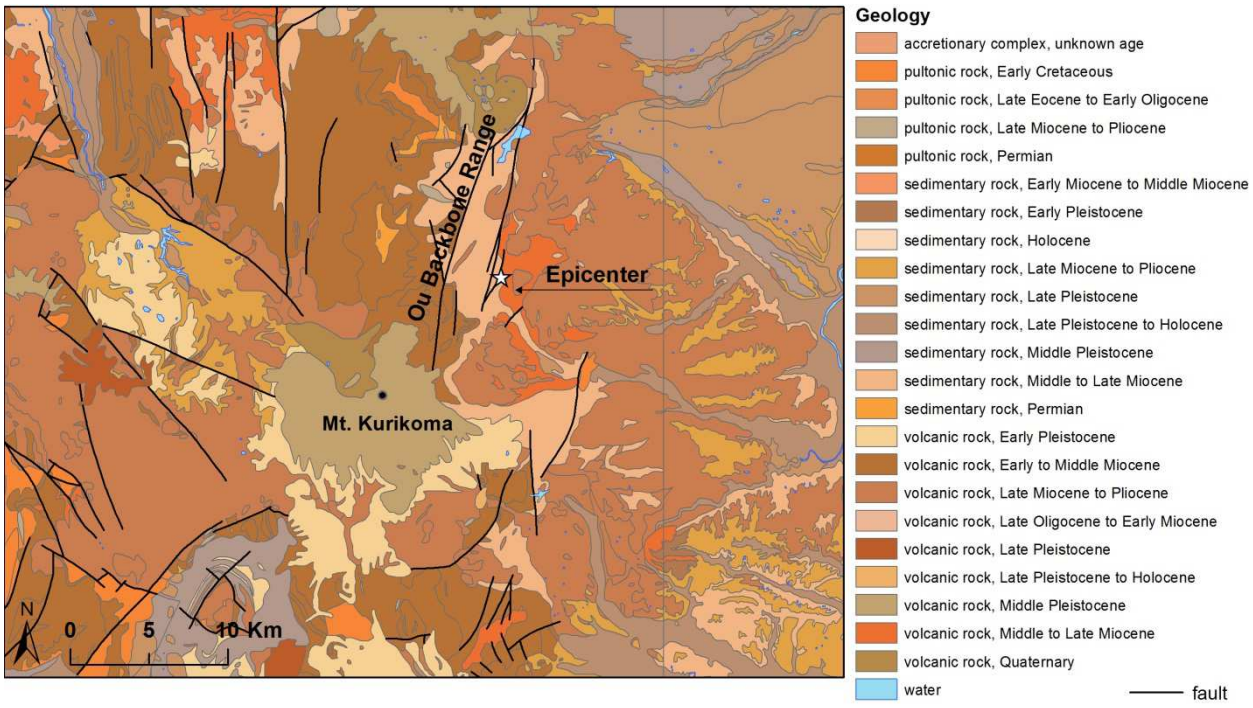

Figure 51. Digital geological map of Japan at a scale 1:200,000 realized by the Geological Survey of Japan (2012).

The earthquake occurred in a region of convergence between the Pacific Plate and the Okhotsk section of the North American Plate in northern Japan, where the Pacific plate is moving west-northwest with respect to North America at a rate of approximately 8.3 cm/yr (http://earthquake.usgs.gov/). The geological structure of Northeastern Japan is characterized by the Miocene back arc rift systems of NS–NNW trend that are filled with Cenozoic successions exceed 5 km in thickness. The study area is located in the eastern fringe of the rift. Normal faulting that formed the rift turned into reverse faulting around 10 Ma. Subsequently, the Ou Backbone Range started to uplift, and clusters of large calderas developed after 8 Ma (Sato 1994; Yoshida 2001). Southern part of the study area is located upon the old caldera filled with Pleistocene tuffaceous lacustrine sediments and Quaternary pyroclastics (Ohba et al. 2009) (Figure 51). Topography of the study area is featured by Quaternary volcanoes, Mt. Kurikoma (Figure 51), and the hilly terrain distributed in its eastern and southern outskirts that consist of pyroclastic flow or mud flow. Summit level of the hilly area ranges from 400 to 600 m, and it is incised by the streams which form deep gorges in the southern part of the study area. Interpretation of aerial photographs before the event clarifies that old dormant landslides (deep-seated slide type) are widely distributed in the hilly outskirt of Mt. Kurikoma volcano, disrupting the continuity of pyroclastic flow surfaces. The hypocenter of the earthquake indicates shallow thrusting motion in the upper (Okhotsk) plate, above the subducting Pacific plate, which lies at approximately 80 km depth at this location (http://earthquake.usgs.gov/). The earthquake occurred in a region of upper-plate contraction, probably within the complicated tectonics of the Ou Backbone Range, known to have hosted several large earthquakes in historic times (http://earthquake.usgs.gov/). The largest of these events occurred in 1896, approximately 70 km north of the June 13th event, and killed over 200 people in the local area (http://earthquake.usgs.gov/).

4.5.3 Analysis

The relation between the lithology, relief, peak ground acceleration, epicentral distance were analysed. The lithologies identified in the area were grouped in five groups, starting from the digital geological map of Japan at a scale 1:200,000 realized by the Geological Survey of Japan (2012). (see Table 5). The definition of the lithological classes were already available in the 1:200,000 Digital geological map of Japan (Figure 51).

Table 5. Simplified geology of Iwate–Miyagi Nairiku Earthquake.

#	Lithology	Group Name
1	Plutonic rock	Plutonic rock
2	Pyroclastic roc	Pyroclastic roc
3	Sedimentary rocks and deposits	Quaternary
4	Sandstone	Sandstone
5	Volcanic rock	Volcanic rock

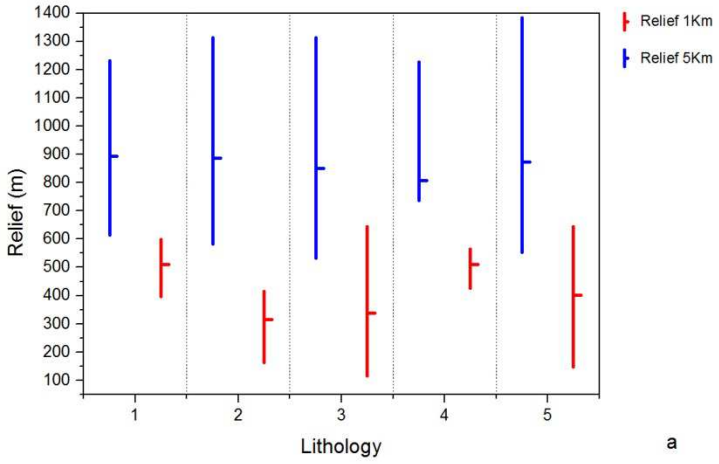

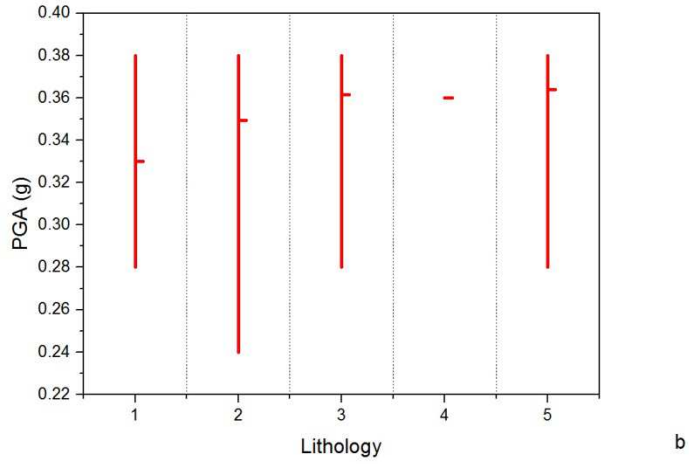

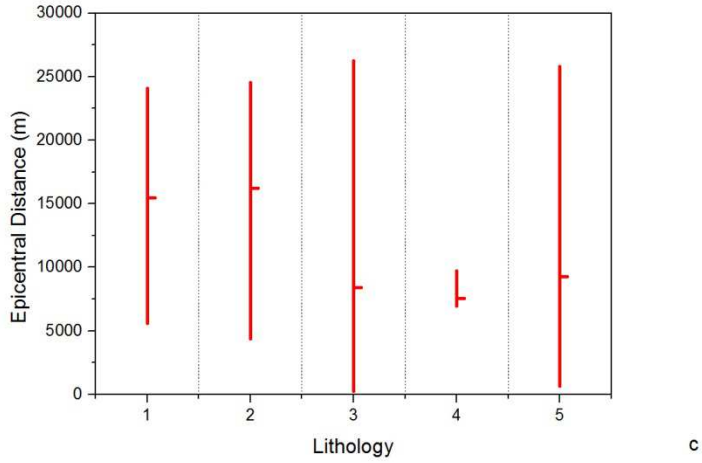

Figure 52. Graphs showing the relationships of the lithology with: a) Relief (m); b) PGA (g); c) Epicentral Distance (m).

While the relief identified with 5 km range shows the same values between the lithologies, there is a change between the different lithologies with 1 km range (Figure 52a). This indicate that for this earthquake the 5 km range is too large, and it does not allow an actual representation of this parameter in the affected area. There is a clear relationship between the value of PGA (g) experienced by each lithology and the relative position respect the epicenter of the Iwate-Miyagi Nairiku Earthquake, considering that the epicenter is located in the area with the high values of PGA. Quaternary deposits, Sandstone, and Volcanic rocks show high values than the others, because they are close, in mean, to the seismic source (Figure 52b and c).

4.5.4 Landslide Dataset

The inventory of the landslides triggered by the Iwate–Miyagi Nairiku Earthquake in 2008 was carried out by interpreting aerial photographs of 1:10,000 scale that were taken soon after the earthquake (Yagi et al., 2009; Figure 53). Older landslides were mapped by interpreting aerial photographs taken in 1977 of 1:20,000 scale (Yagi et al., 2009) in order to recognize these effectively triggered by 2008 Iwate–Miyagi Nairiku Earthquake.

A total number of 3502 landslides triggered by the earthquake were detected in the study area. Most of the landslides are densely distributed along the uppermost courses of the Ichihazama, Nihazama, and Iwai Rivers. The earthquake-induced landslides are classified (Yagi et al., 2009) into five types following the classification proposed by Varnes (1978): deep-seated slide, debris slide, shallow debris slide, secondary shallow debris slide, and debris flow.

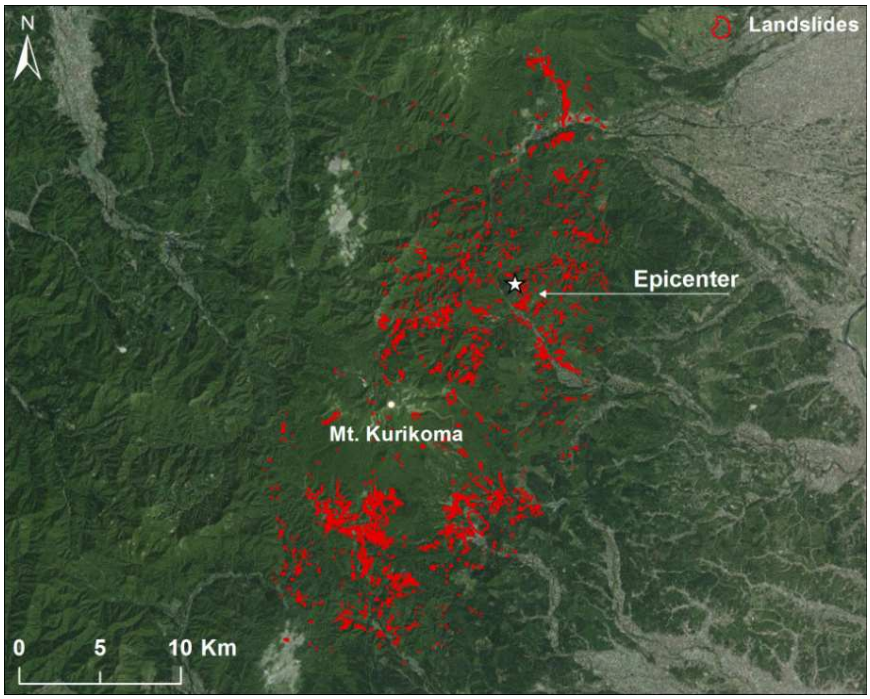

Figure 53. Landslides dataset related to the 2008 Iwate-Miyagi Nairiku Earthquake (Yagi et al., 2009).

However, these classes were partially modified by the authors. Deep-seated slide includes rotational and translational slides of Varnes (1978). Definition of debris slide is same as that of Varnes (1978). Shallow debris slide is a type in which thin surface materials slide down and are scattered towards the lower slope. Secondary shallow debris slide is detected as a subsequent partial movement from the toe part of a deep-seated slide body. The deep-seated slide in scale of a few hectares are distributed along the gorges in the eastern and southern flank of Mt. Kurikoma. They are rotational slides of "cap rock" type that occur along the slopes where hard-competent volcanic rocks or welded tuff of the Quaternary age overlies soft incompetent sediments of the Pliocene age. Large slides were presumably caused by such a geological setting. Some of them are reactivated landslides, but more than half are primary ones. There is a giant landside of 70 million cubic meters in volume called Aratozawa landslide (Figure 54).

A deep and long depression develops parallel to the straight main scarp due to separation, and original surface of the slided mass remained in spite of long travel. It implies that the slide surface is flat and gentle along the geological contact in the Quaternary sediments. Consequently, it is classified as a translational slide. It is not a primary landslide but a reactivated one of dormant landslides, forming a secondary main scarp onto a primary moving body. Old deep-seated slides which seem to be dormant because of their topographic features are also detected. However, the number of the reactivated slides of large scale is very rare in the eastern part of Mt. Kurikoma except the case just adjacent to the Iwai River.

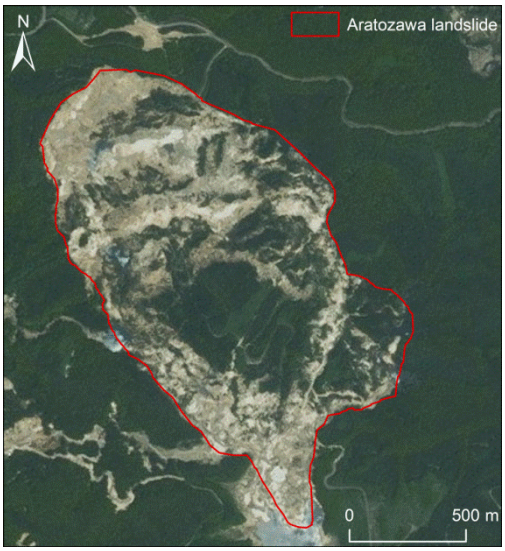

Figure 54. Aratozawa Landslide.

There are a few cases along the Sanahazama and Nihazama Rivers where toe parts are incised deeply. Most of the landslides induced by the earthquake are shallow debris slides and subsequent debris flows. They are intensively distributed along steep or almost vertical walls along river gorges of 100–300 m deep. They are located in the uppermost courses of Ichihazama (Nuruyu area) and Iwai Rivers that deeply incise the Mt. Kurikoma, consisting of welded pyroclastic flow deposits and lacustine sediments of the Pleistocene age. The earthquake caused a catastrophic change of landscape in this area. Naked rock walls of brown color and rugged surface of debris are densely distributed along the valleys. Crowns of those shallow debris slides are located just below breaks of slopes, which fringes depositional surface of pyroclastics. However, the scale of shallow debris slides in the northern side of Iwai River just above the epicenter, where Tertiary pyroclastic flow deposits underlie and denudated hilly terrain develops, are smaller than that along the Ichihazama, Nihazama, and Sanhazama Rivers, in the southern hilly area. This implies that causative factors of shallow debris slides due to the earthquake are attributed to gradient of slopes and depth of gorge. Debris slides intensively occurred along steep walls consisting of welded ignimbrites where deep gorges incise the southern foot slopes of Mt. Kurikoma. The volume of debris slide is much larger than that of shallow debris slides. Debris slides densely occur along Hiyashisawa River, the uppermost course of Sanhazama River in Koei area. Most of the flow-type landslides are debris flow. Many traces of debris flow are recognized along the river floors in Koei and Nuruyu areas in the southern lower flank of Mt. Kurikoma Volcano, although they were transformed from debris slides and shallow debris slides.

The spatial distribution of the landslides area was analysed in relation to the different lithologies present in the area (Figure 55), the relief reclassified (threshold of 500 m) (Figure 56), the mean slope at which each landslide occurred (Figure 57), for the epicentral distance.

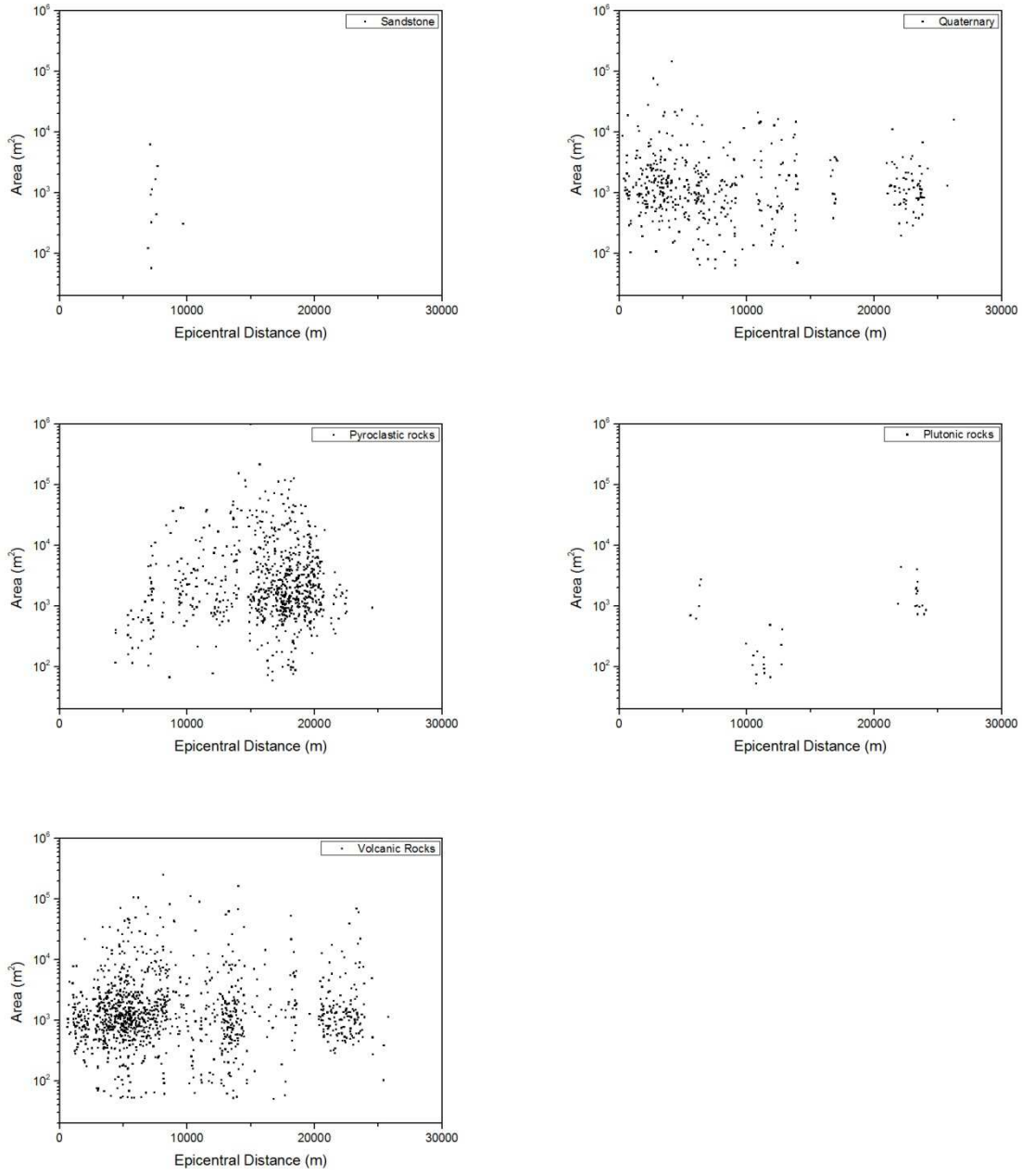

Figure 55. Landslide size as function of the epicentral distance, for each lithology.

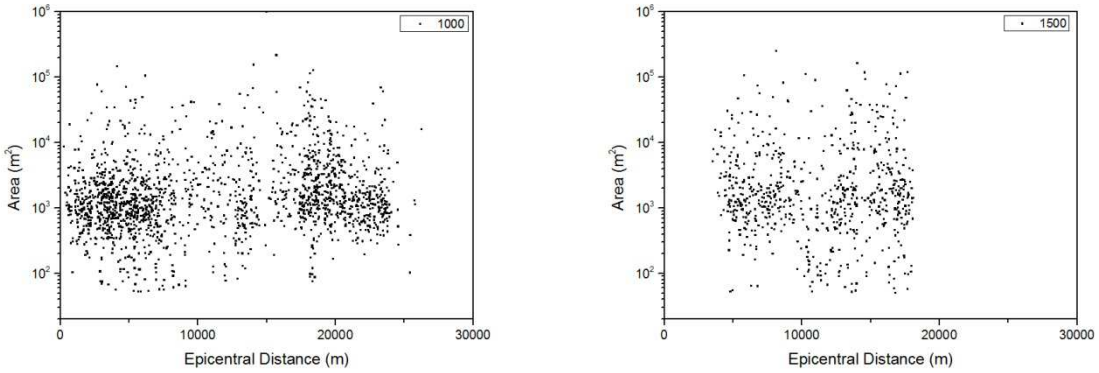

Figure 56. Landslide size as function of the epicentral distance, for each relief class.

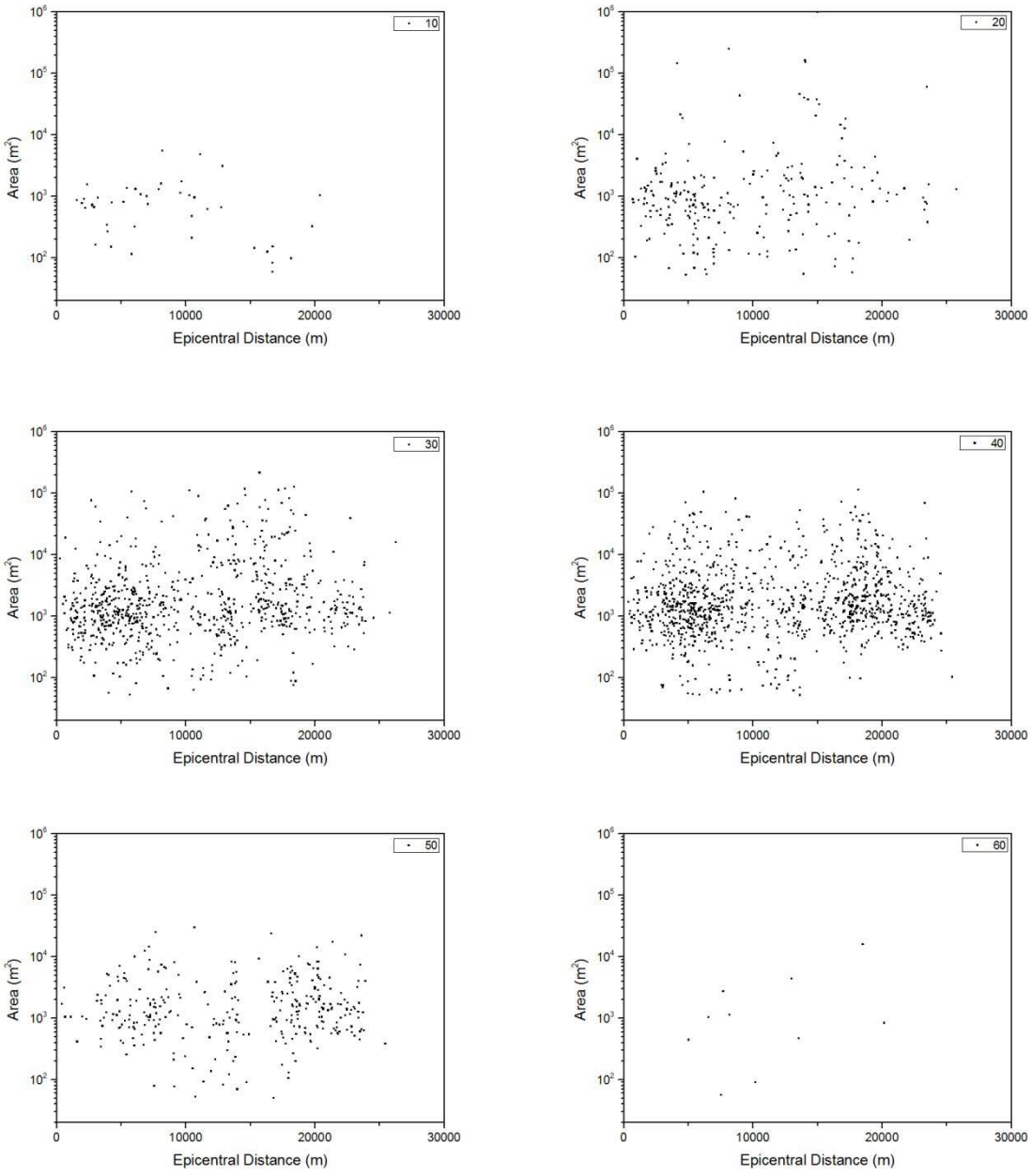

Figure 57. Landslide size as function of the epicentral distance, for each slope class.

Landslides in Quaternary deposits show a decrease of the size with the increase of the epicentral distance (Figure 55). Instead the landslides in Plutonic rocks have larger size far from the seismic source. In the Volcanic rocks the landslide size seems to increase at the beginning, but after 10 Km, it decrease with the distance. In these lithologies the small landslides are present at all distances from the epicenter. The relief in the affected area is higher than 500 m, but lower than 1,500 m. The landslide size distribution seems to not be affected by the relief. Most of the landslides occurred in a slope gradient between the 20° and 40° classes. The landslide size distribution is not affected by the slope gradient. The same size is present in the different slope gradient classes.

4.6 Tohoku Earthquake, 2011

The magnitude 9.0 Tohoku earthquake on March 11, 2011, which occurred near the northeast coast of Honshu, Japan, resulted from thrust faulting on or near the subduction zone plate boundary between the Pacific and North America plates. At the latitude of this earthquake, the Pacific plate moves approximately westwards with respect to the North America plate at a rate of 83 mm/yr, and begins its westward descent beneath Japan at the Japan Trench. The location, depth, and focal mechanism of the March 11 earthquake are consistent with the event having occurred on the subduction zone plate boundary (http://earthquake.usgs.gov/). Modeling of the rupture of this earthquake indicates that the fault moved upwards of 30-40 m, and slipped over an area approximately 300 km long (along-strike) by 150 km wide (in the down-dip direction). The Japan Trench subduction zone has hosted nine events of magnitude 7 or greater since 1973 (http://earthquake.usgs.gov/). At least 15,703 people were killed, 4,647 missing, 5,314 injured, 130,927 displaced and at least 332,395 buildings, 2,126 roads, 56 bridges and 26 railways were destroyed or damaged by the earthquake and tsunami along the entire east coast of Honshu from Chiba to Aomori. The total economic loss in Japan was estimated at 309 billion US dollars. Horizontal displacement and subsidence was also observed. Landslides occurred in Miyagi prefecture. Liquefaction observed at Chiba, Odaiba, Tokyo and Urayasu. The ShakeMap realized by the USGS show a peak ground acceleration (PGA) ranging between 0.02 g and 2.02 g (Figure 58).

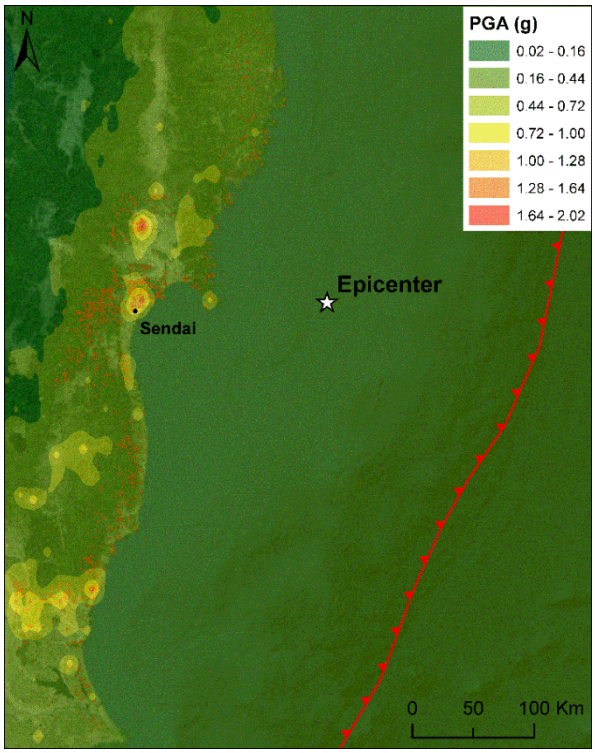

Figure 58. Peak Ground Acceleration (g) of the 2011 Tohoku Earthquake. ShakeMap model produced by the U.S. Geological Survey Earthquake Hazards Program (Wald et al, 2006).

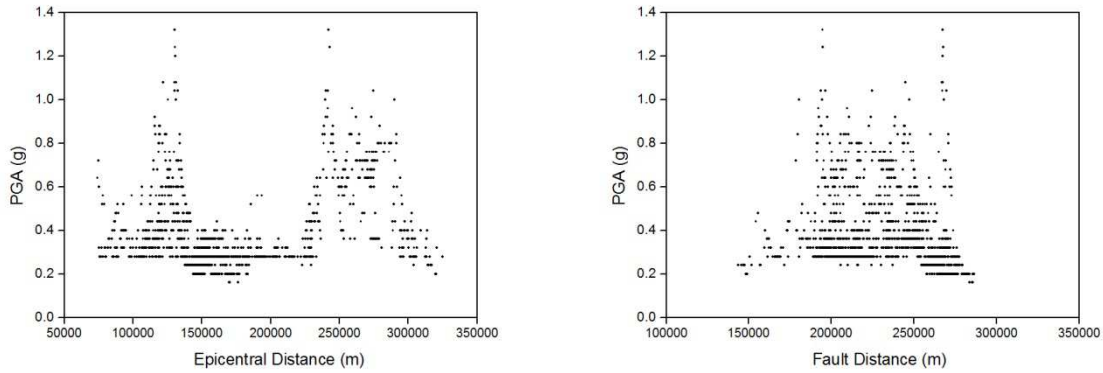

Figure 59. Graphs showing the distribution of the PGA (g) in relation to the epicentral and the fault distance (m).

The relation between the epicentral and fault distances with the PGA (g) is not clear (Figure 59), this is related to the anomalous concentration of the peak ground acceleration in some area, also flat.

4.6.1 Digital Elevation Model

The ASTER GDEM is used as a GeoTIFF format with wgs84 geographic lat/long coordinates and a 1 arc-second (30 m) grid of elevation postings. Two maps were realized from this DEM: the slope gradient map (Figure 60) and the relief map (Figure 61). (*See 1993 Papua New Guinea and 1994 Northridge Earthquakes for more details*).

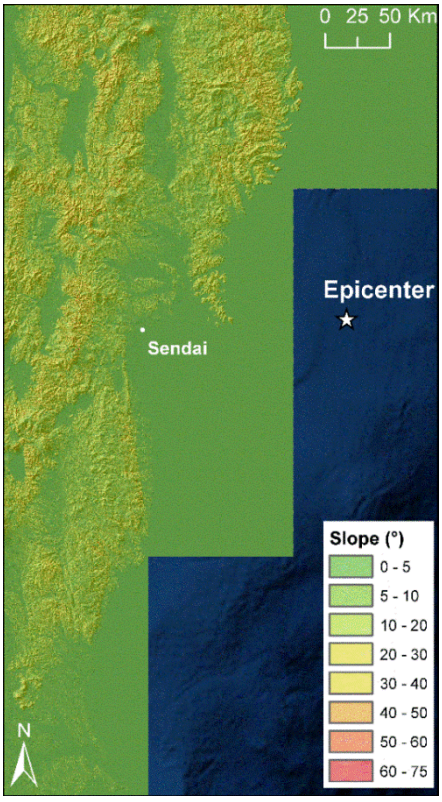

Figure 60. Slope Map of the area affected by the Tohoku Earthquake.

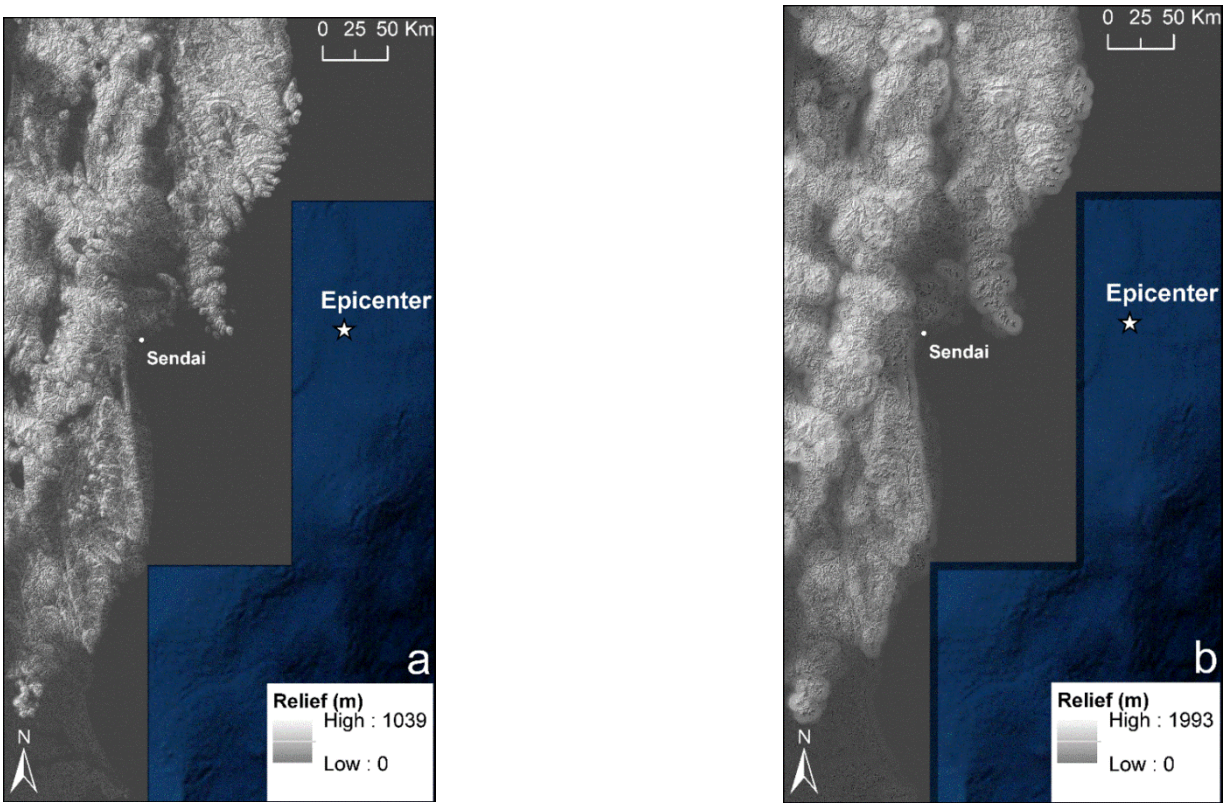

Figure 61. Relief at 1Km (a) and at 5Km (b) for the area affected by the Tohoku Earthquake.

4.6.2 Geological setting

Honshu is located within a highly active subduction region characterized by active volcanism, seismicity, orogeny, and mass wasting (Figure 62). The crust of Honshu was initially generated by Paleozoic to Mesozoic accretionary processes, and later by voluminous intrusion of granitic rocks during the late Cretaceous. The subsequent rifting of Honshu from the Eurasian continent from 25 to 15 Ma was accompanied by emplacement of volcanic materials over portions of the island (Sato et al., 2002). Honshu includes several prominent north–south oriented geologic features that are common in island-arc settings (Yoshii, 1979), such as an active volcanic front located across the middle/eastern portion of the island, a foreland backarc zones along the Pacific Ocean and the Sea of Japan, respectively, and a large accretionary complexes and zones of regional metamorphic rocks (Hashimoto, 1991). Additionally, recent (i.e., Quaternary) erosion has deposited unconsolidated materials along Honshu's coastal margin. A consequence of this complex geologic history is that a wide range of landforms is found across the forearc (eastern) portion of Honshu (Prima et al., 2006). Major landforms include the Kitakami Mountains, Sendai plain, the Ou Backbone Range, the Abukuma Mountains, and Kanto plain (Figure 62).

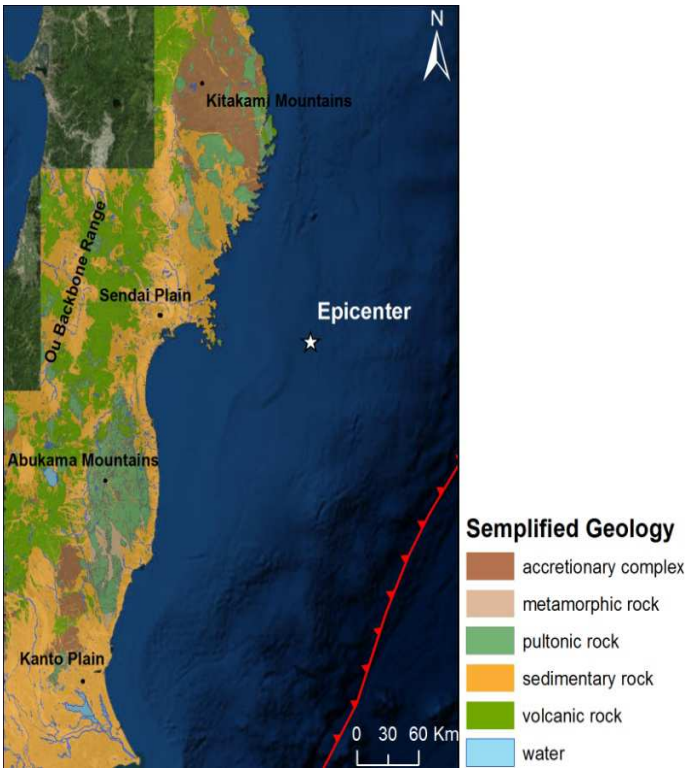

Figure 62. Simplified Digital geological map of Japan at a scale 1:200,000 realized by the Geological Survey of Japan (2012). Red line indicate the seduction zone.

Additionally, a narrow (~10 km) coastal margin is located along the eastern edge of the island. The northern segment of the Kitakami Mountains largely comprises Mesozoic sedimentary rocks that are part of a large accretionary complex (Mikoshiba et al., 2004). The southern segment consists of shallow-marine Silurian to Cretaceous sedimentary rocks, along with Paleozoic ultramafic rocks, and a smaller amount of high-pressure/low-temperature type metamorphic rocks (Ujiie-Mikoshiba et al., 2006). Additionally, the Kitakami Mountains have been intruded by several large Cretaceous plutons, which occupy about a quarter of the area (Mikoshiba et al., 2004). The Ou Backbone Range defines the volcanic front of Honshu (Ujiie-Mikoshiba et al., 2006) with many Quaternary stratovolcanoes. Since the late Miocene, voluminous magmatic intrusions have been uplifting the Ou Backbone Range along its adjoining Uwandaira (east) and Senya (west) reverse faults (Sato et al., 2002). In consequence, the base (ridge) elevation of the volcanoes is quite high (~750 to ~1000 m) and many volcanic peaks exceed 2000 m. Within the study area, landforms of the Ou Backbone Range classify as low mountains near the volcanoes and as smooth to rough hills along the central ridge (Dragut and Eisank, 2012)In the southern portion of the study area lies the Abukuma Mountains, an uplifted peneplain. The bedrock of the Abukuma Mountains primarily consists of Cretaceous plutonic rocks (granite) and also includes large regions of Cretaceous high-pressure/low-pressure regional metamorphic rocks (gneiss; Miyashiro, 1958; Faure et al., 1986).

The study area also includes the Sendai and Kanto plains, which comprise unconsolidated Quaternary sediments.

4.6.3 Analysis

The relationships of the lithology with the relief, the PGA (g), the epicentral distance and the fault distance have been analyzed (Figure 63). The lithologies identified in the area were grouped in eleven classes, starting from the digital geological map of Japan at a scale 1:200,000 realized by the Geological Survey of Japan (2012) (see Table 6). Some sedimentary rocks have been classified on the basis of the age (tertiary or quaternary).

The values of the relief have a high variation in the range between the two adopted radius. The local variation of the PGA with the distances from the epicenter and the fault rupture has not clear, due also to the strange distribution of the values as cited above. For example the Mudstone group have low values of the PGA, despite it is one of the lithologies closer to the seismic source, in particular to the epicenter. This strange trend could be related to the low number of landslides occurred in such lithologies. Considering the values of the PGA there is a relationship more pronounced with the fault rupture respect to the epicenter.

Table 6. Simplified geology of Tohoku Earthquake (2011).

#	Lithology	Group Name
1	Conglomerate	Conglomerate
2	Limestone	Limestone
3	Metamorphic rock	Metamorphic rock
4	Mudstone	Mudstone
5	Plutonic rock	Plutonic rock
6	Pyroclastic rock	Pyroclastic rock
7	Sedimentary rocks and deposits	Quaternary
8	Sandstone	Sandstone
9	Sedimentary rocks	Tertiary
10	Turbidite	Turbidite
11	Volcanic rock	Volcanic rock

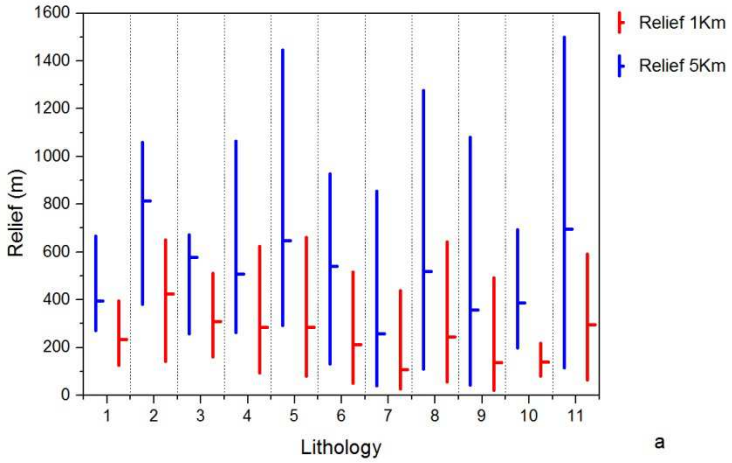
Relief 1Km
Relief 5Km
Relief (m)
Lithology
1600
1400
1200
1000
800
600
400
200
0
1
2
3
4
5
6
7
8
9
10
11

a

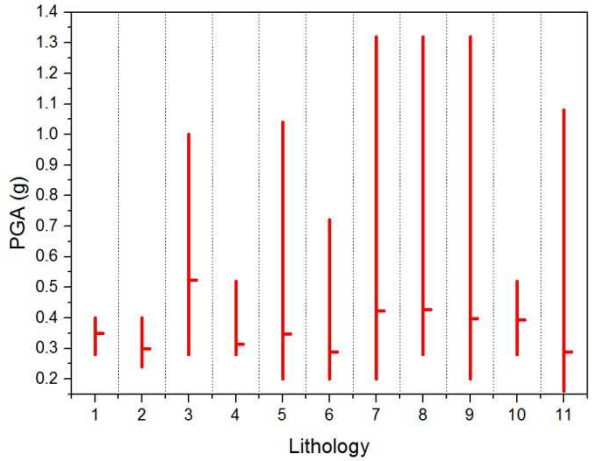
PGA (g)
Lithology
1.4
1.3
1.2
1.1
1.0
0.9
0.8
0.7
0.6
0.5
0.4
0.3
0.2
1
2
3
4
5
6
7
8
9
10
11

b

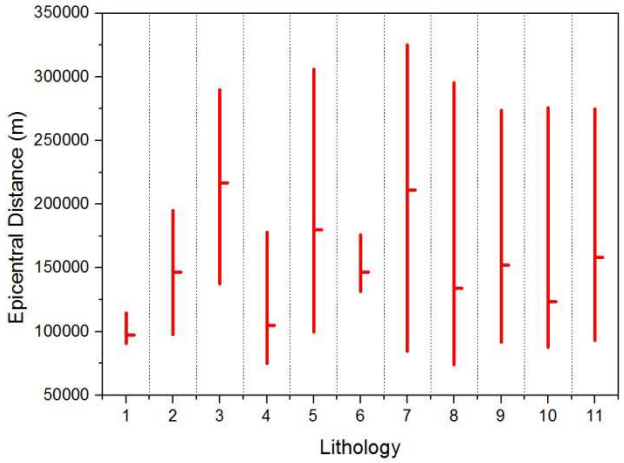
Epicentral Distance (m)
Lithology
350000
300000
250000
200000
150000
100000
50000
1
2
3
4
5
6
7
8
9
10
11

c

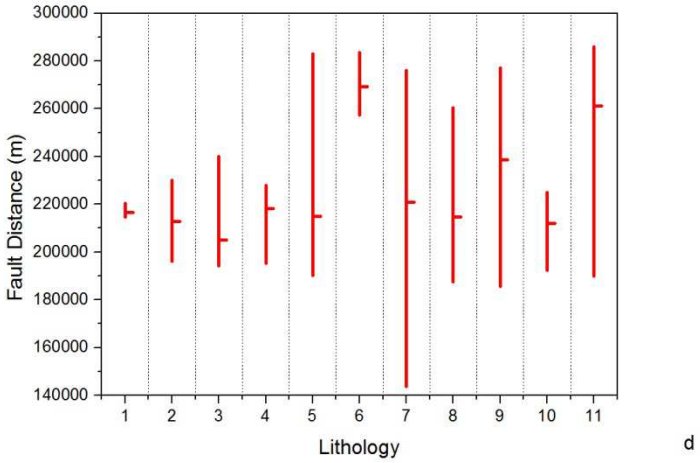

Figure 63. Graphs showing the relationships of the lithology with: a) Relief (m); b) PGA (g); c) Epicentral Distance (m); d) Fault Distance (m).

4.6.4 Landslide Dataset

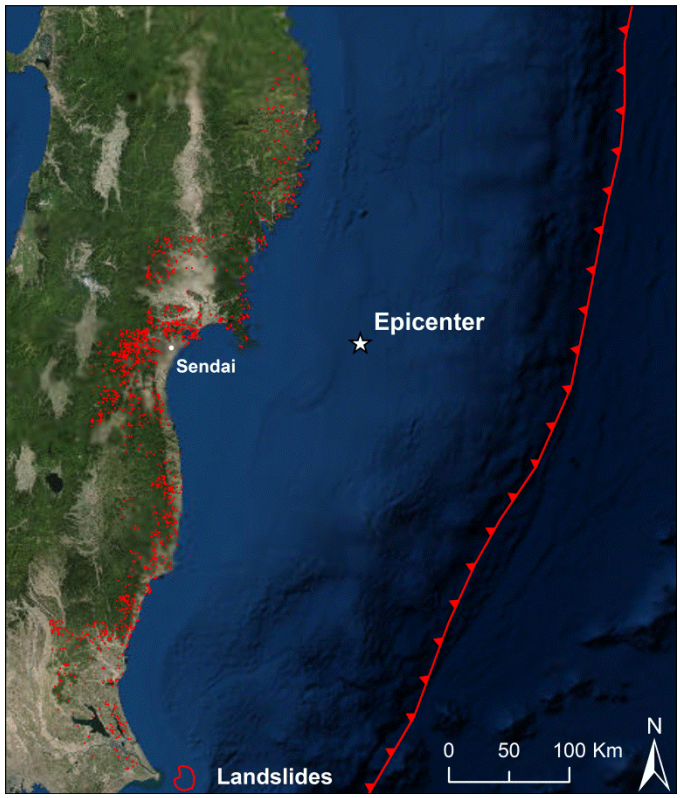

Figure 64. Landslides dataset related to the Tohoku Earthquake; Wartman et al. (2013)

The landslide database was developed based on field mapping conducted during the post earthquake reconnaissance, and additionally from examination of satellite imagery (Wartman et al., 2013). The study area was generally well vegetated, which often allowed landslides to be first identified based on changes in the appearance of vegetation or other land surface features. Landslide features in the

low-lying coastal areas severely impacted by the tsunami were not considered and are not represented in the database. Wartman et al. (2013) verified the seismogenic origin of landslides by comparing the postearthquake imagery with scenes from Google Earth's historical archives. They also found that aftershocks did not significantly contribute to landsliding and thus they believe that nearly all of the landslides in the database were triggered by the mainshock. Once identified, landslides were assigned a reference number, delineated, measured, and classified based on the landslide categorizations defined by Keefer (1999): 1) Disrupted Landslide, that are landslide characterized by a rapid movement by free fall, sliding, and/or rolling of debris. The debris masses were typically dry and brittle. In this landslides the deposition occurred along or at the base of slope, and involving long runout displacement. The landslides have a high to very high levels of internal disruption. 2) Coherent Landslide, with a slow to moderate movement by slumping, translation, and/or rotational sliding of mass. Debris masses often are partially to fully saturated. 3) Lateral Spreads with a movement typically rapid, by translational displacement of a viscous mass, or of a stiffened crust of dry soil moving over a viscous surface. Movement can also involve flow.

Delineation of the landslides was aided by the terrain feature of Google Earth, which allowed visualization of the landscape to be enhanced by draping imagery over a Shuttle Radar Topography Mission (SRTM) derived 30 m digital elevation model (DEM).

The accuracy of the landslide measurement made by Wartman et al. (2013), both location and size, is a function of several factors, which vary across the study area including nadir (angle of satellite view), cloud cover, image resolution, and size of feature, among others. The authors are confident that the inventory represents a comprehensive cataloging of disrupted and coherent landslides having features larger than 1-4 m. The morphological features of lateral spreads were subtler, and additionally, permanent deformation of these landslides was often less than the 1–4 m identification threshold. During this thesis, starting from this inventory, a new one was realized through the elimination of some landslides with strange form or suspected characteristics.

Analyzing the relationships between the distribution of the landslides area, it is possible to observe how the high number of landslides are present in unconsolidated sediments of tertiary age. In this lithology, in the volcanic rocks and in the quaternary deposits, there are the landslides with the larger area ($>10^5$ m^2). The relief in the area is not so high and the landslides occurred prevalently under 500 m of relief (in according also to the type of lithologies in which they occurred). Also, the slope gradient at which, in mean, the landslides are triggered is very low, but it is also related to the kind of lithology, types of landslides, the morphometric characteristic of the area and, above all, to the magnitude of the earthquake (Mw 9.0).

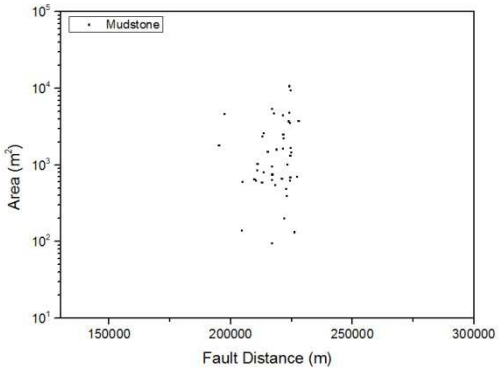
Mudstone
Area (m²)
Fault Distance (m)
150000
200000
250000
300000

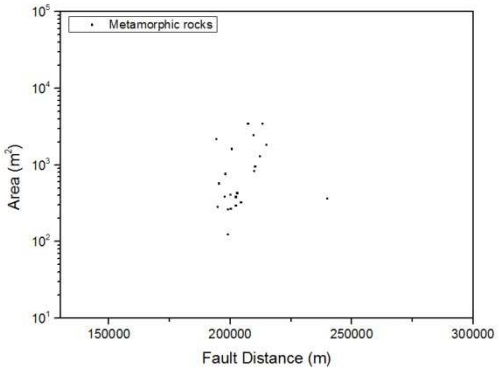
Metamorphic rocks
Area (m²)
Fault Distance (m)
150000
200000
250000
300000

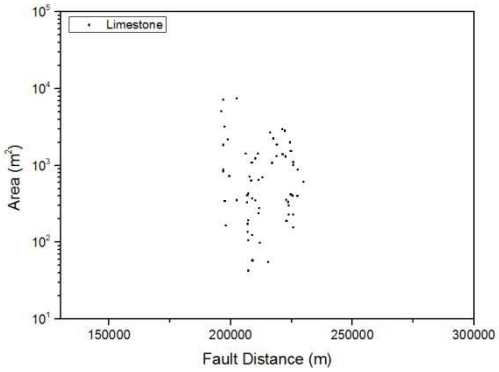
Limestone
Area (m²)
Fault Distance (m)
150000
200000
250000
300000

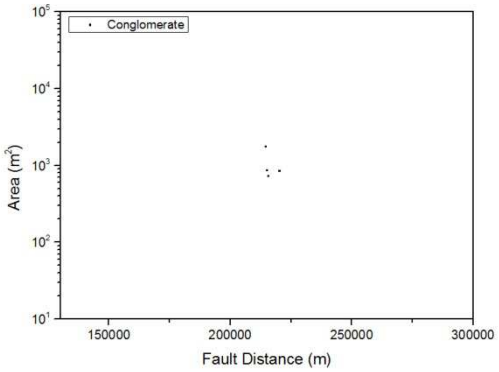
Conglomerate
Area (m²)
Fault Distance (m)
150000
200000
250000
300000

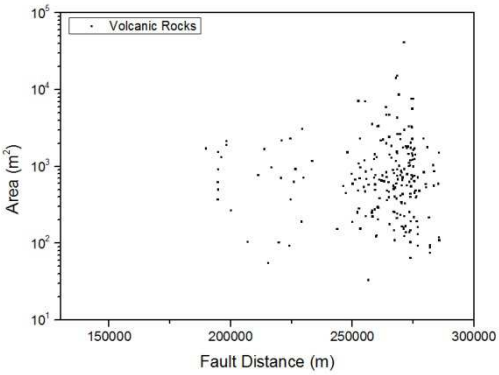
Volcanic Rocks
Area (m²)
Fault Distance (m)
150000
200000
250000
300000

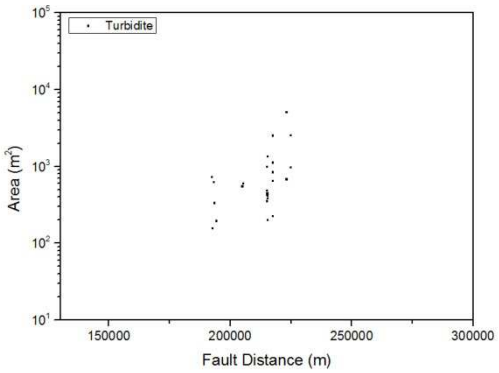
Turbidite
Area (m²)
Fault Distance (m)
150000
200000
250000
300000

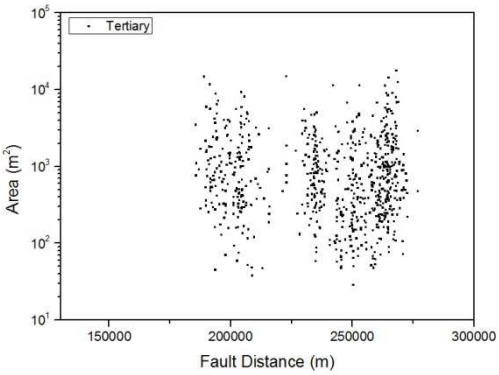
Tertiary
Area (m²)
Fault Distance (m)
150000
200000
250000
300000

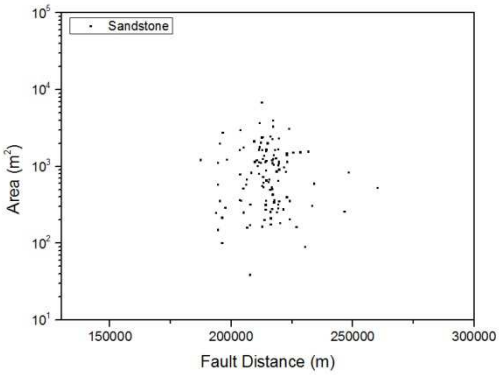
Sandstone
Area (m²)
Fault Distance (m)
150000
200000
250000
300000

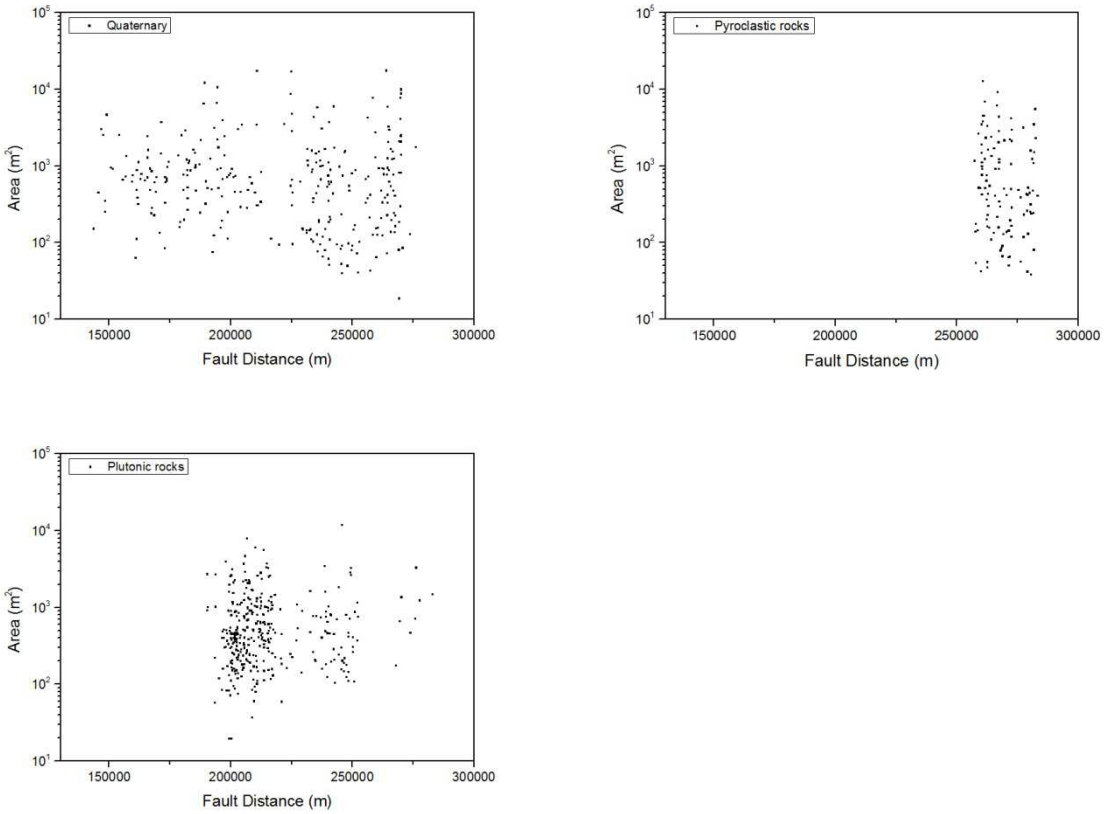

Figure 65. Landslides area distribution for each lithology, for the fault distance, see appendix 1 for the epicentral distance.

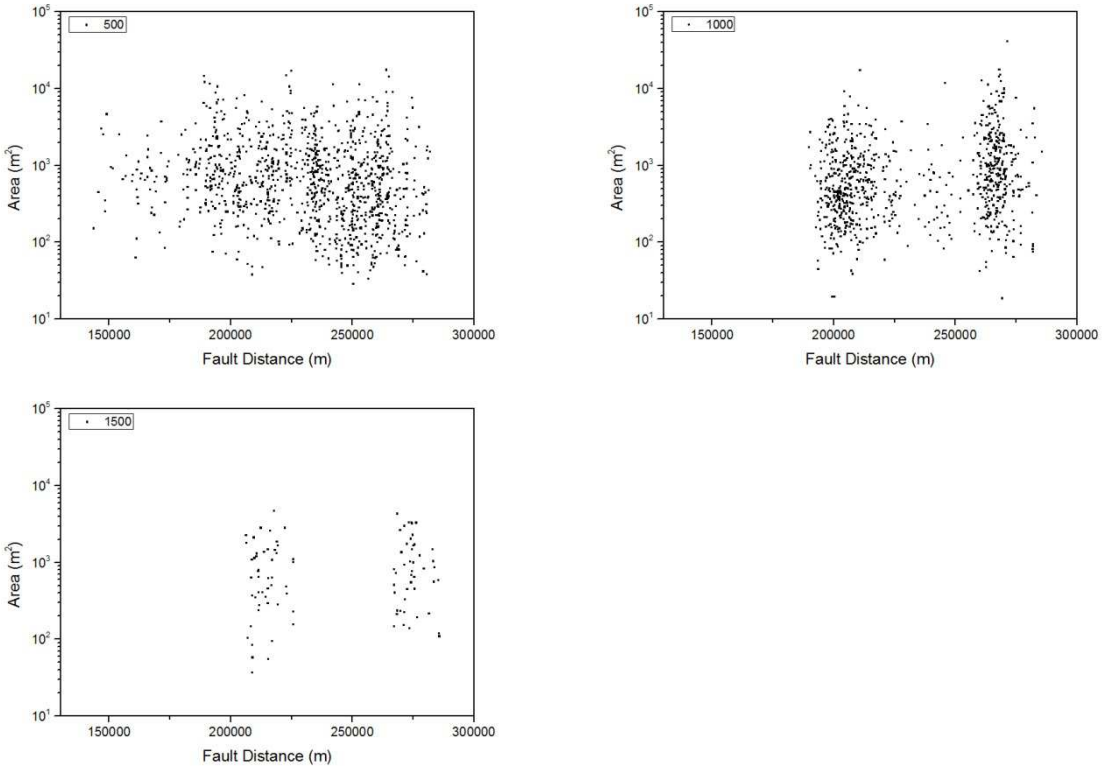

Figure 66. Landslides area distribution for each threshold of relief, for the fault distance, see appendix 1 for the epicentral distance.

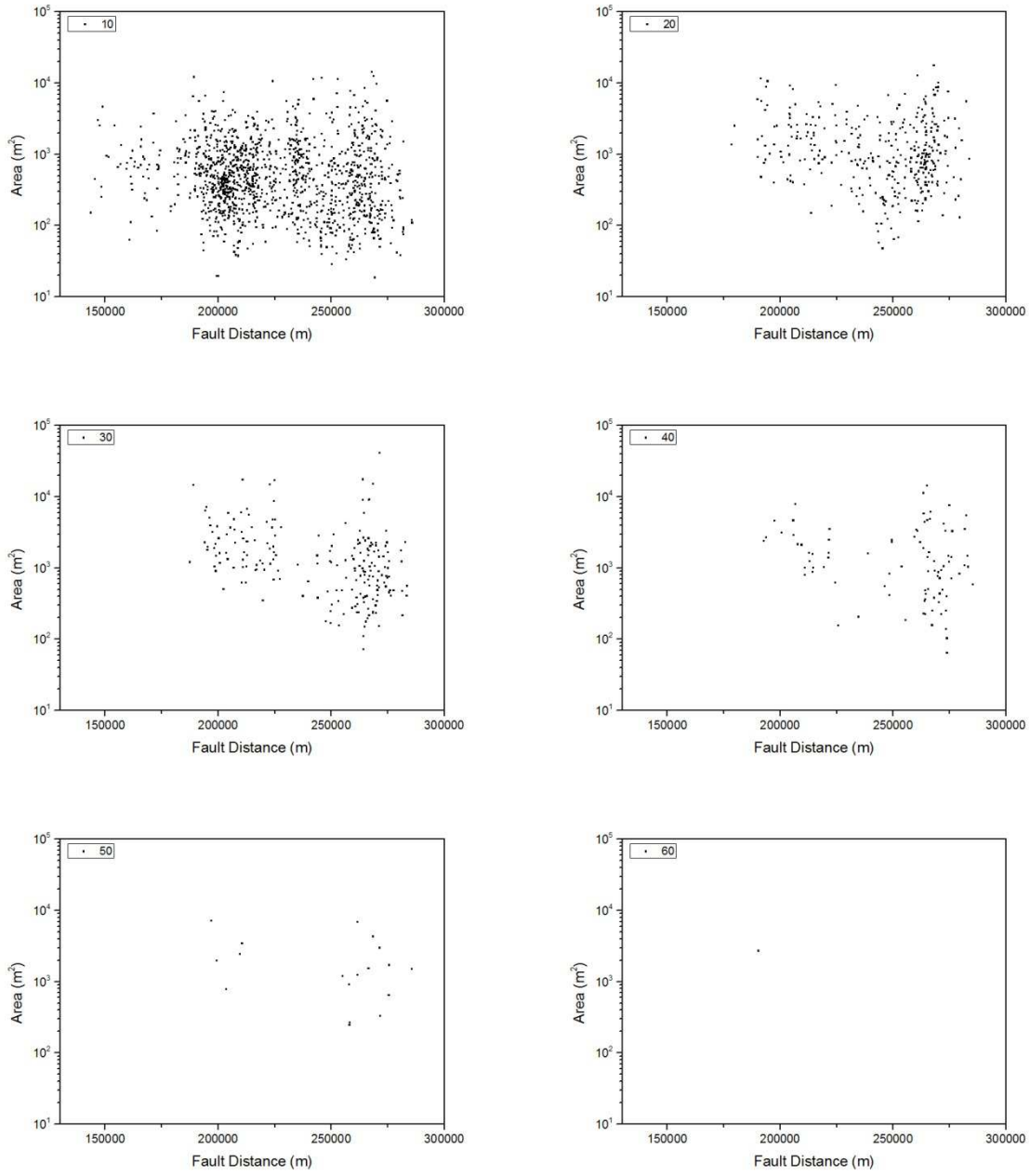

Figure 67. Landslides area distribution for each threshold of slope, for the fault distance, see appendix 1 for the epicentral distance.

The number of landslides for these earthquake compared t the event magnitude is very low, but it is located at a very high distance from the coast. Regardering the distribution of the landslides in each lithology it is possible to see how for the Volcanic rocks, Tertiary and Quaternary deposits the landslides size seem to increase with the distance from the fault rupture. For others lithology groups (e.g. Conglomerate) a reliable analysis it not possible, due to the low number of landslides occurred inside these lithologies. Reordering the relief, a specific trend of the landslide size it is not observed. Instead if the slope gradient is considered, it is possible to see how with the increase of

the distance from the seismic source there is an increase of the small landslides. In any case most of the landslides for the Tohoku earthquake occurred at low slope gradient.

4.7 Maximum distance for earthquake-induced landslide as function of earthquake magnitude

The six earthquakes presented, were plotted with the literature curves of Keefer (1984) (Figure 68 and Figure 69). The data, both for the epicentral distance and the fault distance, are under the upper bound defined by Keefer (1984). Only Tohoku earthquakes (2011) seems to be higher than expected, but the maximum distance is related, in this case, to a disrupted landslide, as consequence, it is under the related upper bound. The data are plotted as single point. Each point represent the maximum distance at which landslides (of any type) are recognized for each earthquake, because in some dataset the distinction between the different type of landslides is not available. In any case, the six analysed earthquake seem to confirm the literature maximum distance, from epicenter or fault rupture, at which an earthquake can induce landslides. A Summary of the earthquakes information with the relative fault rupture name is reported in Table 7.

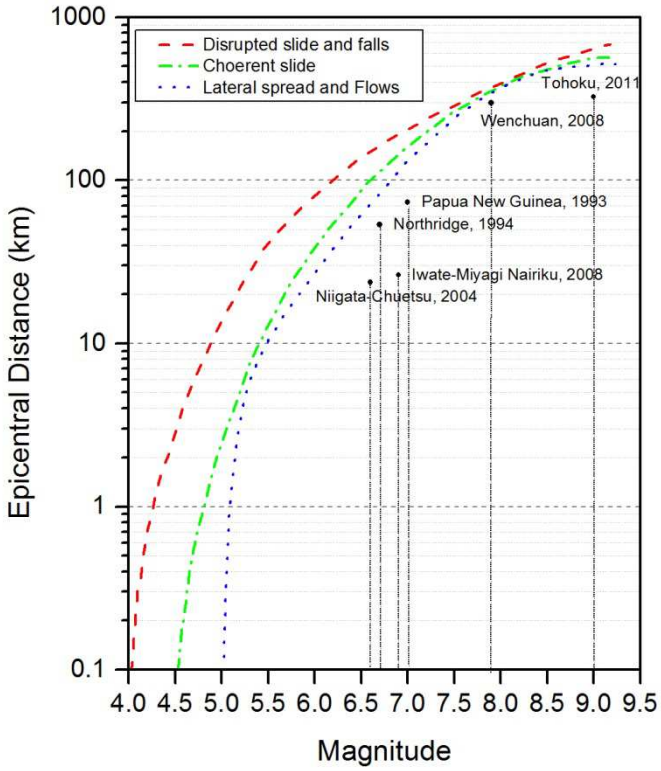

Figure 68. Maximum distance from the epicenter for the available inventories. The lines represent the upper bound of distance for the three types of landslides considered by Keefer (1984).

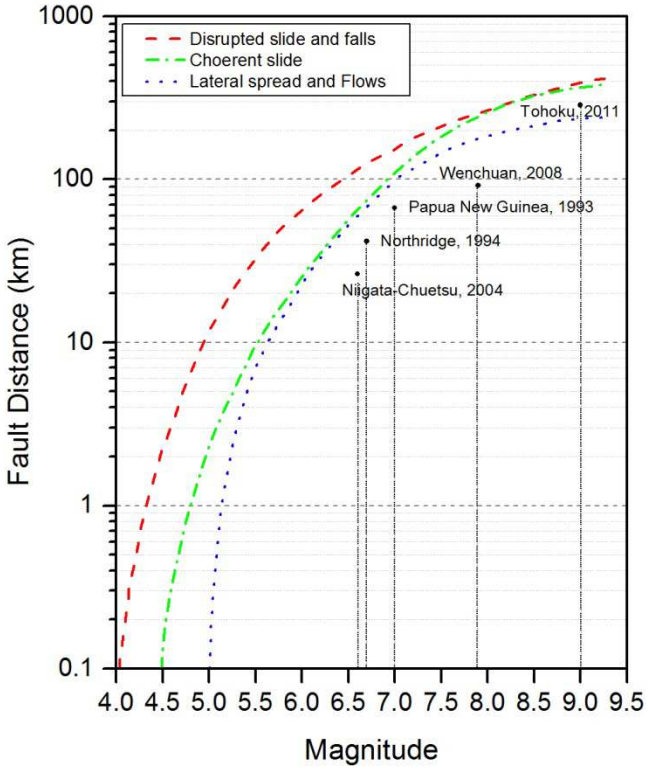

Figure 69. Maximum distance from the fault rupture for the available inventories. The lines represent the upper bound of distance for the three types of landslides considered by Keefer (1984).

Table 7. Summary of the major information for the analysed earthquakes.

	Date	Mw	Fault Rupture	Depth (km)	# landslides
Papua New Guinea	13/10/1993	7.0	Ramu - Markham Fault	25	4789
Northridge	17/01/1994	6.7	Oak Ridge Fault	18	11111
Niigata-Chuetsu	23/10/2004	6.6	Muikamachi and Obiro Fault	16	10525
Wenchuan	12/05/2008	7.9	Beichuan and Pengguan Fault	19	197481
Iwate-Miyagi Nairiku	13/06/2008	6.9	- no available	10	3502
Tohoku	11/03/2011	9.0	Subduction zone	30	1978

4.8 Northern Chile

The northern Chile area is subject to a high seismicity associated to earthquakes of different type: interplate (superficial and intermediate depth), subduction zone earthquakes (Figure 70). Shallow thrust earthquakes have been historically the most important with magnitude above 8 and return periods around 80-130 years. Megathrust earthquakes have a longer return period. The study area (Figure 70) is located in the Northern Chile forearc. It extends between Iquique (19.4°) and Arica (10.0°), and from W to E including the Coastal Cordillera (up to average elevation of 1500 m a.s.l.), the Central Depression (500-2300 m a.s.l.) and the Precordillera (up to 3700 m a.s.l.). These last two are often defined as the Atacama Pediplain and characterised by an interfluves denudation rate extremely low in the last 6 Ma (Kober et al., 2007). The area of interest for this study is characterized by extremely low precipitations (Arica: 0.5 mm a-1; Iquique: 0.6 mm a-1; Quezada et al., 2010) close to the coast to about 300 mm a-1 in the upper part of the Western Cordillera. Seismicity in the area is extremely high: this sector of Northern Chile is well known as the Iquique Gap, lacking a major earthquake since 1868/1877 (Kausel et al, 1992).

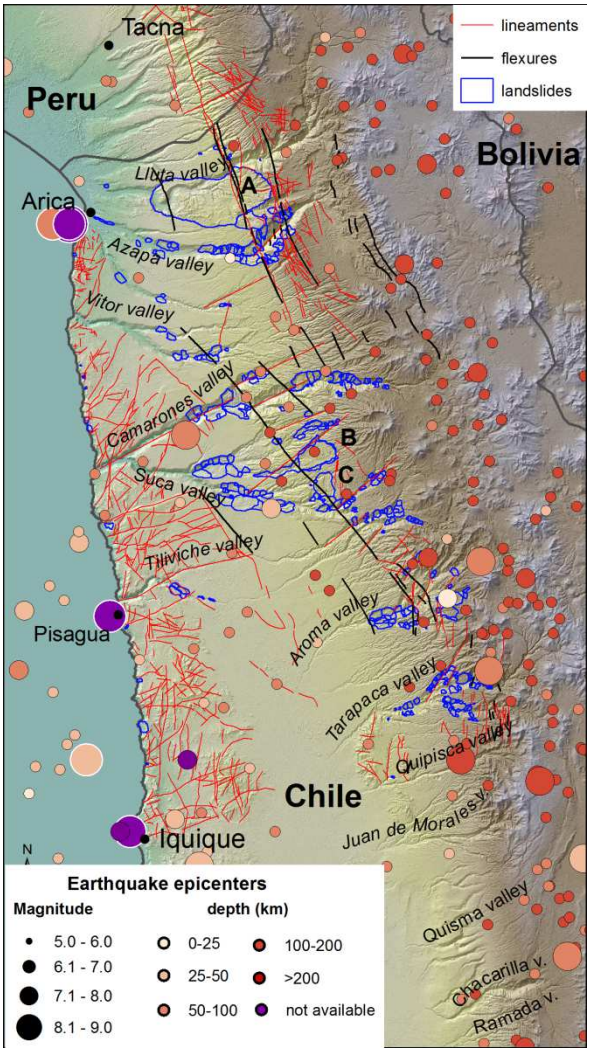

Figure 70. Study area and landslide inventory (A: Lluta landslide; B: Minimini landslide; C: Latagualla landslide). Earthquake epicenters: post-1900, from USGS ANSS Comprehensive Catalogues (circles with black outline); pre-1900, from Centro Sismológico National, Universidad de Chile (circles with white outline). Flexures from 1:1.000.000 geological map of Chile. Lineaments from photointerpretation.

4.8.1 Geological setting

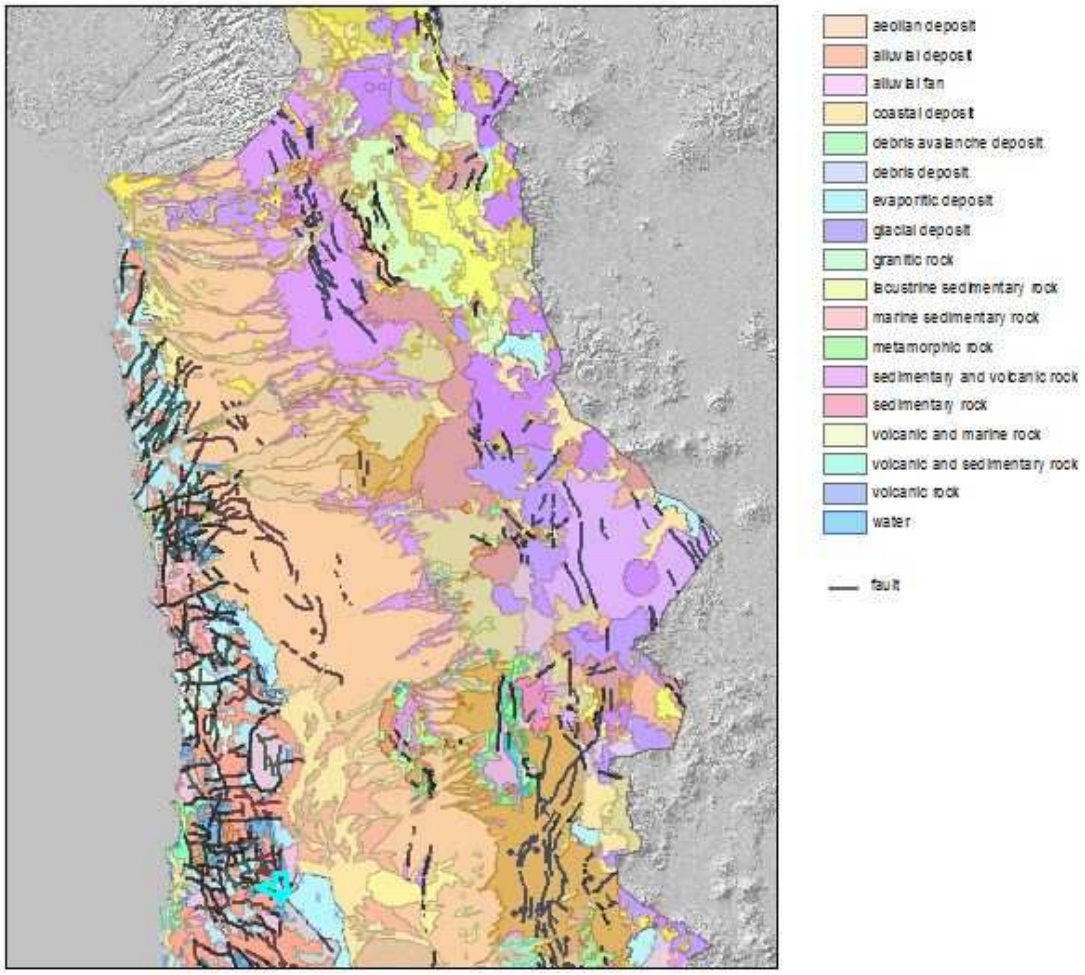

Figure 71. Geological map of the study area.

The W Escarpment and Precordillera are formed by a coarse-grained clastic formation (fluvial conglomerates and sandstones of the Azapa Fm.) and volcanoclastic (Oxaya Ignimbrite, rhyolitic-dacitic tuffs, Oligocene and Miocene in age, 26 to 17 Ma), and fluvial deposits (Huaylas and El Diablo Fms.), up to the present day surface (upper El Diablo Fm., 13.7 to 8.3 Ma), in a homoclinalic setting (Sucuna homocline, dipping 2-3° to the W) (Figure 71). This homocline is affected by NW and NS trending folds (Hauylillas, Oxaya Anticline from N to S, in the northern sector) about 1 km in amplitude, bounded to the W by the Ausipar Fault, and flexures (Humayani, Moquella and Aroma-Soga to the S) along the Precordillera western limit. The western slope of the Andes of northern Chile - southern Peru, forming the modern Andean forearc, is characterized by intense seismicity, associated to the subduction of oceanic Nazca plate below the S-American continent at rates between 63 and 84 mm a^{-1}. This area is subdivided from west to east into four main morpho-tectonic units: Coastal Cordillera, Central Depression, W-Escarpment-Precordillera and W Andean Cordillera. The Atacama Desert in Northern Chile is characterized by the presence

of a hierarchized drainage network cutting through the Precordillera, the Central Depression and the Coastal Cordillera. The large and deep canyons in the lower half of the valleys suggest an important base level lowering. At the same time, the exceptional long term hyperaridity (probably started since the Middle Miocene) of the Atacama Desert, and attributed to different causes (e.g. cold upwelling Humboldt Current, Andean rain-shadow effect), is the cause of the preservation of many landforms typical of this landscape. The canyon incision in this part of the Andes has been a recent subject of various studies (Garcia et al., 2011; Thouret et al., 2007; Hoke et al., 2007; Schlunegger et al., 2006) and some suggest the presence of lakes in the Central Depression between Late Miocene and Early Pliocene (Kirk-Lawlor et al., 2013), and so of a possibly wetter climate with respect to present day hyperaridity. This than relates to different mechanisms responsible for the late valley incision.

4.8.2 Landslides Dataset

The landslide inventory covers an area about 220 km long and 80 km wide, between Iquique and Arica. The inventory includes, landslides, main tectonic structures and other morphological features (Figure 1). Mapping has been performed by use of satellite images and direct field surveys (Crosta et al., 2014). A total of 379 landslides have been mapped in the area, prevalently including large phenomena. The landslide area ranges from 2 10-3 km^2 to 464 km^2 (Lluta landslide, Figure 72). The total area, inclusive of the landslide scarp and of the deposit amounts to about 1.77 103 km^2. The mega landslides already described in the literature (Strasser & Schlunegger, 2005; Pinto et al., 2008) can be classified as large block slides that can evolve in large rock avalanches (e.g. Minimini, Figure 72). Their initiation seems to be strongly associated to the presence of secondary faults and large fractures transversal to the slope. These landslides show evidence suggesting a re-incision by the main canyon network. This seems particularly true for the Lluta collapse where the main “landslide” mass is masked or deleted by the successive erosion. These landslides have been associated mainly to the uplift in the Precordillera (Pinto et al., 2008). Other landslides have been mapped along the Coastal Escarpment and some of the major tectonic escarpments with an E-W trend. Landslides along the canyon flanks affect volumes generally lower than 1 km^3 and can be mainly classified as large compound slides, complex phenomena and in some cases lateral spreading, supposedly by multiple retrogressive failure events with a relatively long spreading so that deposits often cross or develop along the valley bottom and have been re-incised exposing undeformed bedrock material. Few studies on selected mega-landslides show that they occur along the Precordillera slope and sectors with minor valleys affecting mainly interfluvial slopes at the macro scale.

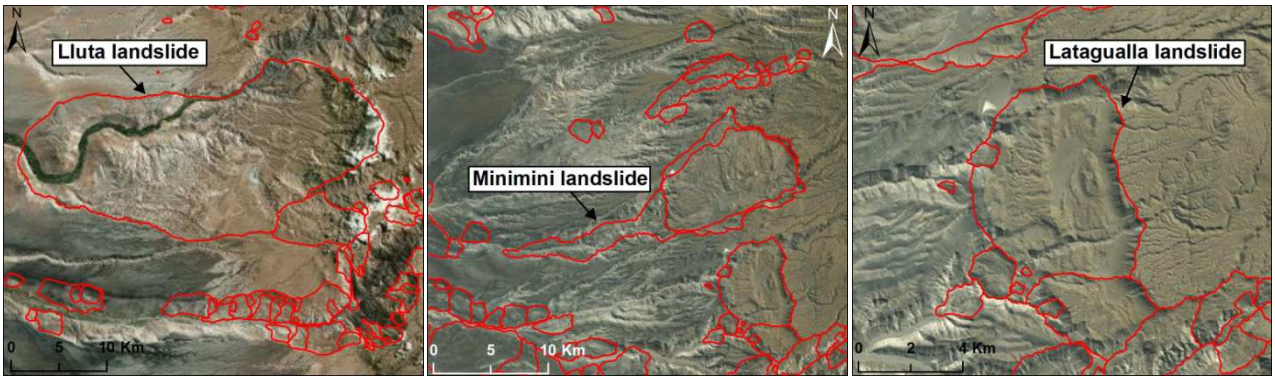

Figure 72. Lluta, Minimini and Latagualla landslides, in Northern Chile

These major landslides seem to be controlled by the presence of important NNW trending open fractures and graben like features with a relevant longitudinal continuity (up to 8-9 km). These coincide, in the northernmost part, with the western side of the Oxaya block, characterized by an eastward backtilting (Minimini and Latagualla landslides, Pinto et al., 2008; Lluta collapse, Strasser and Schlunegger, 2005). A completely different type of landslides is observed along the main fluvial valleys cutting deeply through the Precordillera and the Central Depression to reach the Pacific Ocean through the Coastal Cordillera. These valleys are 10 to 25 km apart from each other.

In Chile, no dating is available for the landslides along the canyon flanks. Nevertheless, some age constrains can be proposed relative to the pediment surface, ignimbritic deposits and strath terraces along the canyons, canyon incision rates and the migration of the knickpoints within the valleys. Pediplain surface age (ca 7-8 Ma) and ignimbritic deposits some tens of meters above the valley bottom (ca 2.5 Ma) give two initial constrains. Incision rates range between 25 m and 137 m Ma^{-1}.

In general, it is has been suggested that valley incision tends to start later and proceed slower moving southward in the area (Hoke et al., 2007). This is supported by the main knickpoints position with respect to the valley outlet, assuming a linear retrogression of the knickpoints, constant climatic conditions and a minor role of geological and lithological constrains. For the exorheic valleys, from the Azapa to the Tiliviche valley (northern area, Fig. 1), the distance ranges between 120 and 75 km (so 10 to ca 17 km Ma-1), whereas for the endorheic valleys, from Tarapaca to Ramada (southern area, Figure 70), it ranges between 75 and 25 km (3.6 to 10.7 km Ma-1). Therefore, assuming a progressive linear increase in time along the valley profile, it is possible to determine the approximate maximum age for each of the landslides along the valley flanks. At the same time, more options should be consider: the uniform incision through the entire valley length, at rates slightly changing from W to the E; the fact that some landslide toe lies well above the valley bottom and could have occurred at earlier stages of valley incision. Due to the width (parallel to the river course) of some of the landslides, the total time needed to completely clear the landslide toe and the failure to occur can be quite long with the given erosion/incision

rates. For the same reason, failures could have progressively propagated upstream with valley erosion. In this last condition, the groundwater level within the slopes could have been higher than along a well-developed valley flank, so favouring the failure process.

5 Relationship between landslides size distribution and distance from the seismic source

One of the purpose of this work is to characterize the variation of the landslide size with the increase of the distance from the seismic source. The starting hypothesis is that moving away from the seismic source (epicenter or fault rupture) there is a decrease in the size of the landslide related to the decrease of the earthquake intensity. To verify this hypothesis the available datasets were divided in different sub-set, based on classes of distance, both from the epicenter and the fault (except Iwate-Miyagi Nairiku earthquake, were only the epicenter is available). The number of classes depend on the number of landslides present in each inventory: the larger is the inventory, the more the class. Each sub-set contain the same number of events, independently from the type of landslides. This was done to allow a comparison between the different sub-set. For each sub-set the magnitude frequency curve was built and the four methodology presented before were applied for the identification of the scaling parameter, α. The results are presented for each earthquake considered in this study. In appendix 2 are reported all the fitting curves for the Wenchuan Earthquake (2008), as example.

5.1 Papua New Guinea Earthquake, 1993

The inventory includes 4789 landslides (Meunier et al., 2008). Five distance classes were defined, and the magnitude-frequency curves were built for each class (Figure 73). The curves show that, with the increase of the distance there is an increase of the slope of the curves, probably related to a decrease in number of the landslides with large area, moving away from the source.

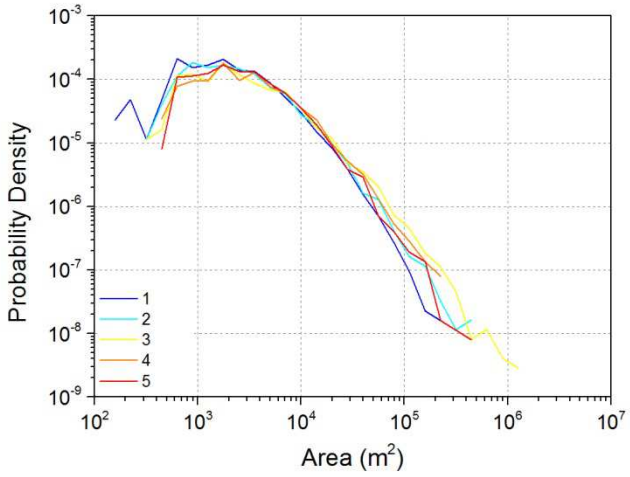

Figure 73. Probability Density curves for each class of distance from the epicenter. See the following table for the legend.

Table 8. Classes of distance, from the epicenter, identified for the Papua New Guinea Earthquake, number of landslides in each class, and values of the scaling parameter, *α*, defined through the different methodologies. PL: Maximum likelihood estimator of non-cumulative power-law function; LF: Least square regression of non-cumulative log power-law function; DP: Maximum likelihood estimator of Double Pareto distribution; ML: Maximum likelihood estimator of cumulative power-law distribution (Clauset et al, 2009).

Classes of Distance (m)	Code	# landslides	PL	LF	DP	ML
0 - 11,357	1	956	1.83	2.06	2.38	2.35
11,357 - 19,751	2	960	1.92	2.22	2.21	2.22
19,751 - 27,356	3	957	1.97	2.12	2.05	2.21
27,356 - 40,132	4	959	2.09	2.10	2.16	2.13
40,132 - 73,387	5	957	2.77	2.69	2.50	2.61

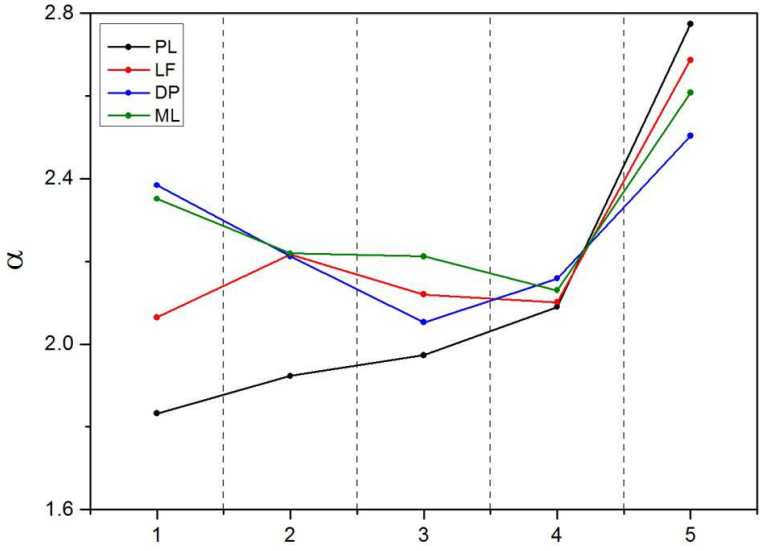

Figure 74. Graph showing the values of the scaling parameter, *α*, for the distance from the epicenter. See Table 8 for the legend. The x values referred to the code, and then to the distances, in Table 8.

Considering the values of the scaling parameter, α (Table 8, Figure 74), defined through the four methodology, it is possible to observe that the PL method show an increase of the exponent, with the epicentral distance. While the LF and ML methodologies shows an exponent in a range of 2.0 and 2.4 without a clear trend (growth or degrowth), and increase in the last class of distance. The DP method have a decrease in the exponent at the beginning and an increase after the third class.

For the analysis of the distance from the fault rupture, five classes were identified and the relative magnitude-frequency curves built. In this case the trend is not so clear. The first classes seem to have a greater slope than the others.

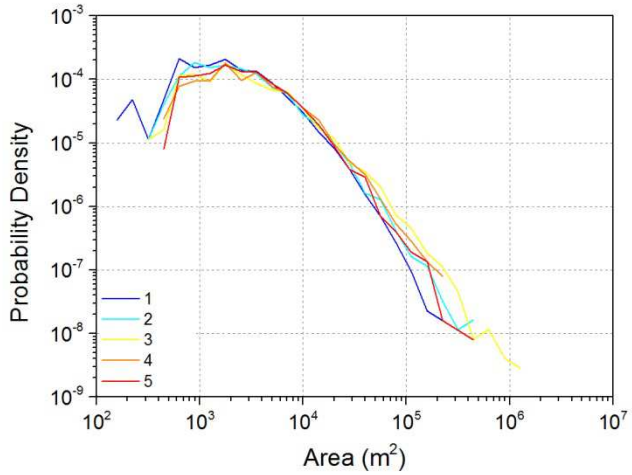

Figure 75. Probability Density curves for each class of distance from the fault rupture. See the following table for the legend.

Table 9. Classes of distance, from the fault rupture, identified for the Papua New Guinea Earthquake, number of landslides in each class, and values of the scaling parameter, *α*, defined through the different methodologies. See Table 8 for the PL, LF, DP and ML meaning.

Classes of Distance (m)	Code	# landslides	PL	LF	DP	ML
0 - 24,617	1	957	2.35	2.53	2.25	2.72
24,617 - 31,257	2	951	2.06	2.21	2.19	2.27
31,257 - 34,239	3	950	1.77	2.01	2.08	1.93
34,239 - 37,787	4	970	2.22	2.09	2.32	2.24
37,787 - 67,289	5	961	2.18	2.27	2.40	2.26

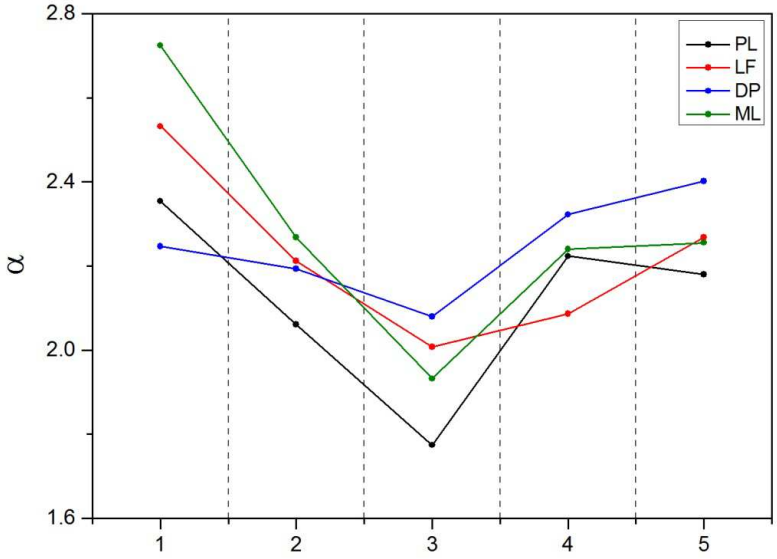

Figure 76. Graph showing the values of the scaling parameter, *α*, for the distance from the fault rupture. See Table 8 for the legend. The x values referred to the code, and then to the distances, in Table 9.

All the methodologies show a decrease of the exponent with the distance for the first classes and after an increase of it (Table 9; Figure 76). This means that after the second class there is an increase of the landslides area, which then gradually returns to decrease with the distance. The DP method has the less variation in the exponent respect the others.

5.2 Northridge Earthquake, 1994

The inventory includes 11,111 landslides (Harp et al., 1996). Ten classes were defined, and the magnitude-frequency curves were built (Figure 77). The curves do not show a clear trend, the first classes seem to have a greater slope than the others, especially for the tails.

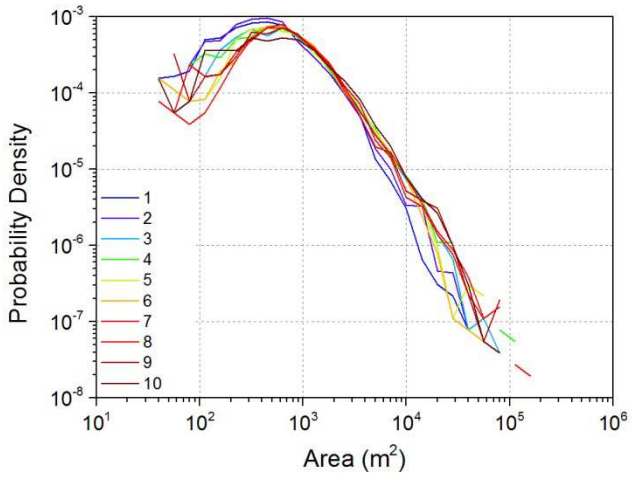

Figure 77. Probability Density curves for each class of distance from the epicenter.

Table 10. Classes of distance, from the epicenter, identified for the Northridge Earthquake, number of landslides in each class, and values of the scaling parameter, *α*, defined through the different methodologies. See Table 8 for the PL, LF, DP and ML meaning.

Classes of Distance (m)	Code	# landslides	PL	LF	DP	ML
0 - 14,515	1	1107	2.19	2.56	1.98	2.55
14,515 - 16,968	2	1109	2.18	2.29	2.02	2.38
16,968 - 19,462	3	1111	1.93	2.34	1.75	2.21
19,462 - 21,724	4	1113	1.78	2.03	2.37	2.67
21,724 - 24,665	5	1111	2.07	2.16	1.47	2.53
24,665 - 28,207	6	1108	2.03	2.58	2.03	3.01
28,207 - 31,000	7	1115	1.98	2.18	1.69	2.31
31,000 - 34,529	8	1109	2.10	1.95	2.20	2.06
34,529 - 38,026	9	1114	2.03	2.07	2.21	2.05
38,026 - 53,483	10	1114	2.19	2.42	1.69	2.23

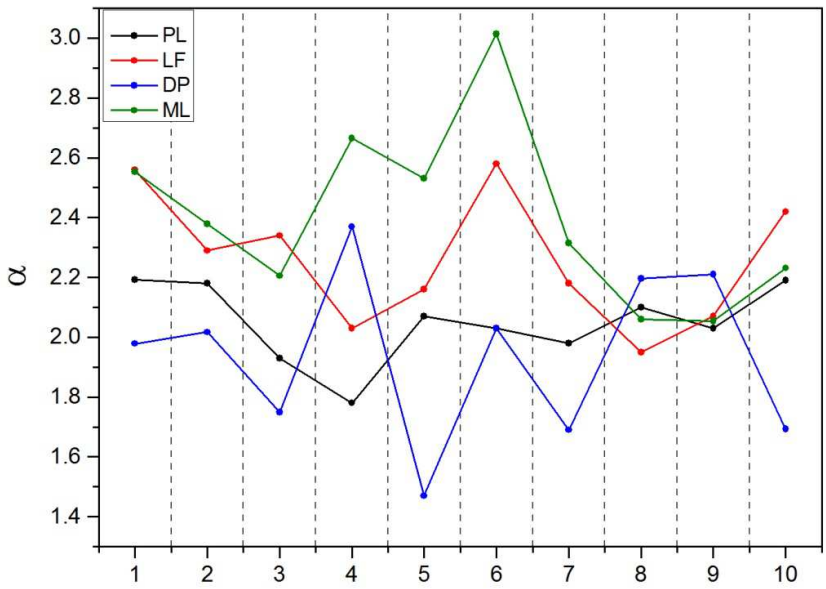

Figure 78. Graph showing the values of the scaling parameter, *α*, for the distance from the epicenter. See Table 8 for the legend. The x values referred to the code, and then to the distances, in Table 10.

From Table 10 and Figure 78, it is possible to observe that, the distribution of the scaling parameter, and then, of the landslides area is not clear. The PL method is the only that has a defined trend, the others have a large variation of the exponent. The ML method in specific classs of distance (#3, #8, #9, #10, Figure 78), show a very low values respect the other exponent identified. This is related to a problem observed for this methodology. The method, in fact, does not fit the tail of the distribution and the fitting curve has a slope less than the actual slope (Figure 79).

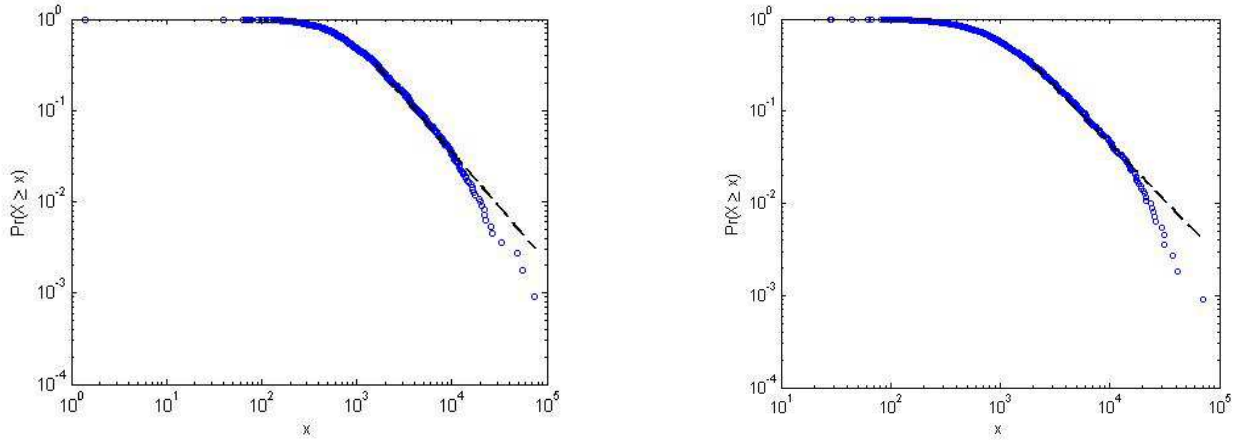

Figure 79. Maximum likelihood estimator of cumulative power-law distribution (ML, Clauset et al, 2009) for the class #3 (sx) and #10 (dx). As showed the methodology do not fit the tail of the distribution, this implies an exponent lower than expected.

For the analysis of the distance from the fault rupture, five classes were defined and the relative magnitude-frequency curves built for each of them (Figure 80). From these curves, it possible to observe that only two curves (7788 and 14741 m) deviated from the trend, without an appropriate trend.

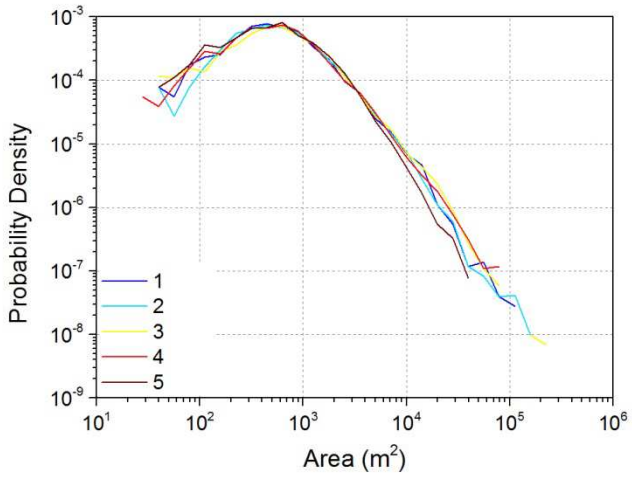

Figure 80. Probability Density curves for each class of distance from the fault rupture. See the following table for the legend.

Table 11. Classes of distance, from the fault rupture, identified for the Northridge Earthquake, number of landslides in each class, and values of the scaling parameter, α, defined through the different methodologies. See Table 8 for the PL, LF, DP and ML meaning.

Classes of Distance (m)	Code	# landslides	PL	LF	DP	ML
0 - 2,032	1	2220	1.97	2.25	2.87	2.44
2,032 - 4,500	2	2222	2.10	2.41	2.60	2.55
4,500 - 7,788	3	2215	2.07	2.23	2.91	2.06
7,788 - 14,741	4	2219	1.85	2.03	3.08	2.28
14,741 - 41,715	5	2219	2.44	2.60	3.12	2.58

Two methodologies show a similar trend (PL, LF), while the DP method, except for the first class, show an increase of the exponent with the distance (Table 11, Figure 81). For this earthquake, the DP method has high values of α respect the others, related to the impossibility for the Double Pareto distribution to correct fit each dataset as showed in Figure 82. Here it is possible to observe that the fitting curve is below the magnitude frequency curve, resulting in a value of the scaling parameter which is higher than the reality. For all the sub-set, this method show the same problem. The ML method show the same problem presented for the epicentral distance. As it possible to observe from Figure 83 the methodology does not fit the tail of the distribution, and as consequence, the exponent is lower than the actual ones.

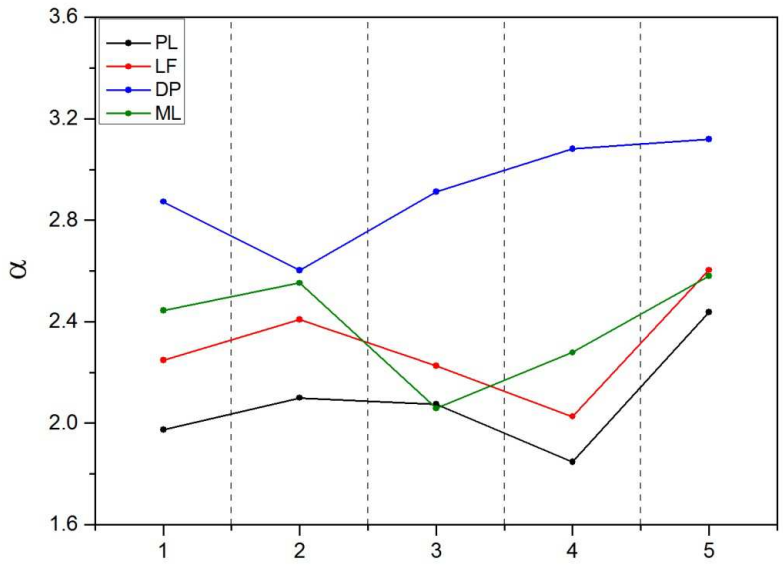

Figure 81. Graph showing the values of the scaling parameter, *α*, for the distance from the fault rupture. See Table 8 for the legend. The x values referred to the code, and then to the distances, in Table 11.

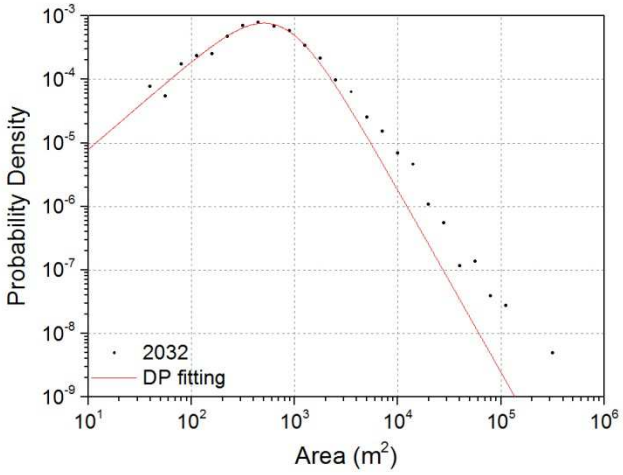

Figure 82. Maximum likelihood estimator of non-cumulative power-law function (DP) for the class of distance number 1.

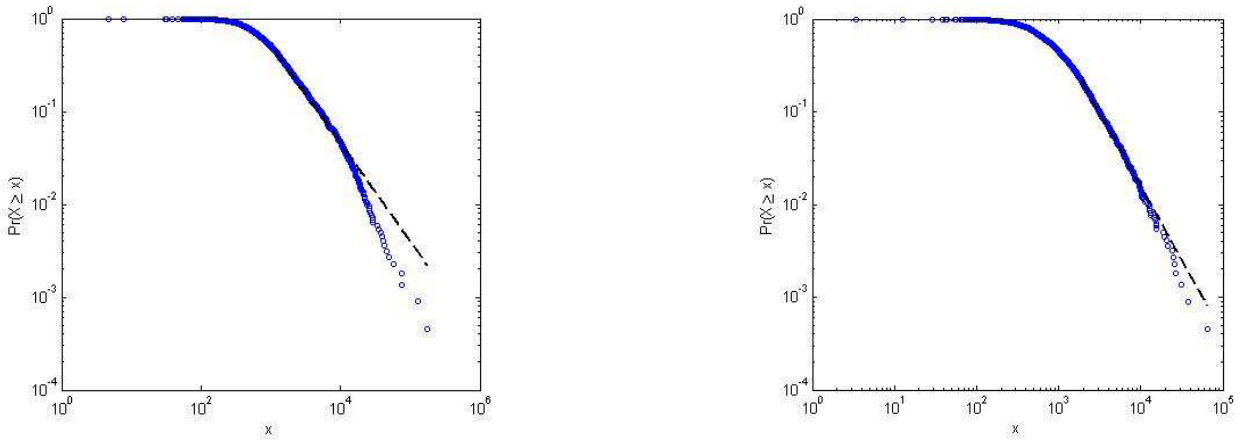

Figure 83. Maximum likelihood estimator of cumulative power-law distribution (ML, Clauset et al, 2009) for the class #3 (sx) and #4 (dx). As showed the methodology do not fit the tail of the distribution, this implies an exponent lower than expected.

5.3 Niigata-Chuetsu Earthquake, 2004

The inventory includes 10,525 landslides (Yagi et al., 2007). Five classes were defined, and the magnitude-frequency curves were built (Figure 84). The curves show that, with the increase of the distance, there is a decrease of the slope of the curves, that meaning an increase, in number, of the landslides with large area, moving away from the source. This is the opposite of what is expected as hypothesis.

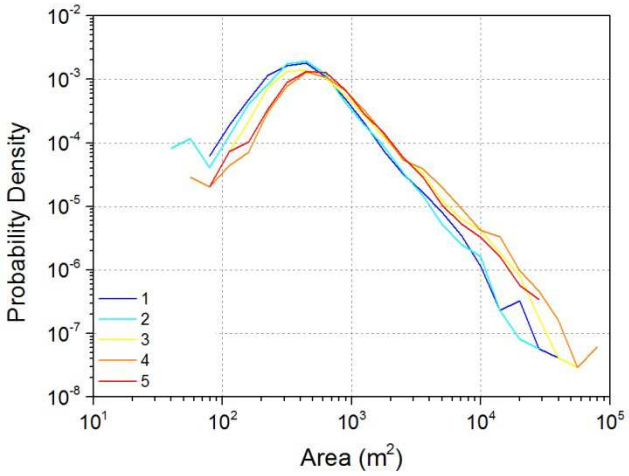

Figure 84. Probability Density curves for each class of distance from the epicenter.

Table 12. Classes of distance, from the epicenter, identified for the Niigata-Chuetsu Earthquake, number of landslides in each class, and values of the scaling parameter, *α*, defined through the different methodologies. See Table 8 for the PL, LF, DP and ML meaning.

Classes of Distance (m)	Code	# landslides	PL	LF	DP	ML
0 - 7,002	1	2105	2.59	2.52	4.00	2.49
7,002 - 10,423	2	2105	2.36	2.67	4.00	2.53
10,423 - 13,658	3	2105	2.14	2.16	3.36	2.18
13,658 - 16,954	4	2105	2.21	2.09	3.62	2.10
16,954 - 23,955	5	2105	2.42	2.16	3.91	2.29

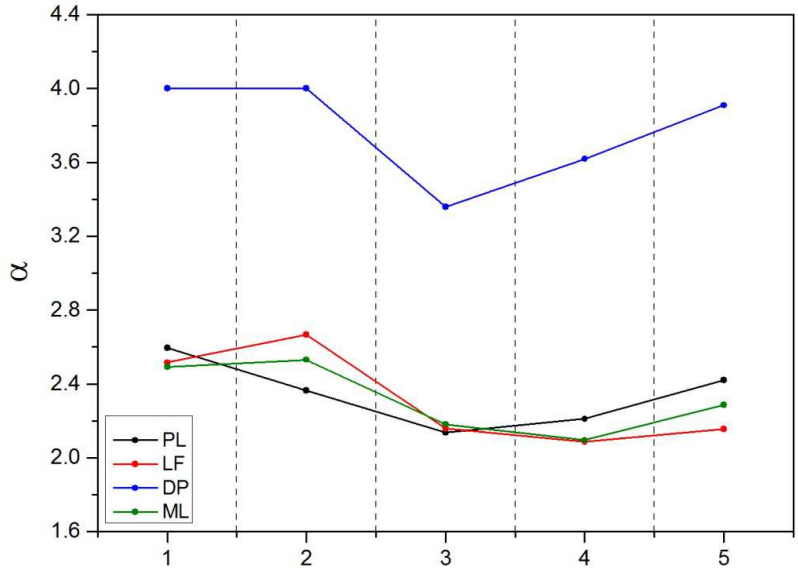

Figure 85. Graph showing the values of the scaling parameter, *α*, for the distance from the epicenter. See Table 8 for the legend. The x values referred to the code, and then to the distances, in Table 12.

The DP method shows the same problem presented for the Northridge Earthquake, where the fitting curves have a slope higher than the actual slope (see Figure 86).

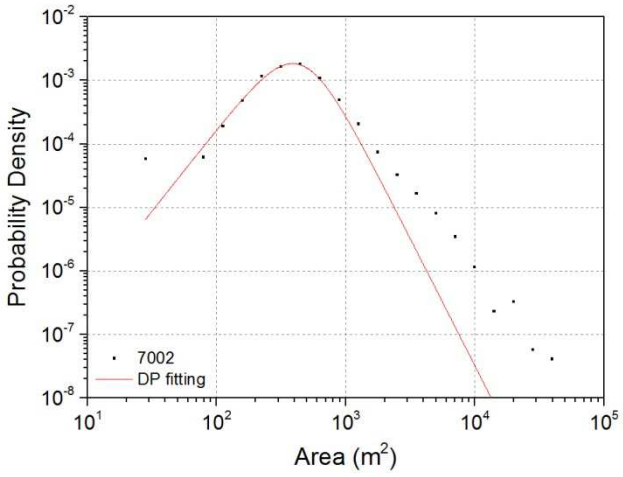

Figure 86. Maximum likelihood estimator of non-cumulative power-law function (DP) for the class of distance number 1.

The others methodologies show the same trend, with higher exponents for the first two classes. From the third classes the exponents show a slight increase.

Regarding the distance from the fault rupture, five classes were defined, with the relative curves (Figure 87). Here, it seems that the higher the distance, the steeper the tail of the curves.

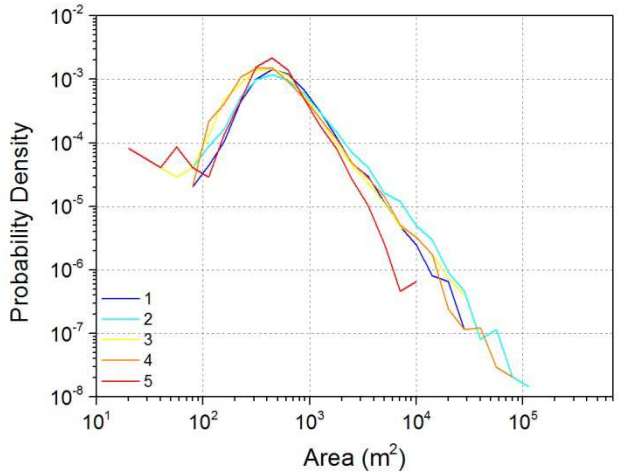

Figure 87. Probability Density curves for each class of distance from the fault rupture.

Table 13. Classes of distance, from the fault rupture, identified for the Niigata-Chuetsu Earthquake, number of landslides in each class, and values of the scaling parameter, *α*, defined through the different methodologies. See Table 8 for the PL, LF, DP and ML meaning.

Classes of Distance (m)	Code	# landslides	PL	LF	DP	ML
0 - 5,061	1	2,105	2.38	2.35	3.82	2.40
5,061 - 10,272	2	2,104	2.01	2.04	3.18	2.06
10,272 - 17,436	3	2,104	2.27	2.26	3.61	2.19
17,436 - 26,342	4	2,106	2.15	2.32	3.26	2.20
26,342 - 72,381	5	2,106	2.76	3.02	4.00	2.85

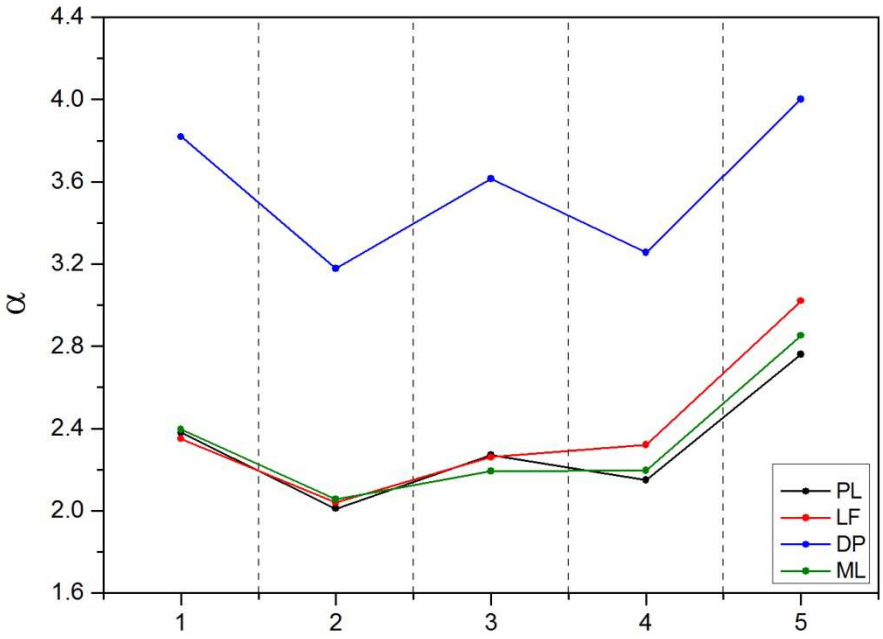

Figure 88. Graph showing the values of the scaling parameter, *α*, for the distance from the fault rupture. See Table 8 for the legend. The x values referred to the code, and then to the distances, in Table 13.

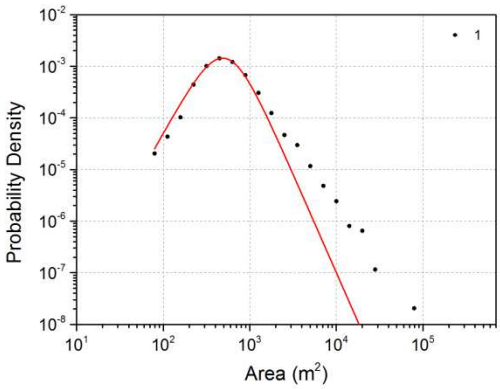

Figure 89. Maximum likelihood estimator of non-cumulative power-law function (DP) for the class of distance number 1.

The DP method has high values that do not reflect the actual slope of the curves (e.g. Figure 89). The others methods have the same trend with very similar values, and show a progressive increase of the exponent with distance, with the exception of the first class. This mean a decrease in frequency of the large landslides with the increase of the distance from the fault rupture, according to the hypothesis.

5.4 Wenchuan Earthquake, 2008

The landslides inventory, that includes 197481 events (Xu et al., 2013), was divided in 10 sub-sets, on the basis of the distance from the epicentre. The magnitude-frequency curves were built for each class (Figure 90). The graph do not show a specific trend in the slope of the curves, and then in the landslides size distribution, with the epicentral distance.

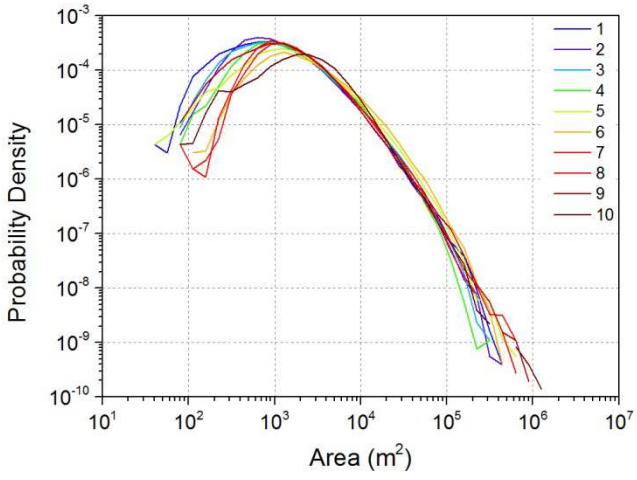

Figure 90. Probability Density curves for each class of distance from the epicenter. See the following table for the legend.

Table 14. Classes of distance, from the epicenter, identified for the Wenchuan Earthquake, number of landslides in each class, and values of the scaling parameter, *α*, defined through the different methodologies. See Table 8 for the PL, LF, DP and ML meaning.

Classes of Distance (m)	Code	# landslides	PL	LF	DP	ML
0 - 15,084	1	19,745	2.01	2.01	2.34	2.23
15,084 - 24,038	2	19,748	2.24	2.41	2.28	2.66
24,038 - 34,161	3	19,744	1.98	2.31	2.16	3.23
34,161 - 44,110	4	19,741	2.79	2.16	2.31	3.62
44,110 - 56,442	5	19,757	1.75	2.16	2.41	3.20
56,442 - 76,422	6	19,750	2.84	2.49	2.25	4.36
76,422 - 92,225	7	19,746	2.71	2.63	2.54	2.97
92,225 - 115,550	8	19,747	2.08	2.22	2.59	2.78
115,550 - 164,412	9	19,755	2.03	2.43	2.63	2.16
164,412 - 380,000	10	19,748	2.51	2.57	3.25	2.57

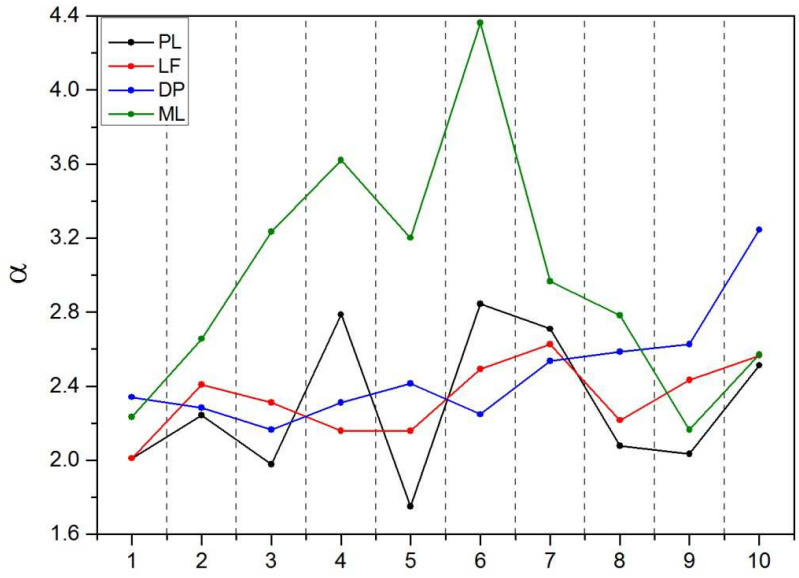

Figure 91. Graph showing the values of the scaling parameter, *α*, for the distance from the epicenter. See Table 8 for the legend. The x values referred to the code, and then to the distances, in Table 14.

The PL and LF methods do not have a clear variation. They increase and decrease with the distance without a specific trend. However the exponents closed to the epicenter are lower than the exponents far from the seismic source. The ML method shows an increase for the first five classes and then a decrease, with a very high variation in the values of the exponent. The curves related to the distances #1, #2, #3, #9 and #10 are not properly fit by the methodology. In contrast to the problem encountered by this methodology, the distance #6 show a very high value, due to the fitting of only the tail of the distribution (Figure 92). The DP method has a constant increase of the exponent with the epicentral distance, and confirm the hypothesis.

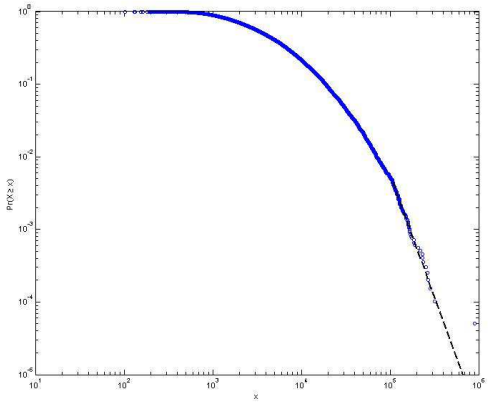

Figure 92. Maximum likelihood estimator of cumulative power-law distribution (ML, Clauset et al, 2009) for the class #6. As showed the methodology fit the tail of the distribution, this implies an exponent higher than expected.

Considering the distribution of the landslide size in relation to the fault rupture, the landslides inventory was divided in 10 sub-sets. The magnitude-frequency curves were built (Figure 93). Taking into account only the tails of the distributions, it is possible to observe an increase of the slope of the curves with the distance. This observation is less evident for area ranging between 10^3 and 10^5 m^2.

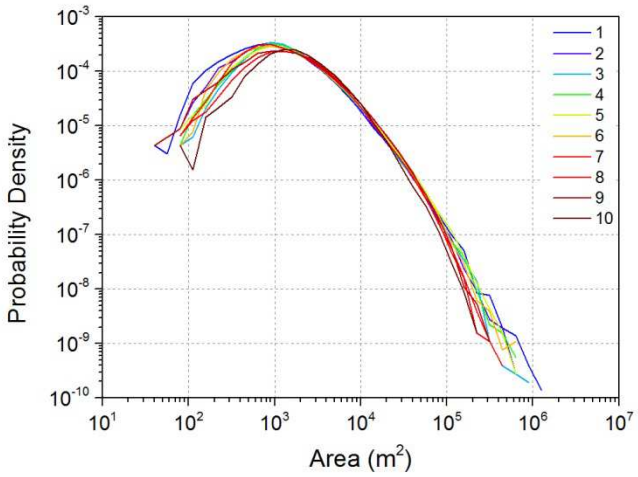

Figure 93. Probability Density curves for each class of distance from the fault rupture. See the following table for the legend.

Table 15. Classes of distance, from the fault rupture, identified for the Wenchuan Earthquake, number of landslides in each class, and values of the scaling parameter, *α*, defined through the different methodologies. See Table 8 for the PL, LF, DP and ML meaning.

Classes of Distance (m)	Code	# landslides	PL	LF	DP	ML
0 - 1,346	1	19,749	2.01	2.49	2.38	2.38
1,346 - 2,800	2	19,747	1.97	2.60	2.42	2.90
2,800 - 4,593	3	19,747	2.29	2.33	2.39	2.91
4,593 - 6,784	4	19,749	2.04	2.68	2.39	2.31
6,784 - 9,820	5	19,748	2.13	2.00	2.30	2.72
9,820 - 12,886	6	19,748	2.21	2.61	2.18	2.41
12,886 - 16,987	7	19,749	2.11	2.50	2.21	3.86
16,987 - 23,242	8	19,749	3.07	3.18	2.39	3.28
23,242 - 32,169	9	19,748	2.54	2.35	2.40	4.12
32,169 - 160,000	10	19,748	2.38	2.50	2.63	2.60

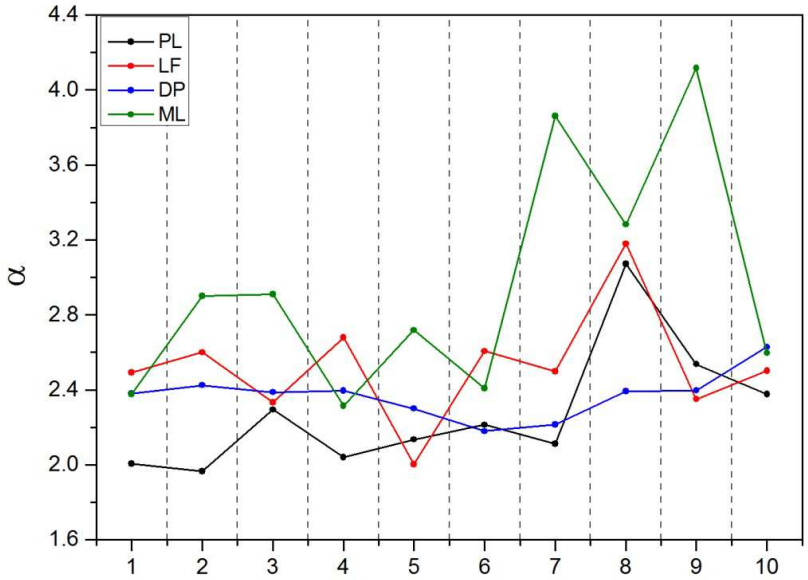

Figure 94. Graph showing the values of the scaling parameter, *α*, for the distance from the fault rupture. See Table 8 for the legend. The x values referred to the code, and then to the distances, in Table 15.

In the case of the distance from the fault ruptures for the Wenchuan Earthquake there is no clear trend for the α exponent (Table 15 Figure 94). In the DP method, the exponent increase with the distance only after a distance of 9,820 m from the fault,. Under this class, α has a little variation.

The PL method shows an increase of the values with the distance, while for the LF and ML methods there is not a clear trend. The curves related to the distances #2, #3, #4, #5, #6 and #10 are not properly fit by the ML method.

5.5 Iwate-Miyagi Nairiku Earthquake, 2008

For this earthquake, it was possible to make only the analysis related to the epicentral distance, due to the unknown fault at the origin of the earthquake. The inventory includes 3502 landslides (Yagi et al., 2009), that were divided in five sub-set. The magnitude-frequency curves were built for each class (Figure 95). A first analysis shows how the trend is completely opposite to the expected. In fact, the lower is the distance, the higher is the slope of the curves. This means that large landslides are far from the seismic source.

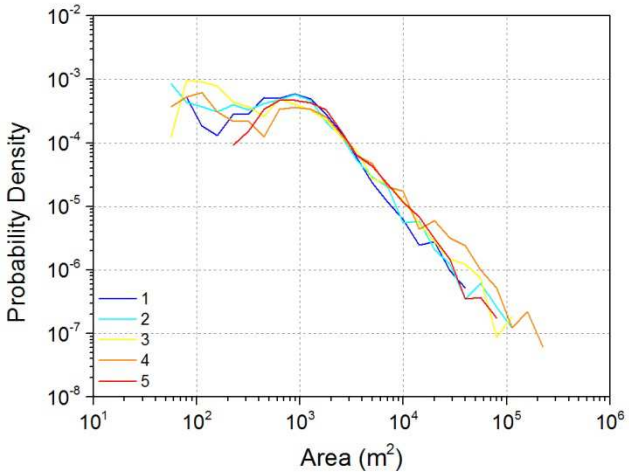

Figure 95. Probability Density curves for each class of distance from the epicenter. See the following table for the legend.

Table 16. Classes of distance, from the epicenter, identified for the Iwate-Miyagi Nairiku Earthquake, number of landslides in each class, and values of the scaling parameter, *α*, defined through the different methodologies. See Table 8 for the PL, LF, DP and ML meaning.

Classes of Distance (m)	Code	# landslides	PL	LF	DP	ML
0 - 4,684	1	700	1.85	1.92	4.00	2.18
4,684 - 7,549	2	700	1.85	1.80	4.00	1.92
7,549 - 13,566	3	702	1.76	1.80	2.00	1.82
13,566 - 18,365	4	700	1.71	1.65	3.50	1.67
18,365 - 26,279	5	700	1.99	1.99	3.09	1.98

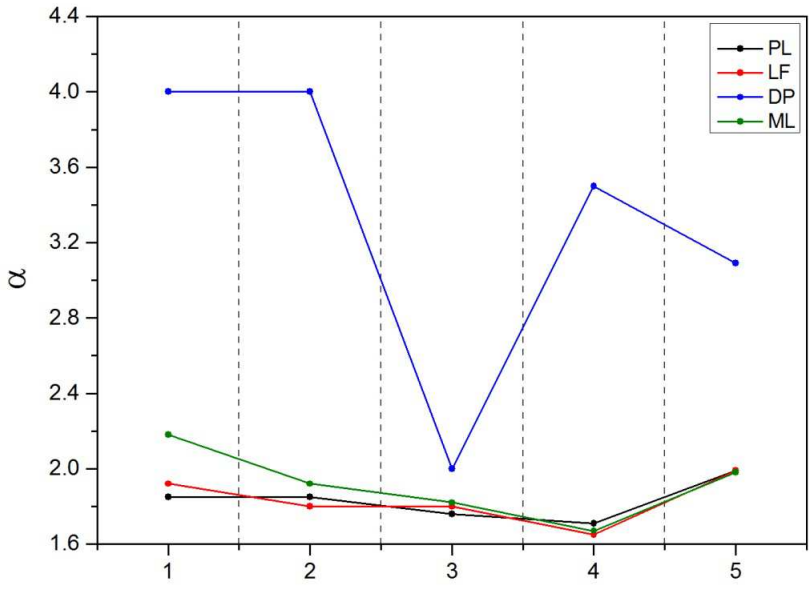

Figure 96. Graph showing the values of the scaling parameter, α, for the distance from the epicenter. See Table 8 for the legend. The x values referred to the code, and then to the distances, in Table 16.

Considering the results in Table 16 and Figure 96, it is possible to observe that the DP method shows strange values of the exponent. This is related to the characteristics of the dataset, that do not have a clear rollover in the distribution, due to the abundance of small landslides in the inventory, as it is possible to see for example in Figure 97. For this reason this methodology cannot be applied successfully to this earthquake. All the other methods show a decrease of the exponents with the distance, and an increase only for the last classes of distance. However for PL and LF methods there is no a clear variation in the values for all the distances, except for the last class, that shows an increase of the exponent.

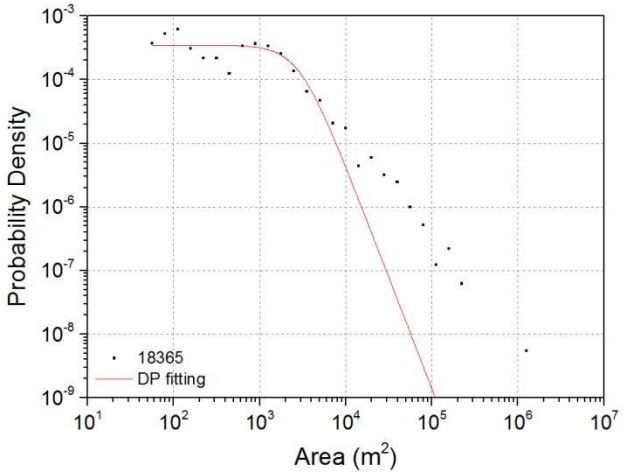

Figure 97. Maximum likelihood estimator of non-cumulative power-law function (DP) for the class of distance class number 4.

5.6 Tohoku Earthquake 2011

The inventory includes 1978 landslides (from Wartman et al., 2013). Even though the number of event is less small, five sub-set and the relative magnitude-frequency curves were built (Figure 98). The landslide areas involved in this inventory are small compared to the others earthquake-induced landslides inventory. The reason is probably related to the high distance of the seismic source with respect to the affected area, and the overall morphology of the area.

Table 17. Classes of distance, from the epicenter, identified for the Tohoku Earthquake, number of landslides in each class, and values of the scaling parameter, *α*, defined through the different methodologies. See Table 8 for the PL, LF, DP and ML meaning.

Classes of Distance (m)	Code	# landslides	PL	LF	DP	ML
0 -123,067	1	395	2.02	2.43	2.08	2.72
123,067 - 144,765	2	396	2.74	3.24	2.07	2.00
144,765 - 156,903	3	396	1.89	1.99	2.40	2.13
156,903 - 202,846	4	396	2.87	2.51	2.15	3.18
202,846 - 325,009	5	395	1.98	2.25	2.21	2.03

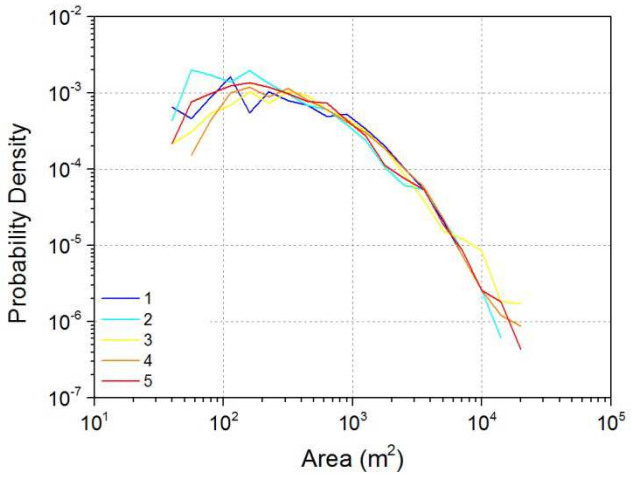

Figure 98. Probability Density curves for each class of distance from the epicenter.

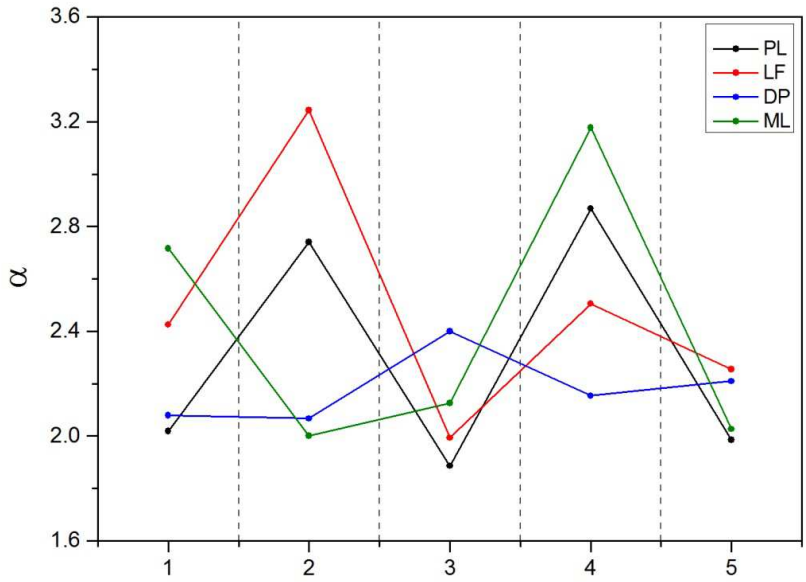

Figure 99. Graph showing the values of the scaling parameter, *α*, for the distance from the epicenter. See Table 8 for the legend. The x values referred to the code, and then to the distances, in Table 17.

The variation of the scaling parameter with the epicentral distance do not follow a specific trend. The only observation that can be made is that the DP method shows an opposite trend with respect to the others. When it increases, the others decrease and conversely. In this earthquake, the DP method shows a good fit for each sub-set.

Also for the fault distance, five sub-set were defined and the relative probability density curves created (Figure 100). The distance from the fault rupture is greater than the epicentral distance: the first class of the fault distance corresponds to the penultimate of the epicentral distance.

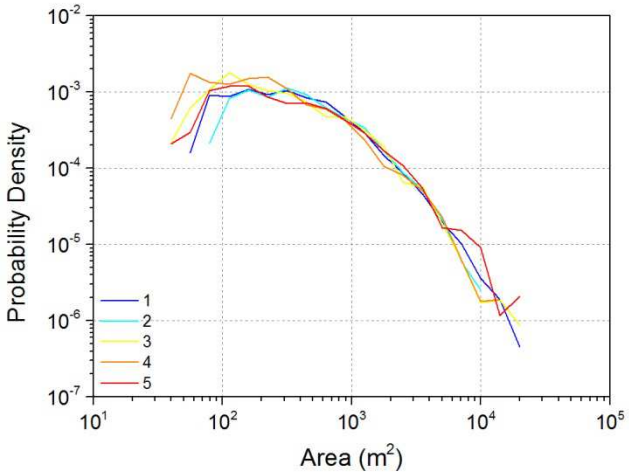

Figure 100. Probability Density curves for each class of distance from the fault rupture. See the following table for the legend.

Table 18. Classes of distance, from the fault rupture, identified for the Tohoku Earthquake, number of landslides in each class, and values of the scaling parameter, *α*, defined through the different methodologies. See Table 8 for the PL, LF, DP and ML meaning.

Distance (m)	Code	# landslides	PL	LF	DP	ML
0 - 203,773	1	380	1.86	1.94	2.28	2.11
203,773 - 218,565	2	407	1.96	2.48	2.22	3.72
218,565 - 246,725	3	394	1.85	2.22	2.00	2.94
246,725 - 264,204	4	384	1.74	1.86	2.15	3.00
264,204 - 286,305	5	412	1.61	2.08	2.00	2.30

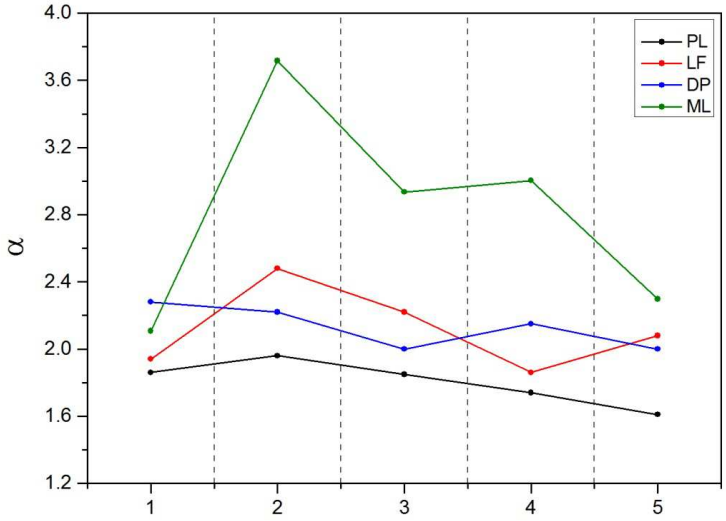

Figure 101. Graph showing the values of the scaling parameter, *α*, for the distance from the fault rupture. See Table 8 for the legend. The x values referred to the code, and then to the distances, in Table 18.

The scaling parameter shows a little range of values the different fault distances for the PL, LF and DP method. All the methodologies have a decrease of the exponent with the distance. In this case the ML method, probably related to the low number of events for each classes of distance, tries to fit the tail of the distribution with an increase of the exponent (e.g. Figure 102).

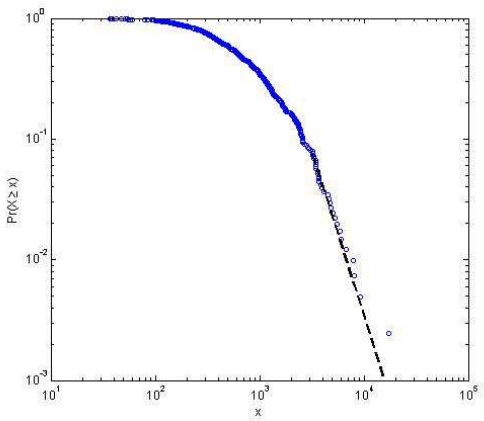

Figure 102. Maximum likelihood estimator of cumulative power-law distribution (ML) for the class #2.

5.7 Discussion

The hypothesis that has been tested with this analysis is that the increase of the distance produces an increase in the power law exponent. As shown in Table 19, this hypothesis was verified only for three earthquakes, not for both the distances analysed (from epicenter and from fault rupture), and not for all the methodologies applied.

Table 19. Summary of the analysis. ✓: the hypothesis is verified; ×: the hypothesis is not completely verified.

Earthquake	Epicentral distance	Fault distance
Papua New Guinea	✓	×
Northridge	×	×
Niigata-Chuetsu	×	✓
Wenchuan	✓	×
Iwate-Miyagi Nairiku	×	×
Tohoku	×	×

Some considerations can be made relatively the methodologies applied to the landslides inventories. The Maximum likelihood estimator of non-cumulative power-law function (PL) and the Least square regression of non-cumulative log power-law function (LF) are highly dependent on the ability of user that applies the procedure, so they have a high subjectivity. In this methods, in facts the user select the best part of the curves for the fit (Figure 103). To reduce this problem the R-Square was considered. The part of the curve whose fitting showed highest values of this parameter was chosen for the fit. This improve the repeatability of the analysis, even if the subjectivity cannot be completely eliminated, for example in the size of the window in which the fit is performed.

The Maximum likelihood estimator of cumulative power-law distribution (ML; Clauset et al, 2009) often gives unreliable results because it does not give importance to the tail of the distribution. As it is possible to see in the graphs in reported examples, the methodology lost the tail of the distribution, due to the fact that the method tends to minimize the error in the upper part of the curve, were the values x_{min} is automatically chosen. The Maximum likelihood estimator of Double Pareto distribution (DP) better describe the landslides distribution from a theoretically point of view. In fact, the method allows to define the rollover of the distribution, and to characterize two scaling parameters (α and β) related to the two scaling regimes exhibited by the landslide distribution.

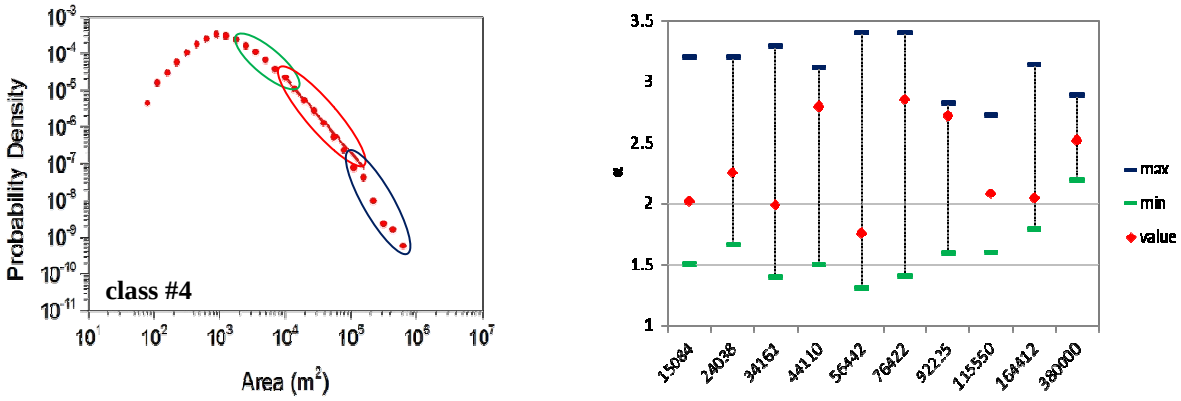

Figure 103. Different part of the probability density curves can be fit, as explain by the figure on the right, with different results on the scaling parameter, *α*. The case of the Maximum likelihood estimator of non-cumulative power-law function (PL), for the fault distance in the Wenchuan Earthquake, is presented. The graph shows the possible range of variation of the exponent on the basis of the different part of the curve that the user can fit. The red dots are the values adopted in this work, the green lines correspond to a possible lower limit of the exponent, and the blue lines to a maximum one.

The two regimes are strictly connected: the small landslides distribution influences the slope of the large landslides in the fit. For this reason, sometimes, the procedure results in strange values of the scaling parameter α. The double Pareto curve, sometimes, has difficulty in predicting landslide distributions at the tails, but it describes the majority of the distribution very well, as found also by Guthrie and Evans (2004).

Some remarks can be done also for the available inventories. In particular, the quality of the inventory influences the results of the fitting procedure. The more the inventory is accurate, the more the results are reliable. In the available inventories, two different problem were found.

The first is the amalgamation of multiple landslides in one single polygon during the compilation of the inventory itself. As found in the literature, most landslide inventories are derived from analysis of optical or multispectral imagery, exploiting the typical texture, color and spectral properties of freshly disturbed areas (Guzzetti et al., 2012). Often, landslides are conspicuous because they clear vegetation that has a very different appearance or radiation intensity spectrum. When landslides are mapped as polygons, whether by man or machine, the general assumption is that the polygon represents a single landslide, most often combining a scar area, a deposit area and sometimes a runout area. Amalgamation, i.e. the combination of several individual landslides in a single polygon, can be due to the actual coalescence of landslides, or the apparent contiguity of disturbed areas in images with low resolution or poor contrast between affected and unaffected areas.

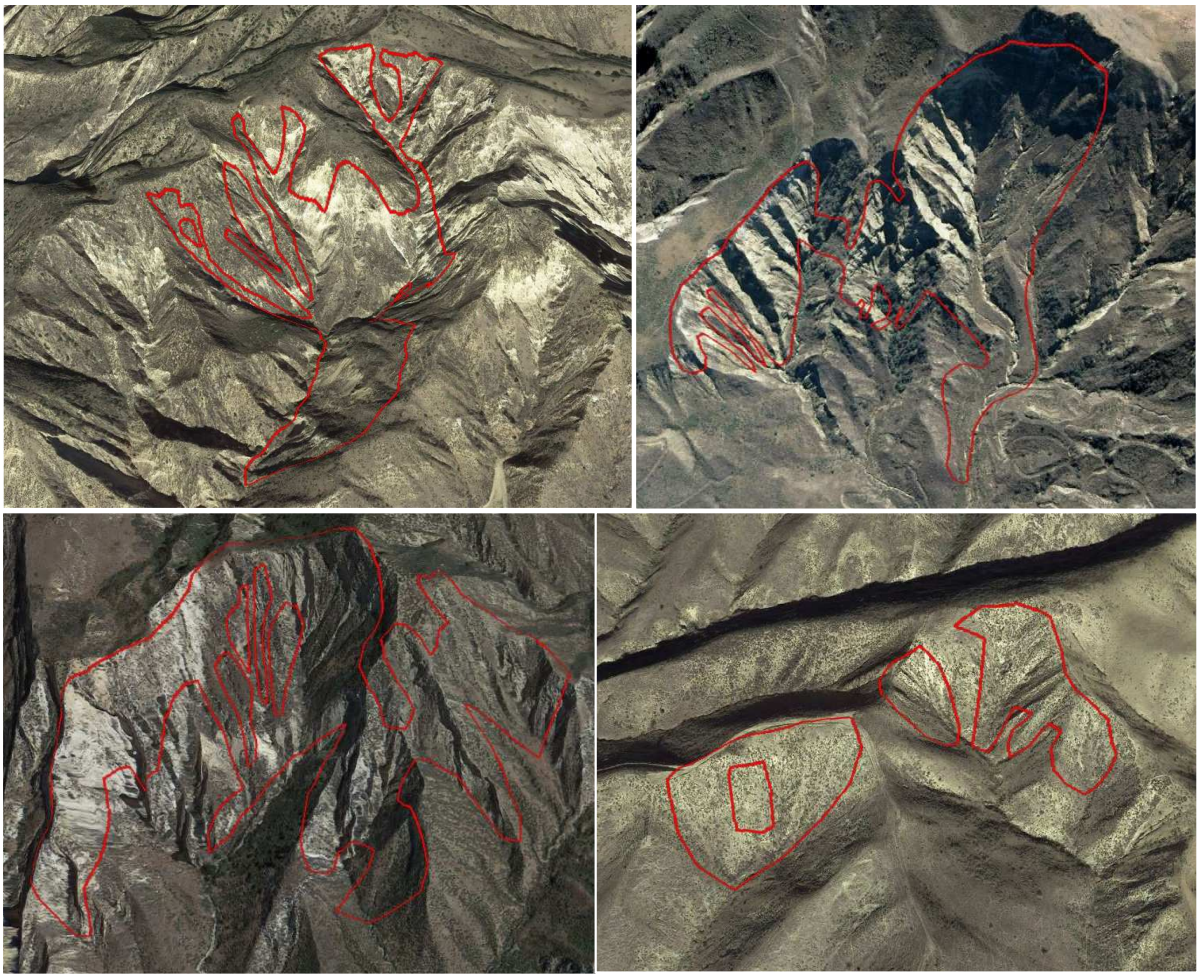

Figure 104. Examples of amalgamation of multiple landslides in one single polygon for the Northridge case study.

Indeed, where landsliding is very dense, several adjacent landslides may have joint runout areas or overlapping deposits, or scars separated by a distance too short to be resolved by the available image (Marc and Hovius, 2014). This issue was found in the Northridge and the Wenchuan inventories (Figure 104). The other inventories seem free from this error. Furthermore, during the digitizing process of the inventories some errors occurred, such as the creation of polygons without an actual shape or in areas without landslides (Figure 105). The available datasets were checked to delete this problem.

The second relevant issue is the undersampling of small landslides for such inventories (e.g. Wenchuan Earthquake, Figure 106), which is a process known as censoring. The peak in the distribution that separate the two regimes in the landslides distribution (the positive and negative power law scaling for small and large landslides, respectively) represents a crossover length scale. This crossover could be set either by the mapping resolution or by the landslide process itself.

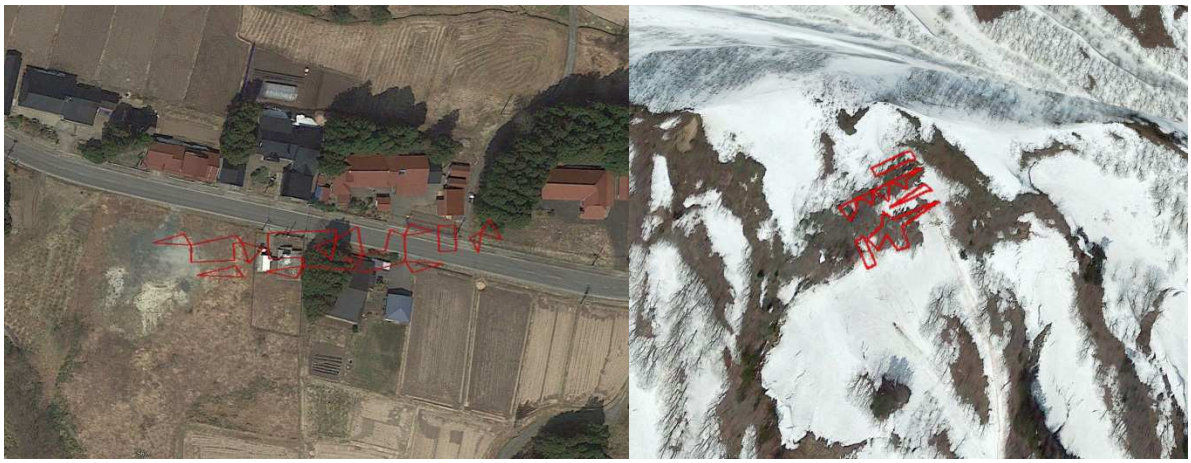

Figure 105. Examples of errors occurred during the digitizing process of the inventories related to the Iwate-Miyagi Nairiku Earthquake 2008.

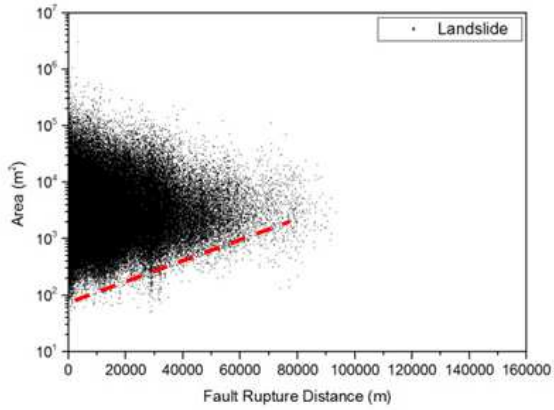

Figure 106. Example of undersampling in small landslides (see red line) for the inventories related to the Wenchuan Earthquake 2008. With the increased of the fault rupture distance the number of small landslides decrease with the same trend of the large landslides.

In other words, the distribution towards small events could be a real crossover from landsliding to other hillslope processes (Frattini and Crosta, 2013) or it could simply reflect the undersampling of landslides that are too small to be mapped accurately (Stark and Hovius, 2001).

Finally, there is also to consider for this analysis that others factors can induce variation in the trend, for example the distribution of the peak ground acceleration (PGA). In fact, there is a strong relationship between the PGA values and the landslides triggered by the earthquakes, In particular an increase in the PGA implies an increase in landslides area. Moreover the increase in magnitude and/or increase in distance shifts the predominant period of spectrum to larger values (Graizer and Kalkan, 2009), resulting in lower frequency signal. The area is generally larger for lower frequencies (Bourdeau et al., 2004). This means that the location, area and the volume of a landslide are likely to be dependent on varying site effects. It can be inferred that large magnitude

earthquakes tend to trigger larger landslides because of the larger ground accelerations and the low frequency content (see Chapter 7).

Other factors that can induce landslide with different can be the geological setting, the geomorphology of the affected area, catastrophic events (e.g. tsunami), hydrological condition, ancient precipitation, human activity on the hillslope. Above all the lithology could be the most important factor in the landslide size distribution, as discussed in the next chapter.

6 Relationship between landslides size distribution and geology in the affected area

Each type of earthquake-induced landslide occurs in a particular suite of geologic environments. These range from overhanging slope of well-indurated rock to slopes of less than 1° underlain by soft, unconsolidated sediments (Keefer, 1984). Few earthquake-induced landslides reactivate older landslides; most are in materials that have not previously failed (Keefer, 1984).

The landslide inventories were divided on the basis of the lithology in which each landslide occurred. In this way, different sub-set were identified for each earthquake, to verify if some lithology is more prone to give large landslides with respect to others in the affected areas. Not all the lithologies were considered. If the number of landslides was less than 100, the lithology was not analyzed because the sample was not sufficient. For this work, only three of the presented methodologies were applied: Maximum likelihood estimator of non-cumulative power-law function (PL); Least square regression of non-cumulative log power-law function (LF), and Maximum likelihood estimator of Double Pareto distribution (DP). This is related to the fact that the Maximum likelihood estimator of cumulative power-law distribution (Clauset et al, 2009) often gives result, that are difficult to interpret.

6.1 Papua New Guinea Earthquake, 1993

The lithology of Papua New guinea was grouped into four classes [see chapter: 4.1]. The probability density curves of the landsides occurred in each lithology were generated (Figure 107).

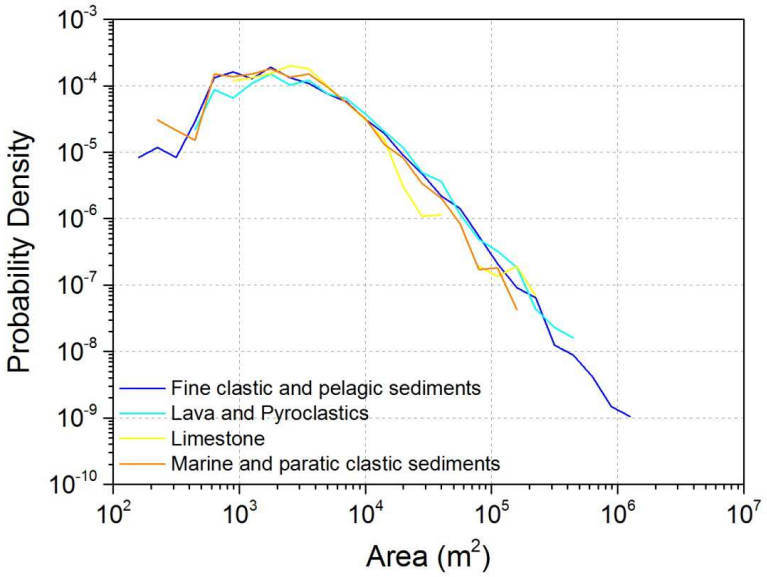

Figure 107. Probability Density curves for each lithology group considered, (geological map by Jaques, 1976).

Table 20. Number of landslides in each lithology, and values of the scaling parameter, *α*, defined through the different methodologies. See text for the PL, LF, DP meaning.

Group	Code	# landslides	DP	LF	PL
Fine clastic and pelagic sediments	1	2,637	2.42	2.09	2.07
Lava and Pyroclastics	2	1,422	2.36	2.11	1.65
Limestone	3	225	4.00	2.05	1.84
Marine and paratic clastic sediments	4	505	2.42	1.96	1.90

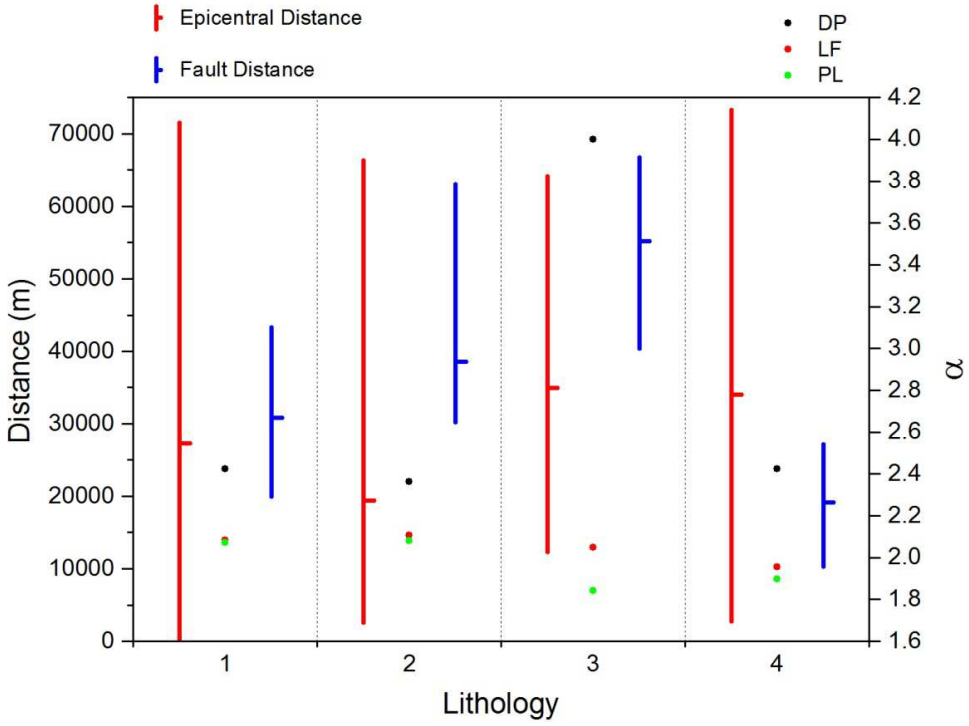

Figure 108. Graph showing the values of the scaling parameter, *α*, for each lithologies reported in Table 20. The information about the epicentral and fault distance for each lithology is shown. The numbers on the x axis referred to the code, and then to the lithology, in Table 20.

The values of the scaling parameter do not show great variations among the different methodologies. Only for the limestone (#3, Figure 108) the DP value is very high; however this could indicate that for this litohlogy, the Double Pareto distribution has not been able to properly fit the curve. For the Papua New Guinea earthquake there is no lithology that is more prone to landslides than others.

As it is possible to observe from Figure 109, the landslides mainly occurred in fine clastic and pelagic sediments at all distances, and then in volcanic rocks, near the epicenter (a) and far from the fault (b). However, it is worth mentioning that the distribution of landslides reflect the distribution of the lithologies with respect to the seismic source.

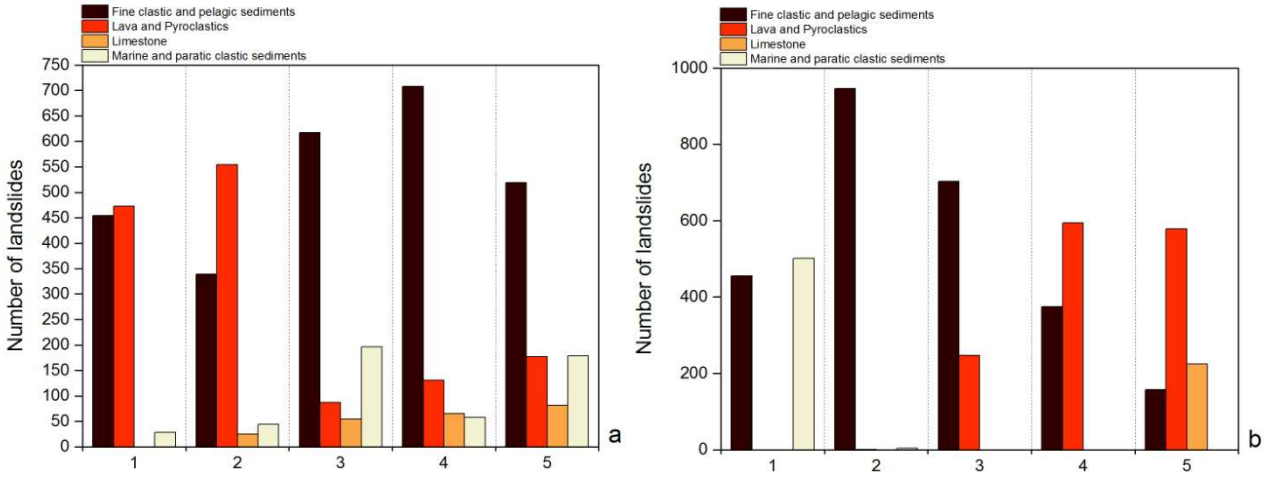

Figure 109. Graph showing the number of landslides each lithology divided on the basis of the epicentral distance (a) and fault distance (b). The numbers on the x axis referred to the code, and then to the distance in Table 8, and Table 9 for "a" and "b" respectively.

6.2 Northridge Earthquake, 1994

The lithology of Northridge was grouped into five classes [see chapter: 4.2]. The probability density curves of the landsides occurred in each lithology were generated (Figure 110).

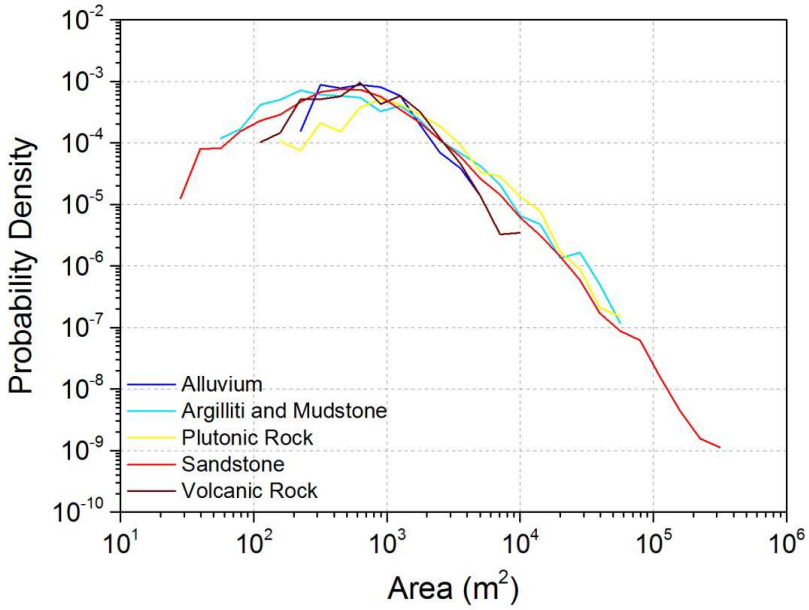

Figure 110. Probability Density curves for each lithology group considered (geological map by Jennings et al., 1977).

Table 21. Number of landslides in each lithology, and values of the scaling parameter, *α*, defined through the different methodologies. See text for the PL, LF, DP meaning.

Group	Code	# landslides	DP	LF	PL
Alluvium	1	99	4.00	2.63	3.06
Argillite and Mudstone	2	515	2.05	2.08	1.85
Plutonic rock	3	408	3.20	2.35	2.11
Sandstone	4	9,679	2.90	2.49	2.21
Volcanic rock	5	297	3.13	2.86	2.85

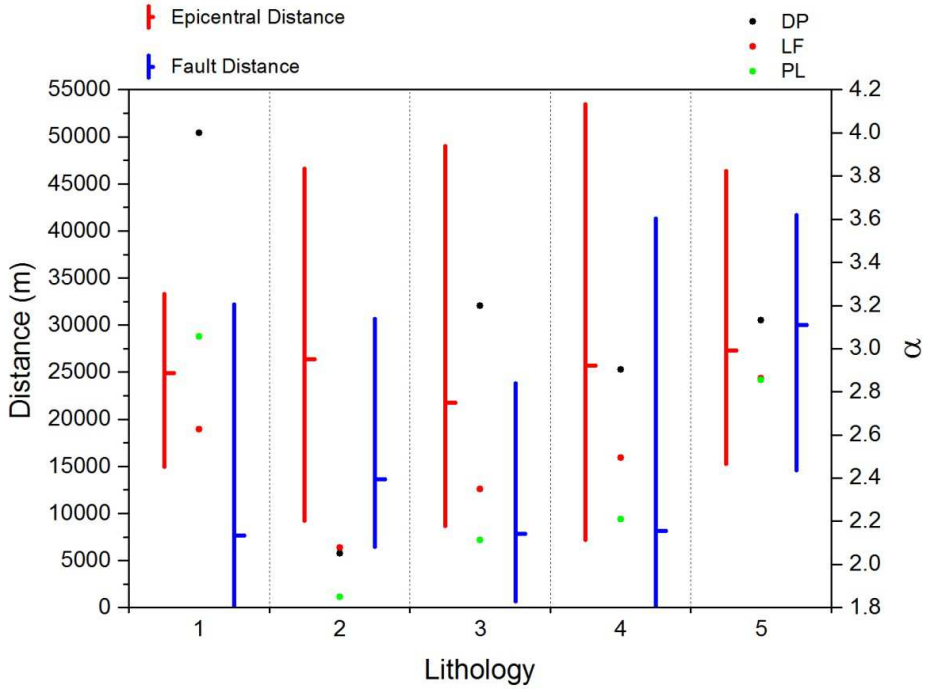

Figure 111. Graph showing the values of the scaling parameter, *α*, for each lithologies reported in Table 21. The information about the epicentral and fault distance for each lithology is showed. The numbers on the x axis referred to the code, and then to the lithology, in Table 21.

In Figure 110 the probability density curve are represented. In the area affected by the Northridge Earthquake, the argillite and mudstone are prone to give landslides with large area, in fact the exponent of the probability density curve is low. While the volcanic rocks seem to have an high value of the scaling parameter and this means landslides with small area (Table 21, Figure 111). Figure 112 shows that landslides in argillite and mudstone are present near and far from the epicenter and far from the fault, while the landslides in volcanic rocks are present at all distances from the epicentre and very far from the fault. These two lithologies seem to influence the exponent of the probability density curves with the distance from the seismic source, but the signal come from this two groups is covered by sandstone that are the predominant lithology in which the

landslides occurred at all distances, and whose exponent has an intermediate value between argillite and mudstone, and volcanic rocks.

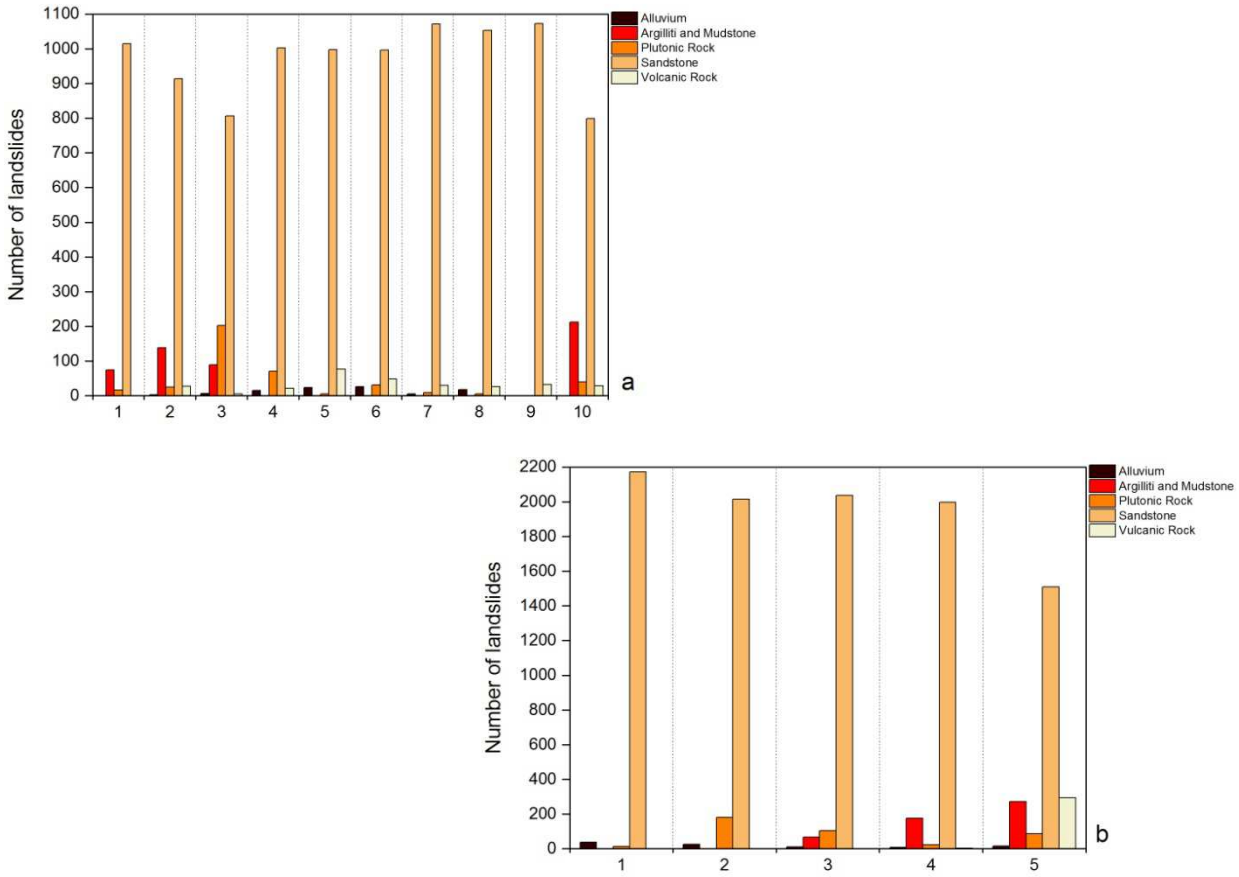

Figure 112. Graph showing the number of landslides each lithology divided on the basis of the epicentral distance (a) and fault distance (b). The numbers on the x axis referred to the code, and then to the distance Table 10, and Table 11 for "a" and "b" respectively.

6.3 Niigata-Chuetsu Earthquake, 2004

In this case one of the lithology present in the area, limestone, was deleted from the analysis due to the low number of landslides occurred inside it. Figure 113 show the probability frequency curves for the earthquake-induced landslides in each lithology. Observing the curves seem to present two regimes, the first consisting of Sandstone and Tertiary group, the other by Quaternary group and Volcanic rocks.

Table 22. Number of landslides in each lithology, and values of the scaling parameter, *α*, defined through the different methodologies. See text for the PL, LF, DP meaning.

Group	Code	# landslides	DP	LF	PL
Quaternary	1	5,717	4.00	2.60	2.73
Sandstone	2	4,457	3.20	2.31	2.11
Tertiary	3	102	4.00	1.79	2.06
Volcanic rock	4	234	4.00	2.54	2.12

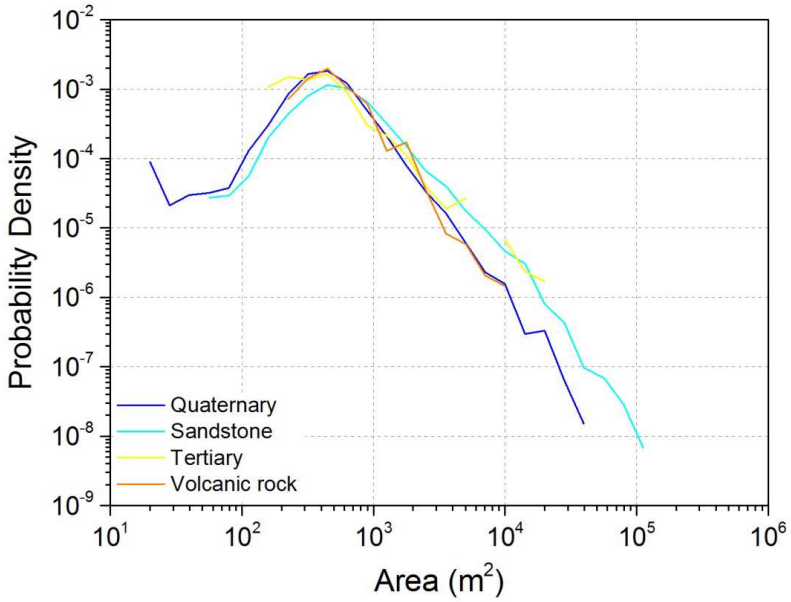

Figure 113. Probability Density curves for each lithology group considered (geological map by by the Geological Survey of Japan 2012).

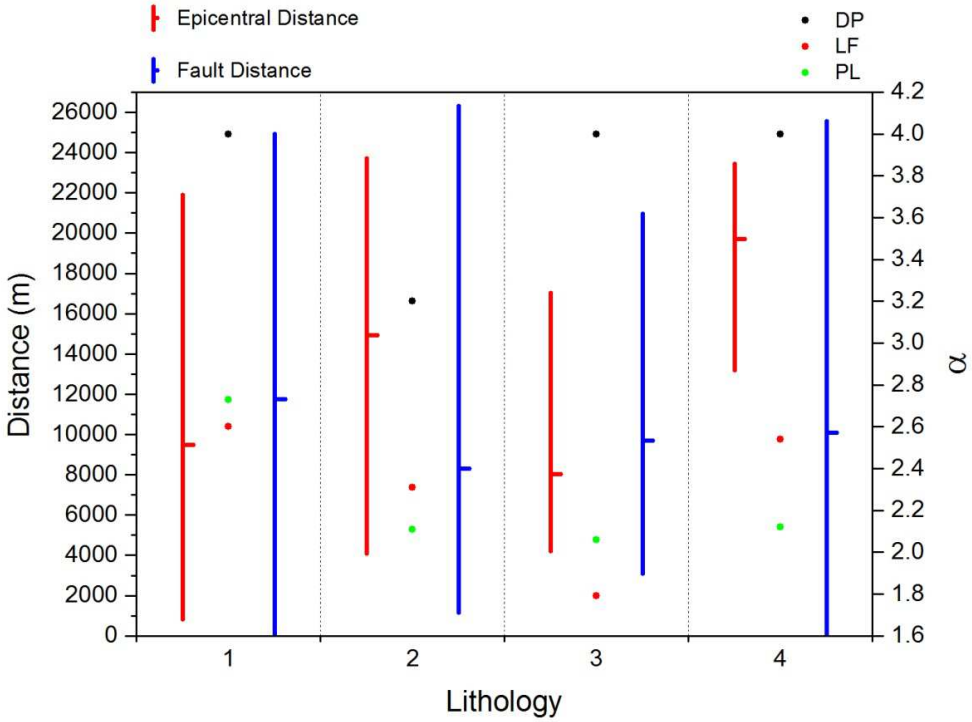

Figure 114. Graph showing the values of the scaling parameter, *α*, for each lithologies reported in Table 22. The information about the epicentral and fault distance for each lithology is showed. The numbers on the x axis referred to the code, and then to the lithology, in Table 22.

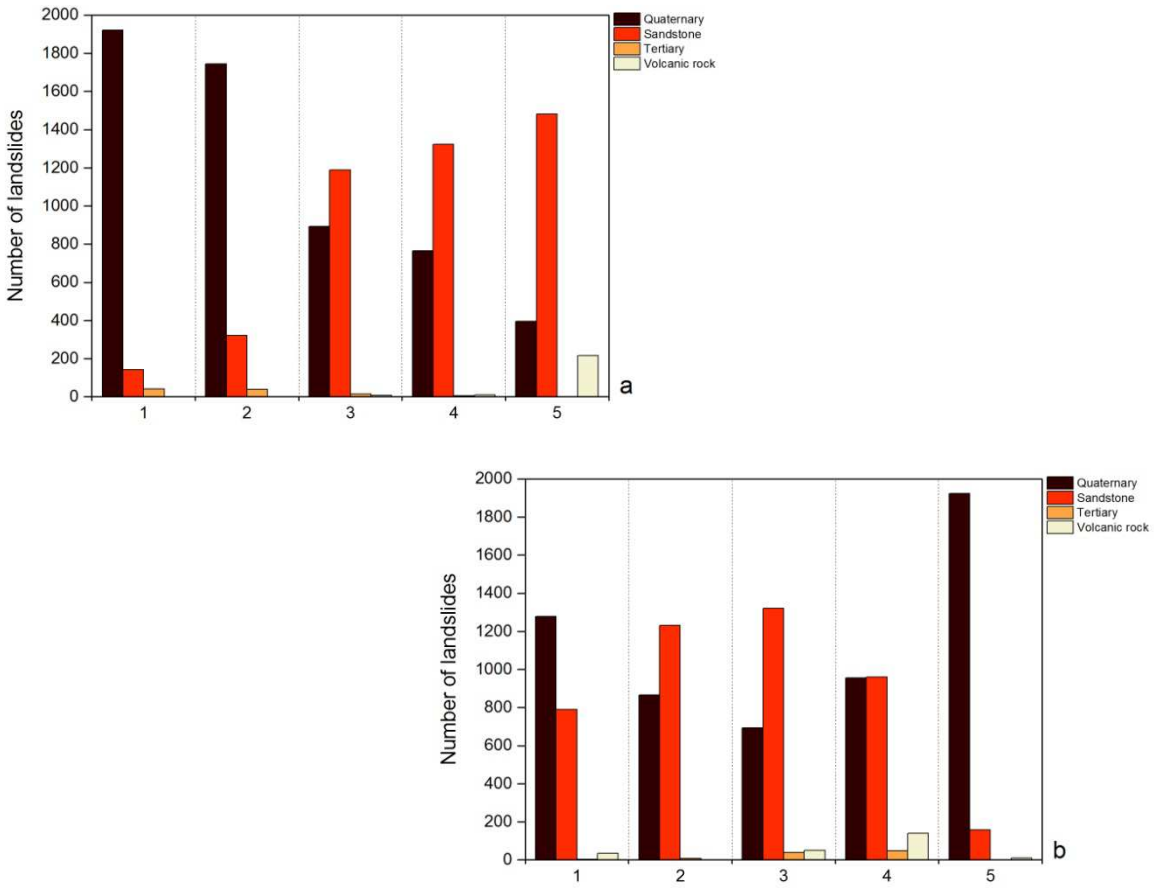

Figure 115. Graph showing the number of landslides each lithology divided on the basis of the epicentral distance (a) and fault distance (b). The numbers on the x axis referred to the code, and then to the distance in Table 12 and Table 13 for "a" and "b" respectively.

The DP methodology in the case of the Niigata-Chuetsu case study, is not able to fit the curves and, as consequence, shows very high values (see appendix 3). The others two methods are characterized by the similar trend (Figure 114). The Quaternary have the highest values of the scaling parameter, α, this meaning that this lithology is prone to give landslides with small area with respect to the others. Figure 115 shows that the landslides occurred predominantly in Quaternary at distance closed to the epicenter. While it is the predominant lithology in the first and last distance from the fault. As it is possible to see, this has an effect on the exponent derived from the sub-set of landslides divided on the basis of the epicentral and fault distance (Figure 85 and Figure 88). Where this lithology is predominant, the exponent of the curves seem higher than the expected trend. Hence the interplay between distance and lithology is quite complex.

6.4 Wenchuan Earthquake, 2008

On the basis of 1:200,000 geological map of China Geological Survey, the landslides were divided in ten lithological groups [see chapter: 4.4] and the relative probability density were built (Figure 116).

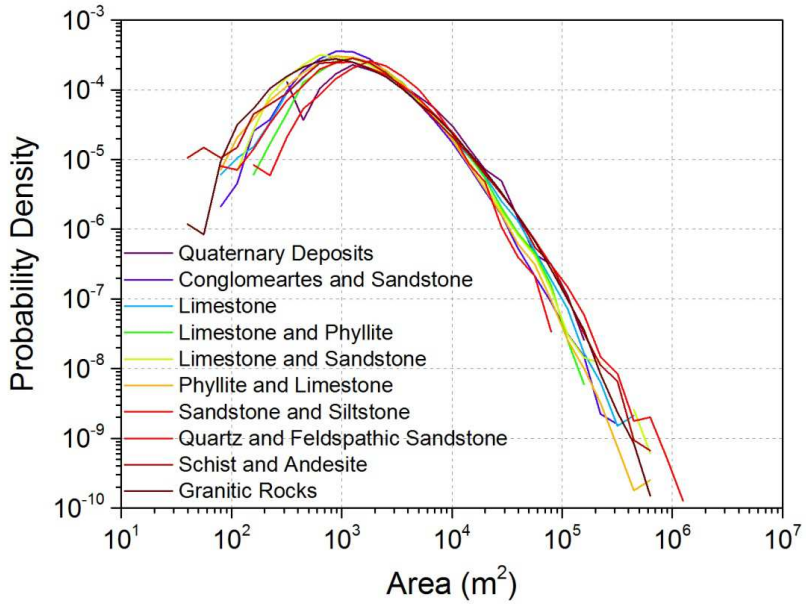

Figure 116. Probability Density curves for each lithology group considered (geological map by the China Geological Survey).

Table 23. Number of landslides in each lithology, and values of the scaling parameter, *α*, defined through the different methodologies. See text for the PL, LF, DP meaning.

Group	Code	# landslides	DP	LF	PL
Quaternary Deposits	1	831	2.71	2.27	1.81
Conglomerates and Sandstone	2	20,380	2.61	2.71	3.05
Limestone	3	14,320	2.35	2.85	2.24
Limestone and Phyllite	4	3,589	2.45	2.23	2.26
Limestone and Sandstone	5	42,725	2.21	2.39	2.45
Phyllite and Limestone	6	8,911	2.60	3.01	2.50
Sandstone and Siltstone	7	21,567	2.26	2.54	2.02
Quartz and Feldspathic Sandstone	8	2,575	3.08	2.76	2.67
Schist and Andesite	9	8,175	2.53	2.76	2.41
Granitic rock	10	72,933	2.15	3.17	3.12

In general, all the lithologies are characterized by medium-high values of the exponent α (Figure 117). As it is possible to observe, the lithologies of the area cover the same distance from the seismic source, except the Quartz and Feldspathic Sandstone group, which is the most distant (#8, Figure 117). This lithology shows high exponents, with consequently small landslides. Two alternative hypothesis can be made: the lithology controls the landslides size, or the distance controls the landslides size (far from the source is more likely to have landslides of lesser area). Figure 118 indicates that the Granitic rocks group and the Conglomerates and Sandstone group have the higher number of landslides in the study area; hence, it is possible that they can influence the landslides size. Both the lithologies show high values of the scaling parameter for all the methodologies applied, and this mean an higher contribution in small landslides (#2 and #10,).

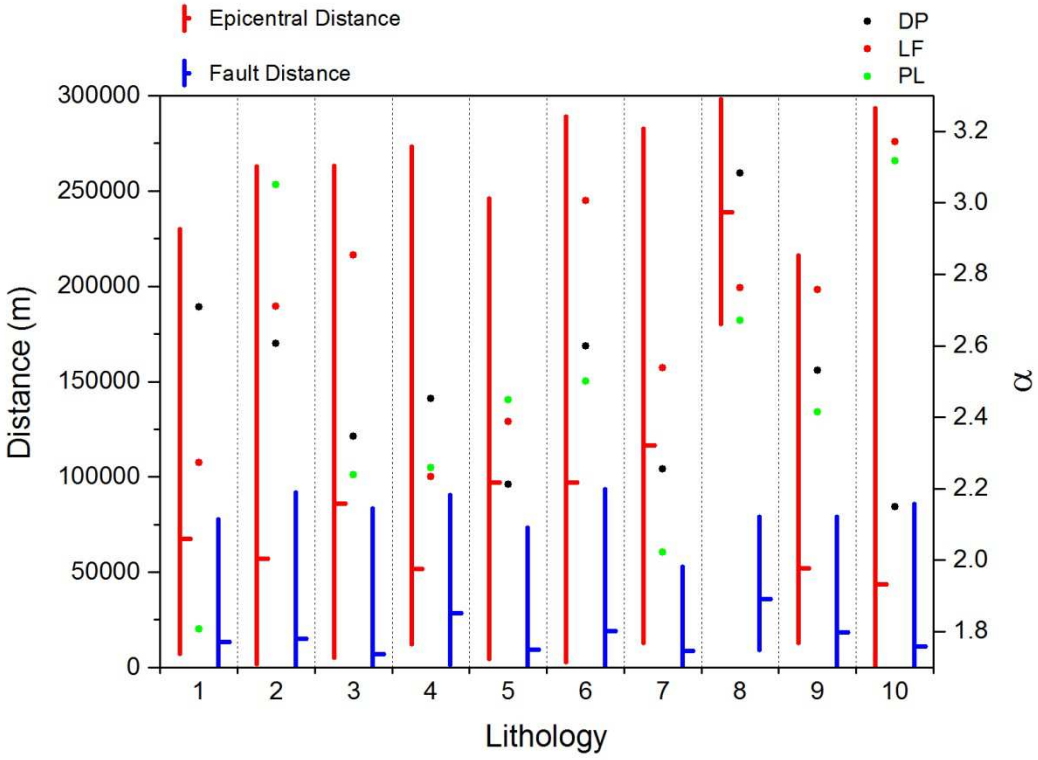

Figure 117. Graph showing the values of the scaling parameter, *α*, for each lithologies reported in Table 23. The information about the epicentral and fault distance for each lithology is showed. The numbers on the x axis referred to the code, and then to the lithology, in Table 23.

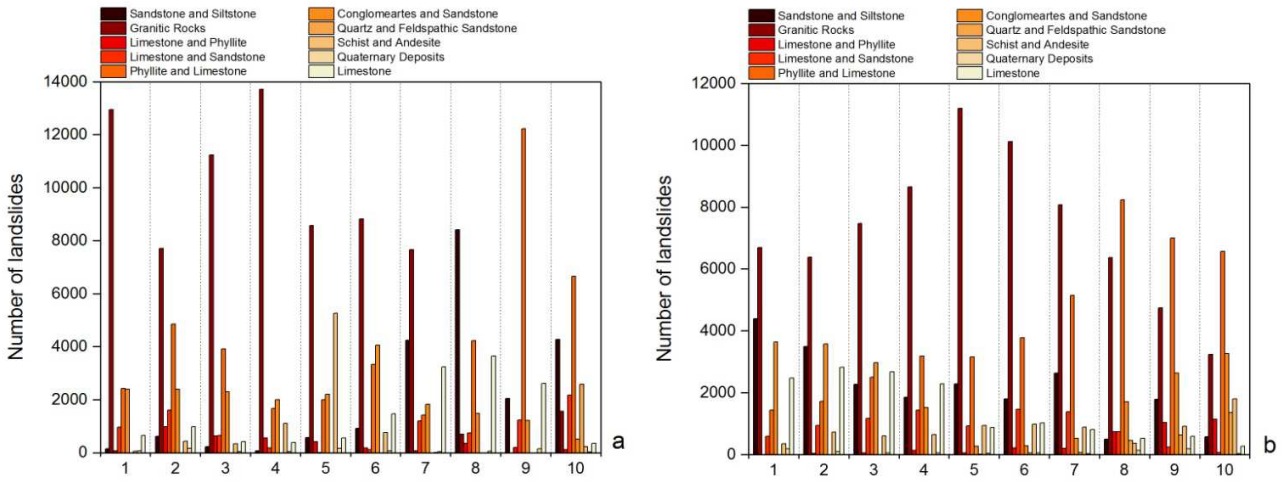

Figure 118. Graph showing the number of landslides each lithology divided on the basis of the epicentral distance (a) and fault distance (b). The numbers on the x axis referred to the code, and then to the distance in T**able 14 and Table 15 for "a" and "b" respectively.**

6.5 Iwate-Miyagi Nairiku Earthquake, 2008

In the area affected by the Iwate-Miyagi Nairiku Earthquake five groups of different lithologies were identified [see chapter: 4.5], but the analysis was performed only on three of them, due to the low number of landslides in the others. The lithologies deleted are: sandstone and plutonic rocks.

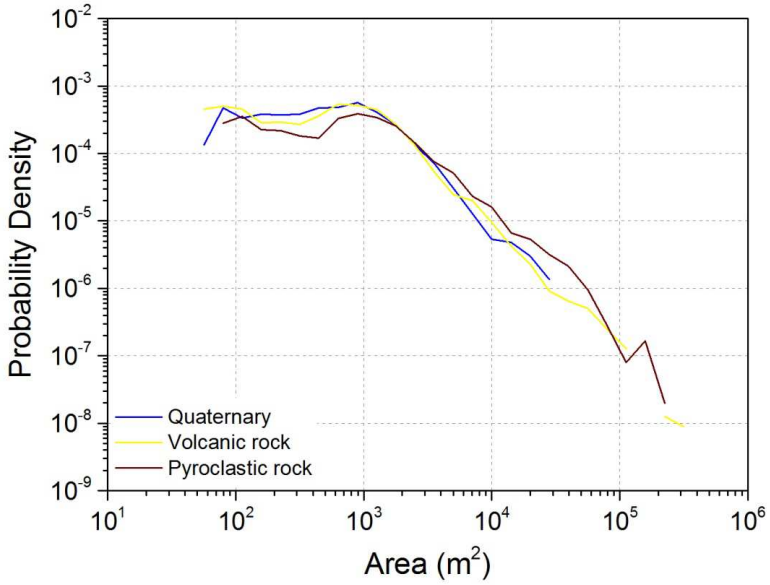

Figure 119. Probability Density curves for each lithology group considered (geological map by by the Geological Survey of Japan 2012).

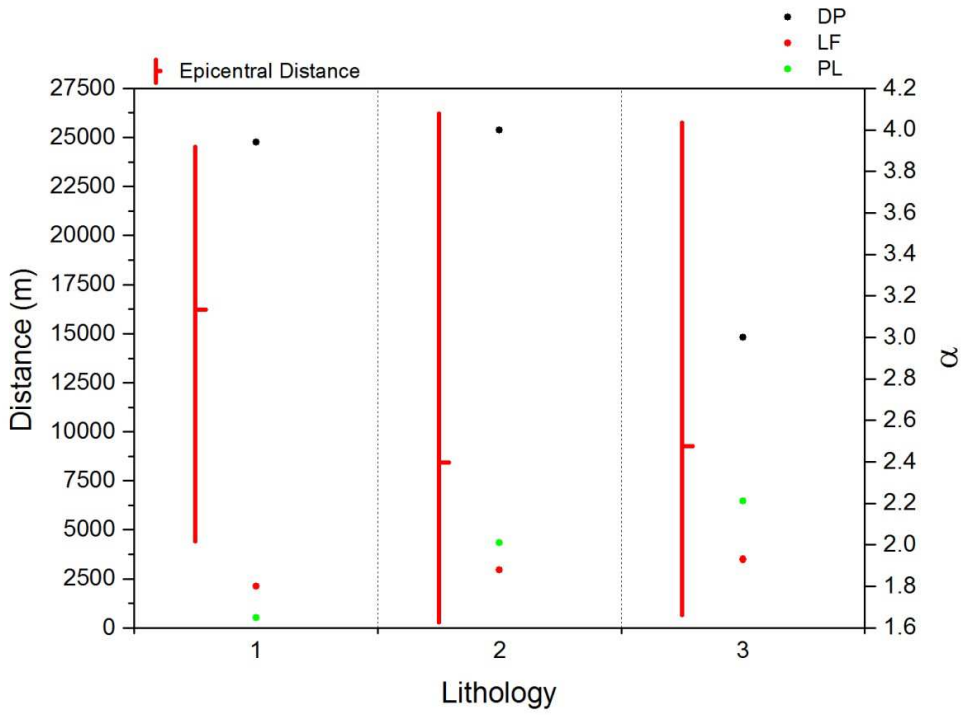

Figure 120. Graph showing the values of the scaling parameter, *α*, for each lithologies reported in Table 24. The information about the epicentral and fault distance for each lithology is showed. The numbers on the x axis referred to the code, and then to the lithology, in Table 24.

Table 24. Number of landslides in each lithology, and values of the scaling parameter, *α*, defined through the different methodologies. See text for the PL, LF, DP meaning.

Group	Code	# landslides	DP	LF	PL
Pyroclastic rock	1	770	3.94	1.80	1.65
Quaternary	2	452	4.00	1.88	2.01
Volcanic rock	3	1,207	3.00	1.93	2.21

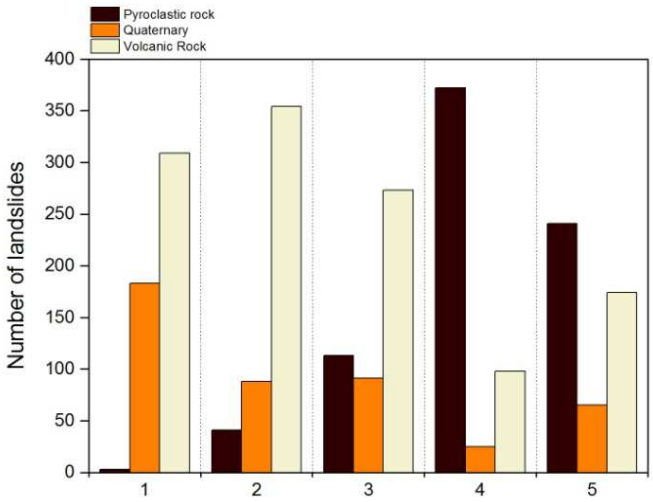

Figure 121. Graph showing the number of landslides each lithology divided on the basis of the epicentral distance. The numbers on the x axis referred to the code, and then to the distance in Table 24.

The volcanic rocks shows the highest value of the exponent in the affected area (Table 24, Figure **120**), and reasonably this means that they can give a greater contribution in small landslides. As the case of Niigata-Chuestsu Earthquake, there is an influence of this lithology in the trend of the exponent moving away from the seismic source. In particular this lithology is predominant in the first classes of distance from the epicenter (Figure 119), where the curves show an exponent higher than the others (Table 16).

6.6 Tohoku Earthquake, 2011

From the available geological map, eleven groups of lithology were extracted [see chapter: 4.6], but only six have been used for the analysis; the relative probability density curves built for the selected lithologies (Figure 122).

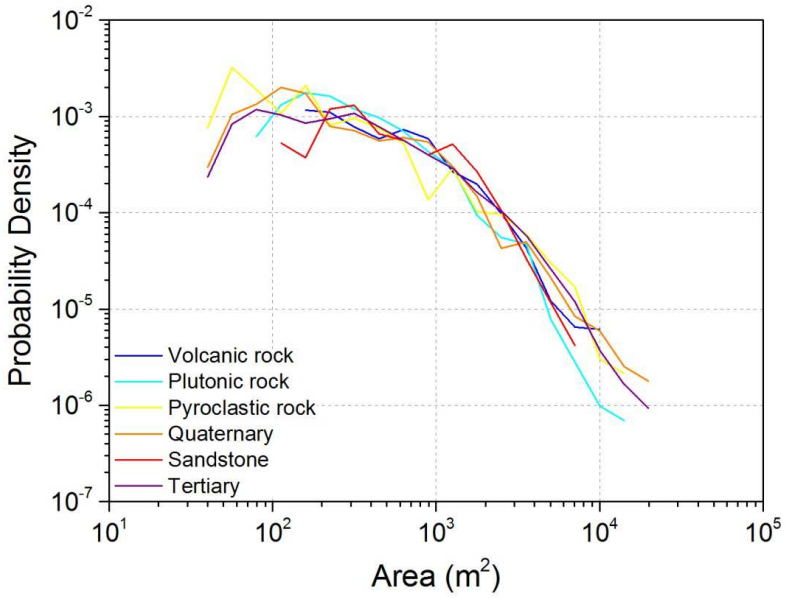

Figure 122. Probability Density curves for each lithology group considered (geological map by by the Geological Survey of Japan 2012).

Table 25. Number of landslides in each lithology, and values of the scaling parameter, *α*, defined through the different methodologies. See text for the PL, LF, DP meaning.

Group	Code	# landslides	DP	LF	PL
Plutonic rock	1	347	2.38	2.61	2.62
Pyroclastic rock	2	113	2.00	1.61	1.36
Quaternary	3	289	2.00	1.87	1.97
Sandstone	4	116	2.00	2.86	2.81
Tertiary	5	734	2.07	2.40	1.60
Volcanic rock	6	223	2.03	1.98	1.83

The exponent of the Pyroclastic rocks is low with respect to the others lithologies considered for this earthquake (Table 25 and Figure 123). The higher number of landsides occurred far from the epicenter (Figure 124). Considering the exponent related to the distance from the epicenter (Figure 99) a lower values than the others has been found. The Plutonic rocks group show high values of the scaling parameter α (Table 25 and Figure 123). The landslides occurred in this lithologies are the more abundant in the second class of distance from the fault rupture (Figure 124) whose exponent show high values respect the others classes (Figure 101). Hence an influence of these two lithologies in the landslide size can be assumed.

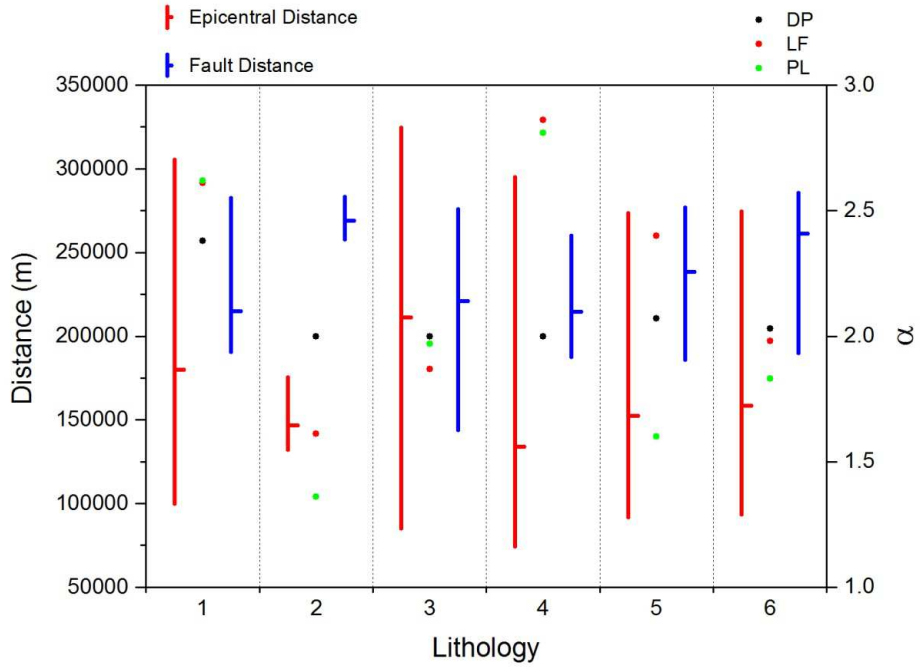

Figure 123. Graph showing the values of the scaling parameter, *α*, for each lithologies reported in Table 25. The information about the epicentral and fault distance for each lithology is showed. The numbers on the x axis referred to the code, and then to the lithology, in Table 25.

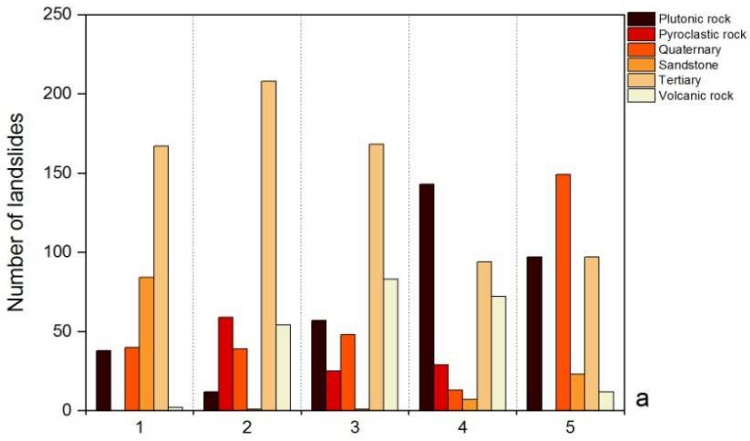

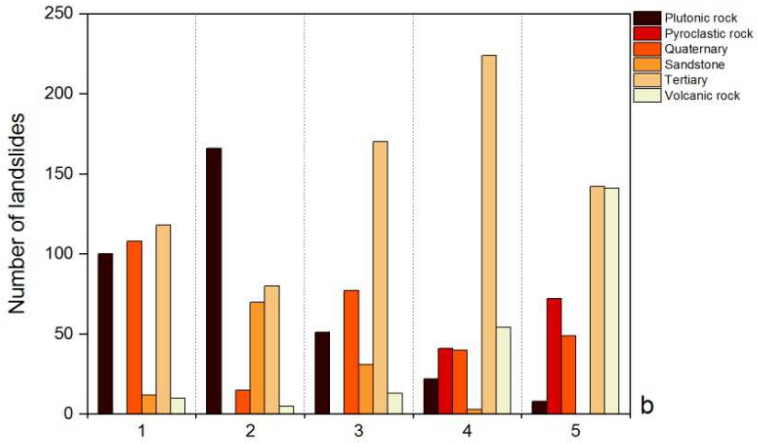

Figure 124. Graph showing the number of landslides each lithology divided on the basis of the epicentral distance (a) and fault distance (b). The numbers on the x axis referred to the code, and then to the distance in Table 17, and Table 18 for "a" and "b" respectively.

6.7 Discussion

The geology is an important factor in the triggering of landslides. In the case of earthquake-induced landslides, it was showed how a particular kind of lithology , that is prone to give a particular size of landslides, can influenced the spatial distribution of the landslides size in the affected area, in relation to their position with respect to the seismic source.

From the analysis, it seems that there is a strong relation between the lithology in which the landslide occurred and the distance at which the landslide occurred. In particular, considering the area of Japan (Table 26), in which three earthquakes with different magnitude are reported, it is possible to observe how some lithologies have very similar exponent values (such as Volcanic rocks), while others, that are analysed, show different values between the three earthquakes (such as Sandstone).

Table 26. Scaling parameter, *α*, for the three Japan Earthquake.

	Pyroclastic rock			**Quaternary**			**Sandstone**			**Tertiary**			**Volcanic rock**		
	DP	**LF**	**PL**	**DP**	**LF**	**PL**	**DP**	**LF**	**PL**	**DP**	**LF**	**PL**	**DP**	**LF**	**PL**
Tohoku	2.00	1.61	1.36	2.00	1.87	1.97	2.00	2.86	2.81	2.07	2.40	1.60	2.03	1.98	1.83
Iwate	3.94	1.80	1.65	4.00	1.88	2.01							3.00	1.93	2.21
Niigata				4.00	2.60	2.73	3.20	2.31	2.11	4.00	1.79	2.06			

This indicates, that some lithologies are not much affected by the distance from the seismic source (major control of the lithology on landslides size distribution), while other are partially affected by the seismic shock, and then on the distance, that influenced the landslides size. This fact, that was found also in the other earthquakes, can have an influence on the previous analysis, as showed, because different factors can control the landslides size distribution and the lithology is one of them. Relatively the methodology applied, the DP method often has problem in the fit of the data, and showed a exponent values of 4: the reasons of this problem are discussed in the previous analysis.

7 Analysis of landslide event magnitude as a function of earthquake magnitude

7.1 Landslide size as a function of earthquake magnitude

The landslide event magnitude can be expressed in terms of landslides area. The area-frequency distributions of landslides were examined by developing logarithmically binned, non-cumulative size frequency distributions that report frequency density (f = dN/dA) as a function of landslide planar area A (dN = number of landslides with an area between A and A+dA). For the analysed earthquakes, a linear fit is performed, after a certain values of landslide size, to define the scaling exponent, α, of the distribution. The following values were found: Niigata-Chuetsu Earthquake, Japan, α = -2.36; Northridge, USA, α = -2.39; Iwate-Miyagi Nairiku Earthquake, Japan, α = -1.93; Papua New Guinea Earthquake, α = -2.05; Iningahua, New Zealand, α = -2.53; Chi-Chi, Taiwan, α = -2.30; Buller, New Zealand, α = -2.42; Wenchuan Earthquake, China, α = -2.64; Tohoku Earthquake, Japan, α = -2.47, (Figure 125).

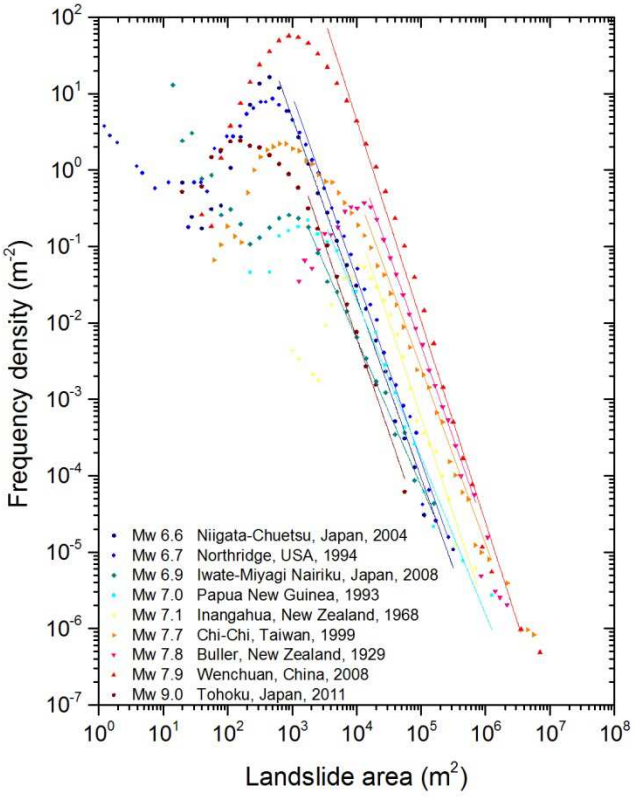

Figure 125. Frequency density vs area for earthquake-induced landslide inventories (Niigata-Chuetsu, Yagi et al., 2007; Northridge, Harp and Jibson, 1995; Iwate-Miyagi Nairiku, Yagi et al., 2009; Papua New Guinea, Meunier 2008; Buller and Iningahua, Parker, 2013; Chi-Chi, Liao and Lee, 2000, Wenchuan, Xu et al., 2013; Tohoku, Wartman et al., 2013). Lines represent the fitting curves of the power-law range of each inventory.

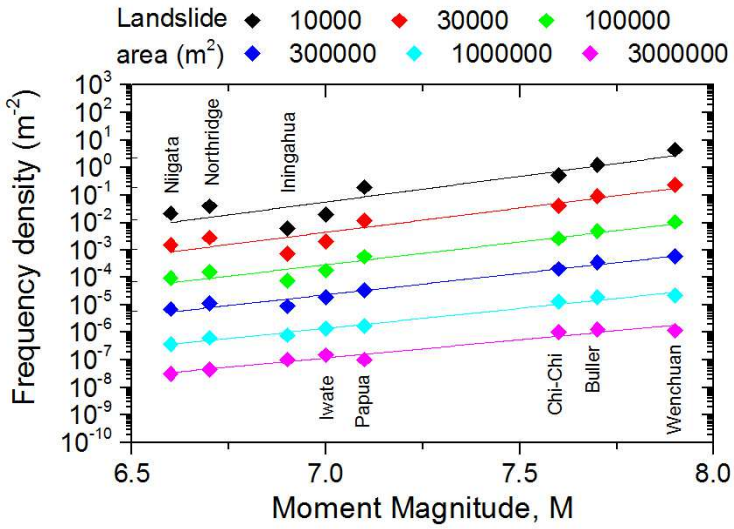

Figure 126. Relationship between the earthquake Magnitude and the frequency density, f, for earthquake-induced landslides.

By analysing the frequency size relationships for earthquake-induced landslides (Figure 125) it is possible to observe that the higher the earthquake Magnitude, the higher the frequency density curve. The only exception is Tohoku earthquake, but this is related to the position of the dataset respect the seismic source. The earthquake occurred at a very high distance from coast of Japan in the seduction zone, for this reason the landslides are small in relation to the magnitude of the earthquake.

To quantify the observation above, the power-law relationships derived for each available inventory were used to calculate the frequency density associated to selected landslide size (in area), and these frequencies were plotted as a function of the magnitude of the respective earthquakes (Figure 126). For each area value, a clear linear trend exists between earthquake magnitude and logarithm of landslide frequency density.

7.2 From landslide inventory to earthquake magnitude

This linear trend can be used to estimate the expected magnitude for historical landslide inventories for which a magnitude is not available, e.g. Chile inventory. The size frequency distribution of the Chile inventory presents a strong undersampling for smaller landslides, due to the extremely old age of the inventory. For landslides larger than $2 \cdot 10^6$ m^2, the distribution exhibits a power-law behavior with scaling exponent, α, equal to -2.24 (Figure 127).

Through the fitting curve identified for each landslide size (Figure 126), it is possible to define the frequency density for the Chile inventory associate to the selected landslide size.

The three largest landslides in the inventory (Lluta, Minimini and Latagualla, see chapter 4.8) have been excluded from this analysis, and three possible scenarios were considered (Figure 128):

1) all landslides triggered during 1 single earthquake;

2) landslides triggered during 3 equal-magnitude earthquakes;

3) landslides triggered during 10 equal-magnitude earthquakes.

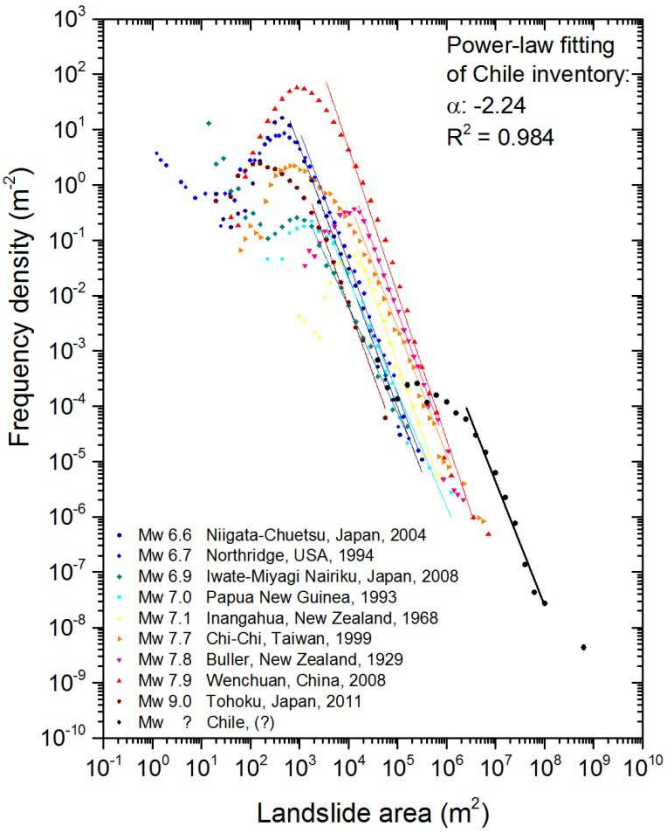

Figure 127. Frequency density vs area for the Chile inventory and the others earthquake-induced landslide inventories. Lines represent the fitting curves of the power-law range of each inventory.

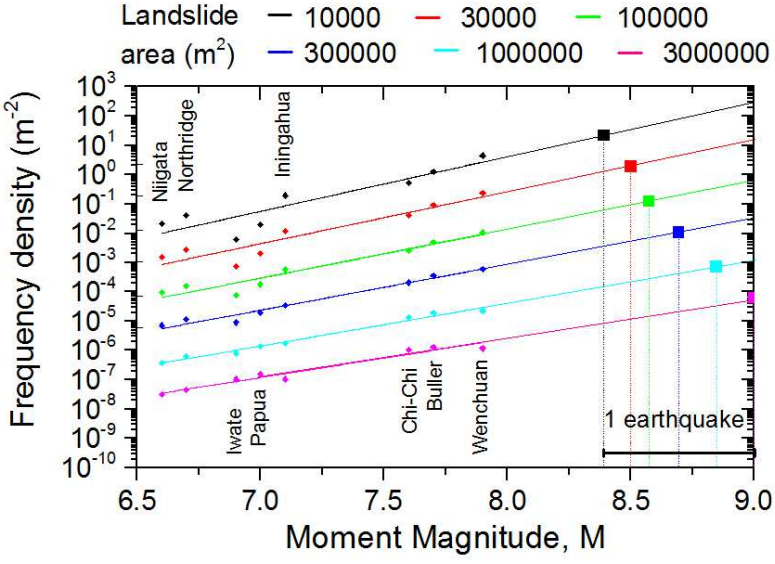

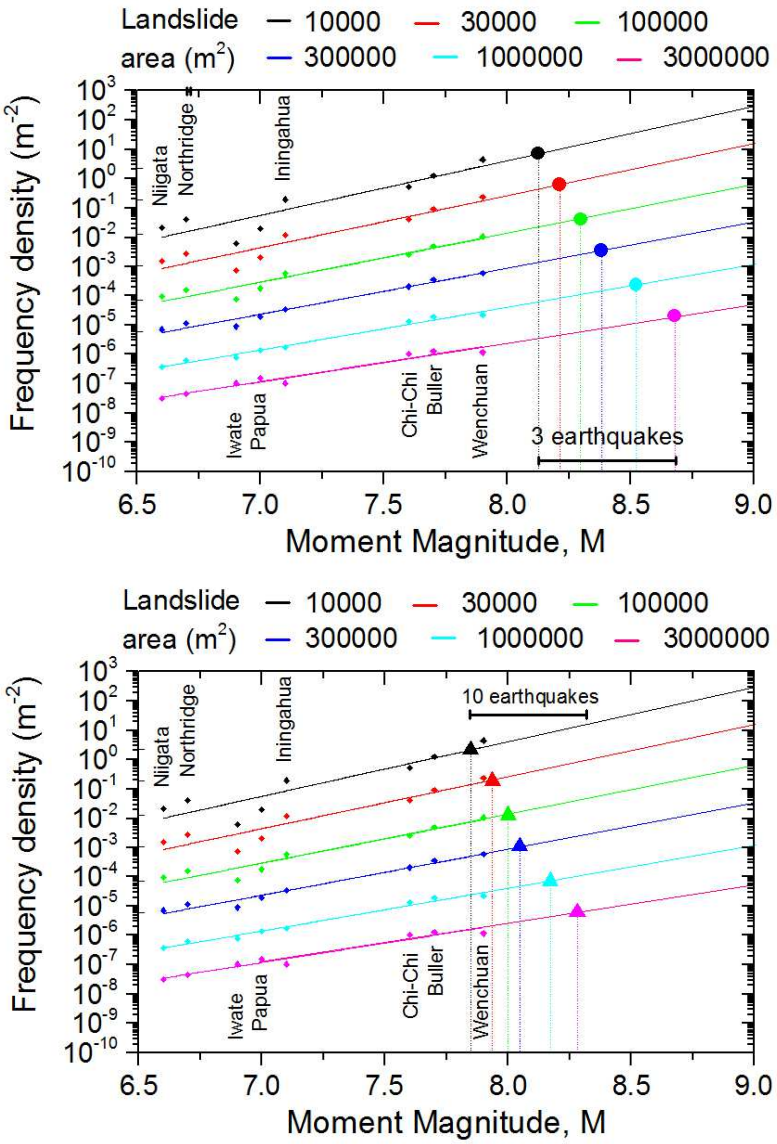

Figure 128. Relationship between the earthquake Magnitude and the frequency density, f, for earthquake-induced landslides. The extrapolated linear relationships between magnitude and log(f) was used to calculate the expected Magnitude of earthquake (or multiple earthquakes) required for Chile landslides triggering.

As a results, for scenario 1, 2 and 3 an estimated earthquake magnitude of 8.67 ±0.23, 8.37 ±0.20, 8.05 ±0.16, respectively were obtained. In a previous work, Crosta et al. (2014) analysed the same literature event reported in this work (Buller and Iningahua; Northridge; Chi-Chi; Wenchuan) and the estimated earthquake magnitude was 8.71 ± 0.05, 8.39 ± 0.02, 8.03 ± 0.02 for scenario 1, 2 and 3, respectively (Figure 129). The inventory of the Wenchuan earthquake in Crosta et al. (2014) referred to the dataset published in Parker (2013) and it is different from the inventory used in this work (Xu et al., 2013). Instead, the inventory of Northridge is the same. As it is possible to see, the uncertainty in the estimation of the magnitude related to the three scenarios is very different in range. In the analysis of this thesis three new inventory related to the Papua New Guinea earthquake, Niigata-Chuetsu earthquake, Iwate-Miyagi Nairiku earthquake were introduce.

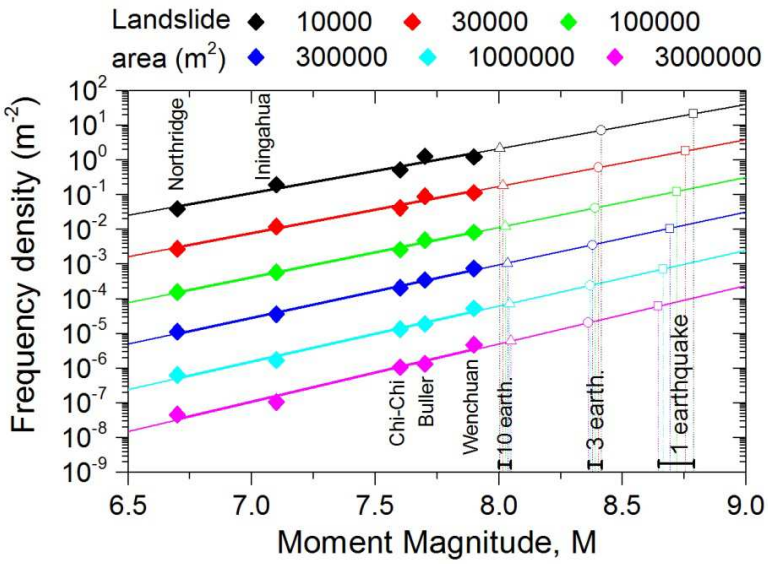

Figure 129. Relationship between the earthquake Magnitude and the frequency density, f, for earthquake-induced landslides., and expected Magnitude of earthquake (or multiple earthquakes) required for Chile landslides triggering; (Crosta et al., 2014).

This three earthquakes have the lowest values of the scaling parameter, α, for the area-frequency distribution (Figure 125 and text). They show high values of frequency density for larger landslides with respect to the earthquake with similar magnitude, and lower values for the smaller landslides. As a consequence, there is a significant change in the slope of the fitting curves (the gap increase with the magnitude), increasing the uncertainty for the estimated earthquake magnitude for the Chile earthquake. Another difference is the area-frequency distribution of the Wenchuan earthquake inventory. The inventory of Xu et al. (2013) show a higher values of the scaling parameter, α, with respect to the inventory of Parker (2013).

7.3 Relationship between the earthquake magnitude and the total landslide volume

An approach, present in literature, to establish a relationship between the earthquake magnitude and the landslide event magnitude, is the relationship between total landslide volume and earthquake magnitude. Keefer (1994) obtained an empirical correlation between the total volume of landslides triggered by an earthquake (V_{LT}) and the earthquake's moment magnitude (M). Keefer (1994) considered the total volume of landslide material generated by 16 historical earthquakes, as determined by several investigators using aerial photographs and field investigations. Despite the wide variety of geological (topography and rock type), geophysical (earthquake type and depth), and climatic conditions associated with these earthquake-triggered landslide events, a reasonably good power-law dependence of the total landslide volume V_{LT} on the earthquake's moment magnitude (M) was established. The data used by Keefer (1994; 2002) are given in Figure 130, the

total landslide volume was obtained by converting each landslide area to a volume and summing. The least-square best-fit line to the log V_{LT} as function of M data, gives:

$$\log V_{LT} = 1.42 \cdot M - 11.26(\pm 0.52)$$

with V_{LT} in km^3. The error bounds (±0.52) represent the standard deviations of the fit. This correlation (solid line), along with the error bounds (dashed-lines), are given in Figure 130.

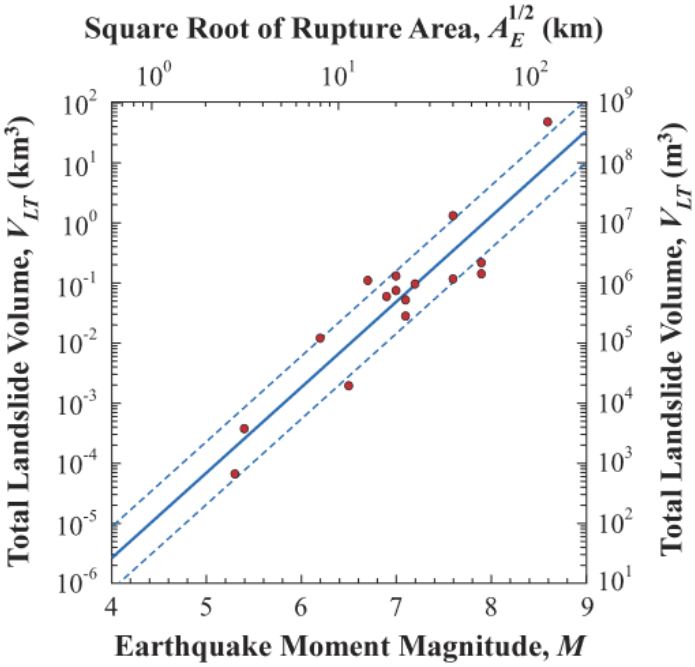

Figure 130. The total volume of landslides V_{LT} triggered by an earthquake is given as a function of the earthquake moment magnitude M. Also given is the square root of the equivalent rupture area $A_E^{1/2}$. Circles are volumes of landslides associated with 16 landslide events. The solid line is the least-square best-fit straight line to the data; dashed lines give the standard deviations of the data with respect to the best fit.

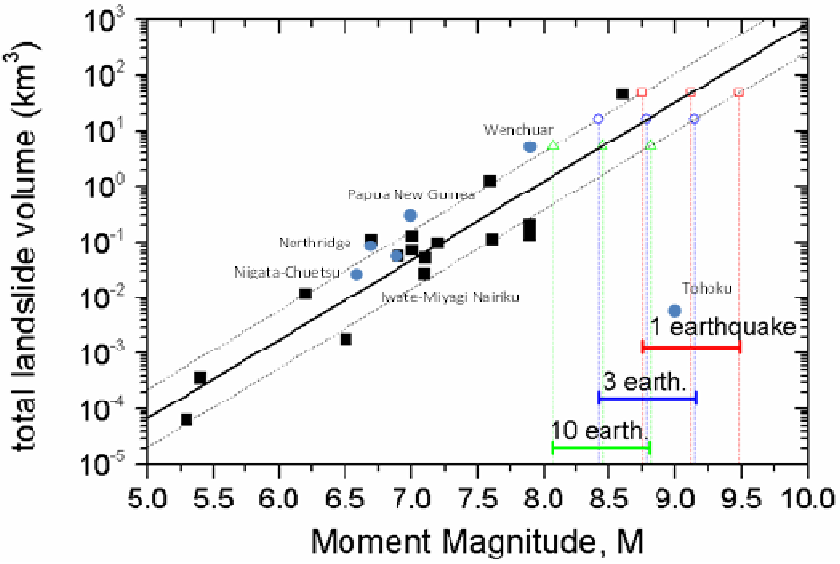

Figure 131. Relationship between the earthquake Magnitude and the total landslide volume of earthquake-induced landslides. The fitting line (Malamud et al, 2004a) was used to calculate the Magnitude of earthquake (or multiple earthquakes) required for Chile landslides. The total volume of the earthquake-induced landslide inventories used, is reported (blue dots).

This approach has been applied to the Chile inventory (Figure 131), by introducing the total volume of landslides calculated from areas by using the relationship proposed by Larsen et al. (2010) for rock slides (amounting to 45 km^3), an estimated earthquake magnitude of 9.11, 8.77, 8.40 were obtained for scenario 1, 2 and 3, respectively. These values are slightly higher than the values estimated above, but this can be due to difficulties to estimate correctly the volumes. In fact, in order to obtain the same magnitudes, the total volume should be about 20 km^3.

7.4 Maximum earthquake magnitude derived by literature curves

Another methodology was applied to identify the magnitude of the earthquake or earthquakes that could have triggered landslides, using literature curves. Keefer (1984) studied 40 historical earthquakes identified the relation between magnitude and maximum distance of landslide from the epicentre. The relation was found for disrupted slide and falls, coherent slide and lateral spread and flows. This relation was applied to Chile dataset through the identification of three main structures that may have triggered the earthquakes (Figure 132). The values identified are 5.43, 5.63, and 5.31 for the structures 1, 2, 3 respectively (Figure 133).

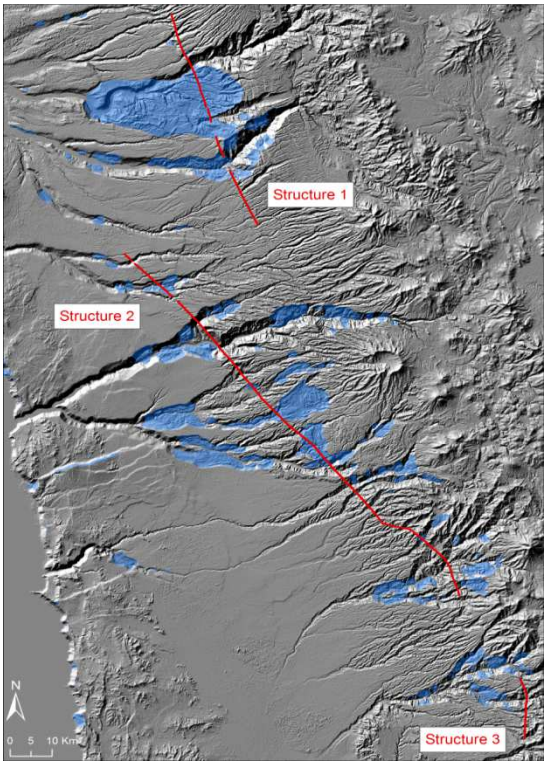

Figure 132. Three structures considered in the analysis.

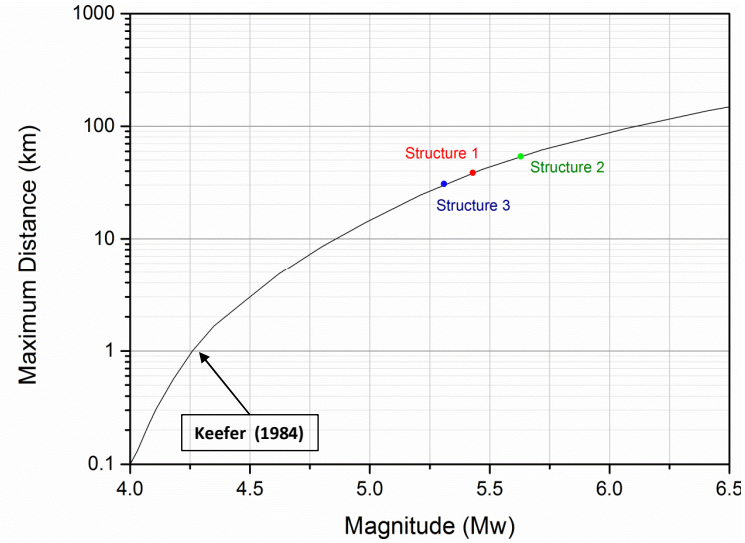

Figure 133. Relationship between magnitude and maximum fault distance from Keefer 1984. For structure 1 a maximum distance of 38.59 Km was identify on the basis of the dataset, for structure 2 a maximum distance of 54.04 Km and for structure 3 a maximum distance of 30.76 Km. In this way on the basis of the Keefer curve a values of magnitude were identified.

Rodriguez et al. (1999) provides a significant extension of the database compiled by Keefer. The relation between magnitude and area affected by landslide was used to define the event magnitude. The area affected by landslides has been found by drawing a boundary around all reported landslide localities and calculating the size of the region enclosed (Figure 135). In this case two scenarios were considered: the scenario in which the landslides were triggered by three different earthquakes related to the three structures and the scenario in which the landslide are related to a single events (Figure 134). The values identified are 6.21, 5.54, 5.93 for structures 1, 2, 3 respectively (first scenario) and 6.55 for a single event (second scenario).

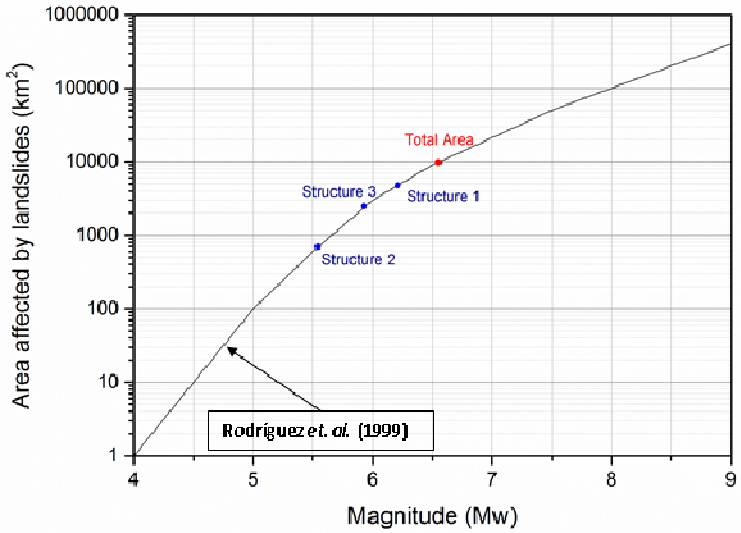

Figure 134. Relationship between magnitude and area affected by landslide from Rodriguez et al. 1999. Through this curve on the basis of the area values a relative values of magnitude were identified.

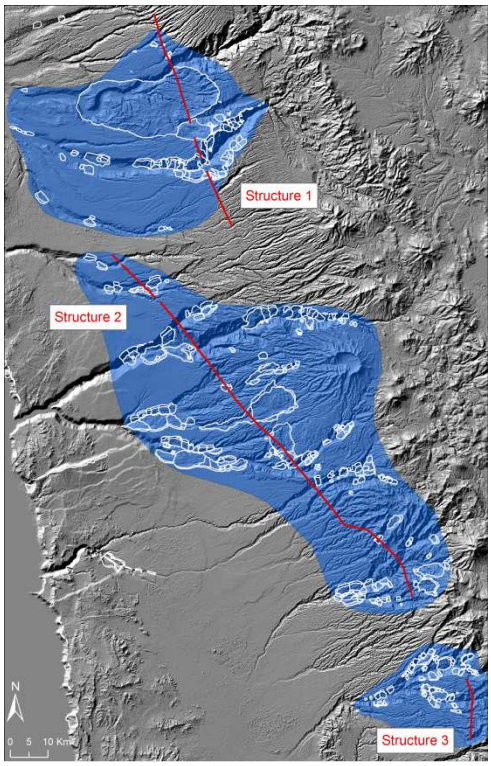

Figure 135. The three boundary around all reported landslide localities, for the first scenario. The second scenario includes these three affected area and the area between them.

7.5 Discussion

The methods adopted for the back calculation of magnitude are extremely different. It is possible to see that methods based on the distance from the fault rupture and the area affected by landslides shown very low values of magnitude. Considering that an earthquake with a magnitude of 7.8 in Tarapaca region (2005) did not trigger landslides, it is not reasonable to think that these values of Mw may be responsible for such extensive landslides. The main reason for such low values can be found in the fact that small landslides are absent in the available dataset. This is related to the fact that the landslides in the region are very old and the smaller ones have been eliminated by the passage of time or incorporated in the major. When considering the maximum distance from the fault rupture, it is possible to assume that the minor landslides are also the most distal and, consequently, there is an underestimation of the maximum distance which leads to lower values of magnitude. Similarly in the case of the area affected by landslides, the limitation of the dataset in terms of extension leads to lower values of area and magnitude.

The method based on the size distribution of landslides for known events is not affected by the absence of small landslide in the dataset. In fact the frequency of the smallest landslides are fitted from the trend of the major events. Hence, the values of magnitude identified are more coherent with the historical information. The method related to volumes, it is less sensitive to undersampling

of smallest landslides, because the values of the volume is strictly controlled by the largest landslides through the formula of Larsen et al. (2010).

As a conclusion, the analysis based on distance and area can only be realized on inventories created immediately after the event and not on an historical dataset in which the smallest landslides can't be recognized. The last two methods are more reliable in term of magnitude values for this study, but other analysis have to be done in order to verify the reliability.

8 Methodology for earthquake induced hazard zoning

The overall methodology adopted in this study for rockfall hazard zoning is presented in Figure 136. Rockfall hazard at a given location on a rockfall-prone slope is assumed to be a function of rockfall annual frequency of transit at each location, f_{annual}, maximum block kinetic energy, e_k, and maximum trajectory height, h. This approach assesses hazard by taking into account both rockfall frequency and intensity, as function of velocity, or energy, and fly height of blocks. The required variables can be computed for each grid cell of a terrain surface by performing 2D or 3D numerical modelling at a suitable level of detail. Similarly to Crosta and Agliardi (2003), rockfall hazard is expressed through and index that represent the magnitude of the modified "Rockfall Hazard Vector" (RHV_{mod}) defined as:

$$\left|RHV_{\text{mod}}\right| = \sqrt{F_{annual}^2 + E_k^2 + H^2} \quad (1)$$

where F_{annual}, E_k and H are indices obtained by reclassifying from 1 to 3 (Table 27) f_{annual}, e_k, and h, respectively. The threshold of e_k and h classes are defined considering the dimension and energy of typical countermeasures (barriers and embankments) (Crosta and Agliardi, 2003). The class thresholds of f_{annual} have been defined considering individual risk acceptability criteria. In fact, assuming that the impact of a block on a person is always lethal, the frequency of transit corresponds to the individual risk, defined, as the probability that an average unprotected person, permanently present at a certain location, is killed (Bottelberghs, 2000). The f_{annual} class thresholds correspond to the limits of tolerability (10^{-5} per year for new developments, 10^{-4} per year for existing developments) for non-volunteer risk such as rockfalls (Geotechnical Engineering Office, 1998).

The annual frequency of transit for each cell, f_{annual} is obtained by combining the annual onset frequency, f_{onset} (i.e., the expected number of detachment events per year) with the results of the rockfall propagation model:

$$f_{annual} = f_{onset} \frac{c}{N} \quad (2)$$

where c is the number of transits for each cell and N is the total number of blocks simulated from the entire cliff.

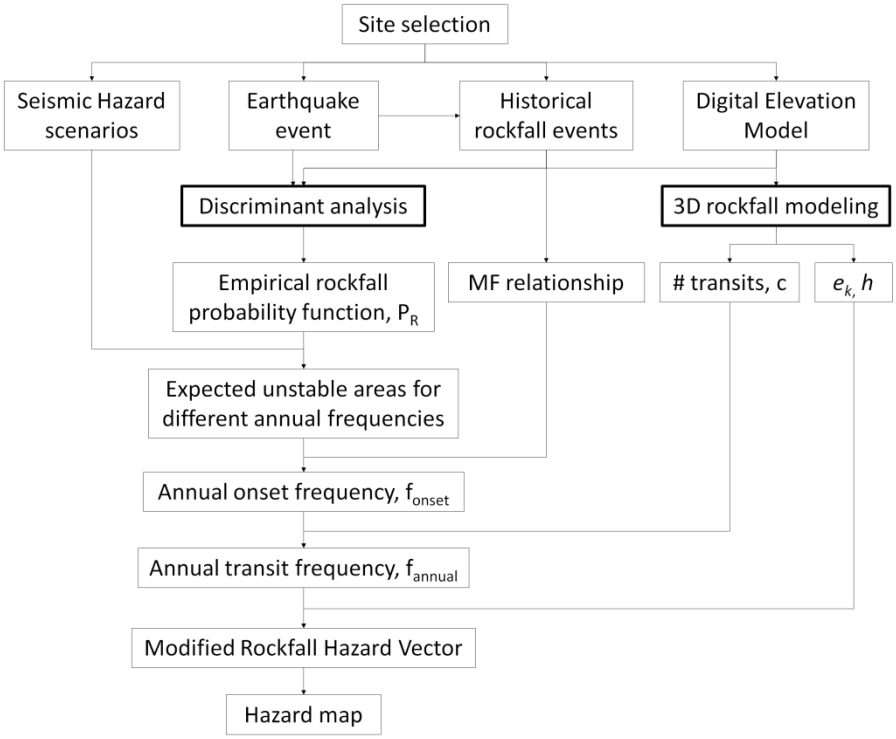

Figure 136. Workflow of the methodology adopted in this article. See the text for more detail.

Table 27. Intervals classification for the variables involved in the modified RHV hazard assessment.

Value	Transit frequency, c (#)	Maximum kinetic energy, e_k (kJ)	Maximum trajectory height, h (m)	Annual transit frequency, f_{annual}
1	0 – 10	0 – 1000	0 - 4	$0 – 10^{-5}$
2	10 – 50	1000 – 5000	4 - 10	$10^{-5} – 10^{-4}$
3	> 50	> 5000	> 10	$> 10^{-4}$

For the calculation of f_{onset} of rockfalls triggered by earthquakes a new procedure is proposed based on a statistical and probabilistic analysis of rockfall triggering. This procedure consists in 3 steps:

- Definition of an empirical function for the probability of rockfall as a function of morphometric variables and PGA, through discriminant analysis;
- Calculation and mapping of the rockfall unstable area for different annual frequency of occurrences by applying the empirical probability function;
- Calculation of the expected annual number of blocks potentially detached for each predefined annual frequency of occurrences combining the unstable area maps with the rockfall Magnitude Frequency (MF) relationship;
- Integration of different scenarios and calculation of the annual onset frequency, f_{onset}.

9 Case study description

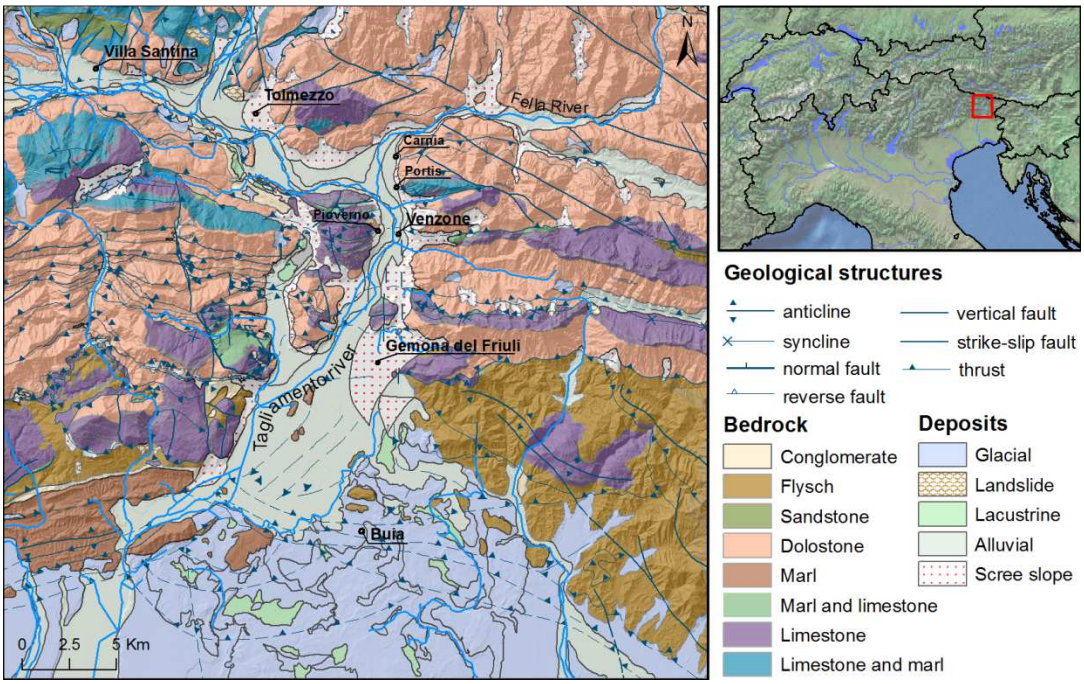

Figure 137. Geological map of the study area (modified after Carulli, 2006).

Rockfall hazard analysis has been performed for a case study in the municipality of Venzone (UD) affected by the 1976 earthquake and for which intense rockfall activity occurred (Figure 137). The discriminant analysis covers an area larger than this, inside the Tagliamento Valley (Figure 137).

The geology of the pre-Alpine area of Friuli Venezia Giulia is characterized by a series of lithologies ranging from the Upper Trias sedimentary rocks to the Quaternary deposits (Carulli, 2006). The most common lithofacies is Norian dolomite, and other formations consist of Jurassic limestones, Cretaceous calcareous marly flysch and of flyschoid and terrigenous, conglomeratic (Eocene-Miocene) sequences more to the south. Massive layers of breccias and cemented conglomerates of Early Quaternary age outcrops in the Tagliamento valley. In the whole region, the recent unconsolidated, alluvial, moraine and talus deposits occur (Figure 137). The tectonic conditions of the area are characterized by intense folding and faulting, with a dominat structural system of E-W trending, N-dipping reverse faults (Carulli, 2006) of which the most important is the "Periadriatic Thrust". Other systems of subordinate faults divide the sedimentary series into irregular blocks. The regional structures strongly influenced the development of the relief consisting of a series of E-W almost parallel ridges interrupted by the broad glacial valley of the Tagliamento river.

The Friuli-Venezia Giulia Region is part of an active geodynamic context between the Adriatic microplate and the European plate. In the Region, 36 earthquakes occurred in the last 700 years

with magnitude larger than 5 (Rovida et al, 2011, Figure 138). The areas most affected by the earthquakes are well defined along the valley of the Tagliamento River (from Buia-Tarcento to Tolmezzo), the last part of the Fella River valley, and neighbouring areas. According to the seismic hazard map of Italy (Working Group MPS, 2004), in this area the peak ground acceleration with a 10% exceeding probability in 50 years (i.e., return period of 475 years) ranges from 0.20 g to 0.275 g. These values are the highest in northern Italy.

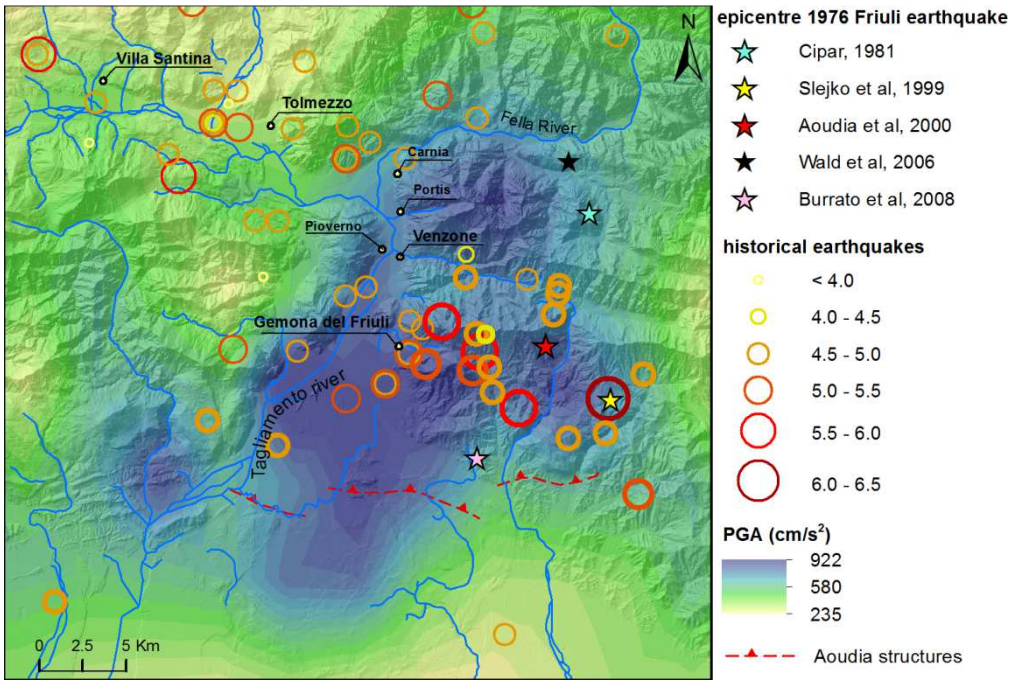

Figure 138. Peak Ground Acceleration map of 1976 Friuli earthquake (after Wald et al, 2006). Stars indicate the epicentres identified in literature. Circles show the historical earthquakes in the area, with a thicker line is evidenced the 1976 sequence. The main geological structures as identified by Aoudia et al. (2000) are also reported.

9.1 1976 Friuli earthquake

The May 6, 1976 Friuli earthquake (Mw = 6.46 ± 0.09, Slejko et al., 1999) was one of the largest historical events in Northern Italy. The affected area was the middle valley of the Tagliamento River (Figure 137), but a huge number of towns near this area suffered intense damages. A total of 119 municipalities in the provinces of Udine and Pordenone were damaged. Despite the well-known high seismicity of the region, most of the affected areas (e.g. Gemona) were not classified as exposed to seismic risk at that time and were not subject to any specific building legislation at the time of the earthquake.

The main shock was preceded by a Mw 4.83 ± 0.22 foreshock (Slejko et al., 1999), and followed by a strong aftershock sequence (Moratto et al, 2012). The largest aftershock occurred on September 15, 1976, with a magnitude of 5.98 ± 0.15 (Slejko et al., 1999).

This seismic sequence has been the subject of several studies (Ambraseys, 1976; Zollo et al., 1997; Cipar, 1981; Slejko et al., 1999; Aoudia et al., 2000; Pondrelli et al., 2001; Perniola et al., 2004; Galadini et al., 2005; Burrato et al., 2008), but the causative geological structure and related fault-rupture process remain partially unknown. Aoudia et al. (2000) and Perniola et al. (2004) models have been recently evaluated as the most reasonable in relation to existing tectonic features and seismological data (Costa et al., 2009). Aoudia et al. (2000) revisited the seismic sequence by combining relocation of hypocentres, inversion of long-period waves and field geology. They identify a single E-trending active deep structure divided into three sectors: the Susans, Buia and M.t Bernadia structures. The fault rupture zone is 18.5 km long and 11.2 km wide. The hypocentre is 7 km deep and located to the North of the Bernadia Mountain. Aoudia et al. (2000) were the first to propose a finite-fault model for the main shock of May 6th, and their model has been adopted in this work to define the distance from the epicentre.

9.2 Rockfalls triggered by 1976 Friuli earthquake

Four inventories have been compiled for rockfalls triggered by the 1976 Friuli earthquake (Figure 139-a and Table 28). The Tagliamento Valley (TV) rockfall inventory covers about 630 km^2 (Figure 137) and was compiled by Govi et al. (1976) through systematic photointerpretation of two series of aerial-photo taken soon after the. The interpretation was completed by field survey on the sites of the most important landslides. The inventory map, 1:50,000 in scale, includes 1,006 rockfall events mapped as points and, only for larger rockfalls, polygons.

Table 28. Areal extent and events number for the prepared rockfall inventories (see Figure 139 for location map).

Rockfall Inventories	Name	Area (km^2)	Authors	n° events
TV	Tagliamento Valley	630	Govi et al. (1976)	1,006
GdF	Gemona del Friuli	33	Broili et al. (1980)	216
VZ	Venzone	28	Broili (1977)	925
VS	Villa Santina	6	Onofri (1995)	19

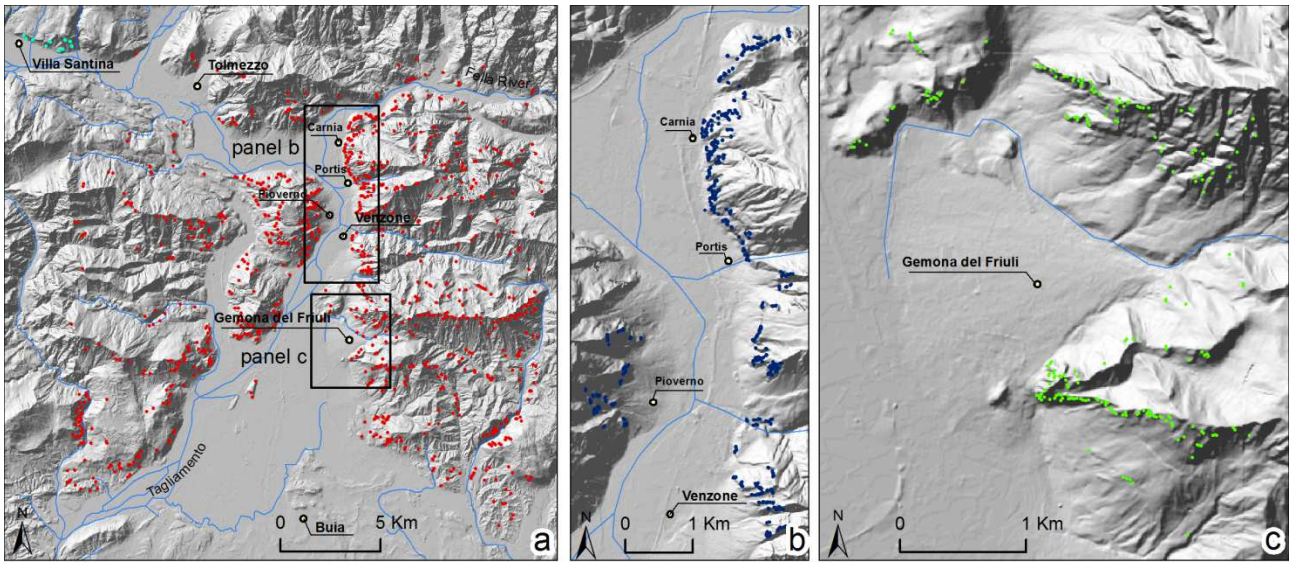

Figure 139. Rockfall inventories acquired of the 1976 Friuli earthquake area. a) Tagliamento Valley inventory (TV, red dots) and Villa Santina inventory (VS, cyan dots); b) Venzone inventory (VZ, blue dots); c) Gemona del Friuli inventory (GdF, green dots).

The Gemona del Friuli (GdF) rockfall inventory covers 33 km^2 of the Gemona municipality (Figure 139-c). The 1:5,000 inventory map was completed by Broili et al. (1980) through an extensive field survey, and it contains 216 rockfall events. For each rockfall, the point-like source areas, the trajectories and the position of the arrested blocks are mapped.

The Venzone (VZ) rockfall inventory covers 28 km^2 of the Venzone municipality and includes rockfall events in the areas of Venzone, Portis, Carnia and Pioverno (Figure 139-b). The map was realized by Broili (1977) through an extensive field survey for the Comunità Montana del Gemonese at 1:5,000 scale. The inventory contains 925 rockfall events. This dataset, unlike the others, shows the rockfall sources as lines. To obtain a point-like source, the midpoint of each line was used. For sources longer than 20 m, the midpoints of the two segments originated by splitting the source line were further used. The inventory also shows the trajectories and the position of the arrested blocks.

The Villa Santina (VS) rockfall inventory (Onofri, 1995) covers 6 km^2 of the Villa Santina municipality (Figure 139-a) and results from an engineering geological survey carried out to redefine the maximum invasion limit of rockfall blocks in Villa Santina. The map, 1:2,000 in scale, includes 19 events mapped as points. The inventories have been digitalized to create a geographic database. Accurate analysis of data and available images has been completed to perform a precise and accurate remapping starting from old topographic maps.

9.3 Magnitude-Frequency relationship for rockfalls

In order to characterize the frequency size relationship of rockfall in the study area, three rockfall volume datasets have been compiled (Figure 140). The first dataset (B_FS) was compiled through a detailed field survey carried out in 2010. During the field activities, the volume and GPS position of 1127 blocks evenly distributed along the scree slope were collected. For these blocks the date of detachment is unknown. However, considering that the 1976 earthquake sequence reactivated the entire slope and that no other major rockfalls have been reported since then, it is reasonable to suppose that most belong to the 1976 earthquakes. The second dataset (B_AF) was compiled through the interpretation of the 1977 aerial photos taken at an altitude ranging from 1,800 and 4,000 m, and includes 634 blocks fallen during the earthquake sequence. Due to limit in the resolution of the aerial photos, blocks smaller than 1 m^3 were not recognized and mapped. The last dataset (B_VZ) comes from Broili (1977) and includes 744 blocks (only 54 with reported volume), also related to the earthquake sequence.

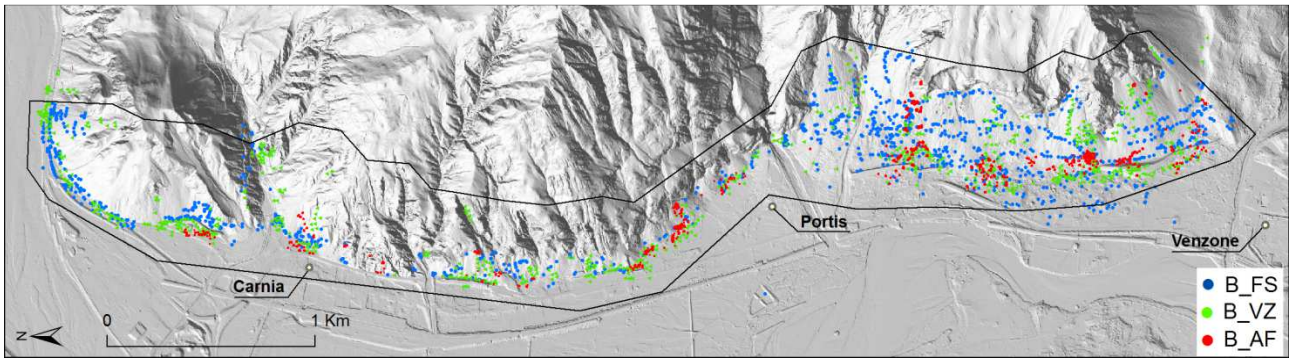

Figure 140. Rockfall blocks datasets for which volume data is available. B_FS: blocks mapped by field survey (2010), B_AF: from 1977 aerial-photos interpretation, and B_VZ: blocks taken from the historical map based on post-event detailed field survey (Broili, 1977).

For the different datasets, non-cumulative logarithmic binned magnitude frequency relationships (MF) were developed (Figure 141), reporting frequency density $f = dN / dV$ as a function of rockfall volume V (dN = number of rockfalls with volume between V and $V+dV$). For all datasets, a deviation from power law can be observed for blocks smaller than 1 m^3 due to undersampling of smaller blocks. For blocks larger than 1$m^{3,}$ magnitude-frequency data have been interpolated with a power law function: $f(V) = aV^{-b}$, where b is the power-law exponent, and a is a constant. The b exponents obtained for the inventories range between 1.34 and 1.75, in accordance with values presented in the literature for rockfall events (Table 29).

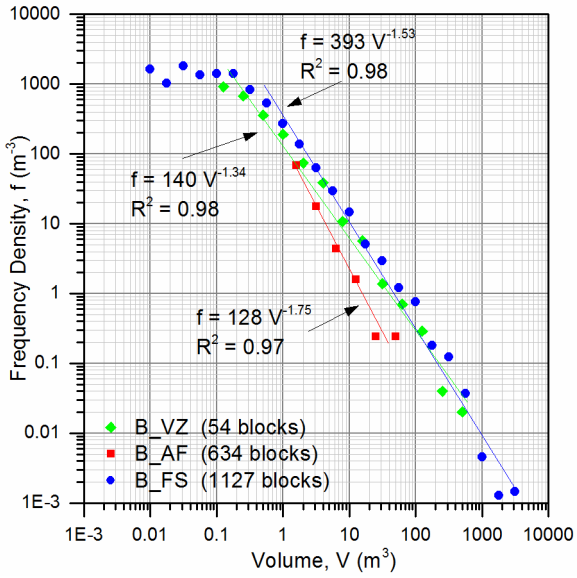

Figure 141. Magnitude-Frequency relationships (MF) for the available datasets (see text for symbols and fig. 4). Least-square best fitting power-law functions are reported for each dataset.

Table 29. Power-law exponents from rockfall inventories in the literature and in this work.

Site		**N**	**b**	**Reference**
Alberta, Canada		409	1.72	*Gardner, 1970*
Yosemite, California		101	1.45	*Wieczorek et al, 1992*
British Columbia, Canada (Highway 99)		389	1.43	*Hungr et al, 1999*
British Columbia, Canada (Highway 1)		123	1.40	*Hungr et al, 1999*
British Columbia, Canada (BCR)		64	1.70	*Hungr et al, 1999*
British Columbia, Canada (CP)		122	1.65	*Hungr et al, 1999*
Grenoble, France		87	1.41	*Dussauge et al, 2003*
Hong Kong, China		201	1.90	*Chau et al, 2003*
Umbria, Italy		157	2.07	*Malamud et al, 2004b*
Santa Coloma, Andorra		5000*	1.92	*Santana et al, 2012*
Christchurch, New Zealand		325	1.07	*Lari et al,2014*
Venzone, Friuli, Italy	B_FS	1127	1.34	*This study*
	B_VZ	634	1.53	
	B_AF	54	1.75	

***** obtained by a stochastic approach based on spacing of discontinuity sets surveyed by Terrestrial Laser Scanning.

9.4 Independent variables for the statistical analysis

The statistical analysis used both topographic and seismic variables. Topographic variables were extracted from two different terrain surfaces: an interpolated 10x10 m DEM derived from contour

lines of 1:10,000 topographic maps and a 1x1 m LiDAR DEM. The LiDAR data (Friuli Venezia Giulia, 2010) were collected by helicopter with an average density of 4 points per square meter.

The considered morphological variables are the slope angle, the slope aspect, the vertical distance from ridge, and the curvatures. Slope angle and slope aspect have been calculated using the Horn (1981) land surface model. Slope aspect is the direction of maximum slope and it is related to some factors that may control rockfall occurrence, such as winds direction, rainfall, exposure to sunlight, control of rock mass discontinuities, direction of seismic waves (Dai et al, 2011). The vertical distance of each point from the ridge was used to express the increase of rockfall susceptibility due to the tendency of seismic waves to be amplified toward the top of the ridge (Meunier et al, 2008). The vertical distance is obtained through a flow path routine. Total and profile slope curvatures also express the effect of topographic amplification along ridges and scarps. They have been calculated using the Zeverbergen and Thorne (1987) land surface model. Negative values represent concave surfaces, a zero curvature represents a flat surface, and positive curvatures represent convex surfaces. To account for the effects of curvatures at different scales, the variables have been calculated with different resolution by resampling DEMs at 1, 10, 30 and 90 m.

Three seismic parameters have been used: the Peak Ground Acceleration (PGA, cm/s^2), the hypocentre distance and the difference between the direction of the seismic wave, in plan, and the local slope aspect. PGA values were obtained from the ShakeMap model produced by the U.S. Geological Survey Earthquake Hazards Program (Wald et al, 2006). The map was developed by using 13 instrumented stations and a large number of Modified Mercalli intensity (MMI) observations used as constraints by treating these intensities and associated ground-motions as "data" (Wald et al, 2006). To convert the MMI values in PGA values a power law relationship is used in the ShakeMap model (Wald et al, 1999). For the range $V \leq MMI \leq VIII$, the power-law equation is:

$$I_{mm} = 3.66 \log(PGA) - 1.66 \quad (\sigma=1.08) \tag{3}$$

The Friuli 1976 earthquake shake map only accounts for the peak horizontal acceleration, since the vertical component was smaller than the horizontal component. In the studied area, the value of the PGA ranges between 235 and 922 cm/s^2.

The hypocentral distance was calculated as the distance in meters of each grid cell from the hypocentre of Aoudia et al. (2000) located at a depth of 7 km. Finally, the absolute value of the cosine of the angle, α, between the direction of the seismic wave, in plan, and the local slope aspect has been calculated. This variable assumes a value of 0 when the slope is perpendicular to the direction of propagation. In this case the direction of vibration, orthogonal to the direction of propagation of the wave, is directed parallel to the slope and it is the most unfavourable condition

for rockfall. Instead the variable assume a value of 1 when the slope is parallel to the wave direction, i.e. the most favourable condition for rockfall, because the direction of vibration is oriented out of the slope. Lithology was not considered in the analysis because the study area lies almost entirely within dolostones.

9.4.1 Field validation of PGA Values through precarious balanced rock approach

In order to assess the reliability of the peak ground acceleration values of the ShakeMap model produced by the U.S. Geological Survey Earthquake Hazards Program (Wald et al, 2006), the precarious balanced rock for the definition of the quasi-static acceleration is applied.

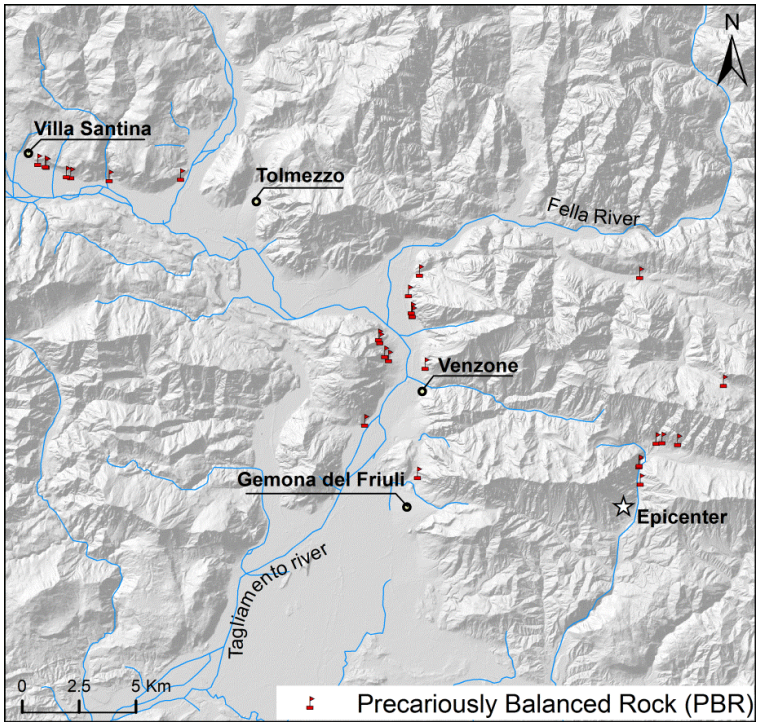

Figure 142. Location of the Precariously Balanced Rocks recognized in the Tagliamento Valley.

In this study, 27 rocks (Figure 142) were tested for the quasi-static toppling acceleration:

$$A = g \cdot \tan\alpha$$

where g is gravitational acceleration, α is the angle between the vertical and the line through the rocking point and the center of mass of the rock. The rocks were identified during a field survey in the area affected by the 1976 Friuli earthquake. They were successively classified on the basis of the level of certainty in three classes: 1 - sure; 2 - possible, but with uncertain boundary conditions; 3 - uncertain mechanism (Table 30, Figure 143).

If we consider the values identified though the proposed methodology versus the values of the ShakeMap model produced by the U.S. Geological Survey Earthquake Hazards Program (Wald et al, 2006) (Figure 144), it is possible to observe how most of the times the ShakeMap acceleration is higher than the corresponding PBRs value. In particular there is a high level of dispersion for the

rocks classified in the third class. The rocks classified in the first class show values always lower than the ShakeMap ones, except for two cases. The rocks in the second class have a good trend with values close to the ShakeMap ones.

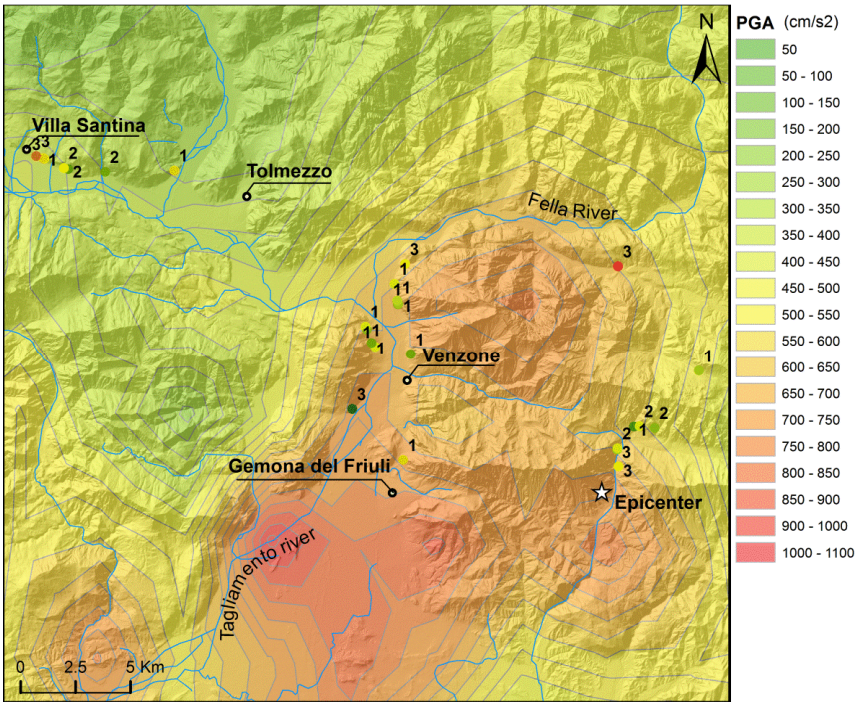

Figure 143. PBR values of peak ground acceleration, with relative level of certainty: 1 - sure; 2 - possible, but with uncertain boundary conditions; 3 - uncertain mechanism. In background the ShakeMap provide by the USGS. The colors for the ShakeMap and the PBRs values is the same.

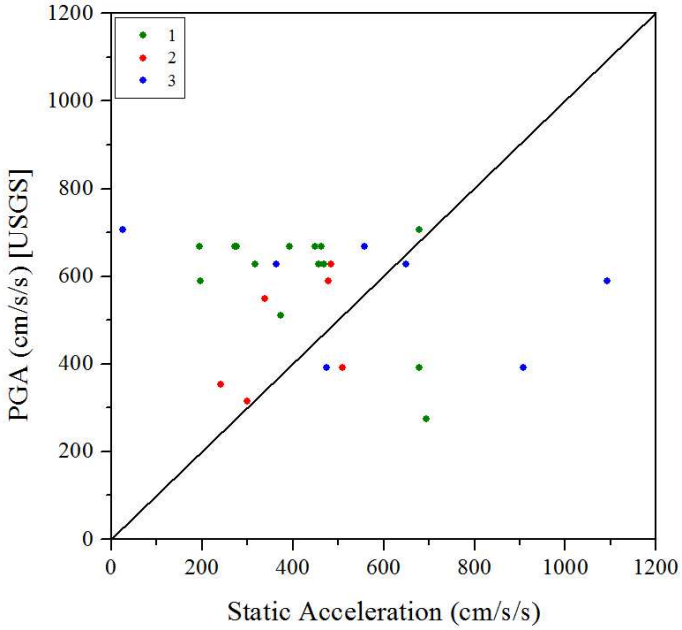

Figure 144. Quasi-static acceleration versus Peak Ground Acceleration derived from USGS shakemap. See text for the legend.

Table 30. Precariously Balanced Rocks recognized on field, with relative level of certainty, Quasi-static acceleration (A, eq.1) and value at the same point for the ShakeMap model produced by the U.S. Geological Survey Earthquake Hazards Program (Wald et al, 2006).

Block name	Certainty	Static Acceleration (A, cm/s/s)	USGS PGA (cm/s/s)
1	1	467.81	628
11-2	1	679.29	706
11-3g	1	679.29	392
1-3g	1	694.33	275
1-4g	1	462.04	667
15-3g	1	448.57	667
16-3g	1	392.68	667
17-3g	1	195.17	667
19-3g	1	275.79	667
2-4g	1	271.70	667
3-4g	1	317.40	628
4-4g	1	457.58	628
5-2	1	195.32	589
5-5g	1	373.11	510
3-3g	2	299.89	314
4-2	2	484.85	628
5-3g	2	240.12	353
6-2	2	477.77	589
7-2	2	339.04	549
7-3g	2	508.96	392
12-3g	3	474.41	392
13-3g	3	908.09	392
1-5g	3	1092.79	589
2	3	649.05	628
2-2	3	558.41	667
3-2	3	363.10	628
8-4g	3	25.63	706

Since the precariously balanced rock data represent the upper bounds, the PBRs values should be, in theory large than the actual acceleration. In the Friuli case study, it seems that the values for the hazard maps proposed by the USGS are too high. However, we have to consider also the low number of precarious rocks present in the study area, and a possible error in the procedure, in particular in the way in which the photo were made. Sometimes it is difficult to realize a picture perfectly perpendicular to the direction of possible movement of the block. For a correct use of this methodology, further investigation, including checking the rock ages, will be required to more definitively reduce the various uncertainties.

In conclusion due to the uncertainty in the methodology the ShakeMap values have been used for the analysis.

10 Analysis

10.1 Annual onset frequency

The first step for the assessment of f_{onset} of rockfalls triggered by earthquakes is the calculation of the extent of rockfall unstable area for different annual frequencies of occurrence. To this aim, a discriminant function analysis has been performed for all the rockfall inventories available in the study area. This analysis allows to classify grid cells along the cliffs as stable or unstable (0 and 1) as a function of morphometric and seismic variables. The discriminant function analysis has been performed on a dataset of points that are a-priori identified as stable or unstable. The unstable points correspond to rockfall source areas of events reported in the inventories used for the analysis (Table 31). The stable group has been created as a set of random points in the cliff area with a distance larger than 50 m from unstable points (Table 31). This allows to avoid overlapping of the two datasets. The distance of 50 m has been selected considering the spatial uncertainty in the mapping of actual rockfall events.

Table 31. Rockfall inventories and DEM used to develop the discriminant models.

Model	Inventory	Area	DEM resolution	Event Points		Random Points		All Points
TV_l1	TV	LiDAR	1m	280	(31%)	625	(69%)	905
TV_l10			10m	280	(31%)	625	(69%)	905
TV10		inventory	10m	1006	(15%)	5780	(85%)	6786
GdF_l1	GdF	LiDAR	1m	216	(35%)	400	(65%)	616
GdF_l10			10m	216	(35%)	400	(65%)	616
GdF10		inventory	10m	216	(35%)	400	(65%)	616
VZ_l1	VZ	LiDAR	1m	925	(36%)	1637	(64%)	2562
VZ_l10			10m	925	(36%)	1637	(64%)	2562
VZ10		inventory	10m	925	(34%)	1800	(66%)	2725
GdF_VS_l1	GdF+VS	LiDAR	1m	235	(35%)	444	(65%)	679

By a stepwise procedure, the discriminant analysis selects variables that are most relevant for the classification of stable and unstable points; 60% of the original inventory was used to train the model, while the 40% to validate the performance of the discriminant analysis. The F-Fisher to enter, F_{in}, and to exit, F_{out}, was adjusted to obtain a comparable number of variables for the different analyses. At each step of the stepwise procedure, the variable is selected into the model if its F-Fisher statistic value is greater than F_{in}, and removed if less than F_{out}. The values were selected to keep low the number of variables. This reduces the performance of the model in classification, but allows a better understanding of the role of different variables, because it reduces the risk of collinearity among the selected variables. The importance of each predictor is evaluated by the value of the standardized discriminant coefficient, whose sign depends on the tendency of the

variable to classify objects in either the positive or the negative group. The positive group is represented by cells with rockfall, hence, a positive coefficient indicates a tendency to favour rockfall susceptibility.

The discriminant models selected from 4 to 8 independent variables (Table 32). Among these variables, the slope angle has been selected by all models. Slope angle almost always shows the highest standardised discriminant coefficient (9/10 models), with positive values. PGA is the second most important variable selected, usually with positive coefficients. The only exception is for all VZ models where the PGA coefficient has a small negative value. This is probably related to the position, the shape and extent of the model area, for which the PGA values are poorly variable.

The third most important variable is the slope curvature with a raster resolution of 90 metres (8/10 models). Only the VZ10 and TV10 models do not include this parameter. Among the other topographical variables, the slope aspect results significant for five models but with different signs and small value of the standardized coefficients. The vertical distance is taken into account by four models, with negative sign, suggesting that an increase of the distance from the ridge causes a decrease of the number of possible source areas. However, the low value of the standardized discriminant coefficients indicate a lower importance compared to the other variables. The profile curvature, with different cell size, is one of the variables less considered in the analysis (at most 3 models of 10). This is probably due to the fact that the profile curvature is strongly correlated to the slope curvature.

About the seismic source parameters, the hypocentral distance and $|\cos\alpha|$ are selected in six and two models, respectively. The hypocentral distance is selected with high standardized coefficients (> 0.3) by four models, but with different sign.

The quality of the models has been evaluated by means of ROC (Receiver Operating Characteristic, Figure 145) curves (Yesilnacar and Topal, 2005, Begueria, 2006, Gorsevski, et al, 2006; Frattini et al, 2010) considering the validation subset for each model. Models based on GdF and GdF+VS inventories have the highest accuracy (Area Under ROC Curve, AUC, between 0.88 and 0.94 for validation dataset). This is probably related to the high quality of the original database, in terms of accuracy in locating events on the map, also due to the scale of the work. The TV models show the lower performance quality (AUC lower than 0.77), due to the greater area covered by the dataset and to the lower reliability of the original information at scale 1:50,000.

In order to proceed with the calculation of the extent of unstable area for the rockfall hazard zoning, a new discriminant model (TV10_3variables) was performed, based on the TV inventory with a 10 m resolution DEM, further limiting the number of predictors to the ones that have been more selected by the whole set of models: the slope angle, the PGA and the 90 m curvature (Table 33).

The TV inventory was preferred for the hazard zoning, because it covers a larger area with a stronger variability of the variables. For this reason, the TV10_3variables model is considered more robust and efficient in prediction than the others.

Table 32. Variables selected by the discriminant models. Variables showing a standardized discriminant function coefficients (SDFC) larger than 0.3 are presented in bold. n.s = unselected by stepwise procedure; n.a. = unavailable for the analysis. The centroids of the groups, that are the mean discriminant scores for each group (0,1), and the F_{in} e F_{out} values are also presented.

		Sdfc, Standardized Discriminant Function Coefficients										# models/total
Models		TV_l1	TV_l10	TV10	GdF_l1	GdF_l10	GdF10	VZ_l1	VZ_l10	VZ10	GdF_VS_l1	
PGA (cm/s^2)		n.s.	**0.30**	**0.77**	**0.41**	**0.39**	0.29	**-0.47**	**-0.53**	**-0.44**	**0.94**	**9/10**
Slope		**0.83**	**0.90**	**0.88**	**0.99**	**0.90**	**0.73**	**0.80**	**0.93**	**0.94**	**1.01**	**10/10**
Aspect		n.s.	n,s	n.s.	-0.13	-0.14	n.s.	n.s.	0.28	**0.405**	-0.12	5/10
Hypocenter Distance (m)		**-0.32**	-0.16	**0.49**	n.s.	0.14	**0.48**	n.s.	n.s.	n.s.	**0.60**	6/10
|cos α|		n.s.	n.s.	n.s.	n.s.	**-0.35**	**-0.38**	n.s.	n.s.	n.s.	n.s.	2/10
Vertical Distance (m)		n.s.	n.s.	-0.10	n.s.	-0.18	-0.20	n.s.	n.s.	-0.17	n.s.	4/10
Slope curvature	**1m**	n.s.	n.s.	n.a.	n.s.	n.s.	n.a.	n.s.	n.s.	n.a.	n.s.	0/4
	10m	n.s.	n.s.	n.s.	0.24	n.s.	n.s.	n.s.	n.s.	n.s.	0.25	2/10
	30m	n.s.	n.s.	n.s.	0.23	n.s.	0.16	**0.32**	**0.51**	n.s.	0.21	5/10
	90m	**1.11**	**0.64**	n.s.	0.17	0.26	0.24	**0.66**	0.16	n.s.	0.16	**8/10**
Profile Curvature	**1m**	-0.28	n.s.	n.a.	n.s.	n.s.	n.a.	n.s.	n.s.	n.a.	n.s.	1/4
	10m	0.21	n.s.	n.s.	n.s.	n.s.	n.s.	n.s.	n.s.	n.s.	n.s.	1/10
	30m	n.s.	-0.21	n.s.	n.s.	-0.24	n.s.	n.s.	**0.39**	n.s.	n.s.	3/10
	90m	**0.95**	**0.52**	n.s.	n.s.	n.s.	n.s.	**0.37**	n.s.	n.s.	n.s.	3/10
Centroid of the "no Rockfall" group		-0.30	-0.32	-0.14	-0.67	-0.78	-0.86	-0.47	-0.53	-0.42	-0.61	
Centroid of the "Rockfall" group		0.69	0.70	0.86	1.26	1.48	1.57	0.82	0.90	0.86	1.17	
F_{in}		2			2			11			2	
F_{out}		1			1			10			1	

Table 33. Standardized discriminant function coefficients (SDFC) of the TV10_3variables The centroids of the groups, the F_{in} e F_{out} values are presented.

TV10_3variables	**sdfc**
PGA (cm/s^2)	**0.551**
Slope	**0.801**
Slope curvature 90m	**0.235**
Centroid of the "no Rockfall" group	-0.137
Centroid of the "Rockfall" group	0.789

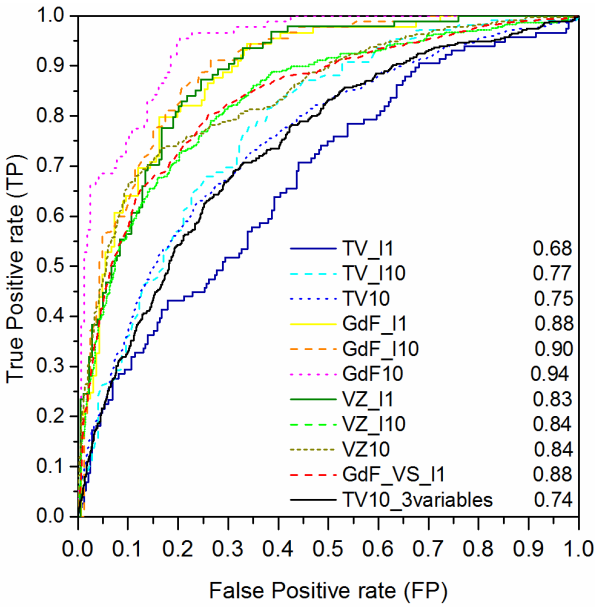

Figure 145. ROC curves for the validation subset of the developed models. Area under curve (AUC) for each model is reported. See tables 2 and 4 for explanation of the legend.

The robustness of the model to variation of the input data has been tested by assessing the uncertainty in the susceptibility estimate of individual mapping units (Guzzetti et al, 2006). Hundred different random sampling of training and validation subsets were generated, and the TV10_3variables discriminant model, with these subsets, was developed. Then, the value of 2 standard deviations for each mapping unit was plotted as a function of the mean value of the unstable-group membership probability (Figure 146). The 2 standard deviation is considered as a proxy for model error (Guzzetti et al, 2006). As a result, it is observed that the error is very low, especially for mapping units characterized by low and high occurrence probability (Figure 146-a). For intermediate probabilities, a higher variability of the model errors is observed, with a few points showing a relatively high error. For comparison, the same analysis for the GdF inventory was performed (Figure 146-b), which show larger model errors and an overall smaller robustness. This result is probably due to the number of mapping units used for the statistical analysis.

For the TV10_3variables model, the raw discriminant function and the unstable-group membership probability, were obtained. The latter, represents an empirical function for rockfall onset probability, P_R:

$$P_R = 1 - \frac{1}{1 + e^{\left(\frac{D - 0.33}{1.08}\right)}} \quad (4)$$

where D is the discriminant function:

$$D = -4.62 + 0.065 * S + 0.004 * PGA + 0.27 * C90m \quad (5)$$

where S the slope angle (degree), PGA the peak ground acceleration (cm/s^2) and C90m the slope curvature with a cell size of 90 m.

By using in this function PGA values with different annual frequency, it is possible to associate the temporal probability to rockfall onset probability. The incremental annual frequencies, i.e. number of occurrences of events with binned PGA values (i.e., PGA falling between PGAi and PGAi + ΔPGA), have been calculated from the exceedance probability values reported in the seismic hazard scenarios published by Working group MPS (2004), by assuming a Poissonian model of event time distribution. In particular, 10 scenarios have been used, as reported in Table 34. For each incremental frequency scenario, the upper PGA value ($PGA_i + \Delta PGA_i$) of the corresponding bin was assigned and used in the discriminant function. This is a conservative approach, since the PGA within each bin actually falls between PGA_i and $PGA_i + \Delta PGA$.

With this approach, an upper and a lower bound should be assigned to the frequencies. For the upper bound, the maximum exceedance annual frequency reported in Working group MPS (2004) is used, corresponding to a return period of 30 yr (Table 34). Since seismically-induced rockfalls have been not observed after the 1976 event, this upper frequency bound seems reasonable. The lower frequency bin (Table 34), was associated to a PGA corresponding to the maximum value observed during the 1976 event (about 0.94 g). This value significantly exceeds the PGA value with a return period of 2500 yr (about 0.48 g).

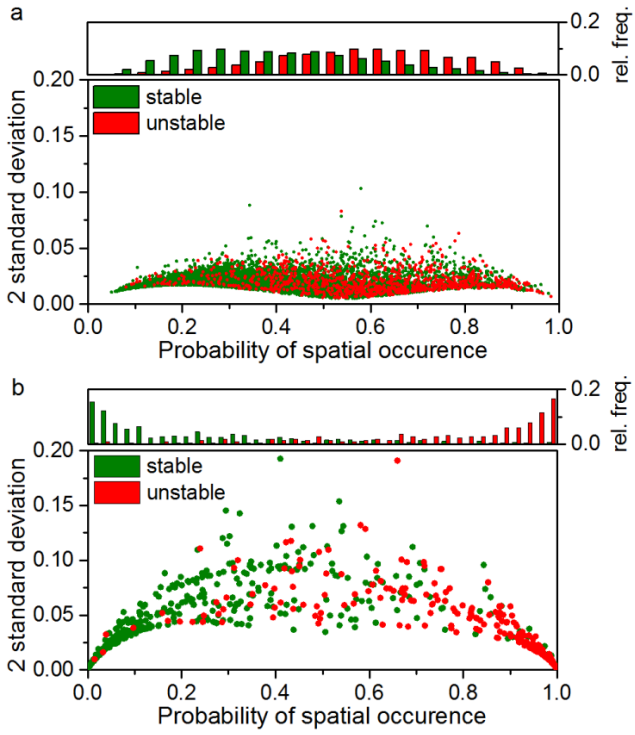

Figure 146. Landslide susceptibility model error. The graphs show the mean probability value of 100 different random sampling of training and validation subsets for the TV inventory (a) and the GdF10 inventory (b). The relative frequency for stable and unstable mapping units is also reported for both the models.

In this way, nine maps of rockfall onset probability, P_R (eq. 4), with different incremental annual frequency of occurrence were obtained (Figure 147). These maps have been reclassified in two classes (stable and unstable) by considering unstable all grid cells with $P_R \geq 0.5$ (
Table 32). The analysis was performed only along the cliffs to exclude the possibility that a high probability was found along human structures such as road embankments, ditches and passive countermeasures.

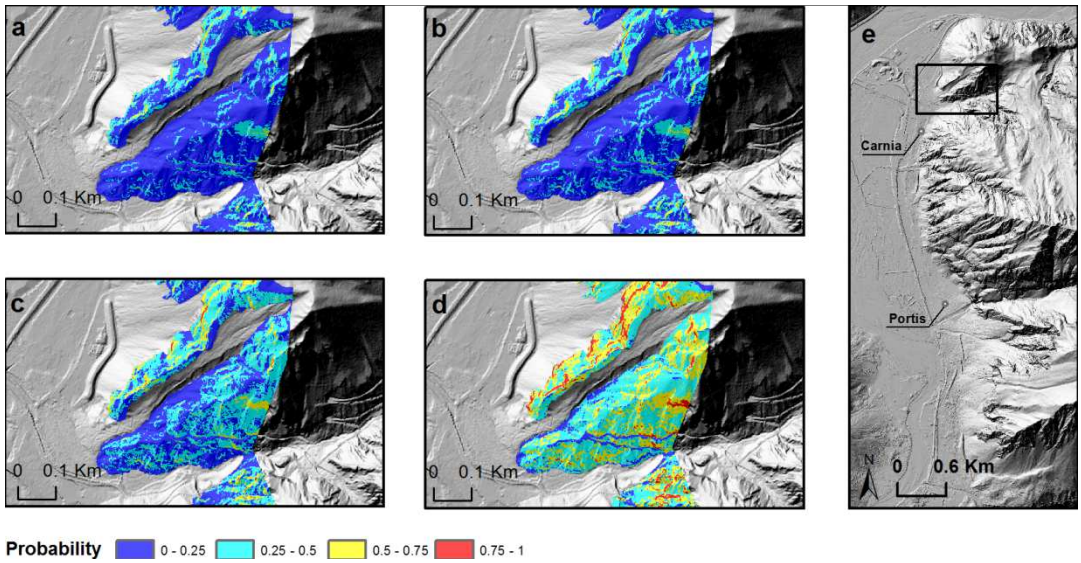

Figure 147. Maps of empirical rockfall onset probability for a part (e) of the the Venzone cliff area with incremental annual frequencies of occurrence of: a) 0.0133, b) 0.0039 c) 0.0029, d) 0.0006. The increase of the rockfall onset probability associated to a decrease of the frequencies of occurrence is due to the PGA values, which are greater for small frequency of occurrence.

The second step for the assessment of f_{onset} of rockfalls triggered by earthquakes is the calculation of the expected annual number of blocks detached for each incremental annual frequency of occurrence, starting from the unstable area maps. Given that the total unstable area is the sum of many different events with different volumes, and assuming that the relative frequency of these events with different volumes follows a known MF relationship (Hungr et al. 1999; Dussauge et al. 2003), then the number of events was calculated by equating the total area with the integral of the MF curve, expressed in terms of area (Table 34, Figure 148). For this analysis, the MF relationship of the field-survey volume dataset 2010 has been used (Fig. 4, red dots), converting the rockfall volumes, *V*, in areas, *A*, considering a cubic shape, $A = V^{2/3}$.

Taking into account all scenarios (Table 34, Figure 148), the total expected annual number of rockfall events amounts to 0.92 per year. This value corresponds to the annual onset frequency, f_{onset}.

Table 34. Expected annual number of blocks for each incremental annual frequency of occurrence. In the table, the hazard scenario from Working group MPS (2004) (in terms of probability of exceedance in 50 years), the corresponding exceedance annual frequency, the unstable area in square meters and the consequent number of potentially detached blocks are also reported.

Hazard scenarios	Exceedance annual frequency	Incremental annual frequency	Unstable area (m^2)	# blocks	Annual # blocks
PGA_1 (2% in 50 yr)	0.033	-	86,219	15.26	-
PGA_2 (5% in 50 yr)	0.020	0.0133	102,122	18.07	0.241
PGA_3 (10% in 50 yr)	0.014	0.0061	114,921	20.34	0.124
PGA_4 (22% in 50 yr)	0.010	0.0039	130,194	23.03	0.090
PGA_5 (30% in 50 yr)	0.007	0.0029	147,583	26.09	0.075
PGA_6 (39% in 50 yr)	0.005	0.0021	170,970	30.25	0.065
PGA_7 (50% in 50 yr)	0.002	0.0029	250,983	44.41	0.129
PGA_8 (63% in 50 yr)	0.001	0.0011	363,565	64.34	0.071
PGA_9 (81% in 50 yr)	0.0004	0.0006	603,675	106.82	0.064
PGA = 0.95 g	0	0.0004	912,650	161.50	0.065

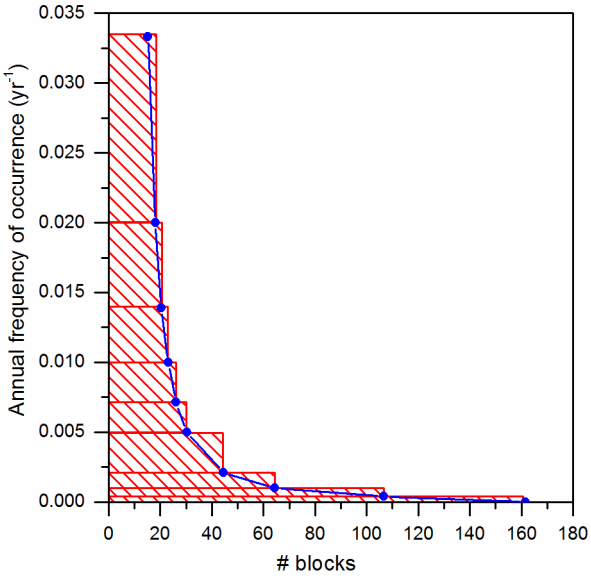

Figure 148. For each annual frequencies of occurrence (yr^{-1}), the number of blocks potentially detached with a PGA value exceeded with the corresponding annual frequency is reported. The sum of the red rectangle represents the expected total number of blocks per year.

10.2 Rockfall propagation modelling

The rockfall runout simulation was performed by using the 3D model Hy-STONE (Agliardi and Crosta, 2003; Crosta et al., 2004). 3D models are able to simulate block motion along a slope by including lateral dispersion of trajectories due to large and small scale morphological complexity (Descoeudres and Zimmermann, 1987: Guzzetti et al., 2002a; Agliardi and Crosta, 2003; Crosta et al., 2004; Dorren et al., 2006). The obtained results are spatially distributed over the entire study

area, without need for any interpolation of data computing along specific trajectories or imposing predetermined fall direction.

Hy-STONE incorporates both kinematic (lumped mass) and hybrid (mixed kinematic-dynamic) algorithms, allowing to model free fall, impact and rolling. Different damping relationships are available to simulate energy loss at impact or by rolling. The topography is described by a raster DEM, which is converted in a vector topographic model (Triangulate Regular Network, Guzzetti et al., 2002a) for the solution of impact and rolling. The stochastic nature of rockfall processes is introduced as a function of model spatial resolution and by random sampling most parameters from different PDF (e.g. uniform, normal, lognormal, exponential). The capability to simulate the effect of passive countermeasures, dynamics of "flying rocks" and the effect of vegetation have been implemented and tested against real events (Frattini et al, 2012a). A special elasto-viscoplastic strain hardening model for impact on soft ground (Di Prisco and Vecchiotti, 2006) has also been implemented. Model results are provided in both raster and vector formats and these include rockfall frequency, fly height, rotational and translational velocity and kinetic energy, as well as information about motion type, impact locations, impact and rebound angles.

The simulations performed in this study are based on the following parameters: spherical blocks with a density of 2600 kg/m^3, mean radius of 0.71 m (max. 2.56 m); source area posed as slope steeper than 55°; stochastic exponential distributions for the radius of the blocks, normal for the coefficients of restitution and friction angle are assumed. A total of 3,233,830 blocks (N) were simulated, 10 for each grid source cell. The calibration was based on the maximum runout identified during the field survey, the extent of mapped debris talus, and the work realized by Broili in the 1977. The presence of the countermeasures of given height (m) and given energy absorption (J) was considered.

Using the modified "Rockfall Hazard Vector" (RHV_{mod}) (eq. 1) a hazard map was created, on the base of the 3D model results. To improve the readability of the hazard map, and considering that the calculated RHV_{mod} values are spatially discontinuous (i.e, "salt and pepper" effect), the RHV_{mod} values have been spatially averaged within a circle with 5 m radius (Figure 149). Considering the area included in a buffer of 50 meters from exposed elements at risk (e.g. roads and houses), the majority of the area belongs to the residual and low hazard classes (54.2% and 33.7%, respectively). The moderate class covers the 11.9% of the investigated area and the highest class only the 0.1%. The buffer has been designed to consider the areas of greatest interest in a perspective of prevention, neglecting the high-risk areas placed high on the cliff. Comparing the location of main rockfall events of the 1976 Friuli earthquake identified on the basis of the aerial-photos with the hazard map (Figure 150), a good agreement was found.

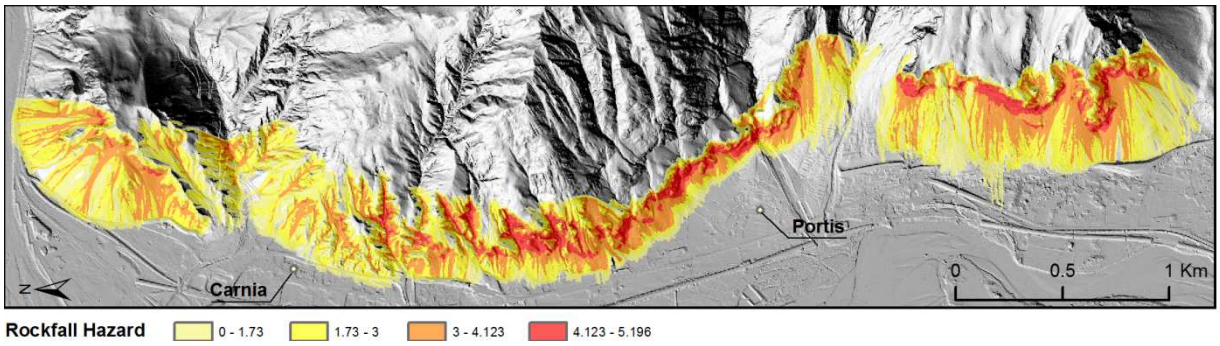

Figure 149. Rockfall Hazard Zoning Map for the Venzone (VZ) area.

The large historical rockfall events, represented as polygons in Figure 150, lie in high-risk areas, demonstrating the validity of the 3D model at the basis of the RHV methodology. In Figure 150-b, the simulated runout is longer than the large rockfall main body, but fits the isolated blocks mapped after the earthquake (B_VZ rockfall dataset). Slight differences between simulated and historical runout could be related also to a variation in the topography after the 1976 rockfall events. In fact, the 3D simulation is based on a 2010 LiDAR topography that include the 1976 rockfall coarse deposits, which increase the surface roughness, thus reducing the simulated runout (Figure 150-a,c). Moreover, the current topography include rockfall countermeasures built after the 1976 earthquake, such as the two embankments built to protect the Portis urban centre (Figure 150-c), and the 20 m high embankment in Figure 150-d. Due to these countermeasures, the simulated runout is shorter than the one registered for historical events.

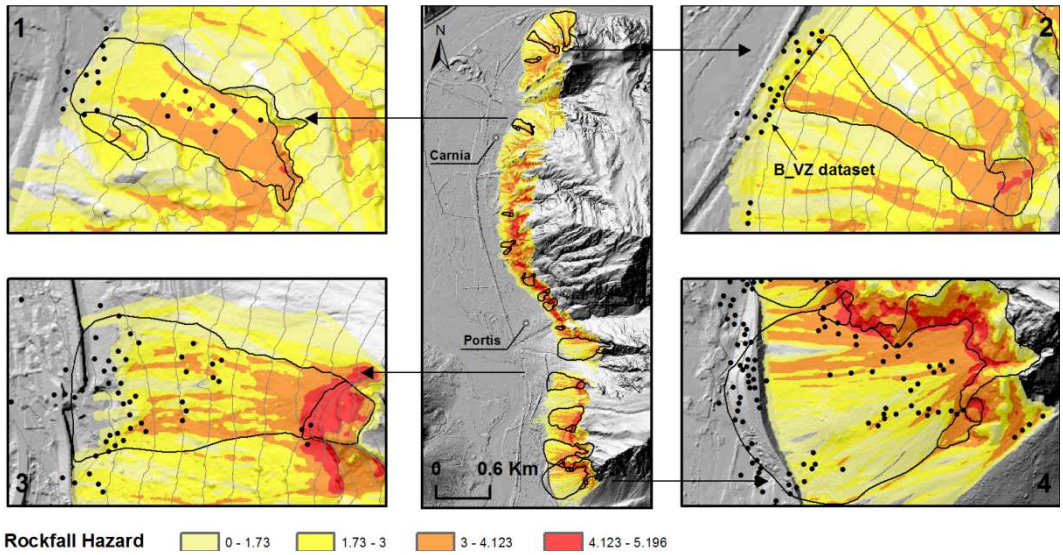

Figure 150. RHV_{mod} and the rockfalls triggered by the 1976 Friuli earthquake from photo interpretation. The black lines delimit the source area, on the cliff, and the runout zone for each event. The black points are arrest points for single blocks fallen during the 1976 earthquake and mapped in Broili (1977). Defense passive countermeasures realized after the 1976 earthquake are recognizable from the hillshaded DEM.

11 Discussion

The presented methodology is proposed for hazard zonation of areas where rockfalls are triggered by earthquakes. The result is a map where the area is divided into classes with different levels of hazard, from low to high. In the definition of hazard, the methodology estimates the intensity as a function of kinetic energy and fly height. For a certain location along the slope, both kinetic energy and fly height can significantly vary due to the intrinsic uncertainties of the parameters which control the rockfall propagation (e.g., slope morphology, slope material and debris grain-size), and also due to the convergence of trajectories coming from different source areas. Hence, in a rigorous approach (Frattini et al, 2012b), probability distributions of kinetic energy and fly height should be used in hazard assessment. However, this approach would be quite complex to be adopted for a simple and easily applicable zoning methodology. In the RHV_{mod} method, the maximum values of kinetic energy and fly height are used, thus adopting a conservative approach for the assessment of rockfall intensity. Unlike other methods (Pierson et al, 1990; Mazzoccola and Sciesa, 2000; Agliardi et al. 2003; Corominas et al, 2003; Budetta et al, 2004; Jaboyedoff et al, 2005; Abbruzzese and Labiouse, 2013) RHV_{mod} relates rockfall occurrence to external factors such as climate or geodynamic environment, which act in different ways as a function of the geological and geomorphological settings. Since these factors are characterized by an occurrence probability, the probability of rockfall is calculated indirectly, and used to assess rockfall hazard, assuming stationarity of geological and environmental conditions. The probabilistic analysis is a valuable tool for the planning of actions, costs/benefits analysis, and risk management.

Regarding the factors controlling the earthquake-induced rockfalls, this work confirms that the slope angle and the PGA plays most important role as reported in previous works (e.g., Marzorati et al, 2002). In addition, the 90m slope curvature has been recognized to play a key role in controlling the rockfall occurrence.

The successful application of the methodology for rockfall hazard assessment requires:

- a complete description of the past rockfall events and source areas, both for the discriminant analysis that relates seismic and topographic variables to the rockfall occurrence, and for the calibration of the rockfall runout model.
- a detailed record of the seismic parameters (e.g. PGA), and a reliable DEM for the discriminant analysis.
- the blocks size distribution (MF relationship) for the calculation of the number of blocks potentially triggered by seismic inputs with different annual frequencies of occurrence.

The intensity and distribution of the past rockfall events were obtained from several works (Govi et al, 1976; Broili et al, 1977; Broili et al, 1980; Onofri, 1995) based on field surveys performed soon after the earthquakes. These data have been implemented through a new aerial photointerpretation of 1976-1977 aerial photos. An important issue is the accuracy of rockfall source area mapping, to attribute the more appropriate value to the variables involved in the analysis. Different inventories with different resolution and characteristics were used, covering different areas. However, a single database was not created due to the different scale (from 1:50,000 to 1:2,000) and precision of the maps. In addition, different authors used different methodologies to report on map the information (e.g. the dataset sources of VZ is made by lines in contrast to the others). The PGA map was obtained from an interpolation of values recorded at 13 instrumented stations and a large number of Modified Mercalli intensity (MMI) observations (Wald et al, 2006). Unfortunately, this data does not account for local topographic amplification of the seismic waves. For the calculation of unstable areas with different annual frequencies of occurrence, the obtained equation (5) is used with different PGA values obtained from the seismic hazard map of Italy (Working Group MPS, 2004). It is assumed that equation (4), calibrated with the 1976 earthquakes, holds for seismic inputs, if applied to the same area under similar environmental and geological conditions. To calculate the morphometric variables used for the discriminant analysis, two different DEMs were used, with 1 and 10 m resolution. A small effect of different DEM resolution on the results of the discriminant analysis has been observed, but this can be related to the accuracy of the rockfall inventories. In other words, a very detailed DEM is not needed if the scale and mapping precision of the rockfall inventory is not consistent. For the calculation of the number of blocks associated to each annual frequency of occurrence, the MF curve was adopted. This could introduce an approximation in the analysis because the MF curve is assumed to completely describe the volume distribution, also for the small classes. In this study, the minimum volume identified on field is 0.0045 m^3; so it possible to assume that the volume distribution is correctly represented. To overcome this problem, it could be possible to extrapolate the MF curve to smaller classes, but this procedure can introduce error in the analysis with an overestimation of these classes. Moreover, it is necessary to consider that the MF curve was derived from field activity carried out years after the event. Finally the size distribution of blocks could change with the intensity of the seismic ground motion parameter and related annual frequency of occurrence. The effect of different lithologies was not included because in the study area there is a minor variation of this variable. This may not be valid for other sites with different types of rocks and structural constraints. In addition, information from geomechanical maps, not available at the moment, could be incorporated, to compare the size of blocks surveyed on the field with the size of potentially unstable blocks on the cliff.

12 Conclusion

In landslide hazard analysis, both the temporal frequency of landslide events and the destructive potential of the events (to be used for vulnerability analysis) depend on the size of the landslides. In particular, to characterize the temporal frequency of landslides, it is necessary to define a function that describe the dependence of the frequency on landslide size, i.e., a Magnitude Frequency (MF) curve. In the literature, many authors tried to assess MF curves for different type of landslides in different regions. Some have tried to characterize the dependence these curves on lithology (e.g, Hungr et al,1998), pattern of soil wetness (Pelletier et al, 1997), the properties of materials (Frattini et al , 2013), and the slope morphology (Frattini et al, 2013). However, for earthquake-induced landslides, none has tried to characterize if the MF curves change as a function of the magnitude of the earthquake and the distance from the seismic source. This could be important for landslide hazard assessment in seismic areas, because it could allow to zone different degree of hazard as a function of the magnitude of the earthquakes, and, for each earthquake, moving from the seismic source to the outer part. Regarding the relationship between the earthquake magnitude and landslide size, Jibson and Keefer (1989) suggested that large to mega landslides are frequently triggered by longer duration shaking, generally related to earthquakes of larger magnitude. By comparing the frequency density curves of all landslides mapped for the studied earthquakes, it is clearly shown that an increase of the earthquake magnitude corresponds to a shift of the curve toward upper-right, that imply the landslides are more abundant, but also larger in size. In other words, the higher the earthquake magnitude, the higher the "landslide inventory magnitude", m_L (Guzzetti 2002) This has been partially investigated by Parker (2013), with a smaller set of landslide inventories. The only earthquake that deviates from this trend is 2011 Tohoku earthquake, but this is related to the particular condition at which the earthquake occurred, that reduced the possibility to have a complete earthquake-induced landslide inventory (very far from the coast, in the subduction zone). This relationship between earthquake magnitude and landslide inventory magnitude is very interesting and useful for hazard assessment of potential future earthquakes. In addition, this relationship can be used to estimate the magnitude of earthquakes when a landslide inventory is available but the events that triggered the landslides is unknown. The back calculation of the magnitude of the earthquake on the basis of the landslides inventory can help the understanding of the past events and the evolution of the landscape in seismic area, than the maximum level of seismicity experienced in the related region (with a view to preventing the territory). The case study of Northern Chile demonstrate this possibility.

When focusing on a single earthquake, it is interesting to understand if the size of the landslides varies in space, and if it is possible to define different MF curves as a function of the distance from the seismic source. However, before investigating the relationship between the landslide size and the distance from the seismic source, it was necessary to investigate which are the variables that control the landslide size most. These variables are among the so-called preparatory variables (Wu and Sidle, 1995) which make the slope susceptible to failure without actually initiating it and thereby tending to place the slope in a marginally stable state, such as relief, slope gradient, geology. From preliminary analyses performed on the landslides inventories for the six earthquake considered, it is clear how the relief and the slope gradient do not play a relevant role in controlling the size of the landslides. From the results, it appears that a relatively high relief is associated also to small landslides, and a low relief with large ones.. In theory, the slope gradient could have a censoring effect on small landslides, especially in cohesive materials (Frattini et al, 2013). However, the inventories can be affected by undersampling in small landslides, which are often not mapped. Moreover, the resolution of the Digital Elevation Model, used in the analysis (cell size between 10 to 50 m), is too low, and it do not give reliable values for high slope gradients. This does not allow a detailed representation of the morphology.

Regarding the distance from the seismic source, both in terms of distance from the epicenter and distance from the linear fault rupture, the observation from Keefer and Manson (1998) and Khazai and Sitar (2003), and the results of numerical modelling by Bourdeau et al. (2004), suggest that the size of landslides should decrease with the distance from the seismic source. In order to demonstrate that, different magnitude-frequency relationships has been derived from landslide inventories on the basis of classes of distance from the seismic source . Four methodologies were applied to the magnitude-frequency curves o characterize the scaling parameter of the landslide size distribution. Among these approaches, it was observed that the Double Pareto distribution is the method that allow a better, automatic, characterization of the landslide distribution, especially in the area of the rollover, but it is subject to some limitation due also to the accuracy of the landslide inventories, and to the presence of a statistically representative sample of the different size classes (also small landslides). As consequence, it cannot be used as a unique method for the fit of the curves.

From the analysis of the different MF curves, it results that the distance from the seismic source do not clearly control the size distribution.In general, the exponent of the probability density curves is higher for the maximum distance with respect to the distance close to the seismic source, thus confirming the initial hypothesis However, there are some exception, that could be explained with problem in the quality of the landslide inventories and to the capability of the method applied to fit the curves. However, for intermediate distance the trend in not so clear, and the initial hypothesis

(i.e., the distance from the seismic source controls the landslide size distribution) is not demonstrated. This fact can be related to different reasons. First of all, there is a strong relationship of the landslide size with the peak ground acceleration (PGA) values registered in the affected area, but the PGA values are not linearly dependent from the distance, because they are also controlled by local site effects. Moreover, over a certain threshold of PGA, that change for the different earthquakes, the landslides size decreases, also due to the small area at which the high PGA occurred. Tohoku earthquake do not show this trend, due to the scattered distribution of the PGA in the ShakeMap used (see earthquake description).

Another important factor that can influence the size of the landslides and that can mask the relationship between landslide size and the distance from the seismic source is the geology of the affected areas. The analysis proved how some lithologies are not affected by the earthquake shaking in the landslide size, and give the same size distribution independently from the earthquake magnitude and the distance from the seismic source. In contrast there are other lithologies that show a relationship with the distance from the seismic source, and give a size distribution according to the position respect to the seismic source.

There is an interdependence between different factors that control the landslide size distribution that is directly linked to the characteristics of the area where the earthquake occurs. Probably, other factors as focal depth, specific ground motion characteristics of individual earthquakes and site effects could be also important, and could allow to better understand the landslide size distribution at local scale. The quality of the earthquake-induce landslides is also important to allow this kind of analysis, and it is necessary an implementation of the available dataset, due to some limitation found, such as the lower limit on the size of landslides that can be detected from satellite images (censoring). Ground-based field studies have also been crucial in preparing most comprehensive landslide inventories.

As said before, the magnitude-frequency curves of earthquake-induced landslide inventories are fundamental in landslide hazard. In this thesis, a simple methodology of earthquake-induced rockfall hazard zoning is presented. This methodology allows combining the onset frequency of rockfalls in seismic areas, the frequency of transit of simulated block along the slope, the kinetic energy and the fly height of the simulated trajectories. For the application of the methodology it is required a complete description of the past rockfall events and source areas, a detailed record of the seismic parameters, a reliable DEM for the discriminant analysis and the propagation modelling, and the blocks size distribution (MF relationship) for the calculation of the number of blocks potentially triggered by seismic inputs with different return period.

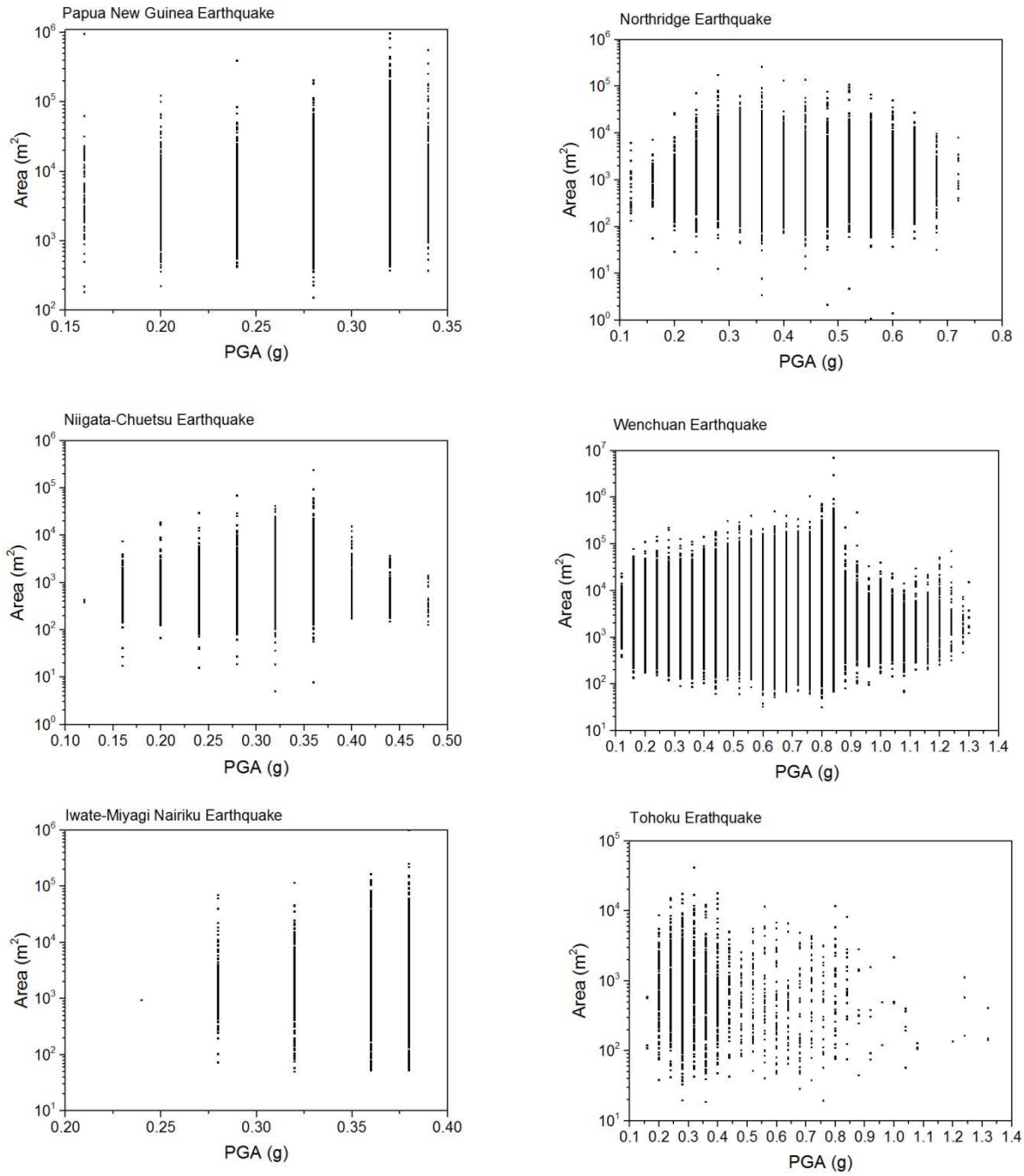

Figure 151. Landslide size distribution (m^2) as function of the peak ground acceleration (g).

The analysis of factors controlling the distribution of earthquake-induced rockfalls shows that the most important factors are the slope angle, the peak ground acceleration and the slope curvature.For the peak ground acceleration, an attempt to validate the values used in the methodology was conducted. The use of the precarious balanced rocks is a valuable tool for the definition of the upper bound of the horizontal acceleration experienced by the affected area from the last larger earthquake, and can give information were data are not available. The method can be applied to

small areas due to the large time for collecting the data and the application of this kind of procedure in large areas affected by high magnitude earthquakes is unthinkable.

Acknowledgments

Odin Marc and Niels Hovius (Helmholtz Centre Potsdam) provided the Papua New Guinea, Niigata-Chuetsu, and Iwate-Miyagi Nairiku inventories.
Chong Xu (Institute of Geology, China Earthquake Administration) provided the Wenchuan inventory.

The Geological Survey of Friuli Venezia Giulia Autonomous Region provided the historical data related to the 1976 Friuli Earthquake within the framework of the MASSMOVE INTERREG project. The Civil Protection of Friuli Venezia Giulia Autonomous Region provided the 1 m cell LiDAR data and the orthophotos of the study area. The research was supported by PRIN Project: Time-Space prediction of high impact Landslides under changing precipitation regimes.

References

Abbott, L.D. (1995). Neogene tectonic reconstruction of the Adelbert Finisterre-New Britain collision, northern Papua New Guinea: Journal of Southeast Asian Earth Sciences v. 11, pp. 33–51.

Abbott, L.D., Silver, E.A., Anderson, R.S., Smith, R., Ingle, J.C., Kling, S.A., Haig, D., Small, E., Galewsky, J., and Sliter, W. (1997). Measurement of tectonic surface uplift in a young collisional mountain belt. Nature 385, 501–507.

Abbruzzese J. M., and Labiouse V. (2013). New Cadanav methodology for quantitative rock fall hazard assessment and zoning at the local scale. Landslides, doi 10.1007/s10346-013-0411-7.

Agliardi F. and Crosta G. (2003): High resolution three-dimensional numerical modelling of rockfalls. International Journal of Rock Mechanics and Mining Sciences, 40(4), 455-471.

Agliardi F., Crosta G. B., and Frattini P. (2009). Integrating rockfall risk assessment and countermeasure design by 3D modelling techniques. Natural Hazards and Earth System Sciences, 9, 1059-1073.

Ambraseys N. N. (1976): The Gemona di Friuli Earthquake of 6 May 1976. UNESCO Technical Report, RP/1975-76/2.222.3, Paris.

Anderson, D. L. (1971). The San Andreas fault. Scientific American, 225, 52-68.

Annaka, T., Satake, K., Sakakiyama, T., Yanagisawa, K., and Shuto, N. (2007). Logic-tree approach for probabilistic tsunami hazard analysis and its applications to the Japanese coasts. In Tsunami and Its Hazards in the Indian and Pacific Oceans (pp. 577-592). Birkhäuser Basel.

Anooshehpoor, A., and Brune, J.N., (2002), Verification of precarious methodology using shake table tests of rocks and rock models: Soil Dynamics and Earthquake Engineering, v. 22, p. 917–922, doi: 10.1016/S0267- 7261(02)00115-X.

Anooshehpoor, A., Brune, J.N., and Zeng, Y., (2004), Methodology for obtaining constraints on ground motion from precariously balanced rocks: Seismological Society of America Bulletin, v. 94, p. 285–303, doi: 10.1785/ 0120020242.

Anooshehpoor, A., Purvance, M., Brune, J., and Rennie, T., (2007), Reduction in the uncertainties in the ground motion constraints by improved field testing techniques of precariously balanced rocks (proceedings and abstracts): SCEC Annual Meeting, Palm Springs, California, September 9-12, 2007, 17.

Aoudia A., Saraò A., Bukchin B., Suhadolc P. (2000). The 1976 Friuli (NE Italy) thrust faulting earthquake: a reappraisal 23 yearslater. Geoph. Res. Lett. 27, 573–576.

Azzoni A., La Barbera G., and Zaninetti A. (1995). Analysis and prediction of rockfalls using a mathematical model. In International journal of rock mechanics and mining sciences & geomechanics abstracts (Vol. 32, No. 7, pp. 709-724). Pergamon.

Bak, P., Tang, C., & Wiesenfeld, K. (1988). Self-organized criticality. Physical review A, 38(1), 364.

Beguería S. (2006). Validation and evaluation of predictive models in hazard assessment and risk management. Natural Hazards, 37(3), 315-329.

Bell, J.W., Brune, J.N., Liu, T., Zerda, M., and Yount, J.C., (1998), Dating the precariously balanced rocks in seismically active parts of California and Nevada: Geology, v. 26, p. 495–498, doi: 10.1130/0091-7613(1998) 026,0495:DPBRIS.2.3.CO;2.

Berger, W. H., Kroenke, L. W., Mayer, L. A., Backman, J., Janecek, T. R., Krissek, L., ... and Lyle, M. (1992). The record of Ontong Java Plateau: main results of ODP Leg 130. Geological Society of America Bulletin, 104(8), 954-972.

Bommer, J. J., and Rodríguez, C. E. (2002). Earthquake-induced landslides in Central America. Engineering Geology, 63(3), 189-220.

Bottelberghs P. H. (2000). Risk analysis and safety policy developments in the Netherlands. Journal of Hazardous Materials, 71(1), 59-84.

Bourdeau, C., Havenith, H. B., Fleurisson, J. A., and Grandjean, G. (2004). Numerical modelling of seismic slope stability (pp. 671-684). Springer Berlin Heidelberg.

Brardinoni, F., and Church, M. (2004). Representing the landslide magnitude–frequency relation: Capilano River basin, British Columbia. Earth Surface Processes and Landforms, 29(1), 115-124.

Broili L. (1977). Comunità Montana del Gemonese (1977). Carta geostatica del Comune di Venzone. Direzione Nazionale dei Lavori Pubblici, Servizio delle Calamità Naturali, Regione Friuli Venezia Giulia. In Italian

Broili L., Cucchi F., Onofri R., Stefanini S., Ulcigrai F., Carraio F. (1980). Studio geologico per la ricostruzione del comune di Gemona. Fenomeni Franosi (with 1:5000 map). Comune di Gemona. In Italian.

Brune, J. N., 1996, Precariously balanced rocks and ground motion maps for southern California: Seismological Society of America Bulletin, v. 86, p. 43–54.

Brune, J. N., Anooshehpoor, A., Purvance, M. D., and Brune, R. J. (2006). Band of precariously balanced rocks between the Elsinore and San Jacinto, California, fault zones: Constraints on ground motion for large earthquakes. Geology, 34(3), 137-140.

Budetta P., (2004). Assessment of rockfall risk along roads. Natural Hazards and Earth System Science, 4(1), 71-81.

Burchfiel, B. C., Zhiliang, C., Yupinc, L., and Royden, L. H. (1995). Tectonics of the Longmen Shan and adjacent regions, central China. International Geology Review, 37(8), 661-735.

Burrato P., Poli M. E., Vannoli P., Zanferrari A., Basili R. and Galadini F. (2008). Sources of Mw 5+ earthquakes in northeastern Italy and western Slovenia: An updated view based on geological and seismological evidence. Tectonophysics 453 (2008) 157–176.

Cancelli A., Crosta G. (1993) Rockfall hazard and risk mapping. 7th ICFL, Int. Conf. & Field Workshop on Landslides, Repub. Ceca, Settembre 1993, Balkema p. 69-76

Capolongo D., Refice A., and Mankelow J. (2002). Evaluating earthquake-triggered landslide hazard at the basin scale through GIS in the upper Sele river valley. Surveys in geophysics, 23(6), 595-625.

Carulli G. B. (2006). Carta geologica del Friuli Venezia Giulia. Regione autonoma Friuli Venezia Giulia, S.El.Ca., Firenze.

CEREIS, Centro Regional de Sismología para América del Sur, 2010. Catálogo de intensidades. www.cereis.org/portal/catal_inten.php 2010

Chau K. T., Wong R. H. C., Liu J., and Lee C. F. (2003). Rockfall hazard analysis for Hong Kong based on rockfall inventory. Rock Mechanics and Rock Engineering, 36(5), 383-408.

Chen, C. Y. (2009). Sedimentary impacts from landslides in the Tachia River Basin, Taiwan. Geomorphology, 105(3), 355-365.

Cipar J., 1981. Broadband time domain modelling of earthquakes from Friuli, Italy., Bull. seism. Soc. Am., 71, 1215–1231.

Clauset, A., Young, M., and Gleditsch, K. S. (2007). On the frequency of severe terrorist events. Journal of Conflict Resolution, 51(1), 58-87

Clauset, A., Shalizi, C. R., and Newman, M. E. (2009). Power-law distributions in empirical data. SIAM review, 51(4), 661-703.

Corominas J., Copons R., Vilaplana J. M., Altimir J., and Amigó J. (2003). Integrated landslide susceptibility analysis and hazard assessment in the principality of Andorra. Natural Hazards, 30(3), 421-435.

Corominas J., Copons R., Moya J., Vilaplana J. M., Altimir J., and Amigó J. (2005). Quantitative assessment of the residual risk in a rockfall protected area. Landslides, 2(4), 343-357.

Corominas, J., Van Westen, C., Frattini, P., Cascini, L., Malet, J. P., Fotopoulou, S., ... and Smith, J. T. (2014). Recommendations for the quantitative analysis of landslide risk. Bulletin of engineering geology and the environment, 73(2), 209-263.

Costa G., Giorgi M., Moratto L., Petronio L., Pettenati F., Sandron D., Sirovich L., Suhadolc P.: Sintesi sullo scenario sismogenetico più plausibile per la scossa del 6/5/76 in Friuli; Relazione OGS 2009/43-GDL 16 SITAR (2009) 8 pp. (in Italian).

Crosta G.B., Agliardi F., (2003): A new methodology for physically-based rockfall hazard assessment. Natural Hazards and Earth System Sciences, 3, 407–422.

Crosta G.B., Agliardi F,. Frattini P. and Imposimato S., (2004): A three-dimensional hybrid numerical model for rockfall simulation. Geophysical Research Abstracts, 6, 04502.

Crosta, G. B., Hermanns, R., Frattini, P., Valbuzzi, E., & Valagussa, A. (2014). Large slope instabilities in Northern Chile: inventory, characterization and possible triggers. In Landslide Science for a Safer Geoenvironment (pp. 175-181). Springer International Publishing.

Crowell, J. C. (1975). The San Andreas fault in southern California, in Crowell, J . C., ed., The San Andreas fault in Southern California: California Division of Mines and Geology Special Report 118, p. 7-27.

Cruden, D. M., and Varnes, D. J. (1996). Landslides: Investigation and Mitigation. Chapter 3-Landslide types and processes. Transportation research board special report, (247).

Dai, F. C., Xu, C., Yao, X., Xu, L., Tu, X. B., and Gong, Q. M. (2011). Spatial distribution of landslides triggered by the 2008 Ms 8.0 Wenchuan earthquake, China. Journal of Asian Earth Sciences, 40(4), 883-895.

Davies, H.L. and Warren, R.G. (1988). Origin of eclogite-bearing, domed layered metamorphic complexes (‘core complexes’) in the D’Entrecasteaux Islands, Papua New Guinea: Tectonics, v. 7, pp. 1–21.

Del Gaudio V., Pierri P., and Wasowski J. (2003). An approach to time-probabilistic evaluation of seismically induced landslide hazard. Bulletin of the Seismological Society of America, 93(2), 557-569.

Del Gaudio V., and Wasowski J. (2004). Time probabilistic evaluation of seismically induced landslide hazard in Irpinia (Southern Italy). Soil Dynamics and Earthquake Engineering, 24(12), 915-928.

Delgado, J., Peláez, J. A., Tomás, R., García-Tortosa, F. J., Alfaro, P., and López Casado, C. (2011a). Seismically-induced landslides in the Betic Cordillera (S Spain). Soil Dynamics and Earthquake Engineering, 31(9), 1203-1211.

Delgado, J., Garrido, J., López-Casado, C., Martino, S., and Peláez, J. A. (2011b). On far field occurrence of seismically induced landslides. Engineering Geology, 123(3), 204-213.

Densmore, A.L., and Hovius, N. (2000). Topographic fingerprints of bedrock landslides. Geology 28, 371–374.

der Hilst, B. H. (2008). A geological and geophysical context for the Wenchuan earthquake of 12 May 2008, Sichuan, People's Republic of China. GSA today,18(7), 5.

Descoeudres F., Zimmermann T., (1987): Three-dimensional dynamic calculation of rockfalls, In Herget, G. and Vongpaisal, S., editors, Proceedings of the Sixth International Congress on Rock Mechanics. Montreal. Rotterdam: Balkema, 37–42.

Di Prisco C., Vecchiotti M. (2006). A rheological model for the description of boulder impacts on granular strata. Geotechnique, 56(7), 469-482.

Dorren L.K.A., Berger, F., Putters, U.S., (2006): Real-size experiments and 3D simulation of rockfall on forested and non-forested slopes. Natural Hazards and Earth System Sciences, 6, 145–153.

Drăguţ, L., and Eisank, C. (2012). Automated object-based classification of topography from SRTM data. Geomorphology, 141, 21-33.

Dussauge, C., Grasso, J. R., and Helmstetter, A. (2003). Statistical analysis of rockfall volume distributions: Implications for rockfall dynamics. Journal of Geophysical Research: Solid Earth (1978–2012), 108(B6).

Earthquake Research Institute, The University of Tokyo (2004) The mid Niigata Prefecture earthquake in 2004. http://www.eprc.eri.u-tokyo.ac.jp/members/satow/danmen.jpg

Editorial Board, State Seismological Bureau, 1989, Lithospheric dynamics atlas of China: Beijing, China Cartographic Publishing House, p. 23.

Evans S. G., and Hungr O. (1993). The assessment of rockfall hazard at the base of talus slopes. Canadian Geotechnical Journal, 30(4), 620-636.

Falvey, D. A. and Pritchard, T. (1984). Preliminary paleomagnetic results from northern Papua New Guinea: Evidence for large microplate rotations. Transactions of the Third Circum-Pacific Energy and Mineral Resources Conference, Honolulu, 1982, pp. 593-599.

Faure, M., Lalevée, F., Gusokujima, Y., Iiyama, J. T., and Cadet, J. P. (1986). The pre-Cretaceous deep-seated tectonics of the Abukuma massif and its place in the structural framework of Japan. Earth and planetary science letters,77(3), 384-398.

Fell, R., Corominas, J., Bonnard, C., Cascini, L., Leroi, E., and Savage, W. Z. (2008). Guidelines for landslide susceptibility, hazard and risk zoning for land-use planning. Engineering Geology, 102(3), 99-111.

Frankel, A. D., Mueller, C., Barnhard, T., Perkins, D., Leyendecker, E., Dickman, N., ... and Hopper, M. (1996). National seismic-hazard maps: documentation June 1996 (pp. 96-532). US Geological Survey.

Frattini P., Crosta G., and Carrara A. (2010). Techniques for evaluating the performance of landslide susceptibility models. Engineering geology, 111(1), 62-72.

Frattini P., Crosta G.B., Agliardi F. (2012a): Rockfall characterization and modeling. In: Clague JJ, Stead D (eds) Landslides types, mechanisms and modeling. Cambridge University Press, Cambridge., pp 267–281. ISBN 978-1-107-00206-7

Frattini P., Crosta G.B., Lari S., Agliardi F. (2012b): Probabilistic Rockfall Hazard Analysis (PRHA). In: Landslides and Engineered Slopes: Protecting Society through Improved Understanding. London: Taylor & Francis Group, 1145-1151.

Frattini, P., and Crosta, G. B. (2013). The role of material properties and landscape morphology on landslide size distributions. Earth and Planetary Science Letters, 361, 310-319.

Galadini F., Poli M.E., Zanferrari A., (2005): Seismogenic sources potentially responsible for earthquakes with M≥6 in the eastern Southern Alps (Thiene–Udine sector, NE Italy). Geophys.J. Int. 161, 739–762.

García M, Riquelme R, Farias M, Herail G, Charrier R, (2011). Late Miocene-Holocene canyon incision in the western Altiplano, northern Chile : tectonic or climatic forcing ? Journal of the Geological Society, 168 (4): 1047-1060.

Gardner J. (1970) Rockfall: a geomorphic process in high mountain terrain, Alberta Geogr. 6, 15-20.

Geist, E. L., and Parsons, T. (2008). Distribution of tsunami interevent times. Geophysical Research Letters, 35(2).

Geographical Survey Institute of Japan (2004) The mid Niigata Prefecture earthquakes in 2004. http://www.cais.gsi.go.jp/research/topics/topic041023/topic_041023.html

Geological Survey of Japan (1982) Geological atlas of Japan, 119 pp.

Geological Survey of Japan, AIST (2012) Seamless digital geological map of Japan 1: 200,000. Jul 3, 2012 version. (Geological Survey of Japan, A., ed.). Research Information Database DB084, Geological Survey of Japan, National Institute of Advanced Industrial Science and Technology. Geological Survey of Japan, AIST, Tsukuba.

Geotechnical Engineering Office (1998). Landslides and boulder falls from natural terrain: interim risk guidelines. GEO Report No. 75. Geotechnical Engineering Office, The Government of the Hong Kong Special Administrative Region.

González, F. I., Geist, E. L., Jaffe, B., Kânoğlu, U., Mofjeld, H., Synolakis, C. E., ... and Yalciner, A. (2009). Probabilistic tsunami hazard assessment at Seaside, Oregon, for near and far field seismic sources. Journal of Geophysical Research: Oceans (1978–2012), 114(C11).

Gorsevski P. V., Gessler P. E., Foltz, R. B., and Elliot W. J. (2006). Spatial prediction of landslide hazard using logistic regression and ROC analysis. Transactions in GIS, 10(3), 395-415.

Gorum, T., Fan, X., van Westen, C. J., Huang, R. Q., Xu, Q., Tang, C., and Wang, G. (2011). Distribution pattern of earthquake-induced landslides triggered by the 12 May 2008 Wenchuan earthquake. Geomorphology, 133(3), 152-167.

Govi M, (1976): Map showing the landslides triggered by earthquake (from aerial photographs of May-June 1976). Reported in: National Research Council Geological and Mining Sciences Committee Italian "Geodynamics" Project. Geology of the Friuli area primarily involved in the earthquake, 1976. Edited by Bruno Martinis (1977). In Italian.

Graizer, V., and Kalkan, E. (2009). Prediction of spectral acceleration response ordinates based on PGA attenuation. Earthquake Spectra, 25(1), 39-69.

Grünthal, G., Thieken, A. H., Schwarz, J., Radtke, K. S., Smolka, A., and Merz, B. (2006). Comparative risk assessments for the city of Cologne–storms, floods, earthquakes. Natural Hazards, 38(1-2), 21-44.

Gutenberg, B., and Richter, C. F. (1954). Seismicity of the Earth 2nd ed., 310.

Guthrie, R. H., and Evans, S. G. (2004). Analysis of landslide frequencies and characteristics in a natural system, coastal British Columbia. Earth Surface Processes and Landforms, 29(11), 1321-1339.

Guthrie, R. H., Deadman, P. J., Cabrera, A. R., & Evans, S. G. (2008). Exploring the magnitude–frequency distribution: a cellular automata model for landslides. Landslides, 5(1), 151-159.

Guzzetti F., Crosta G., Detti R. and Agliardi F., (2002a): STONE: a computer program for the three-dimensional simulation of rock-falls. Computers and Geosciences, 28 (9), 1079-1093.

Guzzetti, F., Malamud, B. D., Turcotte, D. L., and Reichenbach, P. (2002b). Power-law correlations of landslide areas in central Italy. Earth and Planetary Science Letters, 195(3), 169-183.

Guzzetti F., Reichenbach P., Ardizzone F., Cardinali M., and Galli M. (2006). Estimating the quality of landslide susceptibility models. Geomorphology, 81(1), 166-184.

Guzzetti, F., Mondini, A. C., Cardinali, M., Fiorucci, F., Santangelo, M., and Chang, K. T. (2012). Landslide inventory maps: New tools for an old problem. Earth-Science Reviews, 112(1), 42-66.

Hack R., Alkema D., Kruse G. A., Leenders N., and Luzi L. (2007). Influence of earthquakes on the stability of slopes. Engineering geology, 91(1), 4-15.

Haddad, D. E., (2009). Estimating the geometrical parameters of precariously balanced rocks from unconstrained digital photographs, 22 p.

Haddad, D. E., (2010). Geologic and geomorphic characterization of precariously balanced rocks, MS thesis, Arizona State University, Tempe, 207 p.

Haddad, D. E., and Arrowsmith, J. R., (2009), Characterizing the geomorphic situation of precariously balanced rocks in semi-arid to arid landscapes of low-seismicity regions (proceedings and abstracts): SCEC Annual Meeting, Palm Springs, California, September 12-16, 2009, 19.

Hadley, D., and Kanamori, H. (1977). Seismic structure of the transverse ranges, California. Geological Society of America Bulletin, 88(10), 1469-1478.

Hancox, G. T., Perrin, N. D., and Dellow, G. D. (2002). Recent studies of historical earthquake-induced landsliding, ground damage, and MM intensity in New Zealand. Bulletin of the New Zealand Society for Earthquake Engineering, 35(2), 59-95.

Harp, Edwin L., and Jibson, Randall W. (1995). Inventory of landslides triggered by the 1994 Northridge, California earthquake: U.S. Geological Survey Open-File Report 95-213.

Hashimoto, M. (1991). Geology of Japan, Japan: Terra Scientific Publishing Company, Tokyo, 253 pp.

Hergarten, S., and Neugebauer, H. J. (1998). Self-organized criticality in a landslide model. Geophysical Research Letters, 25(6), 801-804.

Hoke, G. D, Isacks, B. L., Jordan, T. E., Blanco, N., Tomlinson, A. J., and Ramezani, J. (2007) Geomorphic evidence for post-10 Ma uplift of the western flank of the central Andes 18°30'–22°S. Tectonics 26.

Horn, B.K.P. (1981): Hill shading and the reflectance map. Proc. IEEE 69:14-47.

Housner, G. W., (1963), The behavior of inverted pendulum structures during earthquakes: Bulletin of the Seismological Society of America, v. 53, no. 2, p. 403-417.

Hovius, N., Stark, C. P., and Allen, P. A. (1997). Sediment flux from a mountain belt derived by landslide mapping. Geology, 25(3), 231-234.

Hovius, N., Stark, C.P., Tutton, M.A., and Abbott, L.D. (1998). Landslide-driven drainage network evolution in a pre-steady-state mountain belt: Finisterre Mountains, Papua New Guinea. Geology 26, 1071–1074.

Hovius, N., Stark, C. P., Hao-Tsu, C., & Jiun-Chuan, L. (2000). Supply and removal of sediment in a landslide-dominated mountain belt: Central Range, Taiwan. The Journal of geology, 108(1), 73-89.

Hudnut, K., Amidon, W., Bawden, G., Brune, J., Bond, S., Graves, R., Haddad, D. E., Limaye, A., Lynch, D. K., Phillips, D. A., Pounders, E., Rood, D., and Weiser, D., (2009), The Echo Cliffs precariously balanced rock; discovery and description by terrestrial laser scanning (proceedings

and abstracts): Southern California Earthquake Center Annual Meeting, Palm Springs, California, September 12-16, 2009, 19.

Hungr, O. (1997). Some methods of landslide hazard intensity mapping. Landslide risk assessment. Balkema, Rotterdam, 215-226.

Hungr, O., Evans, S. G., and Hazzard, J. (1999). Magnitude and frequency of rock falls and rock slides along the main transportation corridors of southwestern British Columbia. Canadian Geotechnical Journal, 36(2), 224-238.

Hungr, O., McDougall, S., Wise, M., and Cullen, M. (2008). Magnitude–frequency relationships of debris flows and debris avalanches in relation to slope relief.Geomorphology, 96(3), 355-365.

Jaboyedoff M., Dudt J. P., and Labiouse V. (2005). An attempt to refine rockfall hazard zoning based on the kinetic energy, frequency and fragmentation degree. Natural Hazards and Earth System Science, 5(5), 621-632.

Jakob, M., and Friele, P. (2010). Frequency and magnitude of debris flows on Cheekye River, British Columbia. Geomorphology, 114(3), 382-395.

Jaques, A.L. and Robinson, G.P. (1977). The continent-island arc collision in northern New Guinea: BMR Journal of Australian Geology and Geophysics, v. 2, pp. 289–303.

Jennings, C. W., Strand, R. G., and Rogers, T. H. (1977). Geologic map of California, California Division of Mines and Geology, scale 1:750,000, Sacramento, CA.

Jibson R. W., Harp E. L., and Michael J. A. (2000). A method for producing digital probabilistic seismic landslide hazard maps. Engineering Geology, 58(3), 271-289.

Johnson, R. W. and Jaques, A. L. (1980) Continent-arc collision and reversal of arc polarity: new interpretations from a critical area. Tectonophysics 63, 111-124.

Jones C. L., Higgins J. D., and Andrew R. D. (2000). Colorado Rockfall Simulation Program: Version 4.0 (for Windows), Colorado Geological Survey.

Jones, L. M., Han, W., Hauksson, E., Jin, A., Zhang, Y., and Luo, Z. (1984). Focal mechanisms and aftershock locations of the Songpan earthquakes of August 1976 in Sichuan, China. Journal of Geophysical Research: Solid Earth (1978–2012), 89(B9), 7697-7707

Katz, O., and Aharonov, E. (2006). Landslides in vibrating sand box: What controls types of slope failure and frequency magnitude relations?. Earth and Planetary Science Letters, 247(3), 280-294.

Kausel E, Campos J, (1992) The Ms=8 tensional earthquake of December 1950 of northern Chile and its relation to the seismic potential of the region, Phys. Earth Planet. Int., 72: 220–235.

Keefer D. (1984): Landslides caused by earthquakes. Geological Society of America Bulletin 1984;95, no. 4;406-421.

Keefer D K, (1994) The importance of earthquake-induced landslides to long-term slope erosion and slope-failure hazards in seismically active regions, Geomorphology. 10: 265–284.

Keefer, D. K. (2000). Statistical analysis of an earthquake-induced landslide distribution—the 1989 Loma Prieta, California event. Engineering Geology,58(3), 231-249.

Keefer, D. K. (2002). Investigating landslides caused by earthquakes–a historical review. Surveys in Geophysics, 23(6), 473-510.

Keefer, D. K., and Wilson, R. C. (1989). Predicting earthquake-induced landslides, with emphasis on arid and semi-arid environments. Landslides in a semi-arid environment, 2, 118-149.

Keefer, D. K., and Manson, M. W. (1998). Regional distribution and characteristics of landslides generated by the earthquake. US Geological Survey professional paper, (1551C).

Khazai, B., and Sitar, N. (2004). Evaluation of factors controlling earthquake-induced landslides caused by Chi-Chi earthquake and comparison with the Northridge and Loma Prieta events. Engineering geology, 71(1), 79-95.

Kirby, E., Whipple, K. X., Burchfiel, B. C., Tang, W., Berger, G., Sun, Z., and Chen, Z. (2000). Neotectonics of the Min Shan, China: Implications for mechanisms driving Quaternary deformation along the eastern margin of the Tibetan Plateau. Geological Society of America Bulletin, 112(3), 375-393.

Kirk-Lawlor N E, Jordan T E, Rech J A, Lehmann S B, (2013) Late Miocene to Early Pliocene paleohydrology and landscape evolution of Northern Chile, 19° to 20° S, Palaeogeography, Palaeoclimatology, Palaeoecology, 387, 76-90, dx.doi.org/10.1016/j.palaeo.2013.07.011.

Kirkpatrick, P., (1927), Seismic measurements by the overthrow of columns: Bulletin of the Seismological Society of America, v. 17, no. 2, p. 95-109.

Kober F, Ivy-Ochs S, Schlunegger F, Baur H, Kubik P W, Wieler R. (2007) Denudation rates and a topography-driven rainfall threshold in northern Chile: Multiple cosmogenic nuclide data and sediment yield budgets, Geomorphology, 83:97-120.

Kolmogorov, A. N. (1950). Grundbegriffe der Wahrscheinlichkeitsrechnung, Berlin, 1933. English translation, Chelsea, New York.

Korup, O., Clague, J. J., Hermanns, R. L., Hewitt, K., Strom, A. L., and Weidinger, J. T. (2007). Giant landslides, topography, and erosion. Earth and Planetary Science Letters, 261(3), 578-589.

Kroenke, L. W. (1984). Cenozoic tectonic development of the southwest Pacific. Tech. Bulletin 6, Committee for Coordination of Joint Prospecting in South Pacific Offshore Areas (CCOP/SOPAC), United Nations Economic and Social Commission of Asia and the Pacific, CCOP/SOPAC, Suva, Fiji, 126 pp.

Labiouse, V., and Abbruzzese, J. M. (2011). Rockfall hazard zoning for land use planning. In: Nicot F, Lambert S (eds) Rockfall engineering. Wiley, New York, pp 211–253.

Lari, S., Crosta, G.B., Frattini, P. (2014). A probabilistic approach for landslide hazard analysis. Engineering Geology, accepted for pubblication.

Larsen, I. J., Montgomery, D. R., Korup, O. (2010) Landslide erosion caused by hillslope material, Nature Geoscience, 3: 247–251.

Lee, C. T., Huang, C. C., Lee, J. F., Pan, K. L., Lin, M. L., and Dong, J. J. (2008). Statistical approach to earthquake-induced landslide susceptibility. Engineering Geology, 100(1), 43-58.

Leine, R. I., Schweizer, A., Christen, M., Glover, J., Bartelt, P., and Gerber, W. (2013). Simulation of rockfall trajectories with consideration of rock shape.Multibody System Dynamics, doi: 10.1007/s11044-013-9393-4.

Liu, Y., Santos, A., Wang, S. M., Shi, Y., Liu, H., and Yuen, D. A. (2007). Tsunami hazards along Chinese coast from potential earthquakes in South China Sea. Physics of the earth and planetary interiors, 163(1), 233-244.

Malamud, B. D., and Turcotte, D. L. (1999). Self-organized criticality applied to natural hazards. Natural Hazards, 20(2-3), 93-116.

Malamud, B. D., Turcotte, D. L., Guzzetti, F., and Reichenbach, P. (2004a) Landslides, earthquakes, and erosion. Earth and Planetary Science Letters. 229: 45-59.

Malamud, B. D., Turcotte, D. L., Guzzetti, F., and Reichenbach, P. (2004b). Landslide inventories and their statistical properties. Earth Surface Processes and Landforms, 29(6), 687-711.

Mallet, R., (1862), The Great Neopolitan Earthquake of 1857: London, Chapman and Hall.

Marc, O., and Hovius, N. (2014). Amalgamation in landslide maps: effects and automatic detection. Natural Hazards and Earth System Sciences Discussions, 2(12), 7651-7678.

Marchi, L., and D'Agostino, V. (2004). Estimation of debris-flow magnitude in the Eastern Italian Alps. Earth Surface Processes and Landforms, 29(2), 207-220.

Marzorati, S., Luzi, L., De Amicis, M. (2002): Rock falls induced by earthquakes: a statistical approach. Soil Dynamics and Earthquake Engineering, Volume 22, Issue 7, September 2002, Pages 565–577.

Mazzoccola, D., and Sciesa, E. (2000, June). Implementation and comparison of different methods for rockfall hazard assessment in the Italian Alps. In 8th Int. Symp. on Landslides (pp. 1035-1040).

Meunier, P., Hovius, N., and Haines, A. J. (2007). Regional patterns of earthquake-triggered landslides and their relation to ground motion. Geophysical Research Letters, 34(20).

Meunier, P., Hovius, N., Haines, J.A. (2008): Topographic site effects and the location of earthquake induced landslides. Earth and Planetary Science Letters, 275, pp. 221–232.

Mikoshiba, M. U., Kanisawa, S., Matsuhisa, Y., and Togashi, S. (2004). Geochemical and isotopic characteristics of the Cretaceous Orikabe Plutonic Complex, Kitakami Mountains, Japan: magmatic evolution in a zoned pluton and significance of a subduction-related mafic parental magma. Contributions to Mineralogy and Petrology, 146(4), 433-449.

Miles, S. B., and Keefer, D. K. (2009). Evaluation of CAMEL-comprehensive areal model of earthquake-induced landslides. Engineering Geology, 104(1), 1-15.

Milne, J., (1881), Experiments in observational seismology: Transactions of the Seismological Society of Japan, v. 3, p. 12-64.

Milne, J., and Omori, F., (1893), On the overturning and fracturing of brick and other columns by horizontally applied motion: Seismological Journal of Japan, v. 1, p. 59-85

Miyashiro, A. (1958). Regional metamorphism of the Gosaisyo-Takanuki district in the central Abukuma Plateau. J. Fac. Sci. Univ. Tokyo, 11, 219-272.

Mora, S., and Mora, R. (1994). Los deslizamientos causados por el terremoto de Limon: Factores de control y comparacion con otros eventos en Costa Rica. Revista Geológica de América Central.

Moratto, L., Suhadolc, P., Costa, G. (2012): Finite-fault Parameters of the September 1976 M > 5 Aftershocks in Friuli (NE Italy) Tectonophysics, 536–537: 44–60.

Motamedi, M., and Liang, R. Y. (2013). Probabilistic landslide hazard assessment using Copula modeling technique. Landslides, published online; doi:10.1007/s10346-013-0399-z.Onofri R. (1995) Indagine geologico-tecnica volta alla ridefinizione dell'attuale limite di massima invasione massi, Comune di Villa Santina. In Italian.

Musgrave, R. J. (1990) Paleomagnetism and tectonics of Malaita, Solomon Islands. Tectonics 9, 735-759.

National Research Institute of Earth Science and Disaster Prevention (2004a) 2004 mid Niigata earthquake. http://www.hinet.bosai.go.jp/topics/niigata041023

National Research Institute of Earth Science and Disaster Prevention (2004b) Landslide topography in Yamakoshi Village and its vicinity, scale 1:25,000. http://www.lsweb1.ess.bosai.go.jp/jisuberi/jisuberi_mini/nigata/img/jisuberi.jpg

OFAT, O. OFEFP (1997) Recommendations. Prise en compte des dangers dus aux mouvements de terrain dans le cadre des activités de l'aménagement du territoire. Edited by OFAT/OFEE/OFEPF, Bern.

Ohba T, Yamamoto M, Kondo A, Suzuki S, Hayashi S (2009) Stratigraphy of the landslide disaster area by the Iwate Miyagi Inland Earthquake, In: The Joint Research Project of Three North

Tohoku National Universities: Research report of the disaster survey of the Iwate Miyagi Inland Earthquake, Akita, pp. 24–35

Papadopoulos, G. A., and Plessa, A. (2000). Magnitude–distance relations for earthquake-induced landslides in Greece. Engineering Geology, 58(3), 377-386.

Parker, R. N. (2013). Hillslope memory and spatial and temporal distributions of earthquake-induced landslides, Durham theses, Durham University.

Pelletier, J. D., Malamud, B. D., Blodgett, T., and Turcotte, D. L. (1997). Scale-invariance of soil moisture variability and its implications for the frequency-size distribution of landslides. Engineering Geology, 48(3), 255-268.

Peng, W. F., Wang, C. L., Chen, S. T., and Lee, S. T. (2009). Incorporating the effects of topographic amplification and sliding areas in the modeling of earthquake-induced landslide hazards, using the cumulative displacement method. Computers & Geosciences, 35(5), 946-966.

Perniola, B., Bressan, G., Pondrelli, S. (2004). Changes in failure stress and stress transfer during the 1976–77 Friuli earthquake sequence. Geophys. J. Int. 156, 297–306.

Pfeiffer T. J., and Higgins J. D. (1990). Rockfall hazard analysis using the Colorado rockfall simulation program. Transportation Research Record, (1288), 117-126.

Pierson, L. A., Davis, S. A., and Van, Vickle R. (1990). Rockfall Hazard Rating System: Implementation Manual (No. FHWA-OR-EG-90-01).

Pinto, L, Hérail, G, Sepúlveda, S A, Krop, P. (2008). A Neogene giant landslide in Tarapacá, northern Chile: A signal of instability of the westernmost Altiplano and palaeoseismicity effects. Geomorphology, 102: 532-541.

Pondrelli, S., Ekstrom, G., Morelli, A., (2001). Seismotectonic re-evaluation of the 1976 Friuli, Italy, seismic sequence.J. Seismol. 5, 73–83.

Prestininzi, A., and Romeo, R. (2000). Earthquake-induced ground failures in Italy. Engineering Geology, 58(3), 387-397.

Prima, O. D. A., Echigo, A., Yokoyama, R., and Yoshida, T. (2006). Supervised landform classification of Northeast Honshu from DEM-derived thematic maps.Geomorphology, 78(3), 373-386.

Purvance, M. (2005). Overturning of slender blocks: numerical investigation n and application to precariously balanced rocks in southern California [PhD thesis]: University of Nevada, Reno, 233 p.

Purvance, M., Brune, J., Anooshehpoor, A., and Brune, R. (2004). Evidence of large fault parallel/perpendicular PGV ratios, in Proceedings and Abstracts of the Southern California Earthquake Center 2004 Annual Meeting, September 20–22, 2004, Palm Springs, California.

Qi, S., Xu, Q., Lan, H., Zhang, B., and Liu, J. (2010). Spatial distribution analysis of landslides triggered by 2008.5. 12 Wenchuan Earthquake, China.Engineering geology, 116(1), 95-108.

Raetzo, H., Lateltin, O., Bollinger D., and Tripet, J. (2002). Hazard assessment in Switzerland–Codes of Practice for mass movements. Bulletin of Engineering Geology and the Environment, 61(3), 263-268.

Rapolla A., Paoletti V., and Secomandi M. (2010). Seismically-induced landslide susceptibility evaluation: application of a new procedure to the island of Ischia, Campania Region, Southern Italy. Engineering Geology, 114(1), 10-25.

Research Group for Active Faults (1980). Active faults in Japan: sheet maps and inventories. University of Tokyo Press, pp 132–133

Ripper, I.D., and Letz, H. (1991). Distribution and Origin of Large Earthquakes in the Papua New Guinea Region, 1900–1989. Geological Survey of Papua New Guinea, Port Moresby. Geological Survey of Papua New Guinea Report 91/5, 74 pp.

Robinson, G. P. (1974). Geology of the Huon Peninsula. Geol. Survey of Papua New Guinea Mere. 3, 71 pp.

Robinson, G. P., Jaques, A. L. and Brown, C. M. (1976). Madang, Papua New Guinea 1:250,000 Geological Series--map and explanatory notes. Geol. Survey of Papua New Guinea, Port Moresby, 29 pp.

Rodriguez, C. E. (2006). Earthquake-induced landslides in Colombia.

Rodrıguez C. E., Bommer J. J., and Chandler R. J. (1999). Earthquake-induced landslides: 1980–1997. Soil Dynamics and Earthquake Engineering, 18(5), 325-346.

Rodrıguez, C. E., Bommer, J. J., and Chandler, R. J. (1999). Earthquake-induced landslides: 1980–1997. Soil Dynamics and Earthquake Engineering, 18(5), 325-346.

Rouiller J. D., Jaboyedoff M., Marro C., Philippossian F., and Mamin M. (1998). Pentes instables dans le Pennique valaisan: Matterock: une méthodologie d'auscultation des falaises et de détection des éboulements majeurs potentiels. vdf Hochschulverlag AG.

Rovida, A., Camassi, R., Gasperini, P. and Stucchi, M. (eds.), (2011). CPTI11, the 2011 version of the Parametric Catalogue of Italian Earthquakes. Milano, Bologna, http://emidius.mi.ingv.it/CPTI. DOI: 10.6092/INGV.IT-CPTI11.

Santana, D., Corominas, J., Mavrouli, O., and Garcia-Sellés, D. (2012). Magnitude-frequency relation for rockfall scars using a Terrestrial Laser Scanner. Engineering Geology. 145, 50-64.

Santana, D., Corominas, J., Mavrouli, O., and Garcia-Sellés, D. (2012). Magnitude–frequency relation for rockfall scars using a Terrestrial Laser Scanner. Engineering Geology, 145, 50-64.

Sato, H. (1994) The relationship between late Cenozoic tectonic events and stress field and basin development in northeast Japan. J Geophys Res 99:22261–22274.

Sato, H., Hirata, N., Iwasaki, T., Matsubara, M., and Ikawa, T. (2002). Deep seismic reflection profiling across the Ou Backbone range, northern Honshu Island, Japan. Tectonophysics, 355(1), 41-52.

Schlunegger, F., Zeilinger, G., Kounov, A., Kober, F, Husser, B., (2006) Scale of relief growth in the forearc of the Andes of Northern Chile (Arica latitude, 18 degrees S). Terra Nova 18: 217–223.

Scholl, D. W. (1960). Relationship of the insular shelf sediments to the sedimentary environments and geology of Anacapa Island, California. Journal of Sedimentary Research, 30(1).

Seed, H. B. (1968). The fourth Terzaghi lecture: Landslides during earthquakes due to liquefaction. Journal of the Soil Mechanics and Foundations Division, 94(5), 1053-1122.

Slejko D., Neri G., Orozova I., Renner G., Wyss M., (1999): Stress field in Friuli (NE Italy) from fault plane solutions of activity following the 1976 main shock. Bull. Seismol. Soc. Am. 89, 1037–1052.

Smirnov, N. V. (1939). Estimate of deviation between empirical distribution functions in two independent samples. Bulletin Moscow University, 2(2), 3-16.

Squires, R.L. (1997) Geologic profile of Simi Valley. In: Havens, P. and B. Appleton (eds.) Simi Valley - A Journey Through Time. Simi Valley Historical Society and Museum. Pp. 293-301.

Stark, C. P., & Hovius, N. (2001). The characterization of landslide distributions. Geophysical Research Letters, 28(6), 1091-1094.

Stark, C. P., and Guzzetti, F. (2009). Landslide rupture and the probability distribution of mobilized debris volumes. Journal of Geophysical Research: Earth Surface (2003–2012), 114(F2).

Stevens, W. D. (1998). RocFall, a tool for probabilistic analysis, design of remedial measures and prediction of rockfalls. M.A.Sc. Thesis, Department of Civil Engineering, University of Toronto. Ontario, Canada, 105pp.

Strasser, M., Schlunegger, F. (2005) Erosional processes, topographic length-scales and geomorphic evolution in arid climatic environments: the ‘Lluta collapse”northern Chile. Int. J. Earth Sci. (Geol. Rundsch.) 94: 433–446.

Straub, D., and Schubert, M. (2008). Modeling and managing uncertainties in rock-fall hazards. Georisk, 2(1), 1-15.

Suzuki, W., Aoi, S., & Sekiguchi, H. (2010). Rupture process of the 2008 Iwate–Miyagi Nairiku, Japan, earthquake derived from near-source strong-motion records. Bulletin of the Seismological Society of America, 100(1), 256-266.

Taliaferro, N. L., Hudson, F. S., and Craddock, W. N. (1924). The Oil Fields of Ventura County, California. AAPG Bulletin, 8(6), 789-829.

ten Brink, U. S., Geist, E. L., and Andrews, B. D. (2006). Size distribution of submarine landslides and its implication to tsunami hazard in Puerto Rico.Geophysical Research Letters, 33(11).

ten Brink, U. S., Barkan, R., Andrews, B. D., & Chaytor, J. D. (2009). Size distributions and failure initiation of submarine and subaerial landslides. Earth and Planetary Science Letters, 287(1), 31-42.

Thouret, J-C., Worner, G., Gunnell, Y., Singer, B., Zhang, X., Souriot, T. (2007) Geochronologic and stratigraphic constraints on canyon incision and Miocene uplift of the central Andes in Peru. Earth and Planetary Science Letters, 263: 151–166.

Tutton, M.A., and Browne, T.J. (1994). A review of damage caused by the 1993 Finisterre Range earthquake, Papua New Guinea. In: Rogerson, R. (Ed.), Proceedings of the PNG Geology, Exploration and Mining Conference 1994, Lae, pp. 33–41.

Uchida, T., Osanai, N., Onoda, S., Takayama, T., and Tomura, K. (2006). A Simple Method for Producing Probabilistic Seismic Shallow Landslide Hazard Maps. In: Marui H, Marutani T,Watanabe N, Kawabe H, Gonda Y, Kimura M, Ochiai H, Ogawa K, Fiebiger G, Heumader J, Rudolf-Miklau F, Kienholz H, Mikos M (Eds.), Proc. Interpraevent Int. Symp, Niigata 2006, Disaster mitigation of debris flow, slope failures and landslides, vol. 2. Universal Academy Press, Tokyo, pp 529–534.Wald D.J., Worden C., Quitoriano V., and Pankow K.L., (2006) ShakeMap®Manual, version 1.0 TECHNICAL MANUAL, USERS GUIDE, AND SOFTWARE GUIDE. Techniques and Methods 12–A1, USGS. Available online at http://pubs.usgs.gov/tm/2005/12A01/pdf/508TM12-A1.pdf.

Ujiie-Mikoshiba, M., Imai, N., Terashima, S., Tachibana, Y., and Okai, T. (2006). Geochemical mapping in northern Honshu, Japan. Applied geochemistry, 21(3), 492-514.

U.S Geological Survey site: http://earthquake.usgs.gov

Valagussa, A., Crosta, G. B., Frattini, P., and Xu, C. (2014a). Analysis of the relationship between landslides size distribution and earthquake source area. In EGU General Assembly Conference Abstracts (Vol. 16, p. 16281).

Valagussa, A., Frattini, P., and Crosta, G. B. (2014b). Earthquake-induced rockfall hazard zoning. Engineering Geology, 182, 213-225.

Van Den Eeckhaut, M., Poesen, J., Govers, G., Verstraeten, G., and Demoulin, A. (2007). Characteristics of the size distribution of recent and historical landslides in a populated hilly region. Earth and Planetary Science Letters,256(3), 588-603.

Varnes, D. J. (1978). Slope movement types and processes. Transportation Research Board Special Report, (176).

Wald, D. J., Quitoriano, V., Heaton, T. H., and Kanamori, H. (1999). Relationships between peak ground acceleration, peak ground velocity, and modified Mercalli intensity in California. Earthquake spectra, 15(3), 557-564.

Wald, D.J., Worden, C., Quitoriano, V., and Pankow, K.L., (2006). ShakeMap®Manual, version 1.0 TECHNICAL MANUAL, USERS GUIDE, AND SOFTWARE GUIDE. Techniques and Methods 12–A1, USGS. Available online at http://pubs.usgs.gov/tm/2005/12A01/pdf/508TM12-A1.pdf.

Wang, H. B., Sassa, K., and Xu, W. Y. (2007). Analysis of a spatial distribution of landslides triggered by the 2004 Chuetsu earthquakes of Niigata Prefecture, Japan. Natural Hazards, 41(1), 43-60.

Wasowski, J., and Del Gaudio, V. (2000). Evaluating seismically induced mass movement hazard in Caramanico Terme (Italy). Engineering Geology, 58(3), 291-311.

Wieczorek, G.F., Snyder J.B., Alger, C.S., Isaacson, K.A. (1992) Yosemite historical rockfall inventory, USGS Open File report, 92-387

Williams, R. E. (1977). Miocene volcanism in the central Conejo Hills. Ventura County, California [MS thesis]: Santa Barbara, University of California.

Working group MPS (2004). Redazione della mappa di pericolosità sismica prevista dall'Ordinanza PCM 3274 del 20 marzo 2003. Rapporto Conclusivo per il Dipartimento della Protezione Civile, INGV, Milano-Roma, aprile 2004, 65 pp. + 5 appendici. (In Italian).

Xu, C., Xu, X., Yao, X., and Dai, F. (2014). Three (nearly) complete inventories of landslides triggered by the May 12, 2008 Wenchuan Mw 7.9 earthquake of China and their spatial distribution statistical analysis. Landslides, 11(3), 441-461.

Yagi, H., Yamasaki, T., and Atsumi, M. (2007). GIS analysis on geomorphological features and soil mechanical implication of landslides caused by 2004 Niigata Chuetsu earthquake. J Jpn Landslide Soc, 43, 294-360.

Yagi, H., Sato, G., Higaki, D., Yamamoto, M., and Yamasaki, T. (2009). Distribution and characteristics of landslides induced by the Iwate–Miyagi Nairiku Earthquake in 2008 in Tohoku District, Northeast Japan. Landslides,6(4), 335-344

Yamagishi, H., Watanabe, N., Ayalew, L. (2005) Heavy-rainfall induced landslides on July 13, 2004. In: Landslide Research Group of Landslide Society of Japan 7.13 Landslide Research Group of Niigata University Niigata K, Takara Y, Tachikawa and NMNS Bandara Nawarathna (eds) Monitoring, prediction and mitigation of water-related Disasters. MPMD, Japan, pp 501–506

Yanagisawa, Y., Kobayashi, I., Takeuchi, K., Tateishi, M., Chihara, K., and Kato, H. (1986). Geology of the Ojiya district with geological sheet map. Geological Survey of Japan, scale, 1(50,000), 177.

Yeats, R. S., and Huftile, G. J. (1995). The Oak Ridge fault system and the 1994 Northridge Earthquake.

Yesilnacar, E., and Topal, T. (2005). Landslide susceptibility mapping: a comparison of logistic regression and neural networks methods in a medium scale study, Hendek region (Turkey). Engineering Geology, 79(3), 251-266.

Yoshida, T. (2001). The evolution of arc magmatism in the NE Honshu arc. Japan. Tohoku Geophys J 36(2):131–149

Yoshii, T. (1979). A detailed cross-section of the deep seismic zone beneath northeastern Honshu, Japan. Tectonophysics, 55(3), 349-360.

Zeverbergen, L. W., and Thorne, C. R. (1987). Quantitative Analysis of Land Surface Topography. Earth Surface Processes and Landforms 12: 47–56.

Zollo, A., Bobbio, A., Emolo, E., Herrero, A., and De Natale, G. (1997). Modelling of ground acceleration in the near source range: the case of 1976, Friuli earthquake (M = 6.5), northern Italy. Journal of Seismology 1: 305–319.

Appendix 1- Landslide size as function of lithology, relief and slope gradient for the epicentral distance.

Papua New Guinea Earthquake

- **Landslide size as function of the epicentral distance, for each lithology:**

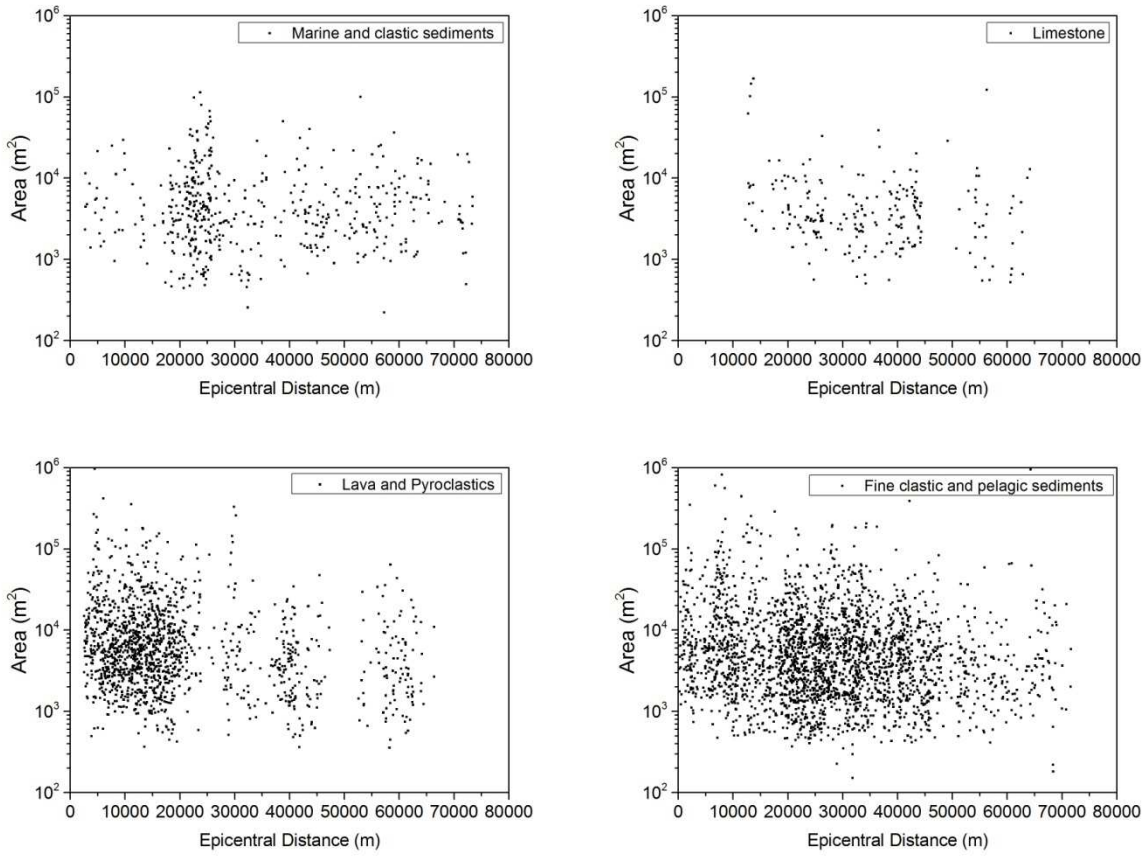

- **Landslide size as function of the epicentral distance, for each relief class:**

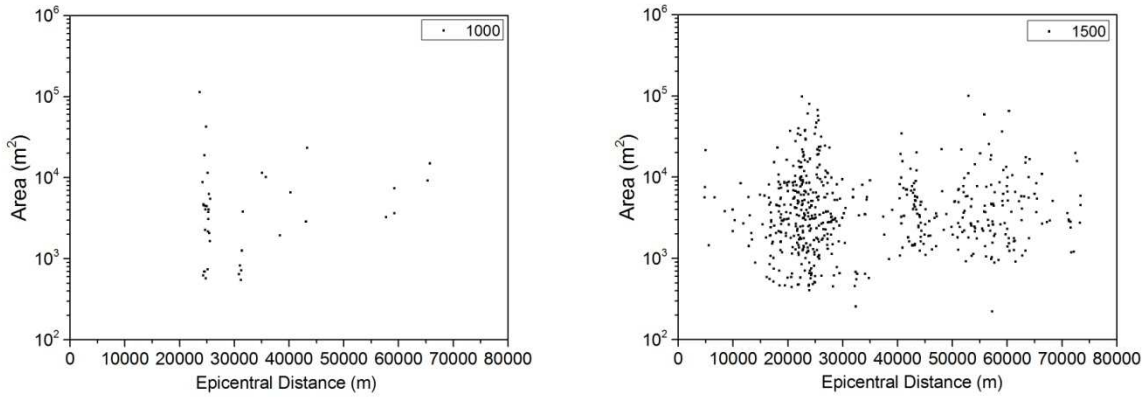

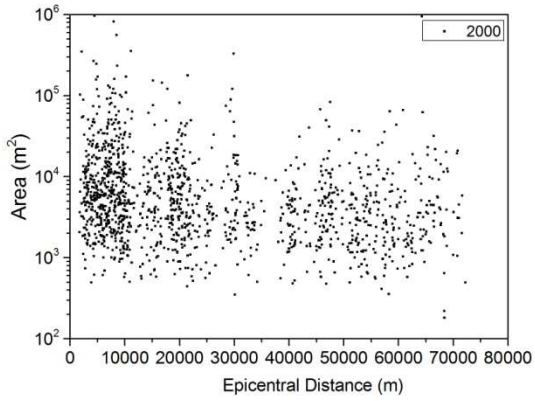

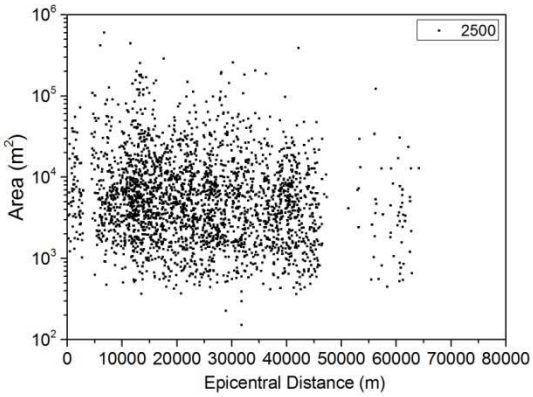

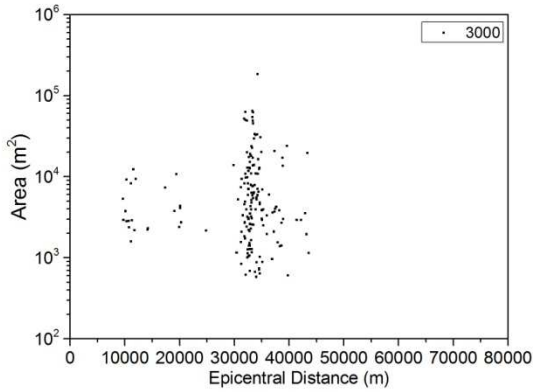

- **Landslide size as function of the epicentral distance, for each slope class:**

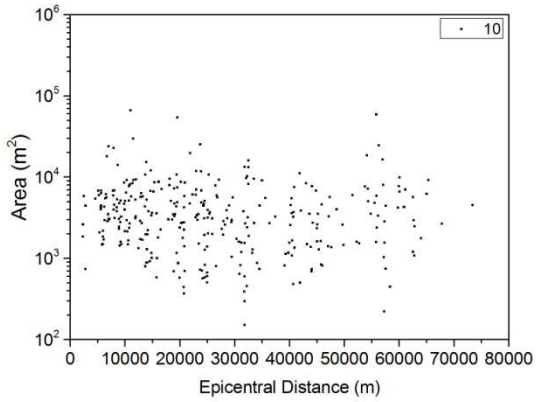

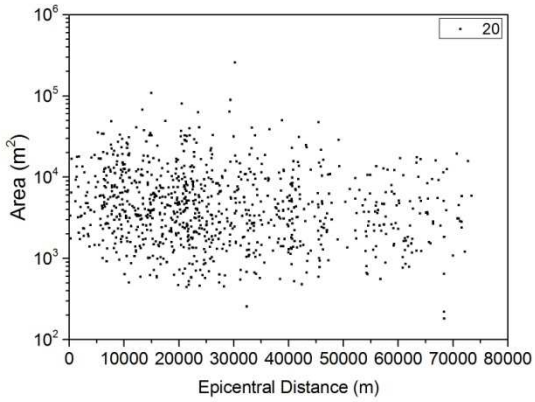

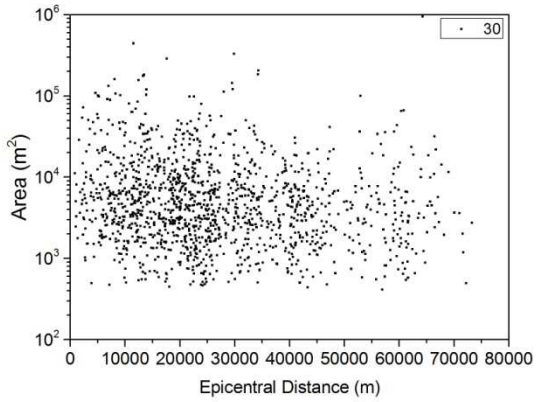

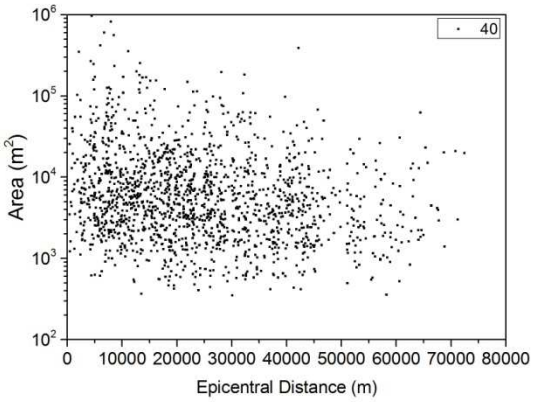

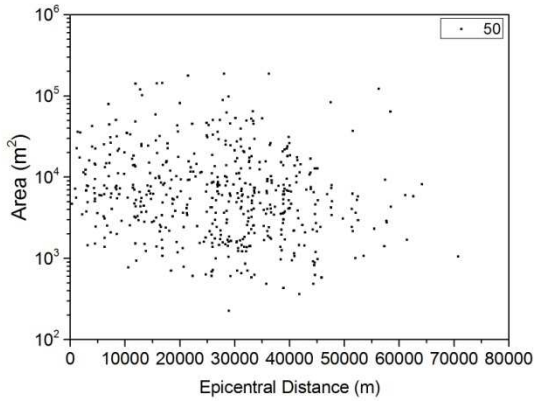

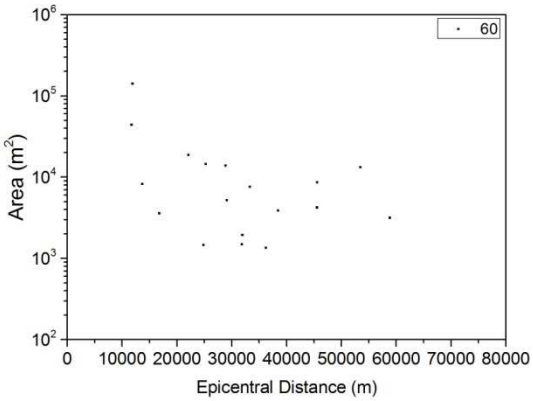

Northridge Earthquake

- **Landslide size as function of the epicentral distance, for each lithology:**

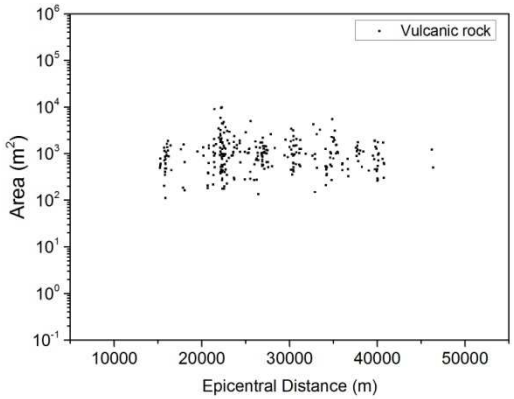

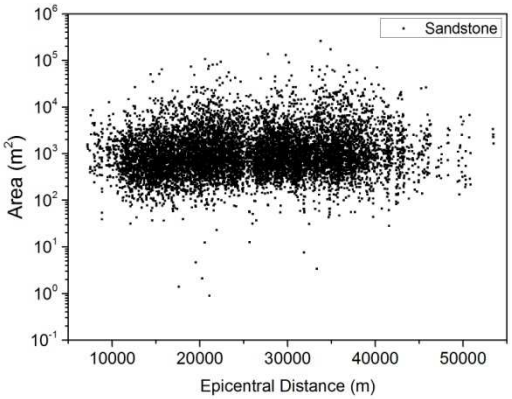

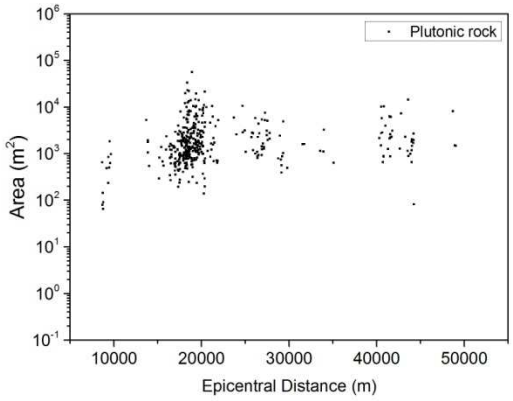

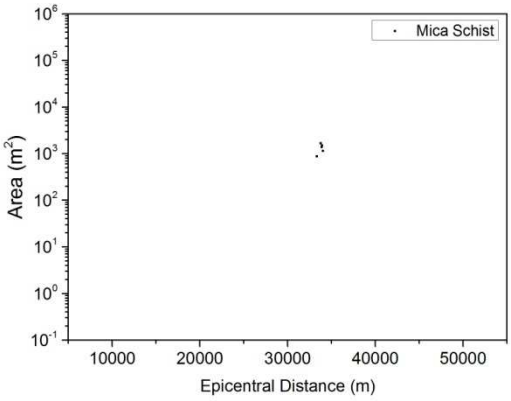

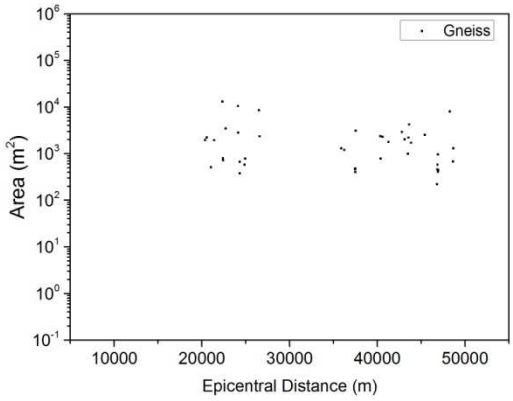

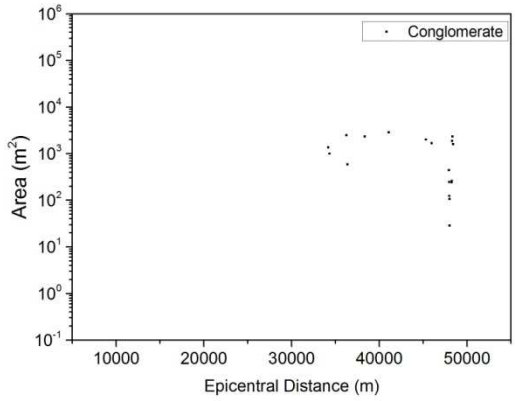

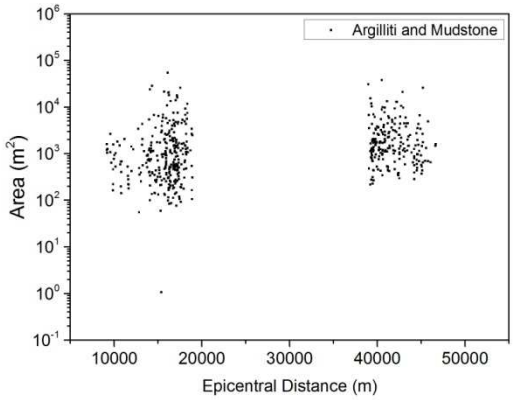

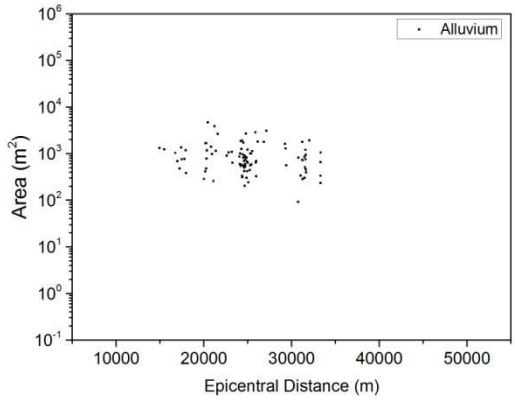

- **Landslide size as function of the epicentral distance, for each relief class:**

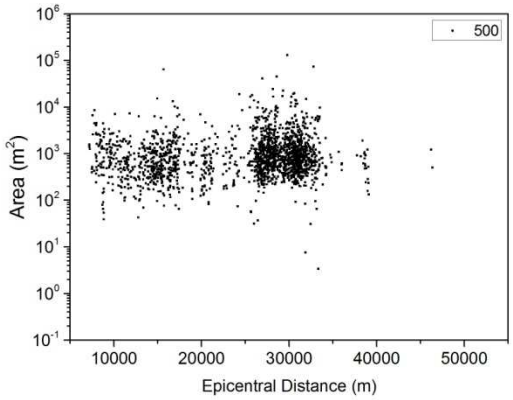

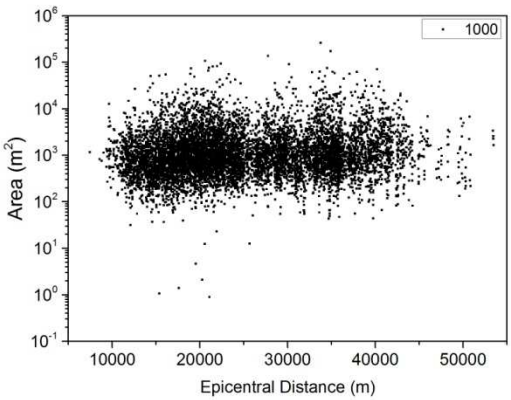

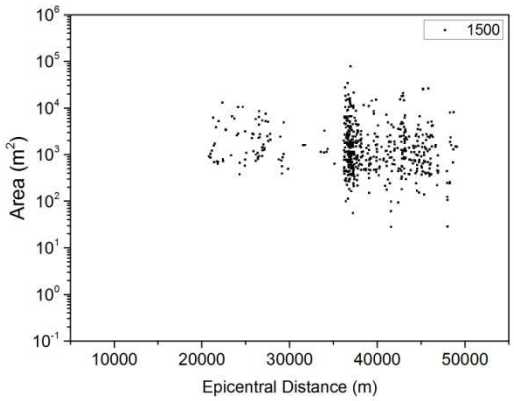

- **Landslide size as function of the epicentral distance, for each slope class:**

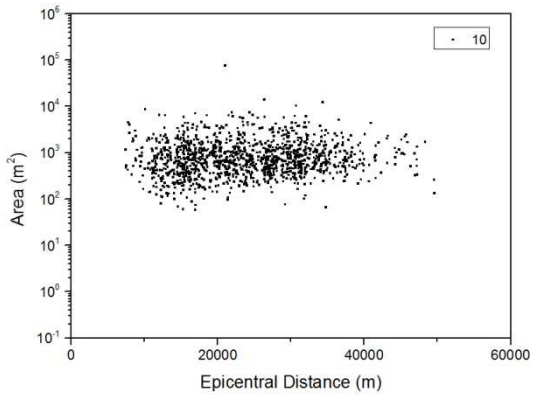

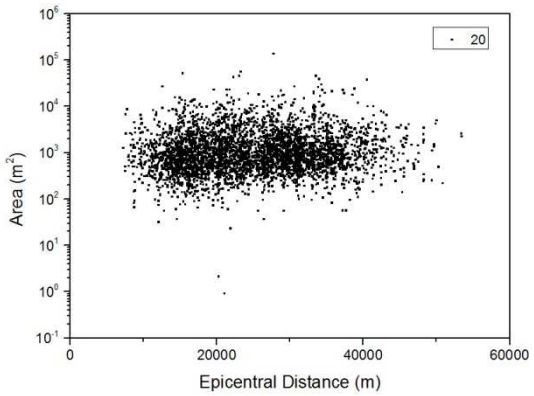

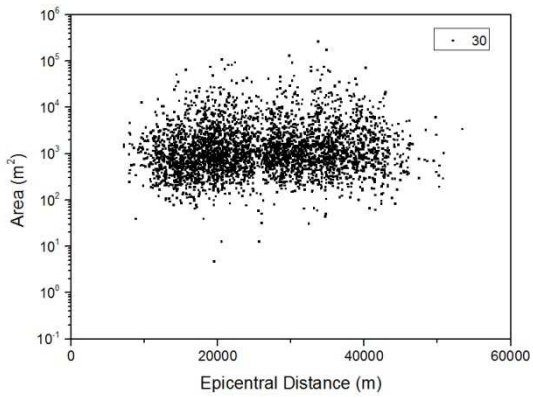

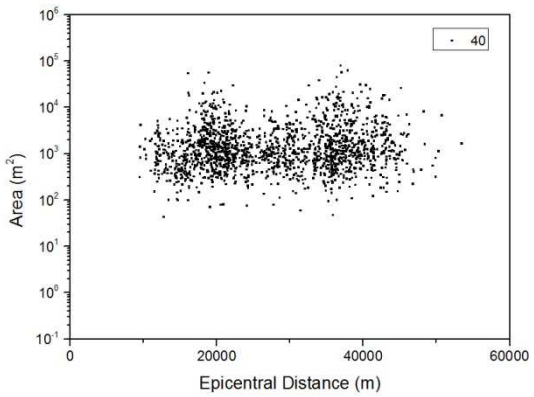

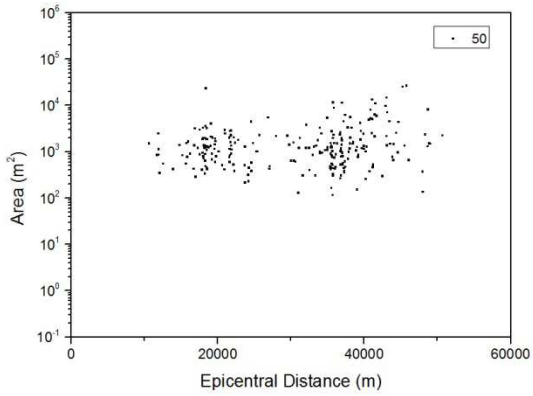

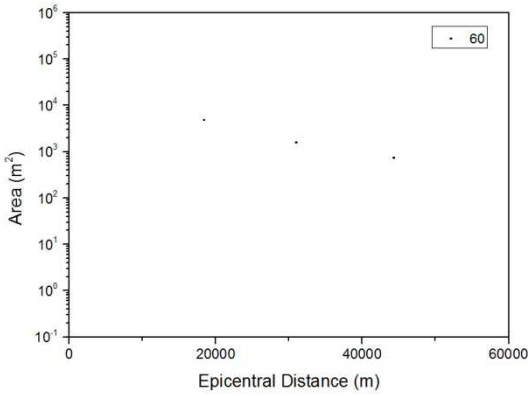

Niigata-Chuetsu Earthquake

- **Landslide size as function of the epicentral distance, for each lithology:**

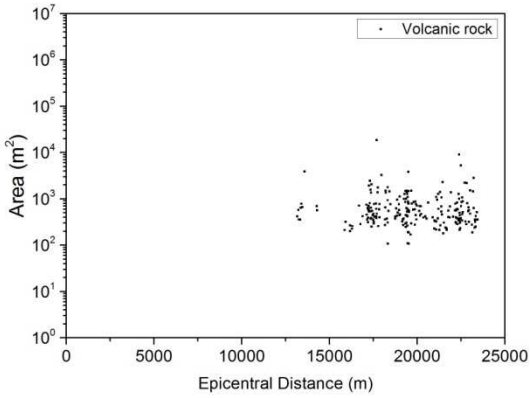

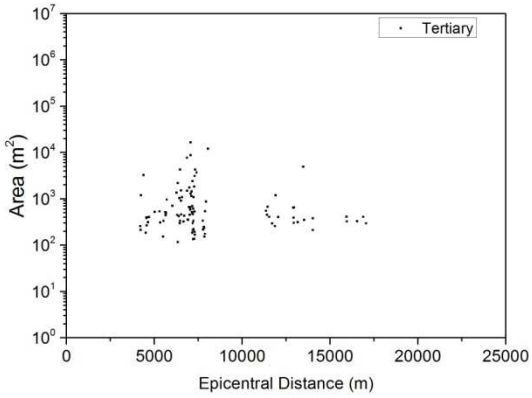

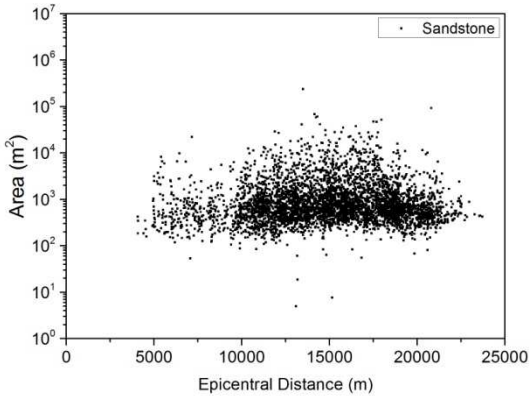

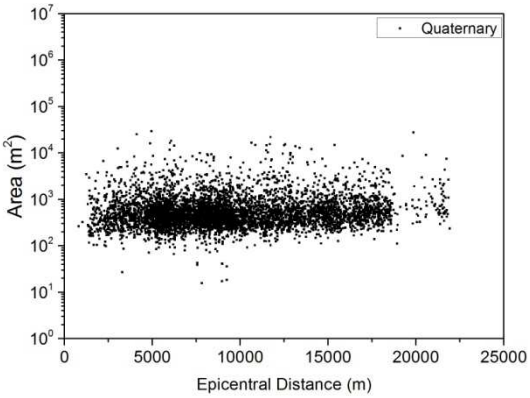

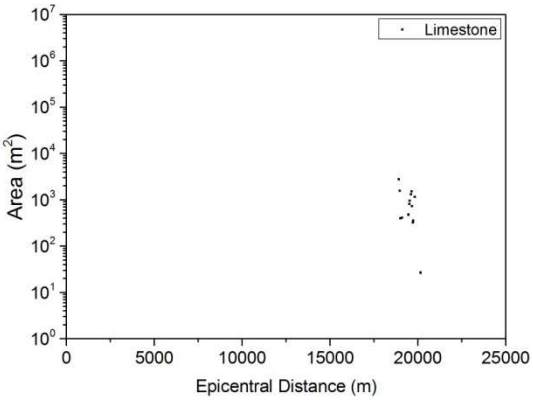

- **Landslide size as function of the epicentral distance, for each relief class:**

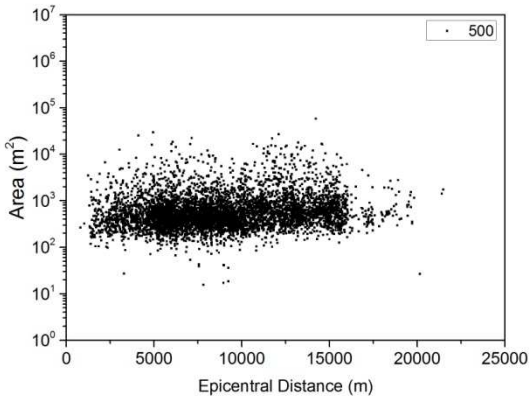

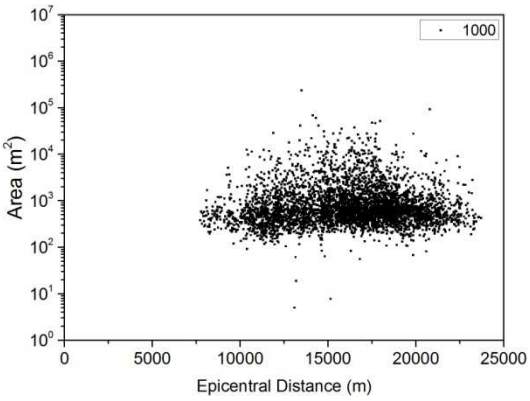

- **Landslide size as function of the epicentral distance, for each slope class:**

-

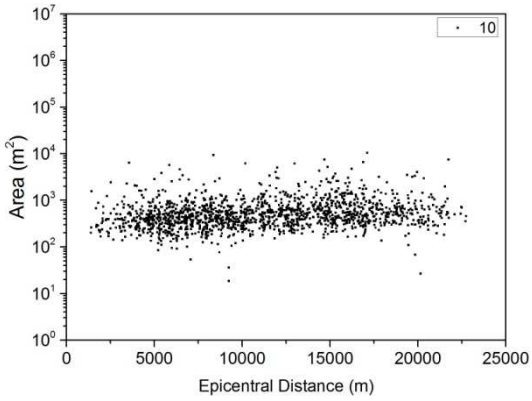

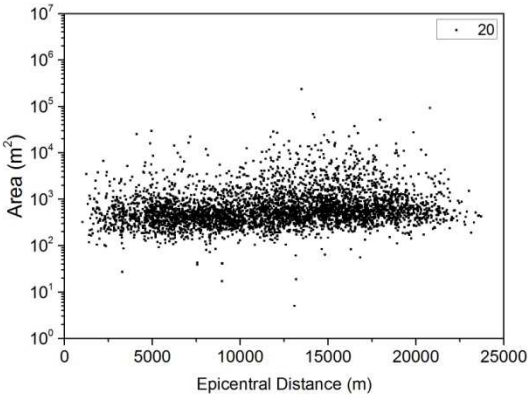

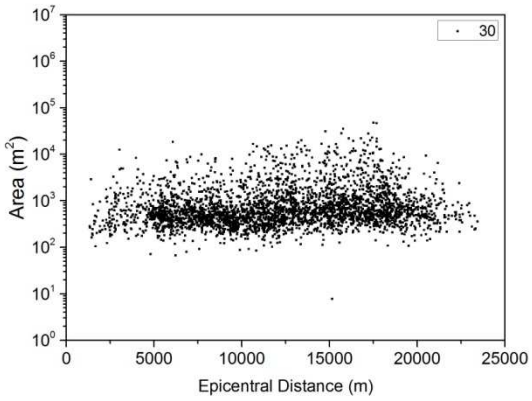

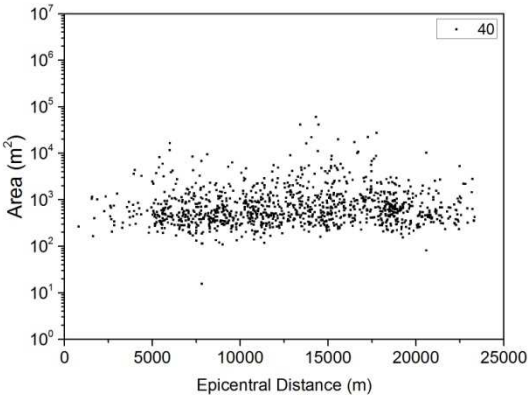

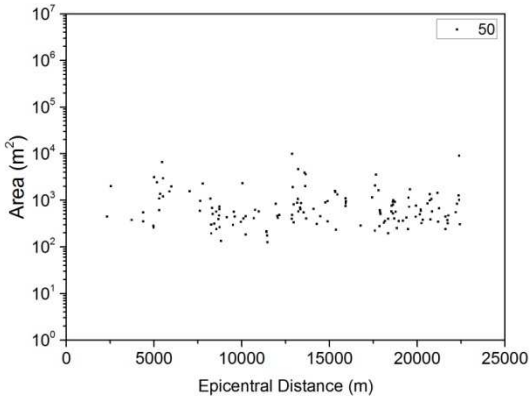

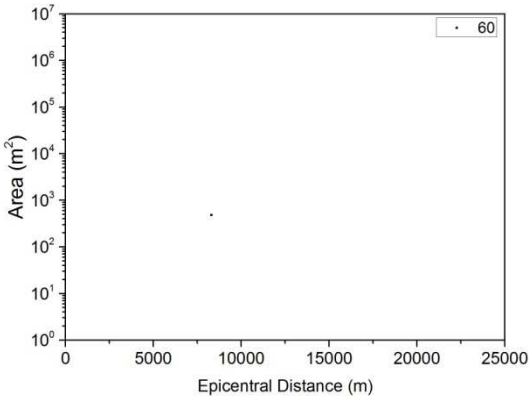

Wenchuan Earthquake

- **Landslide size as function of the epicentral distance, for each lithology:**

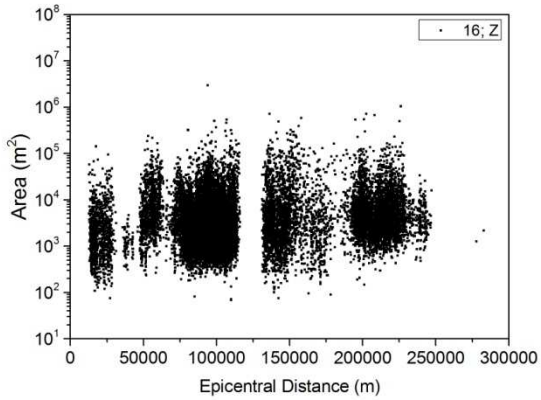

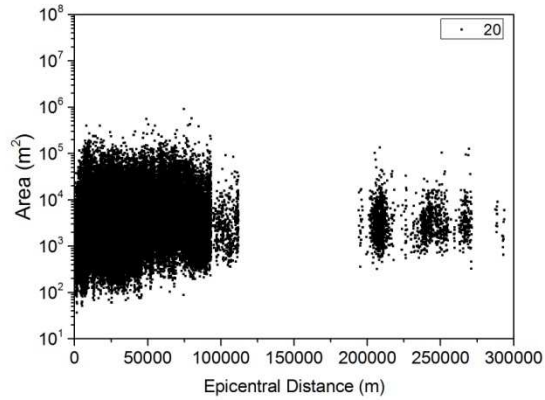

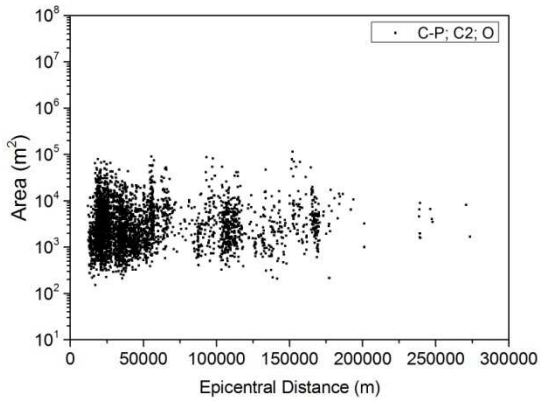

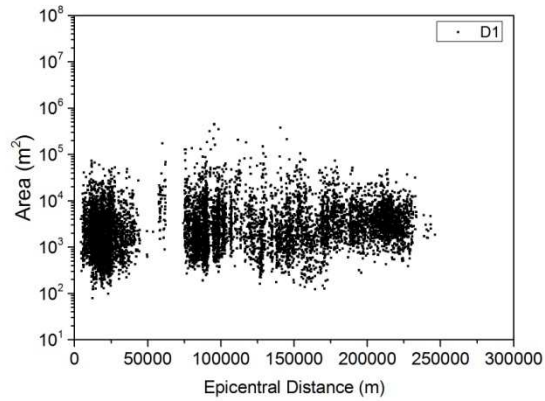

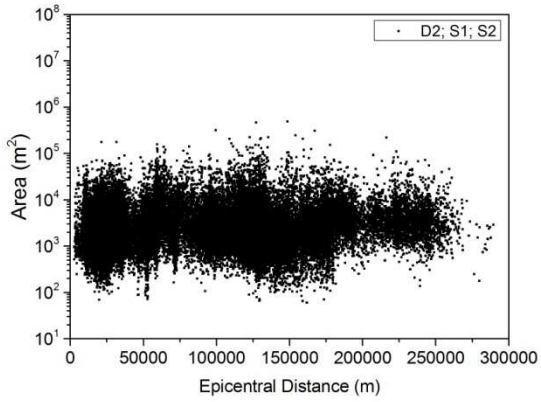

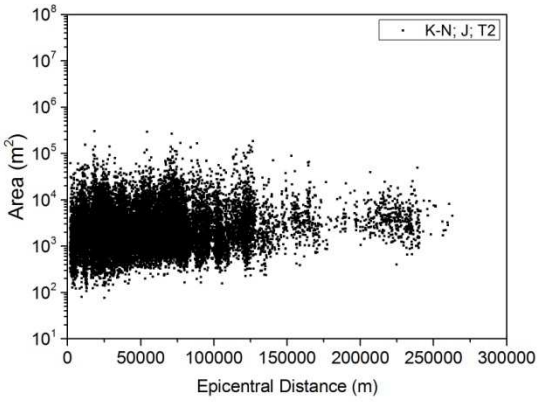

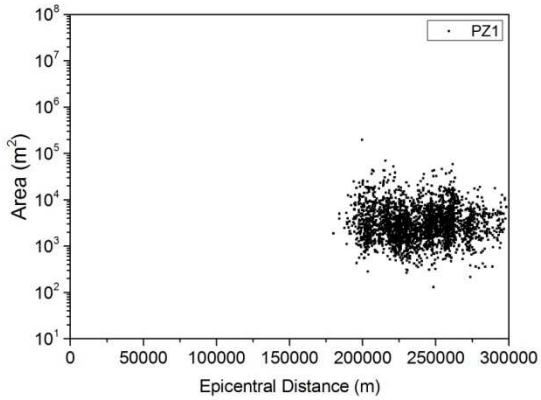

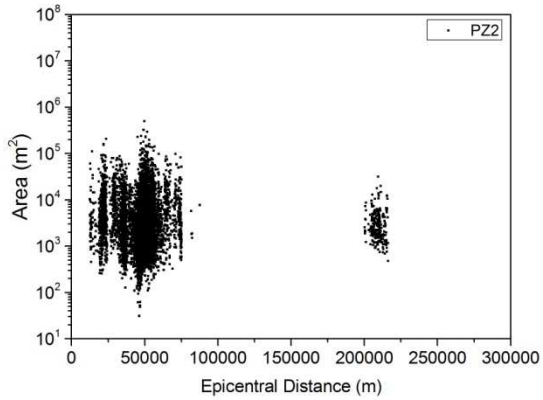

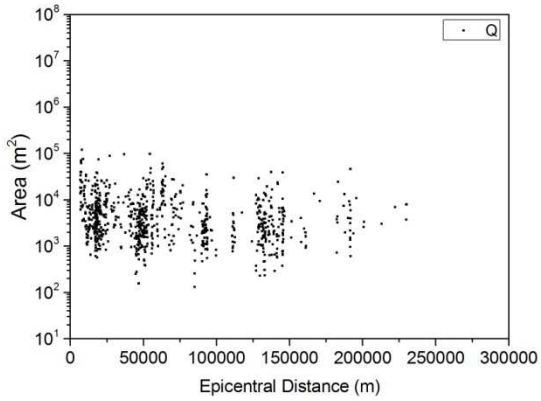

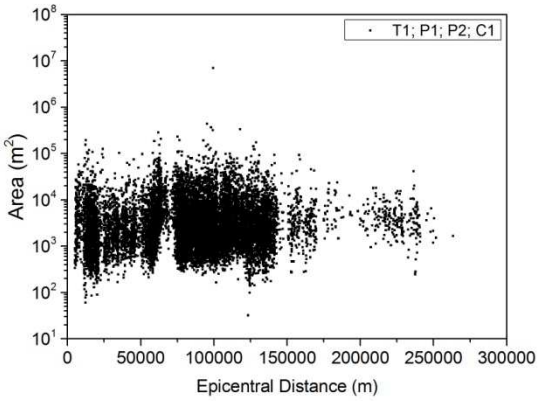

- **Landslide size as function of the epicentral distance, for each relief class:**

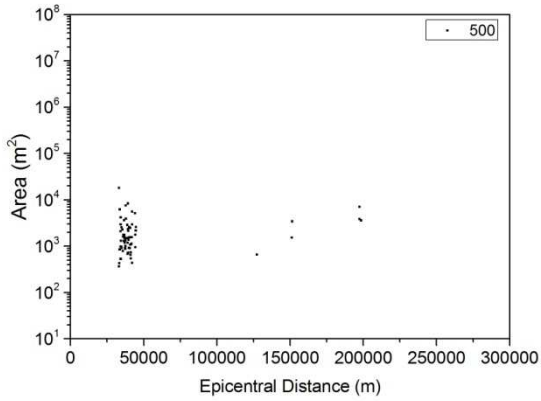

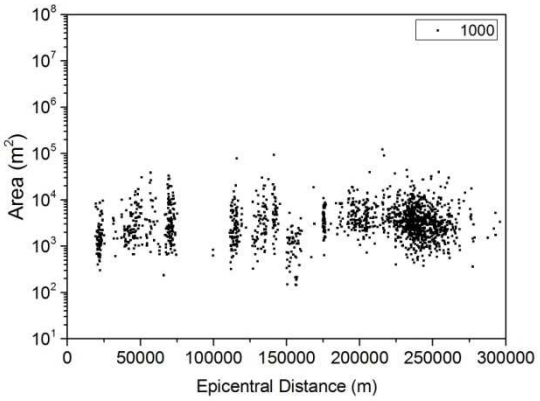

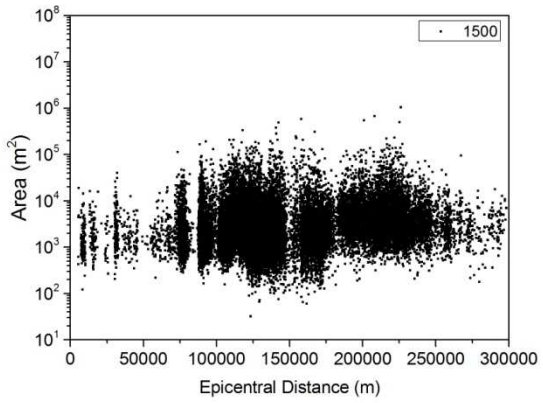
1500
Area (m²)
Epicentral Distance (m)

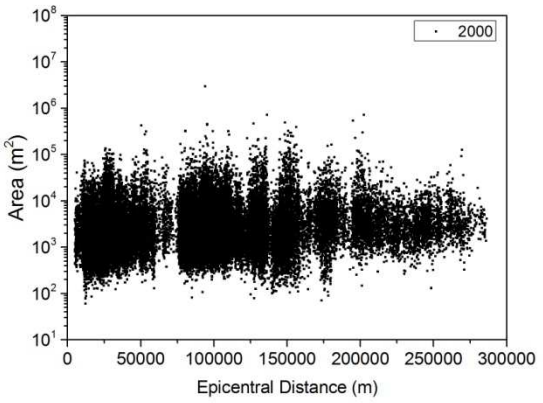
2000
Area (m²)
Epicentral Distance (m)

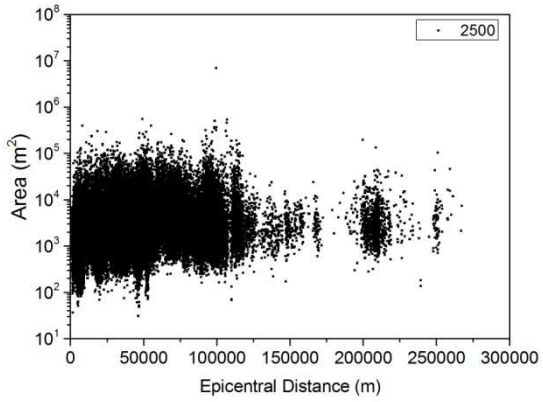
2500
Area (m²)
Epicentral Distance (m)

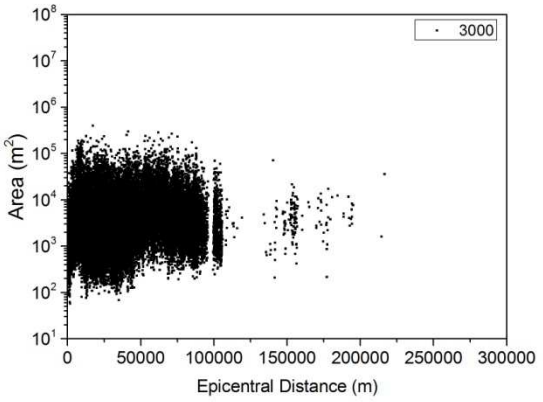
3000
Area (m²)
Epicentral Distance (m)

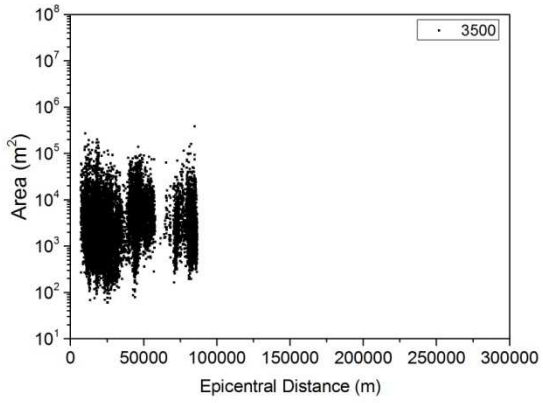
3500
Area (m²)
Epicentral Distance (m)

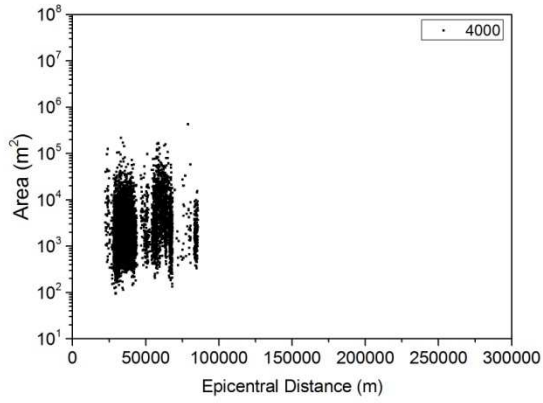
4000
Area (m²)
Epicentral Distance (m)

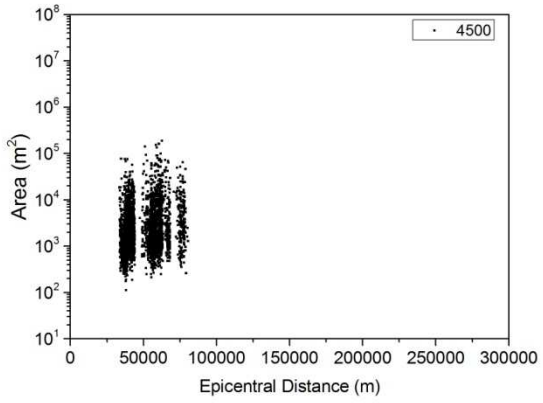
4500
Area (m²)
Epicentral Distance (m)

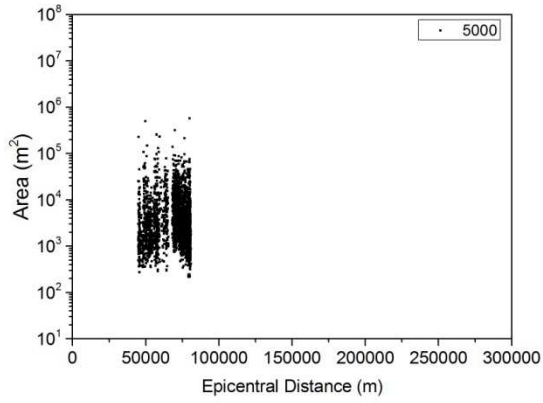
5000
Area (m²)
Epicentral Distance (m)

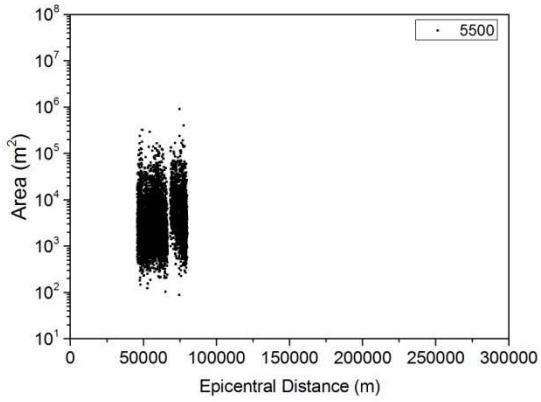

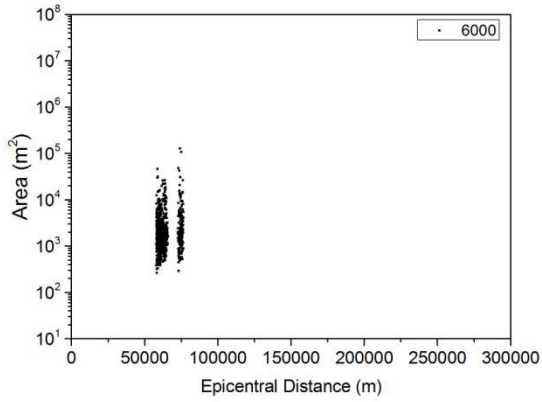

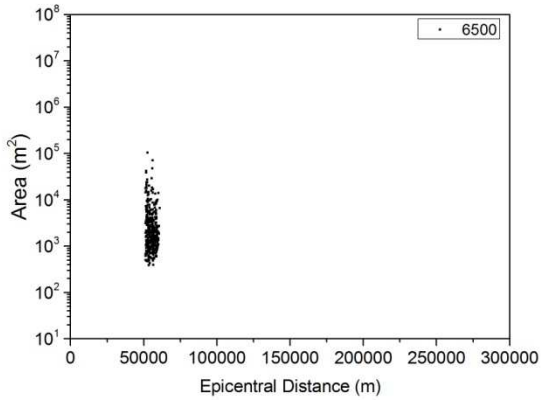

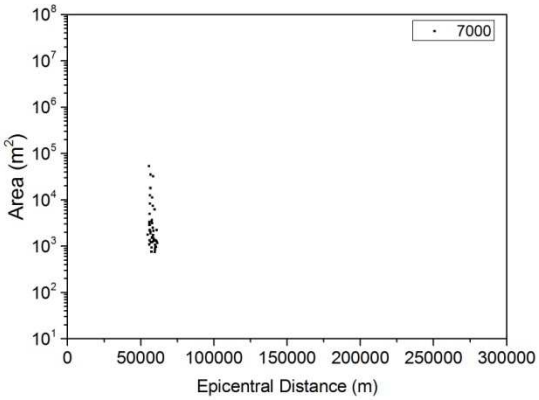

- **Landslide size as function of the epicentral distance, for each slope class:**

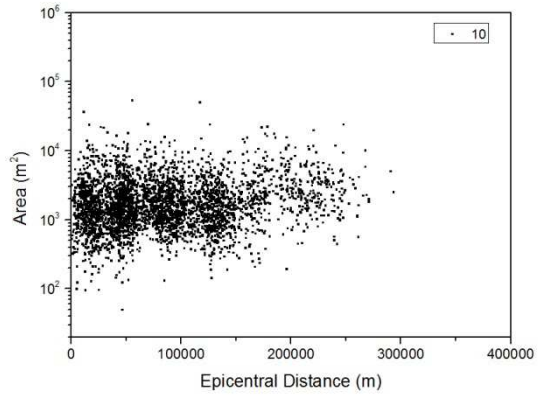

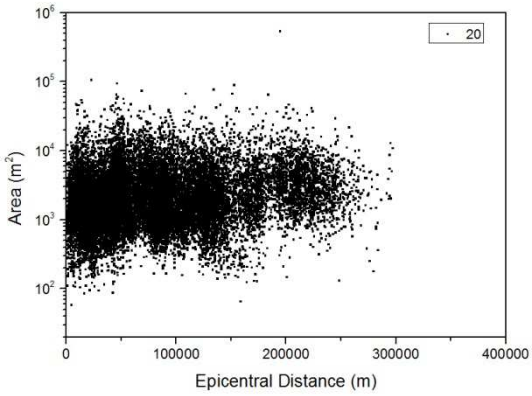

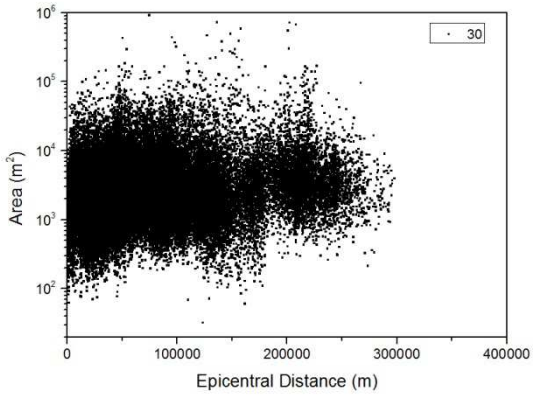
30
Area (m²)
Epicentral Distance (m)

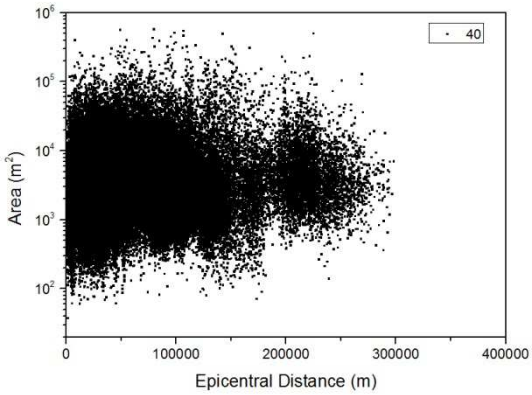
40
Area (m²)
Epicentral Distance (m)

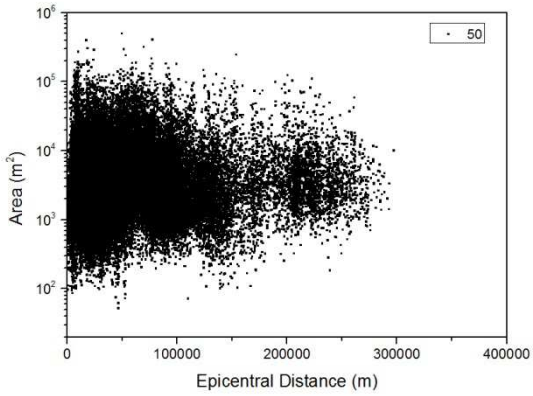
50
Area (m²)
Epicentral Distance (m)

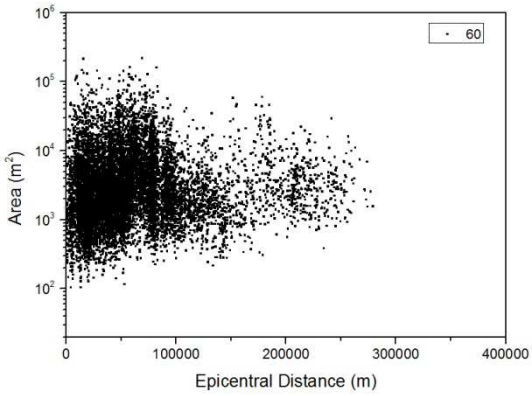
60
Area (m²)
Epicentral Distance (m)

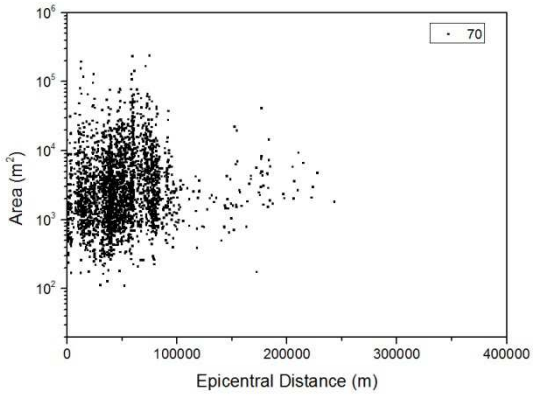
70
Area (m²)
Epicentral Distance (m)

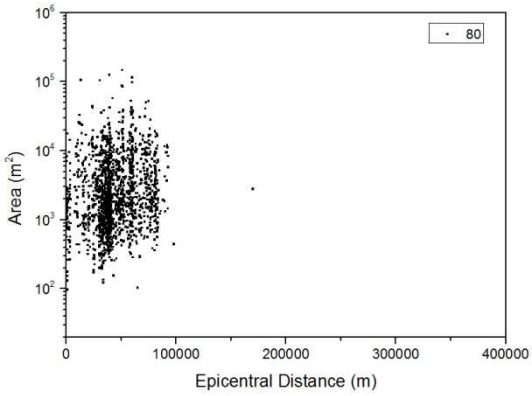
80
Area (m²)
Epicentral Distance (m)

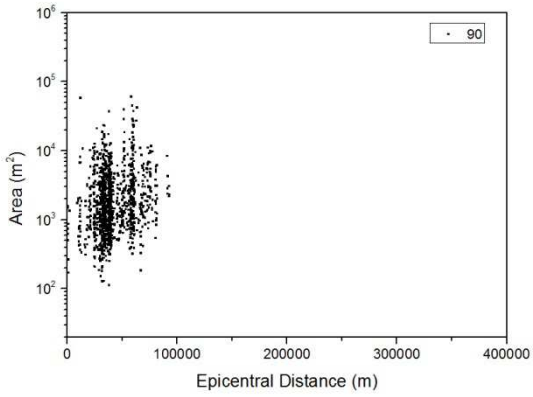
90
Area (m²)
Epicentral Distance (m)

Tohoku Earthquake

- **Landslide size as function of the epicentral distance, for each lithology:**

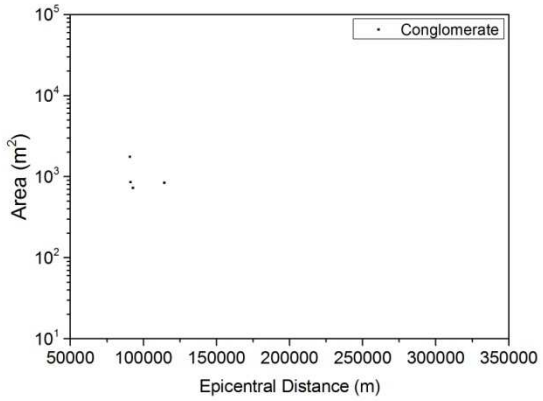

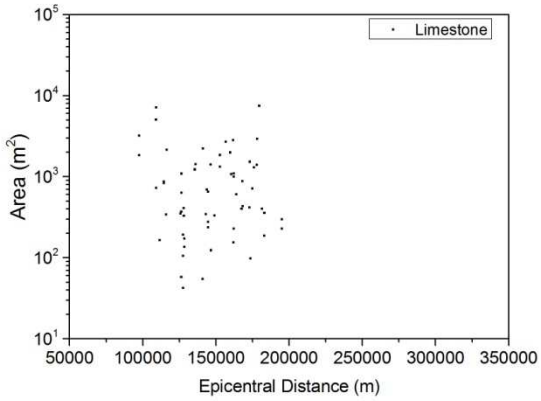

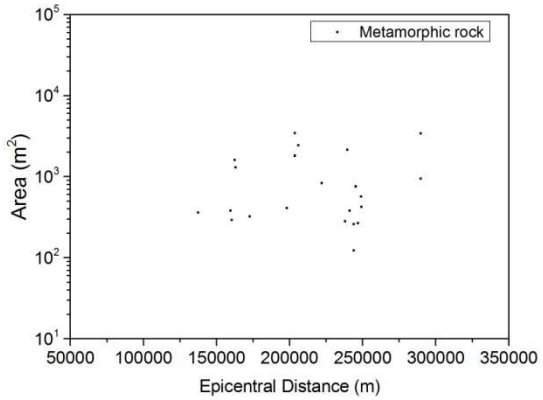

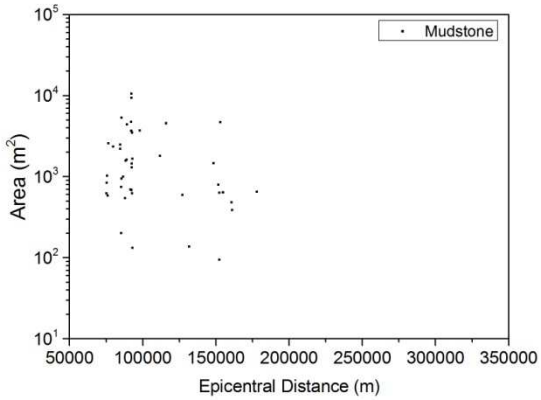

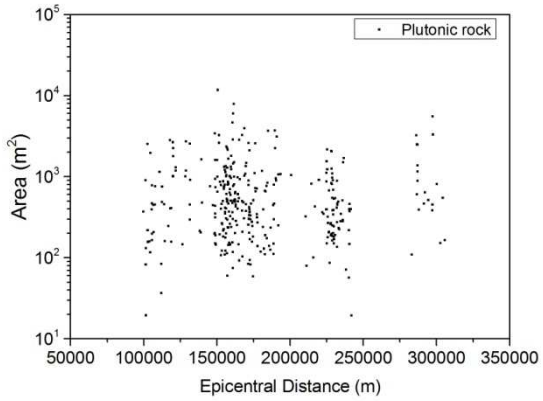

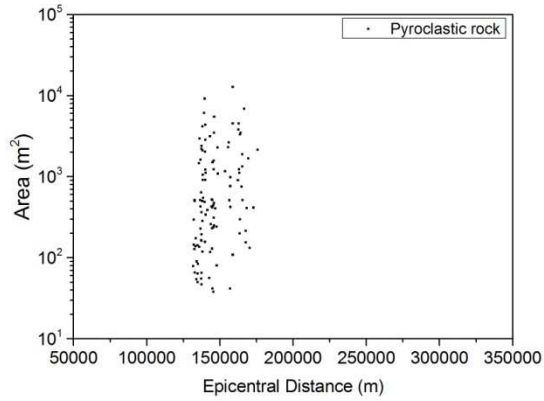

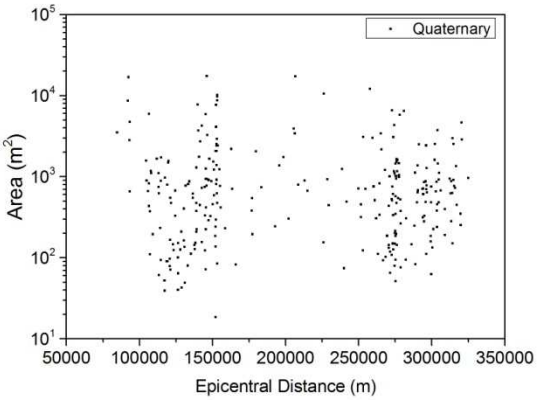

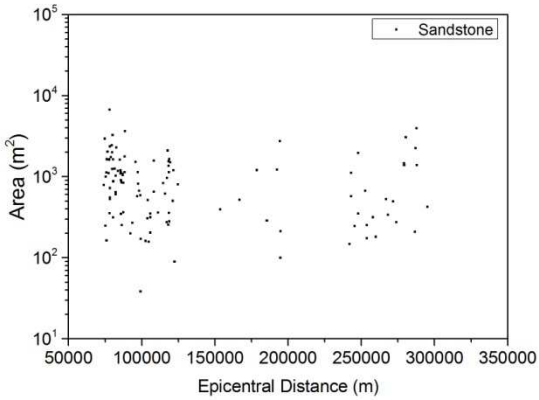

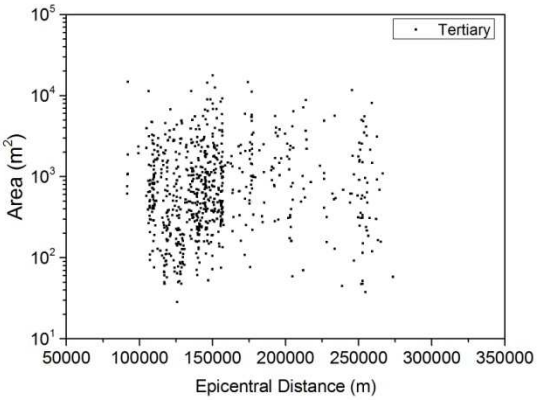

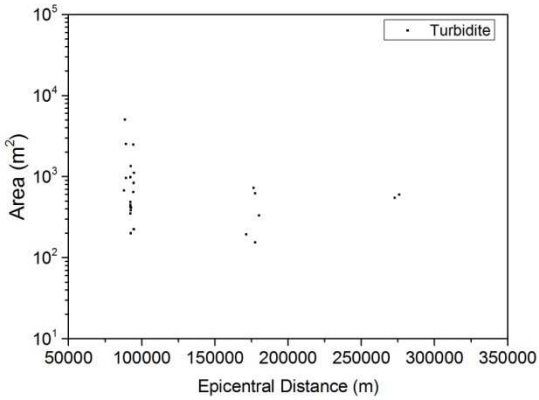

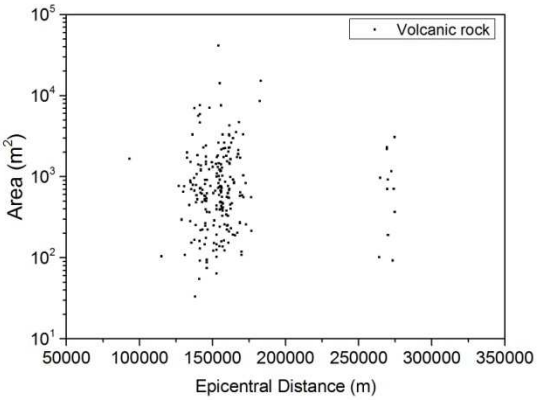

- **Landslide size as function of the epicentral distance, for each relief class:**

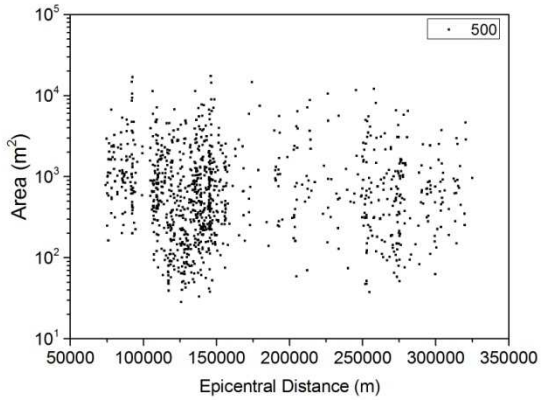

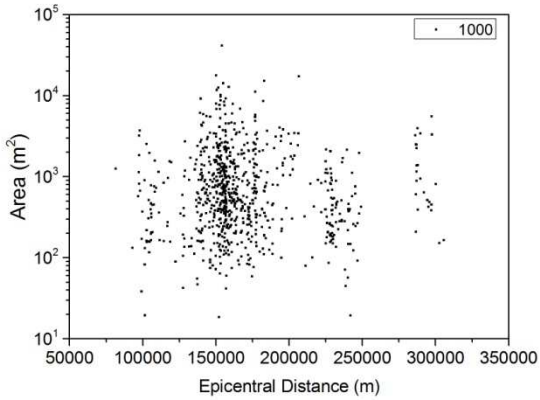

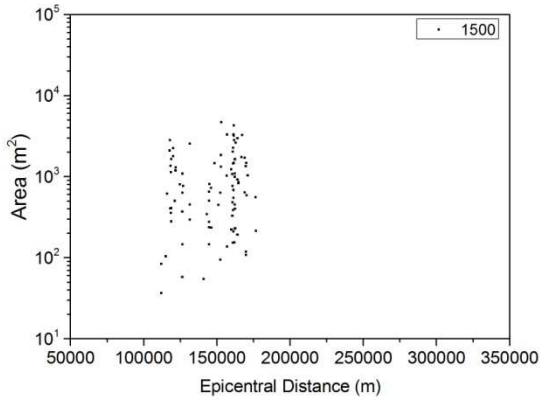

- **Landslide size as function of the epicentral distance, for each slope class:**

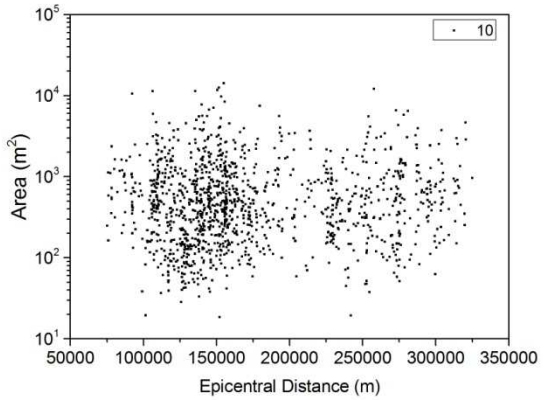

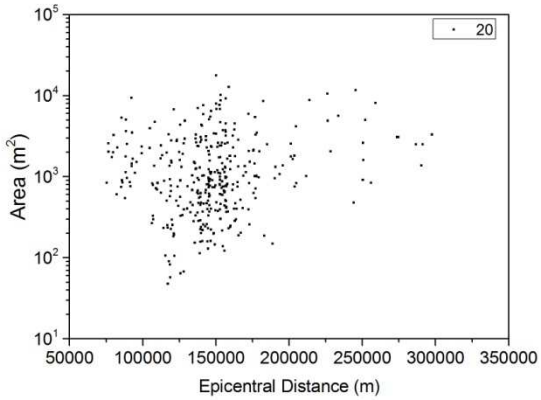

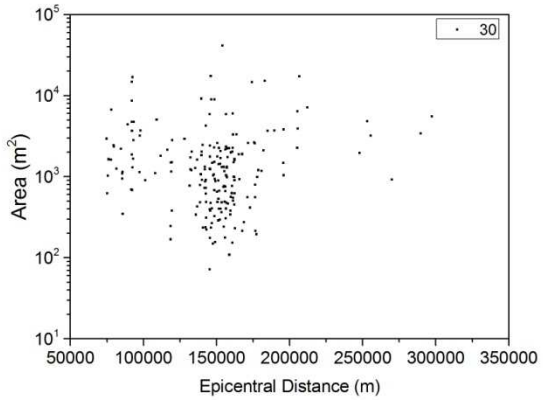

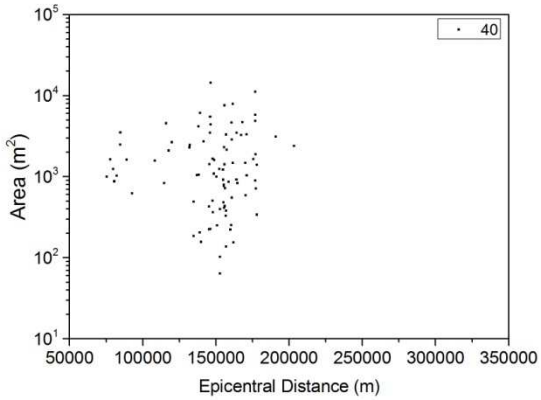

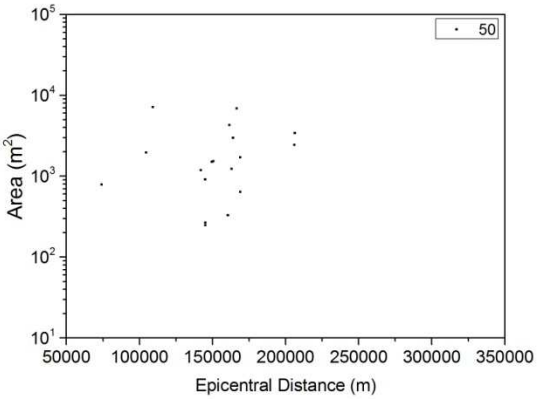

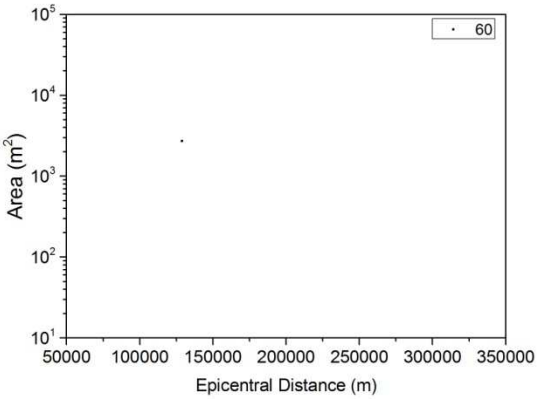

Appendix 2 - Fitting Curves for each class of distance, Wenchuan Earthquake, 2008

Epicentral Distance

Classes of Distance (m)	Code	# landslides	PL	LF	DP	ML
0 - 15,084	1	19,745	2.01	2.01	2.34	2.23
15,084 - 24,038	2	19,748	2.24	2.41	2.28	2.66
24,038 - 34,161	3	19,744	1.98	2.31	2.16	3.23
34,161 - 44,110	4	19,741	2.79	2.16	2.31	3.62
44,110 - 56,442	5	19,757	1.75	2.16	2.41	3.20
56,442 - 76,422	6	19,750	2.84	2.49	2.25	4.36
76,422 - 92,225	7	19,746	2.71	2.63	2.54	2.97
92,225 - 115,550	8	19,747	2.08	2.22	2.59	2.78
115,550 - 164,412	9	19,755	2.03	2.43	2.63	2.16
164,412 - 380,000	10	19,748	2.51	2.57	3.25	2.57

- **Maximum likelihood estimator of Double Pareto distribution (DP):**

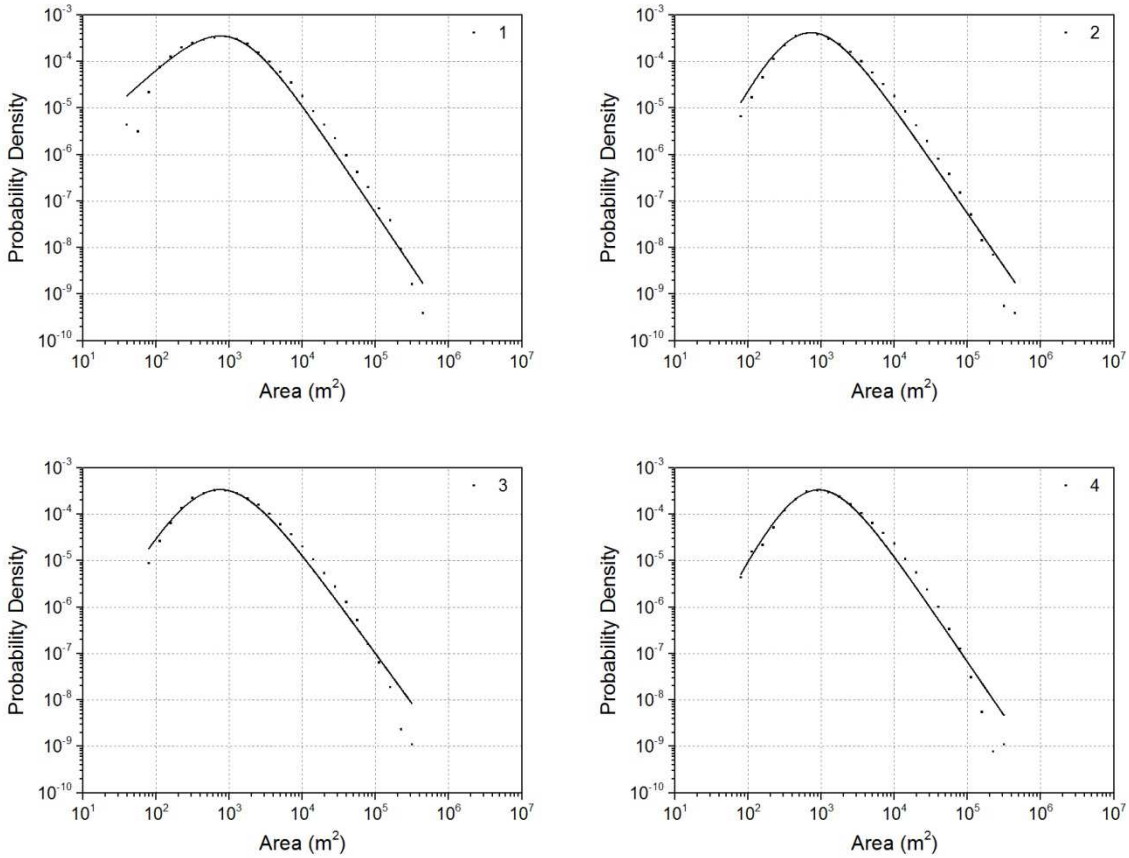

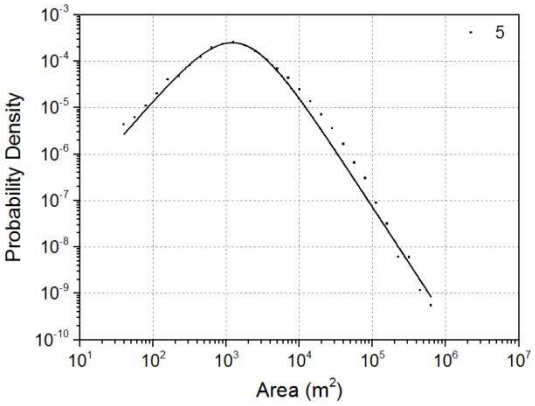

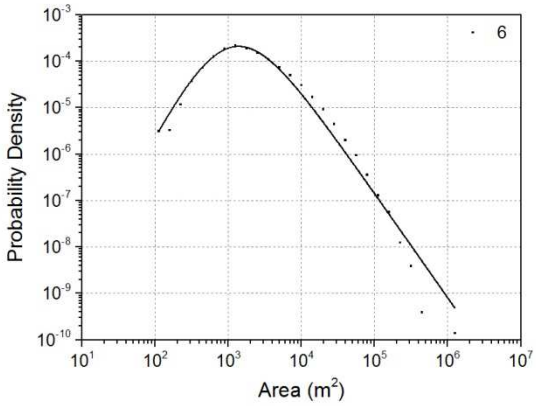

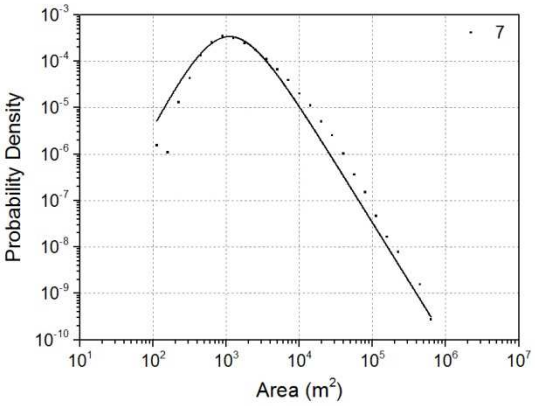

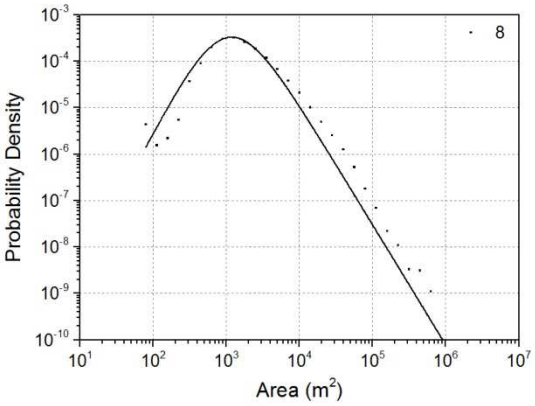

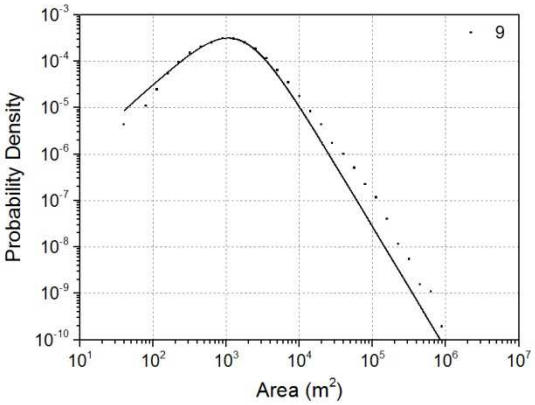

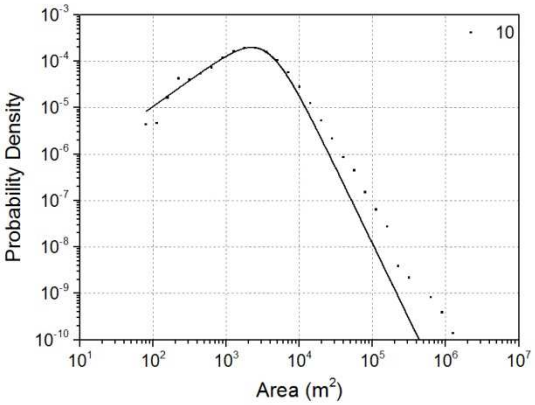

- **Maximum likelihood estimator of non-cumulative power-law function (PL):**

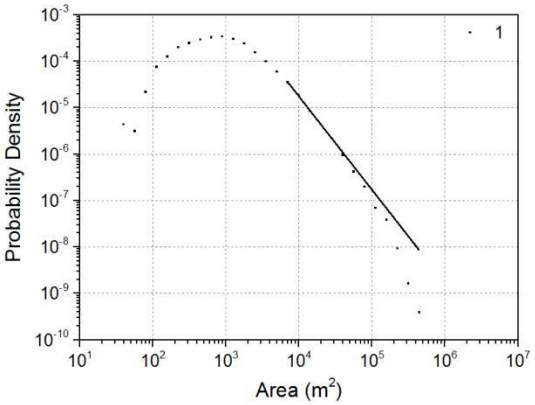

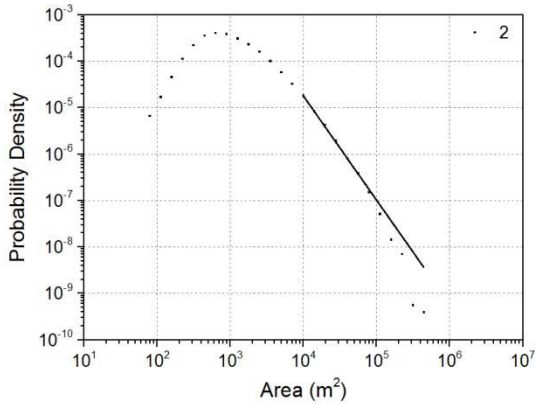

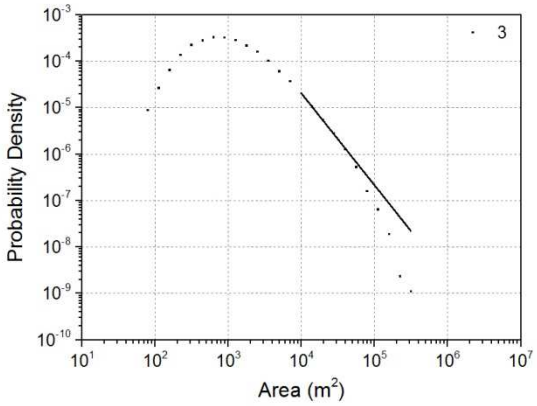
3
Probability Density
Area (m²)

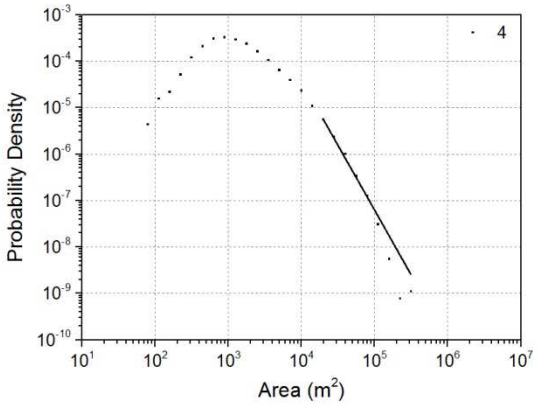
4
Probability Density
Area (m²)

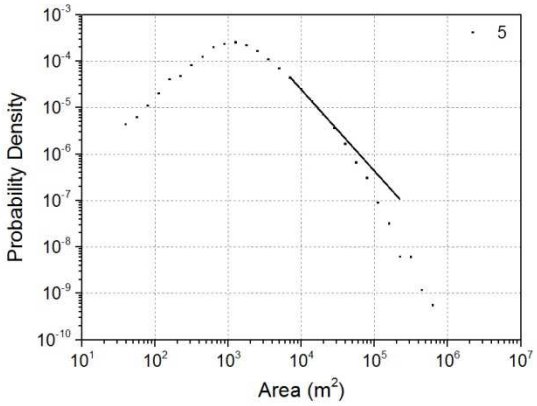
5
Probability Density
Area (m²)

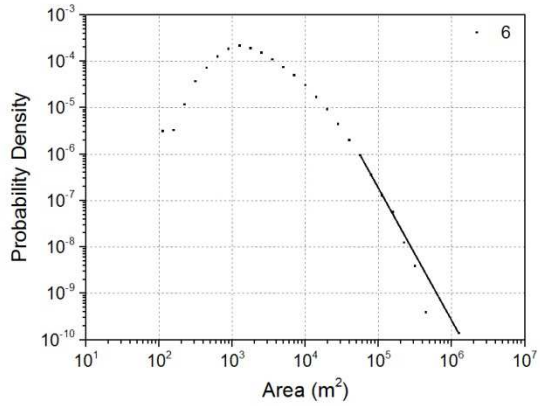
6
Probability Density
Area (m²)

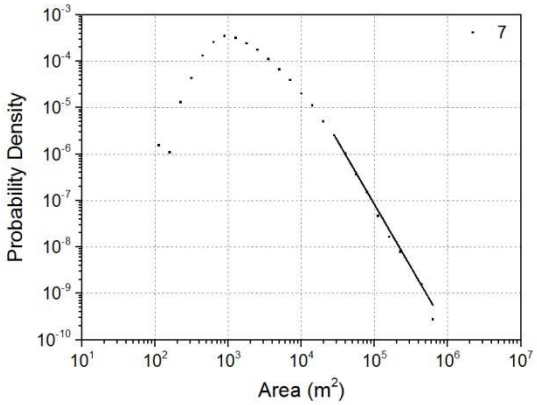
7
Probability Density
Area (m²)

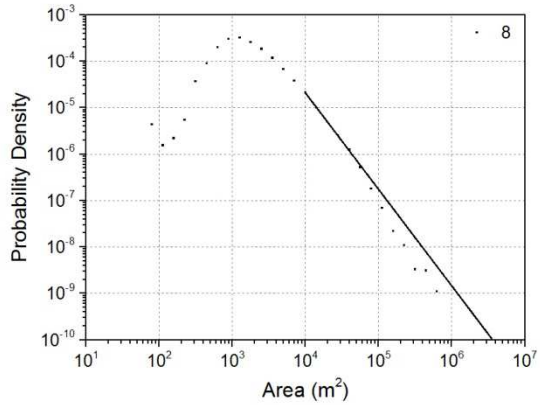
8
Probability Density
Area (m²)

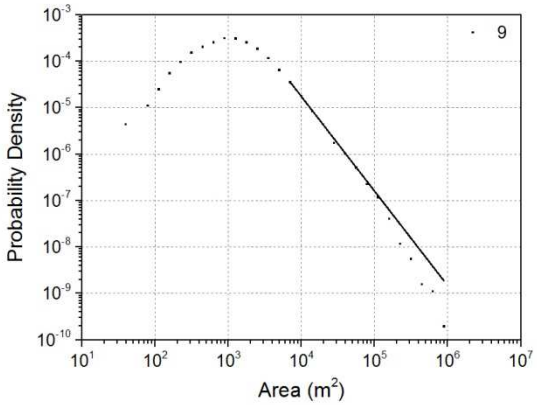
9
Probability Density
Area (m²)

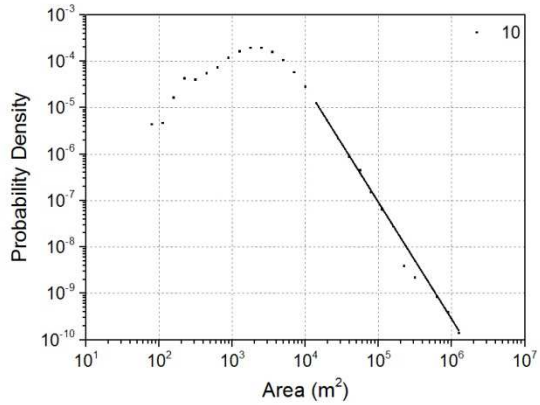
10
Probability Density
Area (m²)

- **Least square regression of non-cumulative log power-law function (LF):**

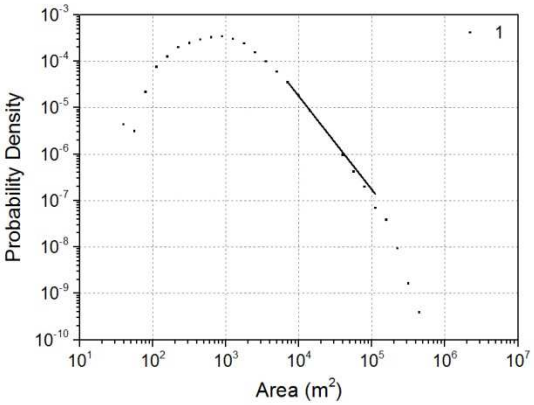

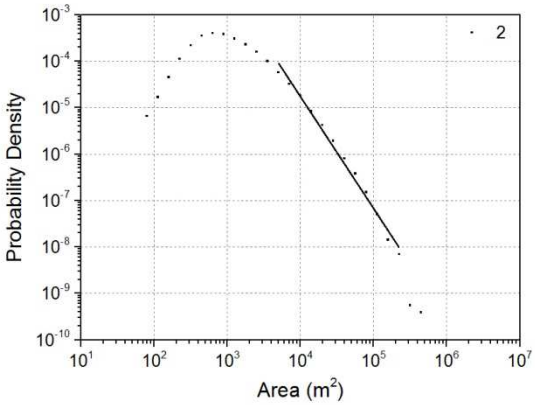

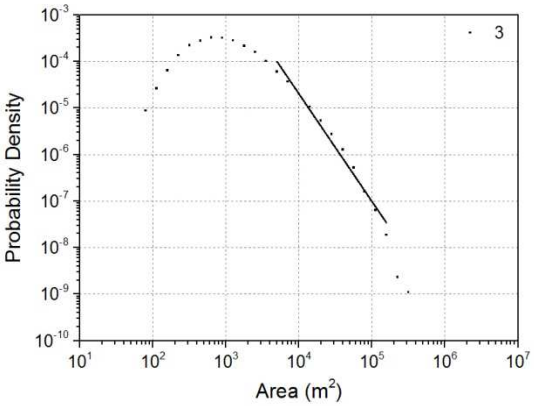

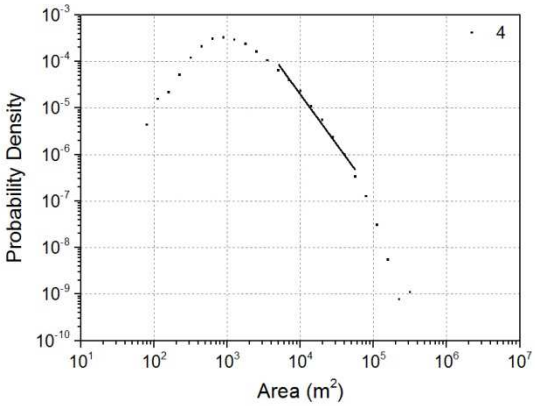

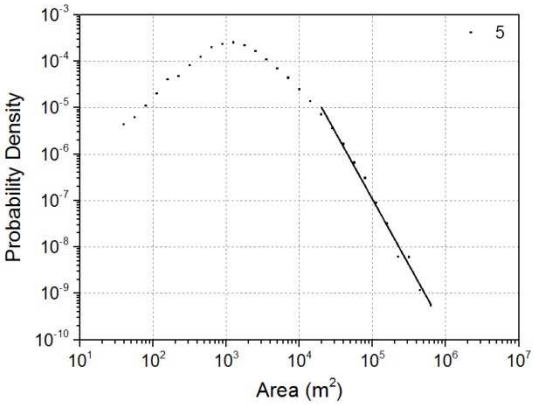

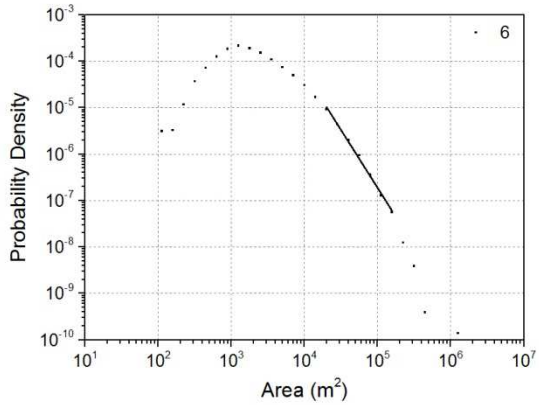

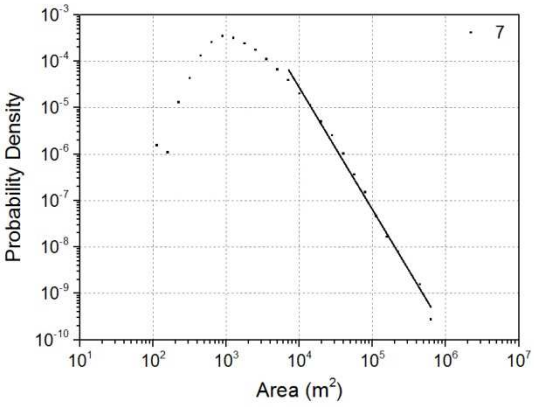

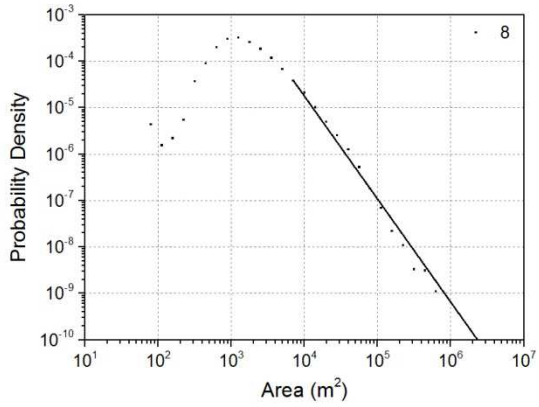

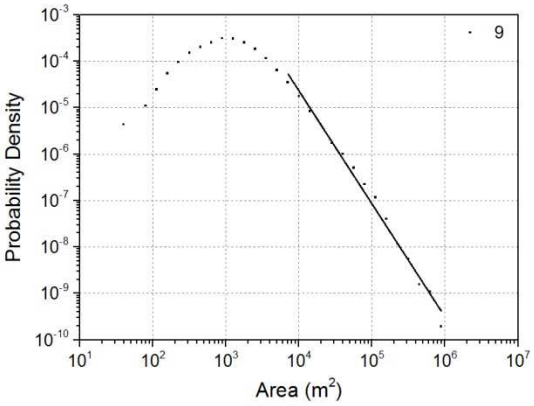

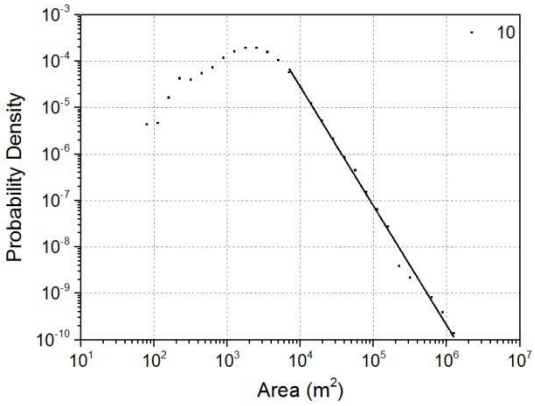

- **Maximum likelihood estimator of cumulative power-law distribution (ML):**

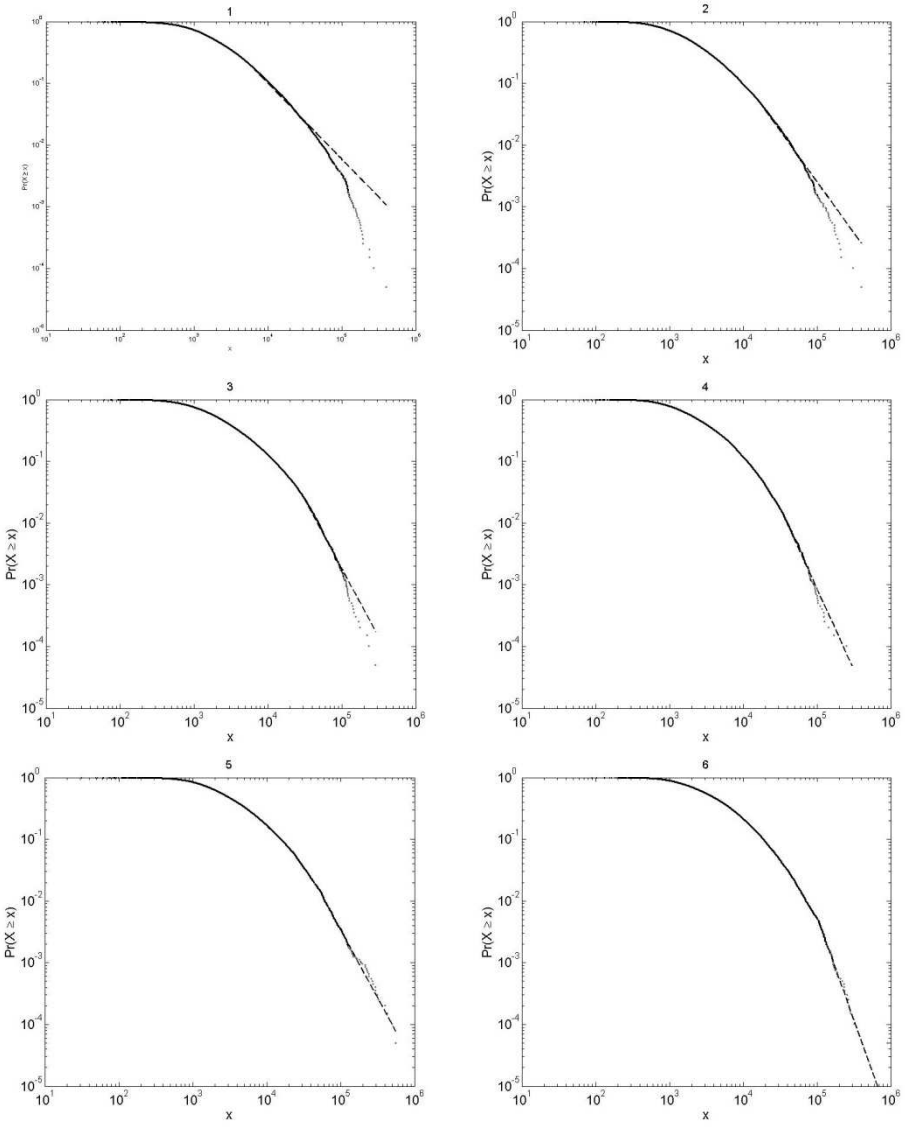

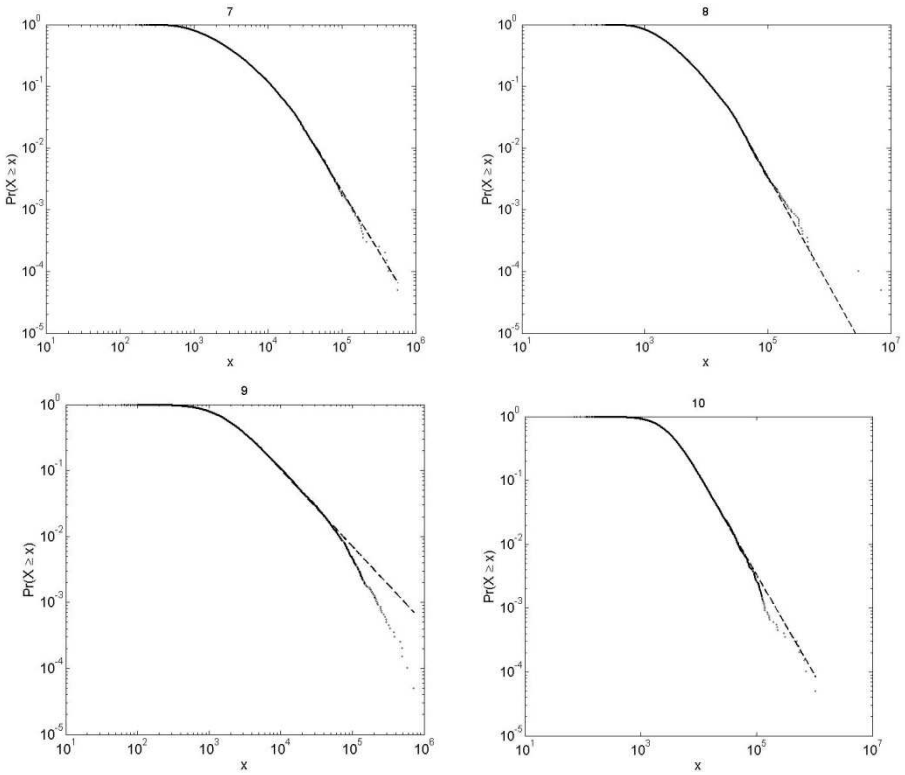
7
8
9
10
Pr(X ≥ x)
x

Fault rupture Distance

Classes of Distance (m)	Code	# landslides	PL	LF	DP	ML
0 - 1,346	1	19,749	2.01	2.49	2.38	2.38
1,346 - 2,800	2	19,747	1.97	2.60	2.42	2.90
2,800 - 4,593	3	19,747	2.29	2.33	2.39	2.91
4,593 - 6,784	4	19,749	2.04	2.68	2.39	2.31
6,784 - 9,820	5	19,748	2.13	2.00	2.30	2.72
9,820 - 12,886	6	19,748	2.21	2.61	2.18	2.41
12,886 - 16,987	7	19,749	2.11	2.50	2.21	3.86
16,987 - 23,242	8	19,749	3.07	3.18	2.39	3.28
23,242 - 32,169	9	19,748	2.54	2.35	2.40	4.12
32,169 - 160,000	10	19,748	2.38	2.50	2.63	2.60

- **Maximum likelihood estimator of Double Pareto distribution (DP):**

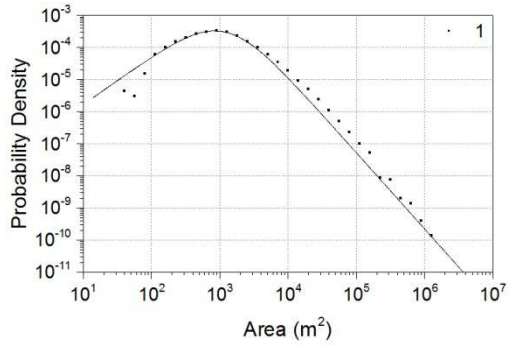

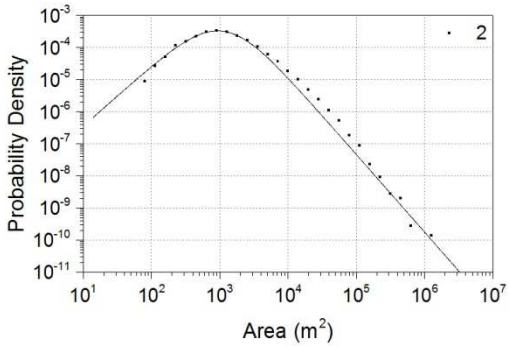

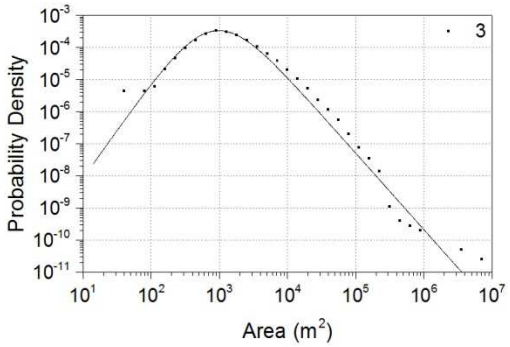

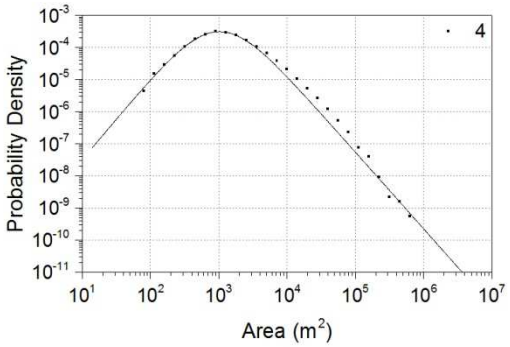

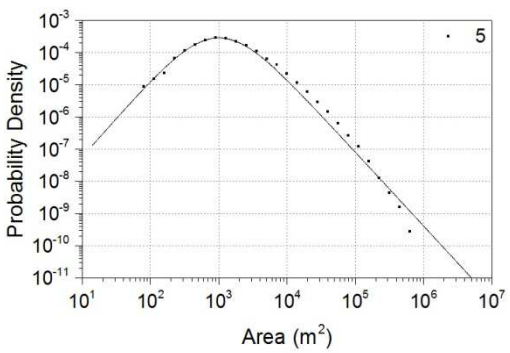

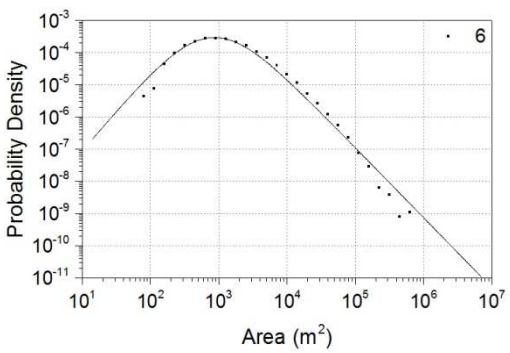

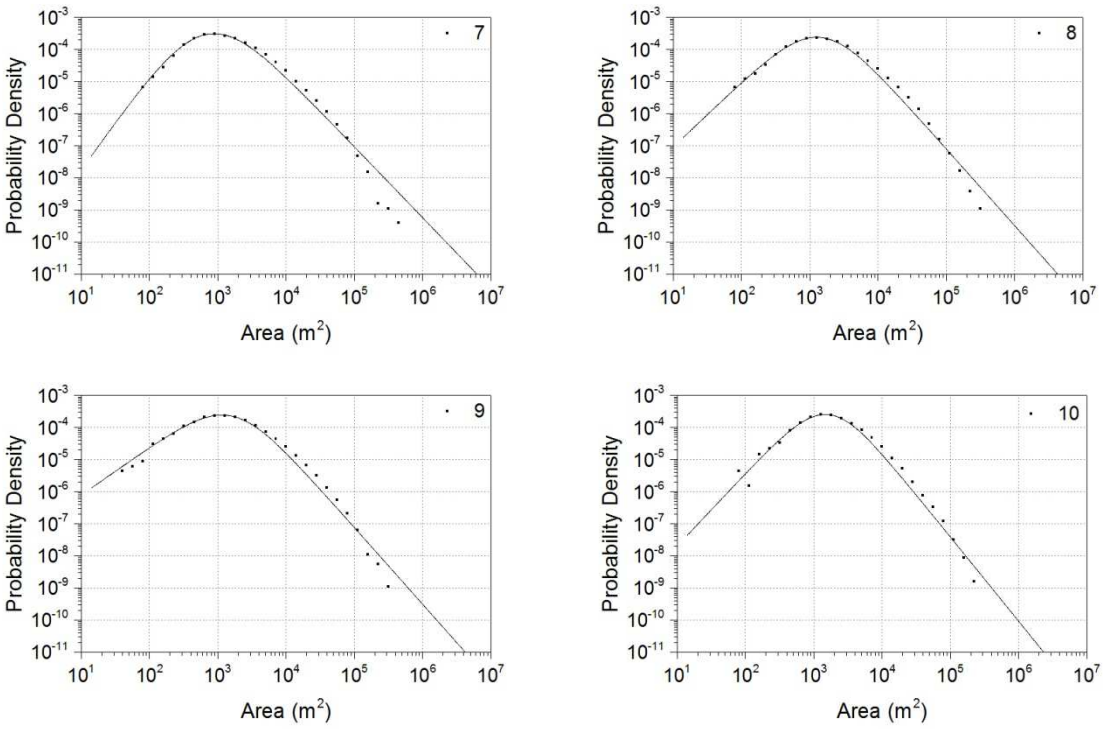

- **Maximum likelihood estimator of non-cumulative power-law function (PL), from 1 to 10:**

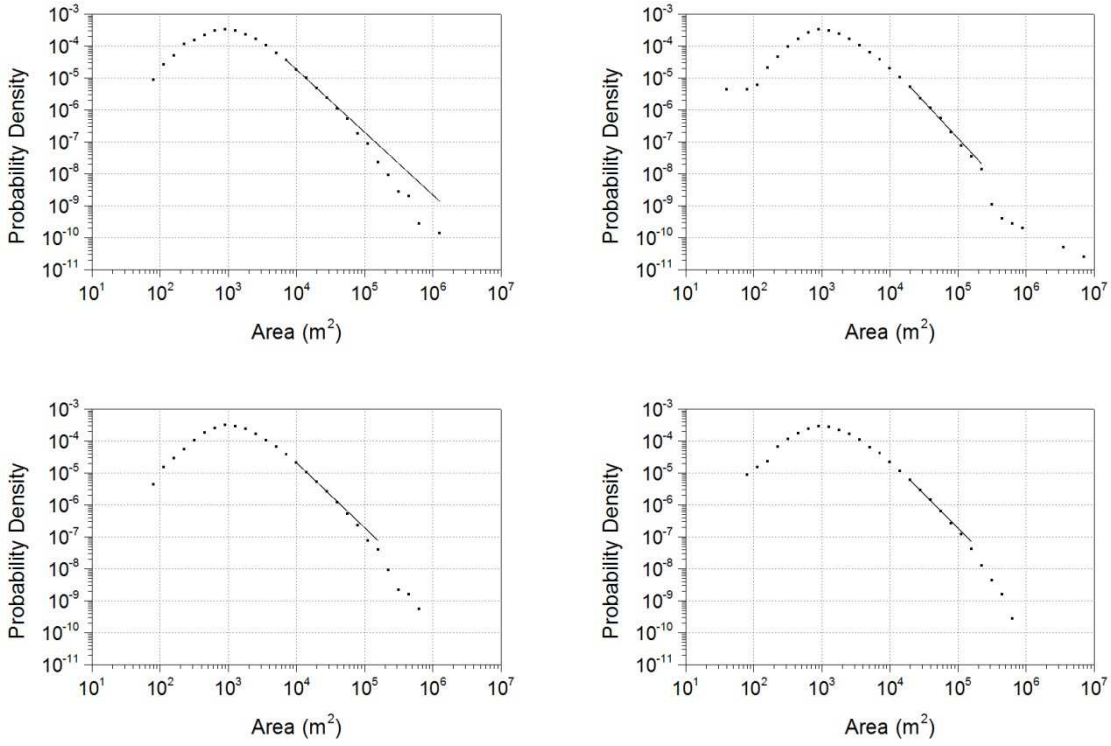

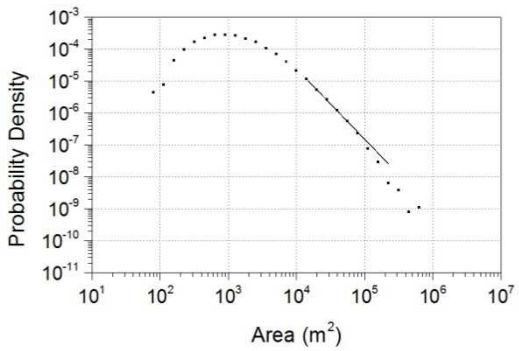

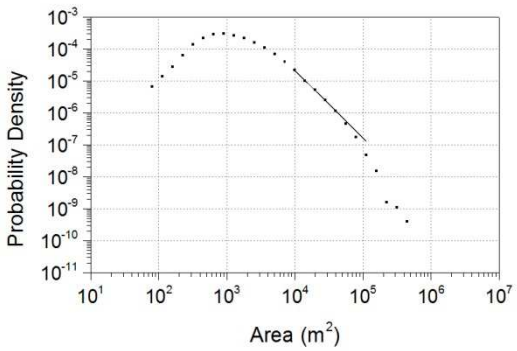

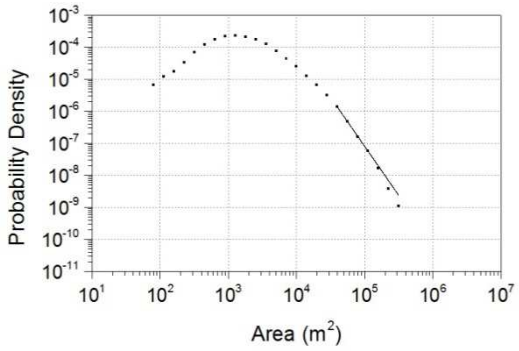

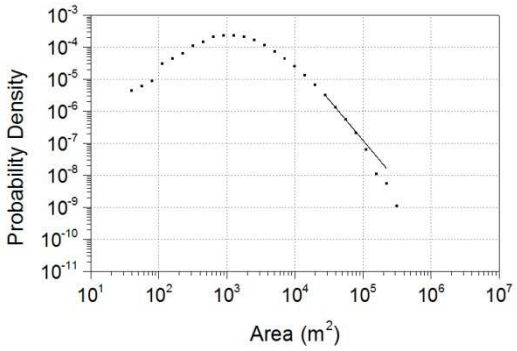

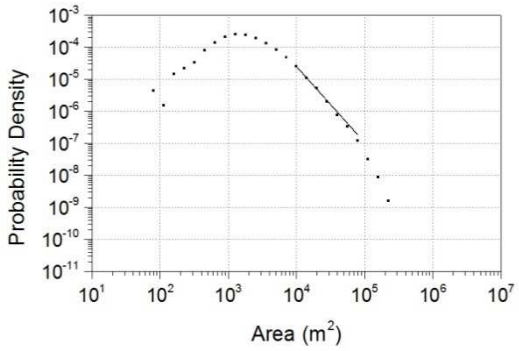

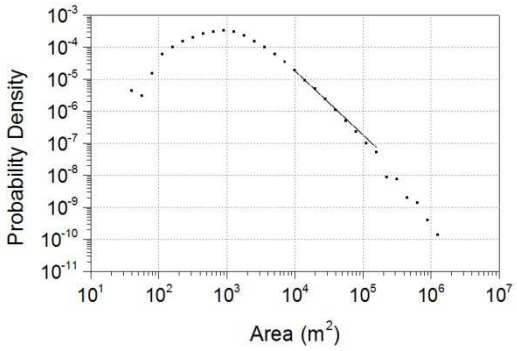

- **Least square regression of non-cumulative log power-law function (LF), from 1 to 10:**

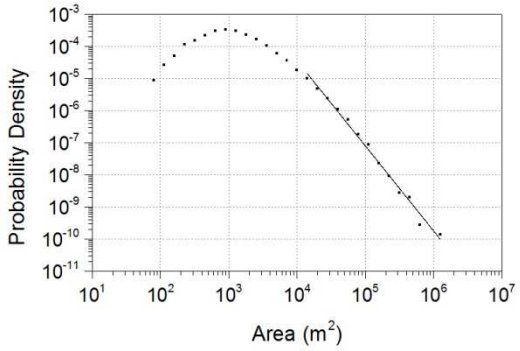

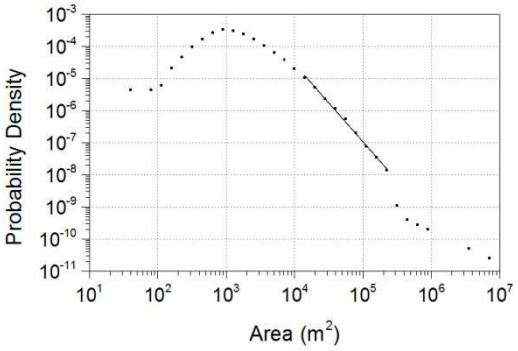

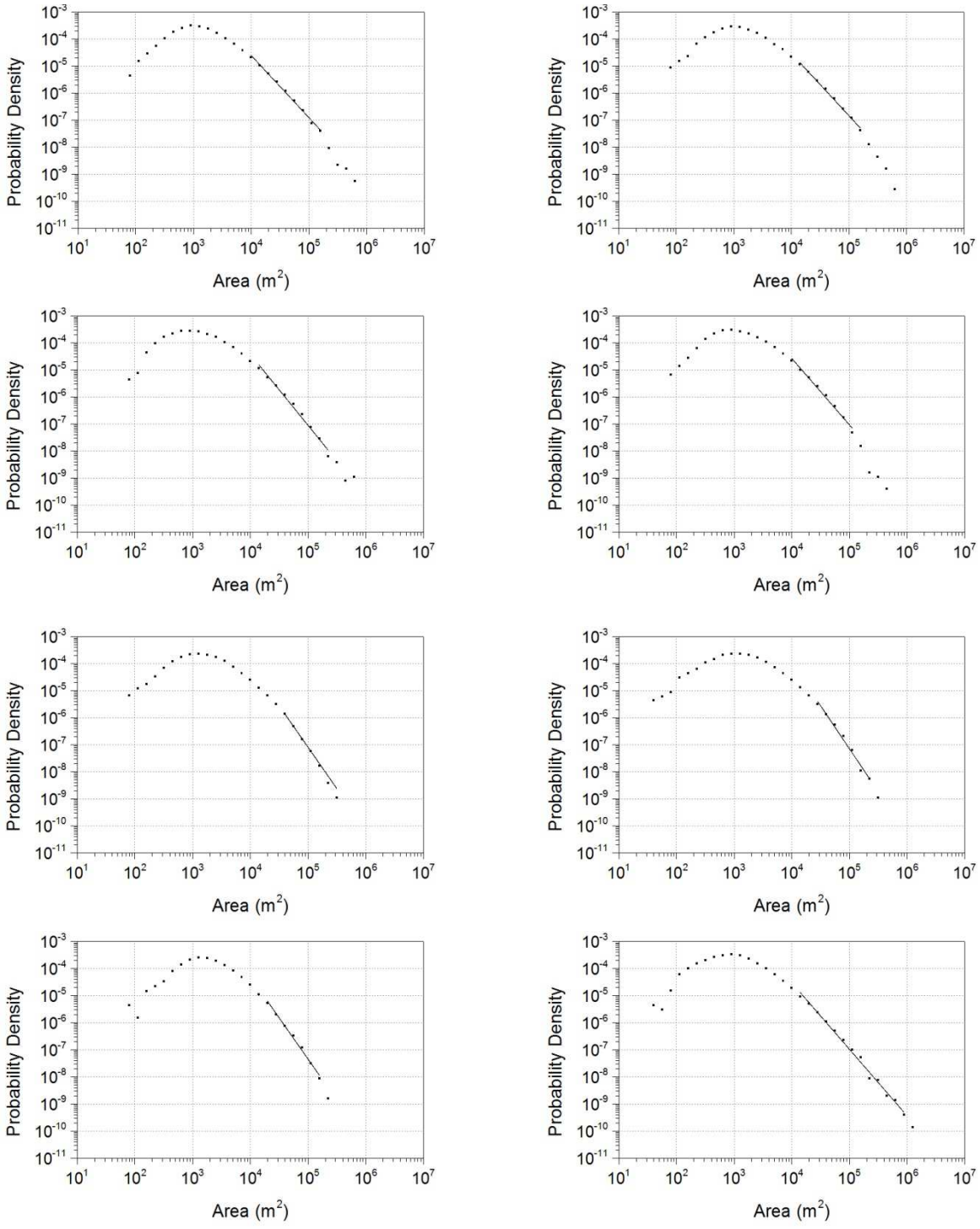

- **Maximum likelihood estimator of cumulative power-law distribution (ML):**

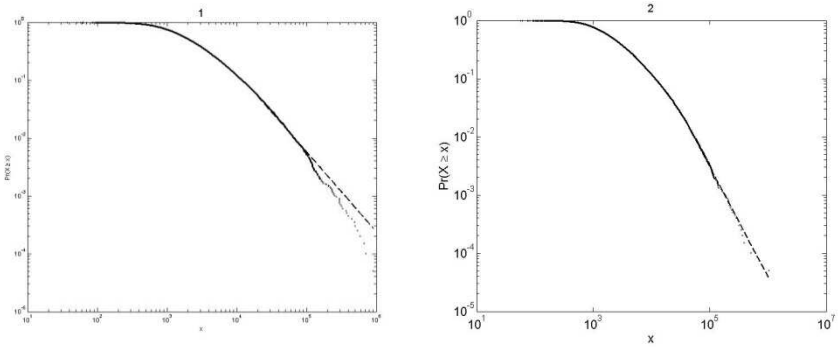

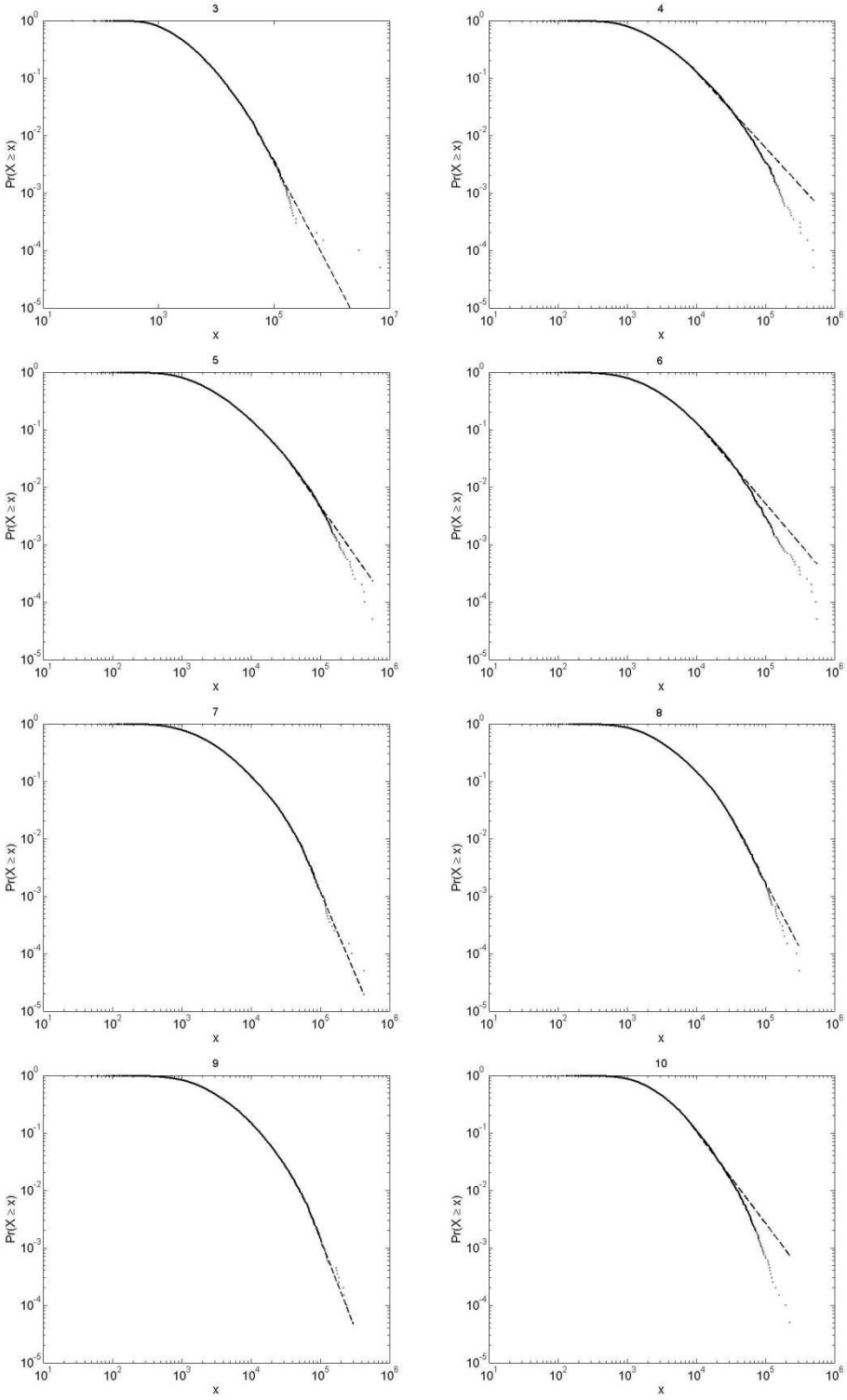
3
4
5
6
7
8
9
10
Pr(X ≥ x)
x

Appendix 3 - Fitting Curves for each lithology group, Wenchuan Earthquake, 2008

Group	Code	# landslides	DP	LF	PL
Quaternary Deposits	1	831	2.71	2.27	1.81
Conglomerates and Sandstone	2	20,380	2.61	2.71	3.05
Limestone	3	14,320	2.35	2.85	2.24
Limestone and Phyllite	4	3,589	2.45	2.23	2.26
Limestone and Sandstone	5	42,725	2.21	2.39	2.45
Phyllite and Limestone	6	8,911	2.60	3.01	2.50
Sandstone and Siltstone	7	21,567	2.26	2.54	2.02
Quartz and Feldspathic Sandstone	8	2,575	3.08	2.76	2.67
Schist and Andesite	9	8,175	2.53	2.76	2.41
Granitic rock	10	72,933	2.15	3.17	3.12

- **Maximum likelihood estimator of Double Pareto distribution (DP):**

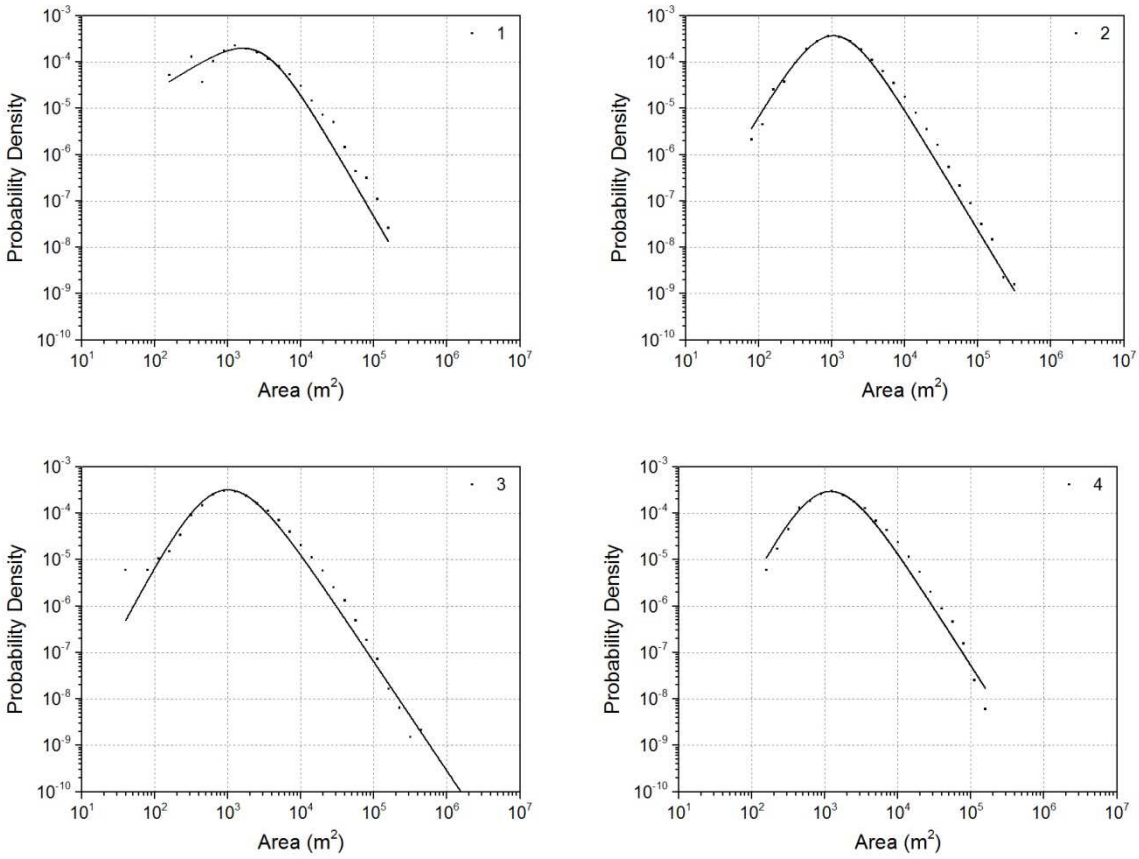

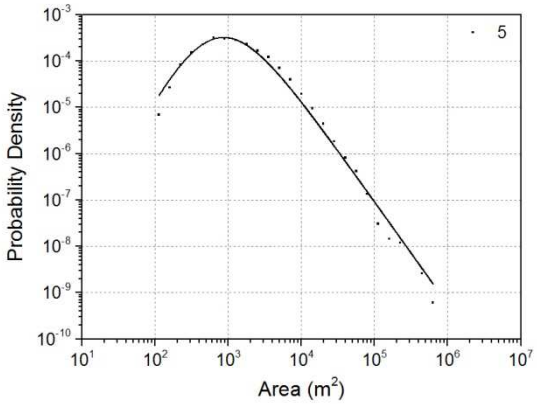

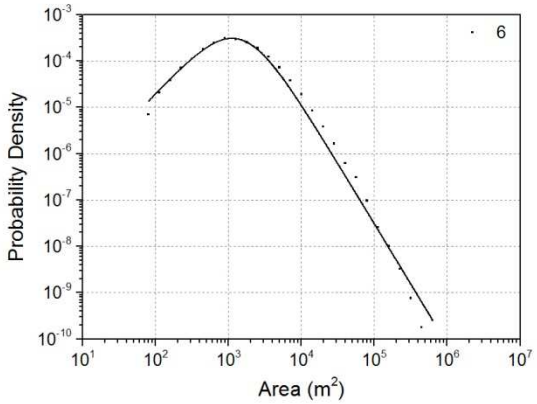

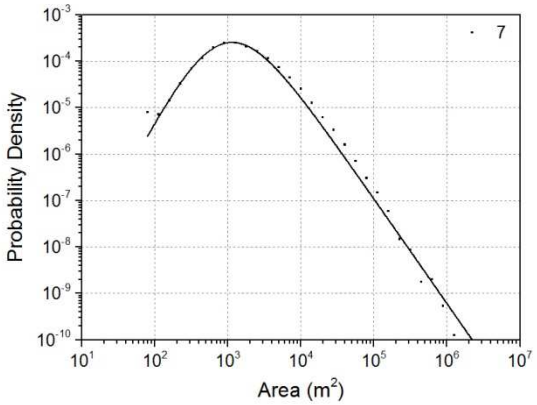

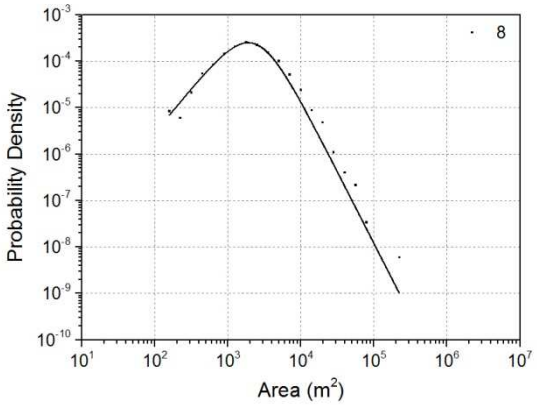

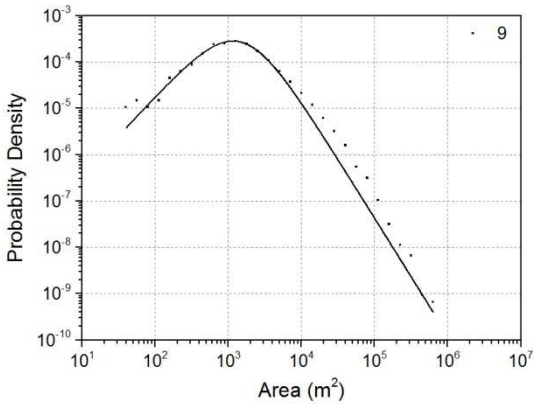

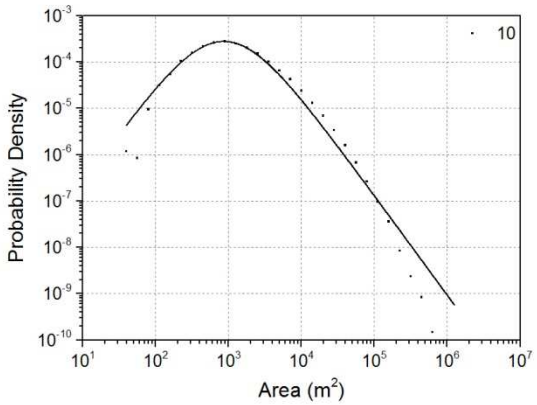

- **Maximum likelihood estimator of non-cumulative power-law function (PL):**

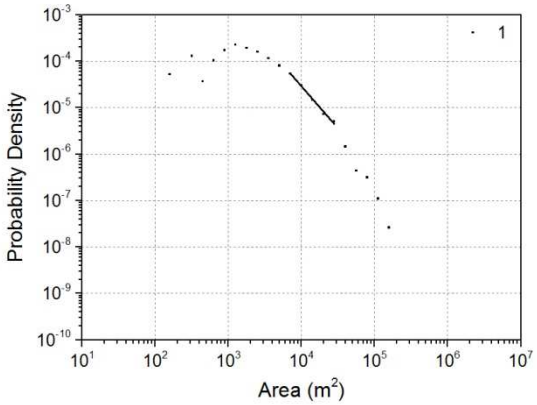

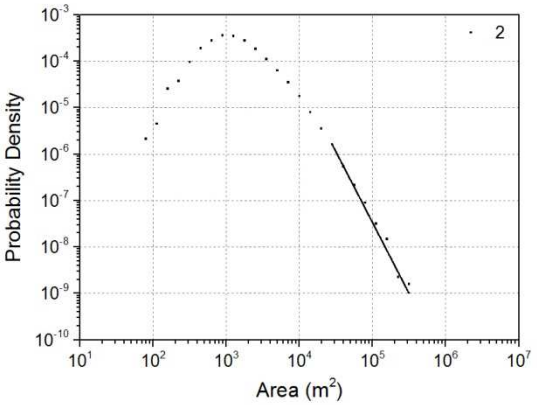

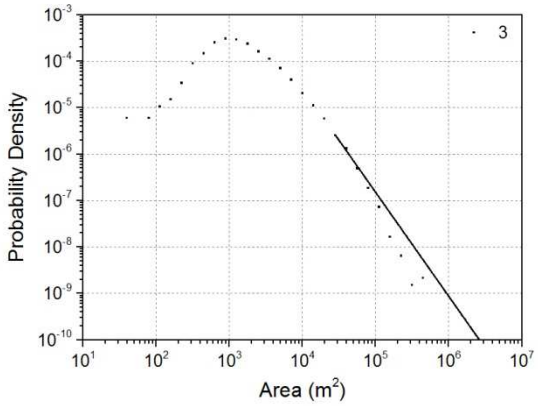
3
Probability Density
Area (m²)

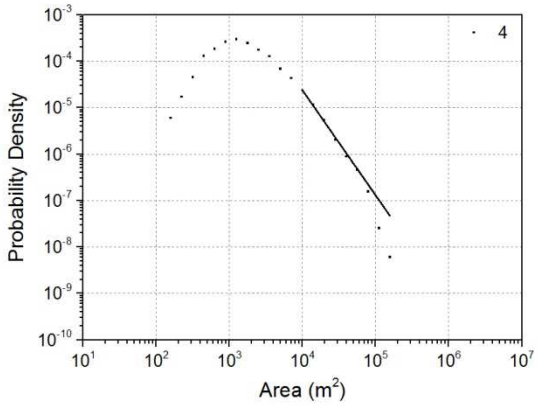
4
Probability Density
Area (m²)

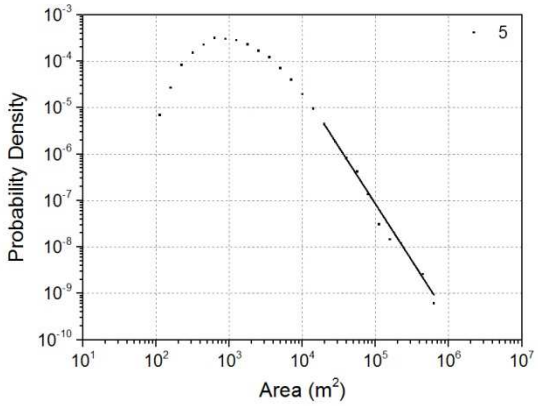
5
Probability Density
Area (m²)

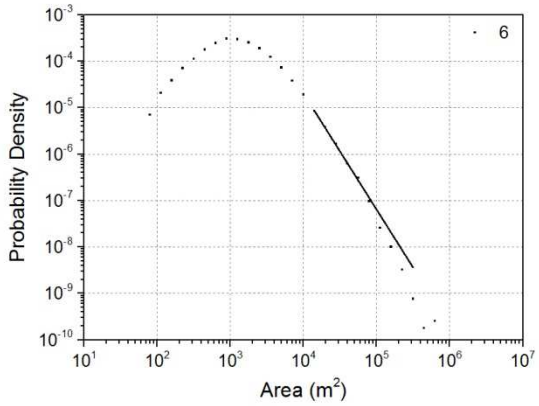
6
Probability Density
Area (m²)

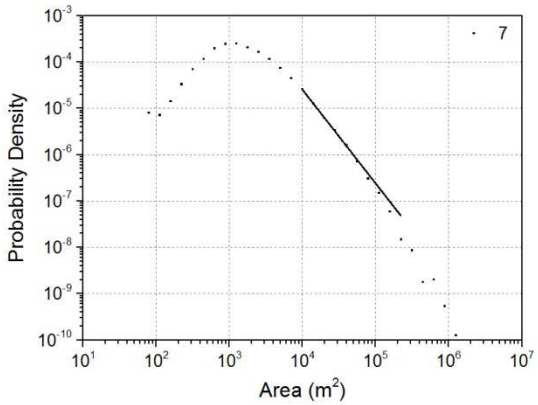
7
Probability Density
Area (m²)

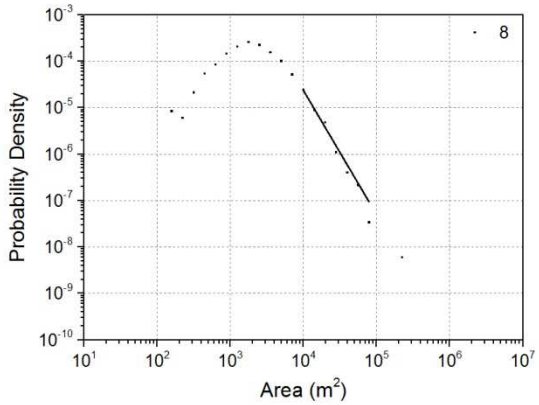
8
Probability Density
Area (m²)

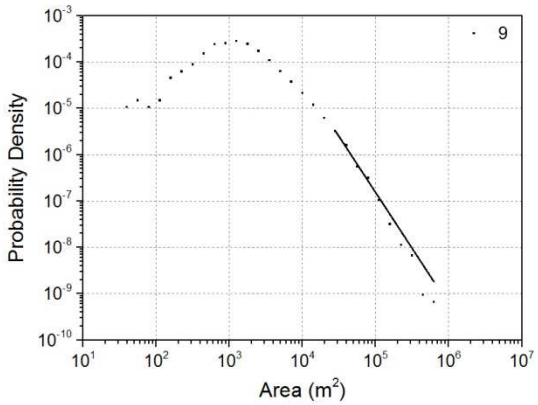
9
Probability Density
Area (m²)

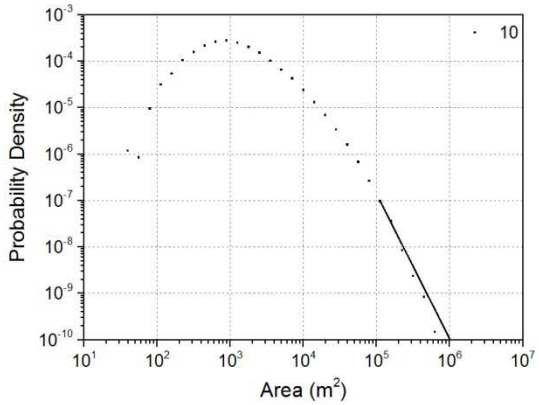
10
Probability Density
Area (m²)

- **Least square regression of non-cumulative log power-law function (LF):**

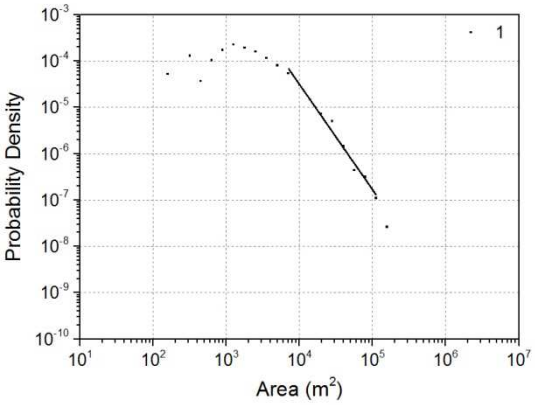

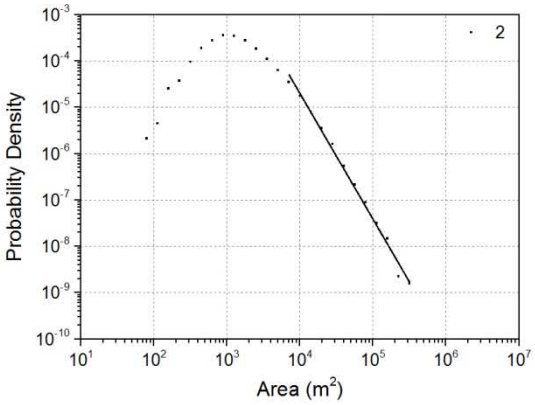

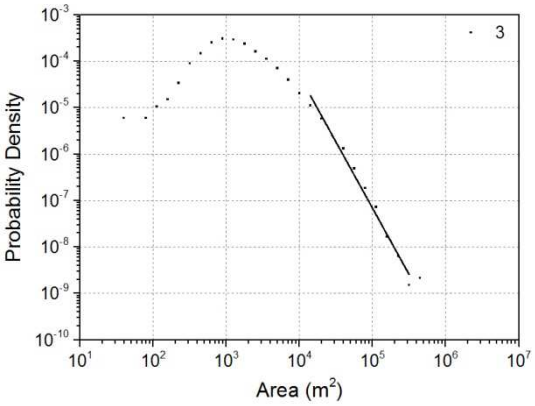

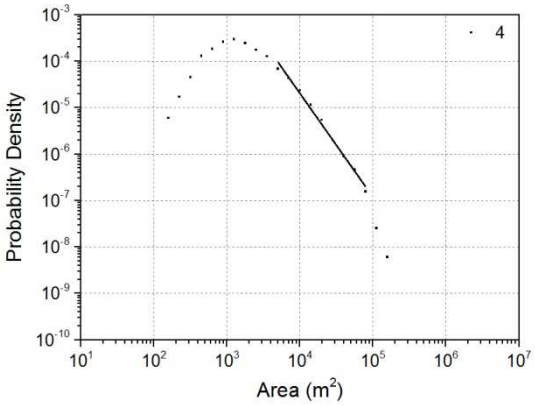

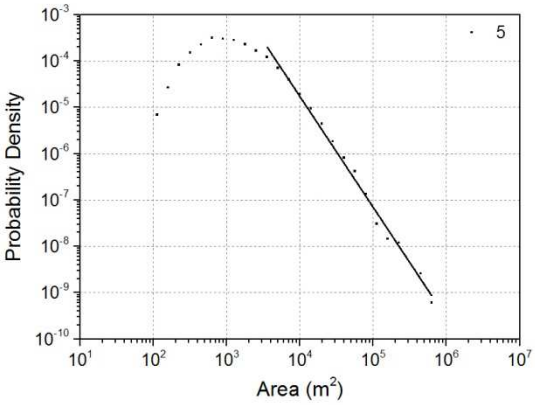

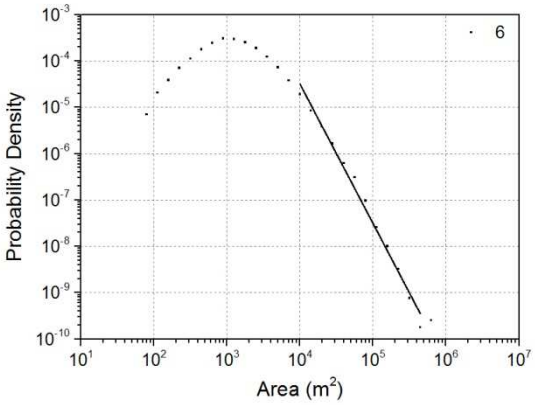

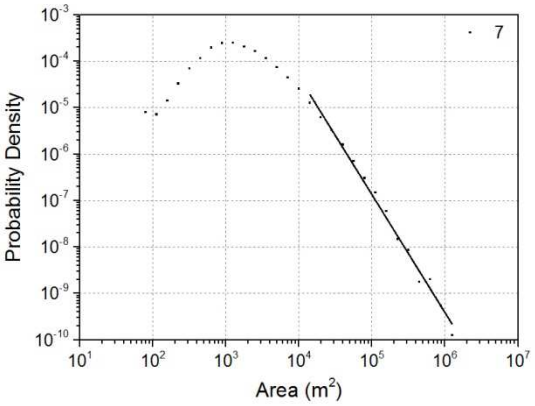

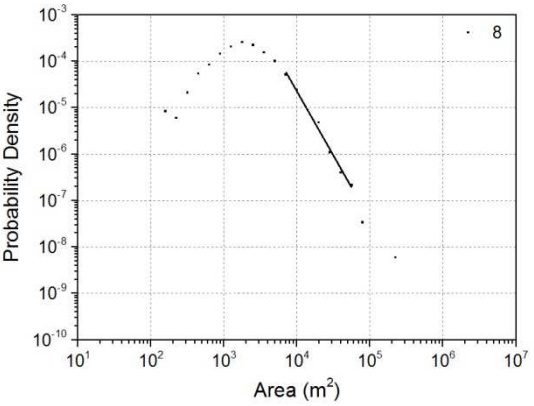

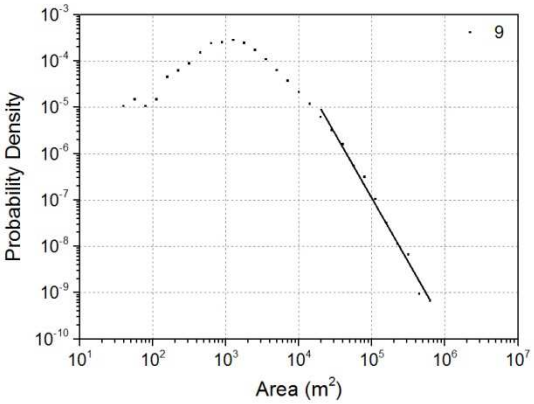
9
Probability Density
Area (m2)

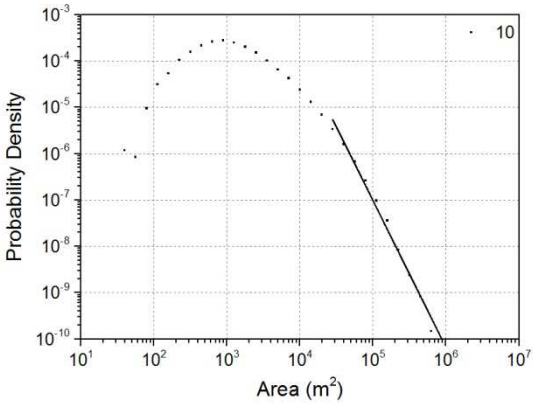
10
Probability Density
Area (m2)